

Radar Remote Sensing of Arid Regions

by

Adel A. Elsherbini

A dissertation submitted in partial fulfillment
of the requirements for the degree of
Doctor of Philosophy
(Electrical Engineering)
in The University of Michigan
2011

Doctoral Committee:

Professor Kamal Sarabandi, Chair
Professor Ronald Gilgenbach
Professor Eric Michielssen
Professor Mahta Moghaddam

© Adel A. Elsherbini 2011

All Rights Reserved

To my father and mother with love and gratitude.

ACKNOWLEDGMENTS

Most importantly, I would like to thank my research advisor and mentor, Prof. Kamal Sarabandi. He offered me the chance to work with him on many interesting and challenging problems. He is a truly outstanding and inspiring advisor. I cannot count the times I almost gave up on some of the research problems but he would encourage me to think on it from a different angle and we end up reaching a solution. I would like also to thank Prof. Eric Michielssen, Prof. Mahta Moghaddam and Prof. Ronald Gilgenbach for their service on my dissertation committee.

During my PhD research period at the University of Michigan, I had the opportunity to interact with many outstanding researchers and to learn a lot from them. In particular, I would like to thank Dr. Adib Nashashibi for his assistance and advice on several research and measurements problems. I would like also to thank Pelumi Osoba, Fikadu Dagefu, Yohan Kim, Dr. Line Van Nieuwstadt, Victor Lee, Danial Ehyaie, Michael Benson, Dr. Wonbin Hong, Dr. Michael Thiel, Dr. Mojtaba Dehmollaian, Scott Rudolph, Amit Patel, Mark Haynes, Yuriy Goykhman, Hatim Bukhari, Young Jun, Dr. Jacquelyn Vitaz, Xueyang Duan, Meysam Moallem, Yong Jun Song, Sangjo Choi, Dr. Alireza Tabatabaeenejad, Onur Bakir, Jungsuek Oh, Xi Lin, Dr. Juseop Lee, Dr. Josh Fu, Chris Berry, Mehrnoosh Vahidpour, Mariko Burgin, Ning Wang and Christine Tannahill for their continuous help and support and for being not only good research colleagues but also good friends.

I wouldn't have reached this stage without the support and encouragement of many of my research colleagues and friends from my previous schools. In particular, I would like to thank my previous advisors, Prof. Alaa Kamel, Prof. Aly Fathy, Prof. Abbas Omar and Prof. Hadia Elhennawy and my uncle, Prof. Moniem Elsherbiny. They encouraged me to work in the field of electromagnetics and they taught me the basics and ethics of doing research. I would like also to thank my research colleagues and friends, Dr. Song Lin, Dr. Ahmed Boutejdar, Dr. Songnan Yang, Dr. Cemin (Alex) Zhang, Dr. Chunna Zhang, Dr. Mohammed Awida, George Isaac, Amr Elshazly, Dr. Telesphor Kamgaing, Dr. Henning Braunisch, Dr. Krishna Bharath, Amr Ali and Amr Amin.

Adel A. Elsherbini

April 29, 2011

Table of Contents

DEDICATION	ii
ACKNOWLEDGMENTS	iii
LIST OF FIGURES	x
LIST OF TABLES	xxiii
Chapter 1 Introduction.....	1
1.1 Motivation.....	1
1.2 Applications	2
1.2.1 Oil Fields and Ground Water Explorations	2
1.2.2 Mine Field Detection	3
1.2.3 Other Applications	5
1.3 Approach.....	6
1.4 Thesis Framework.....	9
Chapter 2 Subsurface InSAR Design	13
2.1 Conventional Interferometric SAR (InSAR)	13
2.2 Extension of InSAR for Subsurface Mapping	15
2.2.1 Sample Scenario.....	15
2.2.2 Proposed System.....	16
2.3 Scattering Phenomena.....	17
2.4 Subsurface InSAR Processing	22

2.4.1	Subsurface Focusing	23
2.4.2	Image Coregistration.....	24
2.5	Left/Right Separation.....	27
2.6	Conclusion	30
Chapter 3	Subsurface Topography Inversion Algorithm	32
3.1	Subsurface Propagation Modeling.....	32
3.2	Inversion Algorithm.....	34
3.3	Sensitivity Analysis of the Height Estimation	39
3.4	Experimental Results	44
3.5	Conclusion	48
Chapter 4	Image Distortion Effects in SAR Subsurface Imaging and a New Iterative Approach for Refocusing and Coregistration	50
4.1	Fast Subsurface SAR Simulator & Subsurface Focusing Technique	51
4.2	Defocusing and Distortion Effects in SAR Subsurface Imaging.....	56
4.2.1	Defocusing Effects.....	56
4.2.2	Geometric Distortion Effects	58
4.2.3	Caustic Surfaces and their Effects	61
4.3	Iterative Approach	66
4.4	Simulation Results	67
4.5	Scaled Model Measurement Results.....	71
4.6	Conclusion	72
Chapter 5	Linearly Polarized Ultra-Wideband Antennas.....	74
5.1	Background.....	75

5.1.1	Definitions.....	75
5.1.2	Design Issues	75
5.1.3	Common Structures	78
5.1.4	Omni-Directional Coupled Sectorial Loop Antenna (CSLA)	78
5.2	Folded CSLA	82
5.2.1	Folded CSLA with Vivaldi Antenna.....	85
5.2.2	Reflector Design for UWB Operation	87
5.2.3	Vivaldi-CSLA Antenna with Reflector	89
5.3	Rectangular Waveguide UWB Antennas.....	96
5.3.1	Introduction.....	96
5.3.2	Antenna Structure and Operation.....	97
5.3.3	Design Process	99
5.3.4	Feed design	102
5.3.5	Measurement Results	104
5.4	Conclusion	107
Chapter 6	High Isolation T/R UWB Antenna Pair	108
6.1	Introduction and Motivation	108
6.2	Antenna Structure and Operation.....	112
6.3	Parametric Study.....	114
6.3.1	Cavity Fins	115
6.3.2	Sectorial Loop Angle	116
6.3.3	The Cavity Height.....	117
6.3.4	Antenna Separation.....	118

6.3.5	Tapered Feed Line	119
6.4	Measurement Results	121
6.4.1	Input Impedance and Pattern Measurements	121
6.5	Comparison to other structures	124
6.6	Conclusion	126
Chapter 7	Dual Polarized UWB Antennas	127
7.1	Dual Polarized Directional Cavity Backed CSLA	127
7.1.1	Antenna Structure	127
7.1.2	Parametric Study	129
7.2	Diversity Omni-Directional CSLA	133
7.2.1	Antenna Structure	133
7.2.2	Measurement Results	136
7.3	Directional Cavity Backed Dual-Polarized CSLA	138
7.3.1	Antenna Structure and Principle of Operation	138
7.3.2	Parametric Study	141
7.3.3	Actual Feeding Structure	144
7.3.4	Measurement Results	148
7.4	Conclusion	150
Chapter 8	Very Low Profile UWB Antennas	151
8.1	Very Low Profile UWB Monopole	151
8.1.1	Introduction	151
8.1.2	Antenna Structure and Operation	153
8.1.3	Parametric Study	156

8.1.4	Measurements Results	160
8.2	Very Low Profile Directive Antenna	162
8.2.1	Antenna Structure and Operation.....	163
8.2.2	Parametric Study.....	166
8.2.3	Measurement Results	169
8.2.4	Improving the Cross-Pol Components.....	171
8.3	<i>Conclusion</i>	173
Chapter 9	Conclusion and Future Work	176
9.1	Conclusions.....	176
9.1.1	Scattering Phenomena.....	176
9.1.2	Subsurface Processing	177
9.1.3	Inversion Algorithm.....	177
9.1.4	Image Correction Algorithm.....	178
9.1.5	Compact UWB Antennas.....	178
9.1.6	Linearly Polarized UWB Antennas	179
9.1.7	High Isolation Antenna Pair.....	180
9.1.8	Dual Polarized Antennas.....	181
9.1.9	Very Low-Profile Antennas	181
9.2	Future Work	182
9.2.1	Scattering from Targets under a Rough Surface.....	182
9.2.2	Scattering from Large Dunes	182
9.2.3	Scattering and Propagation in Dense Random Media	183
	Bibliography	184

LIST OF FIGURES

Figure 1.1: (a) Schematic Diagram of the basic structure of GPR and (b) a photo of a human operated ground based GPR (Reproduced from [9]).	2
Figure 1.2: Seismic test in arid regions for oil field or ground water exploration.....	3
Figure 1.3: (a) An array of point targets under a sand dune, (b) SAR image using conventional SAR focusing and using subsurface focusing.	5
Figure 1.4: (a) Sand dunes in Proctor Crater on Mars [12] and (b) Sand dunes advancing towards the city of Nouakchott (the capital of Mauritania) [13].	6
Figure 1.5: Conventional remote sensing techniques for terrain mapping [14].	7
Figure 1.6: The proposed dual frequency InSAR systems, Ka-InSAR provides top surface height information that are then used to correct the VHF InSAR data to obtain the correct subsurface height.	8
Figure 1.7: The Different Aspects of the Problem of Radar Remote Sensing of Arid Regions.	10
Figure 2.1: Steps for generating the terrain height using InSAR.....	14
Figure 2.2: Using conventional InSAR phase-to-height equations results in severe errors in the estimated bedrock height.	16
Figure 2.3: (a) Wave propagation path for the Ka-InSAR (high frequency) and (b) wave propagation path for VHF-InSAR (low frequency).....	17

Figure 2.4: Arid areas considered (in Saudi Arabia). The two figures on the left show the large scale undulations (with a person standing next to a sand dune in the leftmost photo for comparison) whereas the figure to the right shows the small scale undulations.....	18
Figure 2.5: Promoted scattering mechanisms.	19
Figure 2.6: Simulated backscattering cross-section for the bedrock and sand surfaces using the parameters in Table 2.2. The decrease in the bedrock backscattering at higher frequencies is due to the attenuation through the sand.	21
Figure 2.7: Numerically calculated backscattering coefficient of the c50-70 sand layer as a function of radar frequency. The sand layer was assumed 0.15 m thick, has 0.6 in volume fraction (from [36]).	22
Figure 2.8: Simulation Scenario for VHF SAR focusing on a point target at depth Z_t below the sand surface.	24
Figure 2.9: (a) PSF range section, (b) PSF azimuth section for 20° integration angle, (c) PSF azimuth section for 15° integration angle and (d) PSF azimuth section for 10° integration angle.....	26
Figure 2.10: Image distortion due to top surface undulations (a) geometry and (b) focused SAR image.	26
Figure 2.11: (a) The antenna pattern for conventional SAR operation and (b) for the VHF-SAR showing that the undesired targets on the other side of the plane are no longer suppressed by the antenna radiation pattern.	27
Figure 2.12: Left/right separation diagram.	28
Figure 2.13: Fourier transform of the interferogram.	29

Figure 2.14: The RMS phase error after using two step filters to separate the left and right components for flat topography vs. the baseline for different operating bandwidths.	30
Figure 3.1: Geometrical optics modeling for subsurface imaging VHF InSAR (not to scale for clarity).	33
Figure 3.2: Flow chart of the proposed iterative algorithm for estimating the sand height above the underlying bedrock.	34
Figure 3.3: Illustration of the iterative algorithm.....	37
Figure 3.4: Examples of the results of the iterative algorithm to some sand geometries, (a) Gaussian shaped dune on top of inverse Gaussian shaped bedrock and (b) linear sand dunes on top of flat sloped bedrock.	38
Figure 3.5: Sensitivity of height estimation to sand dielectric constant.	40
Figure 3.6: Sensitivity of height estimation to interferogram phase accuracy.	41
Figure 3.7: Relative sand thickness errors due to finite range accuracy.....	42
Figure 3.8: Bedrock height errors due to (a) errors in sand height estimation and (b) errors in sand slope estimation.	43
Figure 3.9: Scaled model for verification of the inversion algorithm, (a) schematic and (b) photo of the actual system.....	44
Figure 3.10: Experiment scenario, flat sand on top of horizontal bedrock. (a) A photo of the scene (the sand layer thickness is 7.8cm and the radar movement is along the horizontal direction), (b) the two SAR images for the two paths (x corresponds to the azimuth direction)	47

Figure 3.11: Scaled Model Results: (a) The averaged interferogram (4x4 boxcar averaging), (b) the unwrapped interferogram, (c) the estimated heights using the conventional InSAR and (d) the estimated heights using the proposed algorithm...	48
Figure 4.1: 3D SAR Geometry.	52
Figure 4.2: Interpolation over a non-uniform grid to obtain the target range history. The contour represents the electrical range to the radar position. The actual grid points and sand surface are 3D, but the 2D case is plotted for clarity.....	55
Figure 4.3: Azimuth Point Spread Function (APSF) of a point target vs. the target depth when using conventional focusing with focusing plane at the surface with (a) 20° integration angle and (b) 40° integration angle, (c) and (d) same scenarios as (a) and (b) but the target is assumed in air.	58
Figure 4.4: Sample scenario to illustrate geometric distortion in subsurface SAR images due to top layer propagation effects, (a) the simulation scenario and (b) the conventionally focused SAR image.....	60
Figure 4.5: (a) The barchan sand dune, (b) side view and (c) top view of the estimated caustic surface with the sand dune. The dotted arrows in (c) show the caustic surfaces corresponding to each curved feature on the sand dune. The radar position is at (0, 0, 5 km).	63
Figure 4.6: (a) A target at (0, 2025, -60) enclosed within a simple caustic surface appearing at three different ranges and (b) the simulated range history of the target using the extended interpolation technique.....	65
Figure 4.7: The proposed iterative scheme.	67

Figure 4.8: Results of applying the subsurface focusing algorithm: (a) scene consisting of a linear sand dune and a grid of point targets, (b) the improvement in coherence vs. different iterations, (c) normalized image from conventional focusing with 10° integration angle, (d) normalized image from conventional focusing with 40° integration angle, (e) first iteration of the subsurface focusing algorithm and (f) 3rd iteration with 40° integration angle. 69

Figure 4.9: Results of applying the subsurface focusing algorithm: (a) scene consisting of a barchan sand dune and a grid of point targets, (b) the improvement in coherence vs. different iterations, (c) normalized image from conventional focusing with 10° integration angle, (d) normalized image from conventional focusing with 40° integration angle, (e) first iteration of the subsurface focusing algorithm and (f) 3rd iteration with 40° integration angle. 70

Figure 4.10: (a) Conventionally focused SAR image of the scaled model and (b) comparison between the two coherence histograms obtained. 72

Figure 5.1: Some Conventional UWB Antennas 78

Figure 5.2: The CSLA Antenna Structure. 79

Figure 5.3: (a) the fabricated CSLA and (b) its simulated and measured VSWR. 80

Figure 5.4: The normalized radiation pattern of the CSLA antenna in the (a) H-plane and (b) E-plane. (Solid line is the copolar component and the dashed line is the crosspolar component) 80

Figure 5.5: Fully planar CSLA: (a) Structure and (b) simulated VSWR..... 81

Figure 5.6: The magnetic field distribution of the CSLA on the ground plane at 0.5 GHz (a) isometric view and (b) top view. 82

Figure 5.7: The structure of the folded CSLA and its simulated VSWR for different folding angles, β	83
Figure 5.8: The normalized H-plane radiation pattern of the Folded CSLA antenna for a folding angle of (a) 135° and (b) 45° . (Solid line is the copolar component and the dashed line is the crosspolar component).....	83
Figure 5.9: (a) The Folded CSLA antenna and (b) it simulation and measurment results.	84
Figure 5.10: A fully planar folded CSLA (a) the structure and (b) the simulation results.	85
Figure 5.11: (a) The combined Folded CSLA and the Vivaldi Antenna, (b) comparison between the simulated directivity of the two antennas and (c) the H-plane radiation pattern of the combined antenna at different frequencies.	86
Figure 5.12: (a) The structure of the Vivaldi-CSLA antenna and (b) its simulated and measured VSWR.....	87
Figure 5.13: (a) A dipole parallel to a flat ground plane and (b) the resulting H-plane radiation pattern for different reflector spacings.	89
Figure 5.14: (a) The Vivaldi-CSLA placed in front of a flat reflector and the simulated (b) peak directivity of the Vivaldi-CSLA with a planar reflector and (c) the VSWR for different reflector spacing, d	90
Figure 5.15: (a) The Vivaldi-CSLA with the corner reflector, (b) the dimensions of the CSLA part and (c) the dimensions of the Vivaldi part.	91
Figure 5.16: Simulated (a) VSWR and (b) antenna gain for different values of β	92
Figure 5.17: Simulated (a) VSWR and (b) gain for different values of d	93

Figure 5.18: Measured and simulated input VSWR and gain of the directive CSLA.	94
Figure 5.19. Measured radiation pattern over the operating frequency band: (a) H-plane and (b) E-plane.....	94
Figure 5.20: Time Domain Response.	96
Figure 5.21: Comparison between the dimensions of a standard ridged horn and the dimensions of the proposed antenna. λ_{\max} is the wavelength at the minimum operating frequency.....	96
Figure 5.22: The proposed structure (a) isometric view and (b) front view.	98
Figure 5.23: Field distribution at the waveguide aperture at 2.4 GHz using (a) the proposed feed and (b) probe feed (red: highest intensity, blue: zero intensity).....	99
Figure 5.24: Simulation results for (a) the effect of the top slot width h_1 and (b) the effect of the shorting line position on the antenna matching.	101
Figure 5.25: Current Distribution on the feeding structure at 2.95 GHz.	102
Figure 5.26: The used balun for feeding the bowtie fed RWGA: (a) A cross section of the RWGA at its electrical symmetry plane to show the feeding structure and (b) the balun dimensions.	103
Figure 5.27: Photo of the proposed antenna next to a ridged horn antenna operating from the same minimum frequency.	104
Figure 5.28: (a) The measured and simulated VSWR of the proposed antenna and (b) the measured and simulated gain compared to the gain of the ridged horn and that of an ideal TE_{10} aperture.	105
Figure 5.29: The measured and simulated radiation pattern of the antenna at different frequencies (a) E-Plane and (b) H-Plane.....	106

Figure 5.30: Time domain response measurements for the proposed antenna compared to ridged horn.	107
Figure 6.1: Single antenna and dual antenna radar systems.	109
Figure 6.2: Standard methods for increasing the isolation between two antennas (a) increasing the physical separation, (b) use of lossy elements [53] and (c) use of isolating elements.....	111
Figure 6.3: Proposed Antenna structure (a) isometric view and (b) top view.	113
Figure 6.4: The first step for reaching the T/R pair (a) the original dipole version of the CSLA, (b) the cavity backed CSLA and (c) The VSWR of the two antennas showing singificant increase in the minimum operating frequency and in-band resonances.	113
Figure 6.5: The second and third step for reaching the T/R pair (a) adding the annular slots to decrease the minimum operating frequency for the same antenna size, (b) adding the fins to remove the in-band resonances, (c) input matching before and after adding the annular slots and (d) input and output matching before and after adding the fins.....	114
Figure 6.6: (a) Electric field distribution inside the cavity at 2 GHz with the cavity resonance field component encircled and (b) the effect of the fin height near the cavity edge on the antenna input matching.....	116
Figure 6.7: (a) The input matching and (b) isolation between the two antennas as a function of the sectorial loop angle, α	117
Figure 6.8: (a) The input matching and (b) isolation between the two antennas as a function of the cavity height, h_{cyl}	118

Figure 6.9: (a) The input matching and (b) isolation between the two antennas as a function of the antenna separation, W_{sep}	119
Figure 6.10: (a) The input impedance at one antenna port when the other port is matched and (b) the input VSWR as a function of the tapered microstrip line end width....	120
Figure 6.11: (a) The fabricated antenna pair and the measured and simulated (b) input VSWR and (c) isolation.	122
Figure 6.12: Measured (solid line) and simulated (dashed line) single element radiation patterns at the center frequency (1.5 GHz) in the (a) H-plane and (b) E-plane.....	123
Figure 6.13: Time domain responses for (a) single antenna, (b) transmit receive antenna pair and (c) enlarged view of the S21 response overlaid over the ideal sinc pulse.	124
Figure 6.14: Size comparison between the proposed antenna pair and ridged horn antenna pair ((a) and (b)) and a directive folded CSLA pair ((c) and (d)).	125
Figure 7.1: (a) Dual-polarized cavity-backed CSLA structure (cavity walls transparent for clarity) and (b) side view along one of the polarization planes. (The antenna is not drawn with the correct dimensions to clarify some of the dimensions.).....	129
Figure 7.2: Effect of the sectorial loop angle, α , on (a) the input matching and (b) the H-plane radiation pattern at 1.75 GHz.	131
Figure 7.3: Effect of the cavity height, h_{cl} , on the antenna (a) input matching and (b) E-plane radiation pattern at 1.7 GHz.	132
Figure 7.4: Effect of the cavity sidewall heights on (a) the H-plane radiation pattern at 1.75 GHz and (b) the input matching.....	133
Figure 7.5: Diversity CSLA (a) 3D structure and (b) planar structure.	134

Figure 7.6: Current distribution on the antenna for the two polarizations: (a) horizontal and (b) vertical.	135
Figure 7.7: Illustration of the reuse of the same V shaped loops for the two polarizations: (a) horizontal and (b) vertical.....	136
Figure 7.8: Effect of the sectorial loop angle on the matching.	136
Figure 7.9: (a) Structure of the fabricated diversity antenna and (b) enlarged view of the feed region (darker yellow traces are on the bottom layer).	137
Figure 7.10: Input VSWR and isolation of the antenna.....	137
Figure 7.11: Measured (a) E-plane and (b) H-plane patterns and simulated (c) E-plane and (d) H-plane patterns.....	138
Figure 7.12: Antenna structure (a) isometric view and (b) top view showing the ideal feeding structure.....	139
Figure 7.13: (a) and (c) the current distribution on the exciting element and (c), (d) the electric field distribution inside the cavity at 1.5 GHz for both the vertical and horizontal excitation modes.	140
Figure 7.14: The dependence of (a) the MA-VSWR, (b) E-plane and (c) H-plane directivity at 2 GHz on the cavity height, h_c	142
Figure 7.15: Effect of the bowtie angle on the (a) MA-VSWR and (b) the required characteristic impedance of the feed line for optimum VSWR.	143
Figure 7.16: The effect of the feed element width on (a) the MA-VSWR and (b) the E-plane and (c) H-plane radiation patterns.	145
Figure 7.17: The actual feeding structure using multi-section microstrip line, (a) isometric view and (b) top view of the exciting element.....	147

Figure 7.18: (a) The current distribution on the exciting element and (b) the electric field distribution inside the cavity at 1.5GHz when using the MS line feed.....	147
Figure 7.19: Measured and simulated radiation patterns in the (a), (b) E-plane and (c), (d) H-plane of the antenna.	149
Figure 7.20: (a) Measured and simulated VSWR and (b) measured and simulated S_{21}	149
Figure 8.1: (a) Initial PCB compatible monopole and (b) the monopole with the inductive pins. The top circular plate is semi-transparent to show the feed structure. The two antennas are simulated on an infinite ground plane and fed using and SMA coaxial cable at the apex.....	154
Figure 8.2: The (a) real and (b) imaginary parts of the input impedance of the different structures.	154
Figure 8.3: Antenna Structure (a) Isometric view and (b) side view with dimensions (the substrate is not shown for clarity).	155
Figure 8.4: Current distribution on the antenna feed at different frequencies.	156
Figure 8.5: The effect of the inductive pins width on the (a) input VSWR and (b) the real part of the input impedance.....	157
Figure 8.6: The effect of the monopole height on the (a) input VSWR and (b) the real part of the input impedance.....	158
Figure 8.7: Effect of the feed apex height on (a) the input VSWR and (b) the real and (c) the imaginary parts of the input impedance.	159
Figure 8.8: Effect of the ground plane size, l_g , on the input matching.	160
Figure 8.9: Effect of the ground plane size on the E-plane pattern at (a) 1 GHz and (b) 2 GHz.	160

Figure 8.10: (a) The fabricated antenna and (b) the measured and simulated input VSWR.	161
Figure 8.11: Measured (a) E-plane and (b) H-plane and simulated (c) E-plane and (H-plane).....	162
Figure 8.12: (a) Short TEM horn dimensions, (b) its radiation patterns in the E- and H-planes and (c) its input impedance.....	164
Figure 8.13: (a) Shorted TEM horn structure, (b) effect of the shorting trace width on the E-plane radiation pattern and on the (c) real and (d) imaginary parts of the input impedance.	165
Figure 8.14: Antenna structure and dimensions (a) isometric view (ground not shown for clarity) and (b) side view.	166
Figure 8.15: The effect of the antenna length, l , on the (a) input VSWR and (b) the boresight directivity.	167
Figure 8.16: Effect of the antenna length on (a) the input VSWR and (b) the real and (c) the imaginary component of the input impedance.....	168
Figure 8.17: Effect of the antenna height on the antenna's (a) input VSWR and (b) real and (c) imaginary components of the input impedance.....	169
Figure 8.18: (a) A photo of the fabricated antenna and (b) the measured and the simulated input VSWR.....	170
Figure 8.19: (a) Measured and (b) simulated H-plane Co-Pol radiation patterns, (c) measured and (d) simulated E-plane Co-Pol radiation patterns at different frequencies, (e) measured and (f) simulated H-plane Cross-Pol Patterns (normalized to the peak of the co-pol component).	171

Figure 8.20: Current distribution on the TEM horn portion of the antenna at 2 GHz.... 172

Figure 8.21: Variations on the proposed antenna to improve the H-plane cross-pol performance, (a) back to back and (b) TE aperture. 173

LIST OF TABLES

Table 2.1: Comparison of Times Required for Mapping an Area of 100 km x 10 km using the Different Techniques.....	15
Table 2.2: Backscattering Simulation Parameters	21
Table 3.1: The system of nonlinear equations describing the phase difference between the two SAR images (m=1,2).	33
Table 3.2: Sensitivity Analysis Scenario Parameters	39
Table 3.3: Actual InSAR, Ideal Scaled Model and Implemented Scaled Model parameters.	45
Table 5.1: Integrated microstrip balun dimensions.....	103
Table 6.1: Antenna Dimensions.....	114
Table 6.2: Comparison between the different antenna pairs.....	126
Table 7.1: Directional Antenna Dimensions.....	128
Table 8.1: Nominal Antenna Dimensions.....	155
Table 8.2: Nominal Antenna Dimensions.....	166

Chapter 1

Introduction

1.1 Motivation

Mapping the height profile of bedrock or hard clay covered with sand in deserts and arid regions has great potential in reducing the cost of seismic tests for exploration of oil fields and detection of ground water in such environments [1]. Other applications include the study of sand dunes formation and migration which is important in environmental studies [2], archaeological surveys and deep mines detection.

The currently available techniques for mapping the sand layer thickness are based on the use of ground penetrating radars (GPR) [3], [4] and [5]. The basic concept of GPR is shown in Figure 1.1 (a). It consists of a transmitter and a receiver mounted on a ground vehicle or a helicopter and pointed towards the ground. A human operated GPR is shown in Figure 1.1 (b). By transmitting a wideband pulse and measuring the reflected waves, the thickness of the sand layer can be estimated if the propagation velocity of the waves in the sand is known. This technique provides reasonable accuracy. However, the major drawback of this approach is that the height profile can only be estimated along a 1D path. This requires exorbitant amount of time to map the sand layer thickness in large regions. Also, GPR is very labor intensive which prompts the need for a faster and cost effective technique. In this dissertation, a novel approach for measuring sand layer thickness using a two frequency radar system is presented. As will be discussed, one of the radars is to operate at VHF band to achieve signal penetration deep into dry sand layers. For this system it is shown that conventional broadband antennas significantly

limit the operation of this system and thus a number of new wideband antenna architectures are investigated. The designed antennas can be used in several other applications such as foliage penetrating radars [6], see through wall radars [7] and ultra wideband communication systems [8].

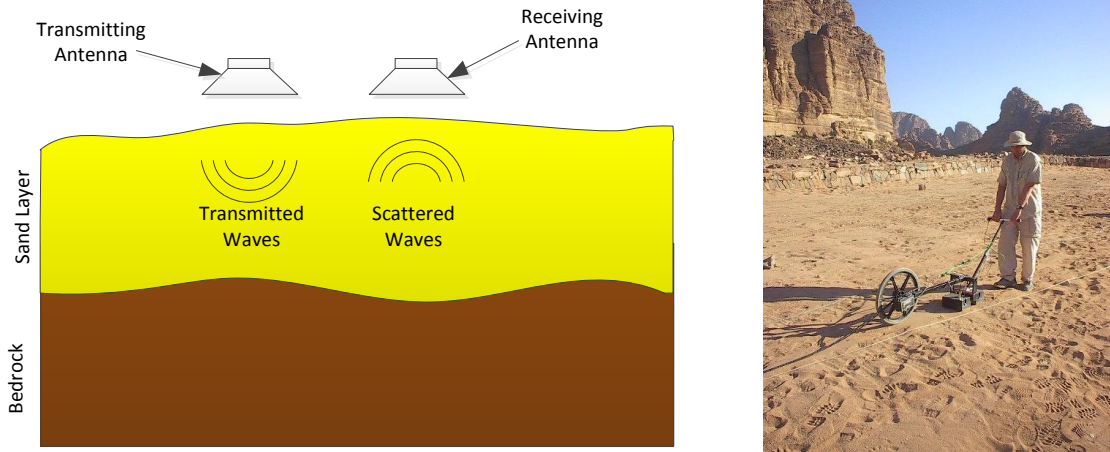


Figure 1.1: (a) Schematic Diagram of the basic structure of GPR and (b) a photo of a human operated ground based GPR (Reproduced from [9]).

1.2 Applications

1.2.1 Oil Fields and Ground Water Explorations

The common method for oil and water explorations is based on seismic measurements [1]. In which, a small explosive charge is placed on top of the sand layer as shown in Figure 1.2. This explosive charge generates a seismic wave which propagates through different soil layers and the scattered/reflected seismic waves are measured using geophones that are placed around the explosive charge position. One problem with this approach is that the seismic waves suffer significant attenuation when propagating in a loose medium such as sand. This requires many experiments to be repeated several times to achieve reliable inversion with their associated costs and time. However, if the sand

layer thickness is known (or equivalently the top and bottom interfaces' topography) experiments can be done in locations with small sand layer thickness. This can significantly reduce the cost and time of oil exploration. Also, the information about the two interfaces can be used as an additional input to the seismic inversion algorithm to further improve its accuracy.

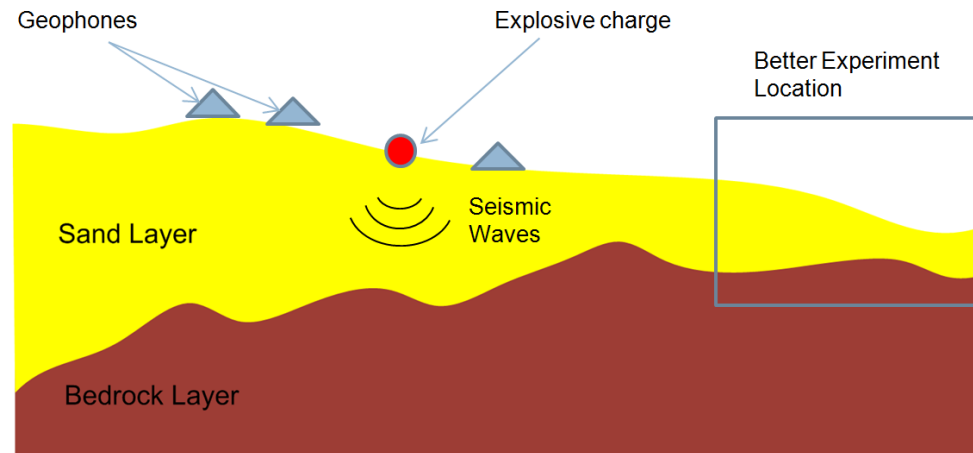


Figure 1.2: Seismic test in arid regions for oil field or ground water exploration.

1.2.2 Mine Field Detection

In several developing and underdeveloped countries around the world, mine fields present a major threat to humans and prevent the use of large areas of lands. These can adversely impact the economy of these countries which are already under economic and social stress. The most commonly used electromagnetic method for landmine detection is GPR [4] and [5], but this method for finding landmines is very hazardous as the instrument has to be physically in the close proximity of the mine before it can detect the mine. Remote sensing tools such as the one presented in this thesis, offer the advantage of standoff detection of mine fields and can provide a fast examination of large areas in a relatively short period of time. In arid areas with moving sand dunes a thick layer of sand

can cover a mine field which, at some point in the future, can be exposed or covered with a thin layer of sand. Detection of such mine fields poses several interesting challenges for an imaging radar system. However, one major problem is the subsurface defocusing and geometric distortion [10], [11]. This scenario is shown in Figure 1.3 (a) where an array of point targets representing mine fields is placed under a barchan sand dune. The resulting SAR image using conventional techniques for SAR focusing is shown in Figure 1.3 (b) where we can see significant defocusing and distortion due to the top surface. If the topography of the sand and the point targets locations are determined, a much more useful image can be generated as shown in Figure 1.3. (c). Using the proposed approach in this thesis, an estimation of the point targets' heights can be obtained and used to accurately focus the image.

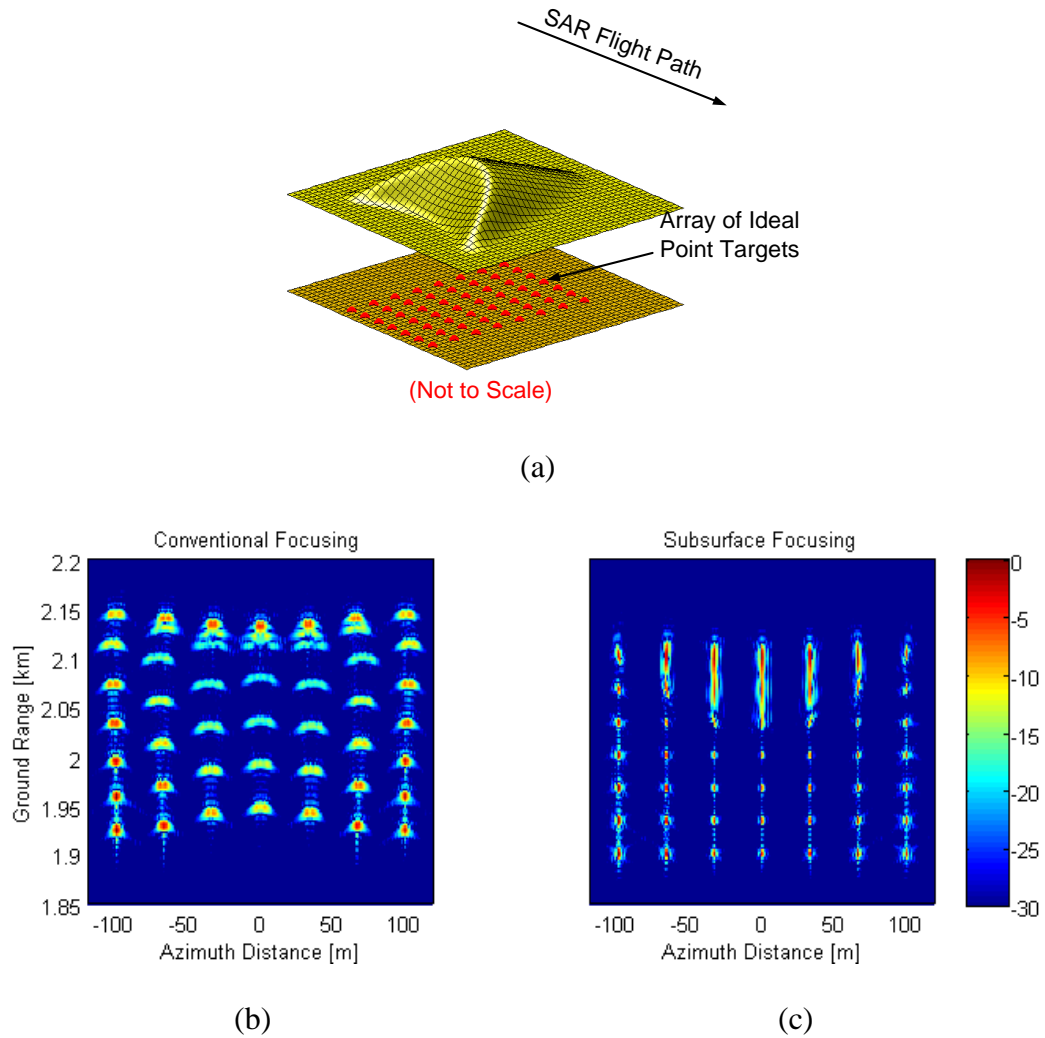


Figure 1.3: (a) An array of point targets under a sand dune, (b) SAR image using conventional SAR focusing and using subsurface focusing.

1.2.3 Other Applications

There are numerous other applications where the knowledge of the bedrock height is very useful. For example, Figure 1.4 (a) shows sand dunes on Proctor Crater on Mars [12]. Determination of the underlying topography in this crater can provide very useful information such as the depth of the original crater and an estimate of the age of the crater. Another example is shown in Figure 1.4 (b) which shows sand dunes advancing towards the city of Nouakchott (the capital of Mauritania) [13]. The migration of these

sand dunes is a serious problem for habilitation and agriculture in many other places in the world. The advancement of these sand dunes is stopped by using oil drenches. However, since there are no accurate models for the movement of these dunes, the use of these drenches is a little more than guess work. Recent studies have shown that the knowledge of the underlying topography of these dunes can help in predicting their migration pattern [2].

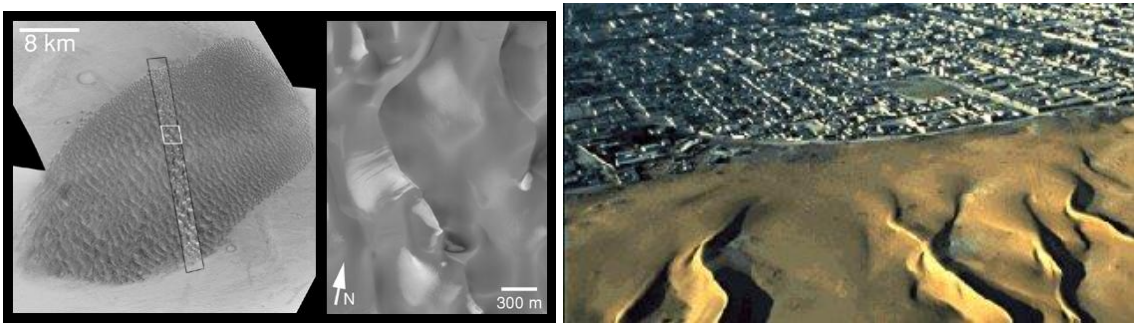


Figure 1.4: (a) Sand dunes in Proctor Crater on Mars [12] and (b) Sand dunes advancing towards the city of Nouakchott (the capital of Mauritania) [13].

1.3 Approach

Height maps (or Digital Elevation Models, DEMs) of the top surface can be obtained using several remote sensing techniques. Some of the most popular techniques are shown in Figure 1.5 [14]. Stereo-SAR uses stereoscopic processing on two Synthetic Aperture Radar (SAR) images and usually provides height accuracies in the order of 10 meters or more [15]. SPOT satellite uses stereo optical images to estimate the height and provides better height accuracy than Stereo-SAR [16]. However, since the sand layer thicknesses of interest are in the order of tens of meters, both of those techniques cannot provide the required height accuracy. On the other hand, height accuracies from Aerial Photography and LIDARs (Light Detection And Ranging) are significantly better [17]. However, they are much more expensive. Furthermore, SPOT satellite, Aerial

Photography and LIDARs are optical techniques and thus cannot be extended to also estimate the subsurface topography. Due to these shortcomings, Airborne Interferometric SAR (InSAR) is chosen since it provides adequate height accuracies with low cost per Km².

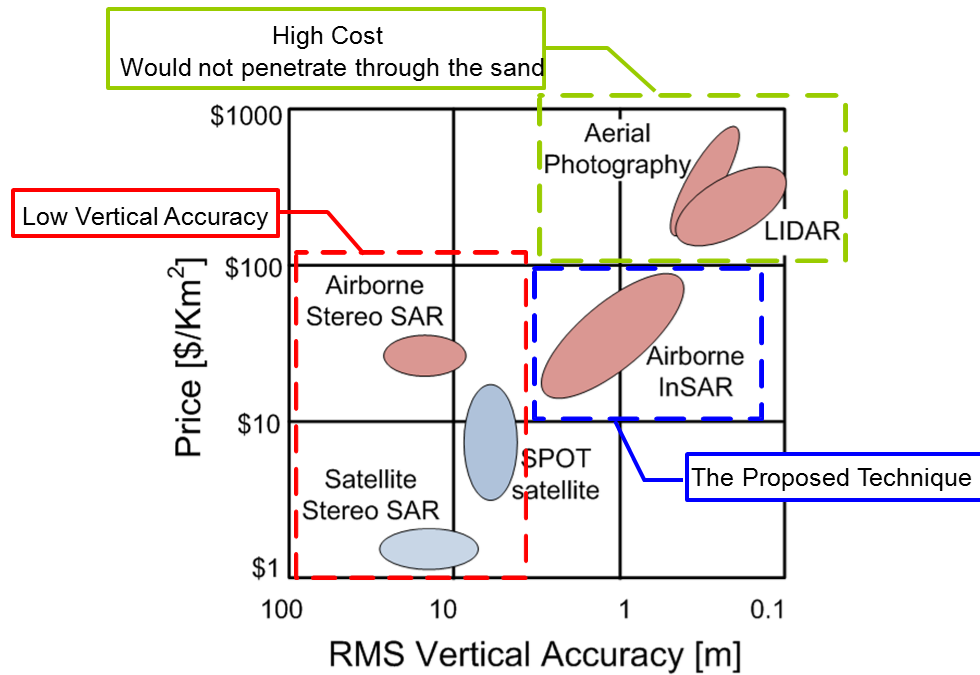


Figure 1.5: Conventional remote sensing techniques for terrain mapping [14].

An additional advantage of InSAR systems is that they can be designed and operated over a wide range of frequencies. By choosing low operating frequency in the VHF range, the waves can penetrate the top layer and obtain information about the subsurface height. As will be shown in the next chapter, when using VHF InSAR data, the top surface undulations generate artificial undulations on the estimated bottom surface height. To remove those artifacts, information about the top surface (sand) height is also required. Thus, another InSAR subsystem operating at Ka band is designed to map the top surface, since at such very high frequencies the penetration depth into the top

layer is negligible and the Ka-InSAR provides the required top surface height information which are then used to correct the VHF-InSAR system using a novel iterative inversion algorithm. The proposed system is schematically shown in Figure 1.6.

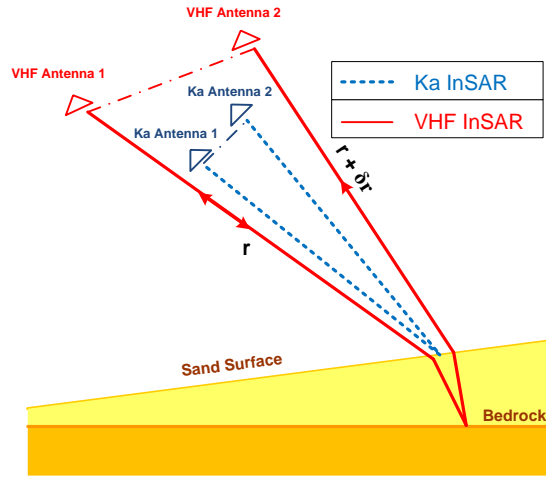


Figure 1.6: The proposed dual frequency InSAR systems, Ka-InSAR provides top surface height information that are then used to correct the VHF InSAR data to obtain the correct subsurface height.

The required height accuracy and map resolution are in the meter range for the proposed applications. This translates to a bandwidth of approximately 60 MHz. At Ka-band, this corresponds to a very small fractional bandwidth (less than 1%) which makes the antenna and the electronics design relatively straight forward. However, at VHF frequencies, it corresponds to a relatively large fractional bandwidth (larger than 40%). This makes the antenna design for these types of Ultra-Wideband (UWB) systems very complex. This is mainly due to the limitations on the antenna electrical size, bandwidth and gain [18], [19] which requires the antenna to be relatively large to achieve good gain and very wide bandwidth. However, since these antennas are to be used for on-plane mounting, they are required to be as compact as possible to minimize the air-drag. Thus we investigated different designs for such antennas to minimize their overall size and

make them low profile. Also, as will be shown in the next chapter, InSAR systems require a few points on the ground where the subsurface height is known. For this number of small points, we proposed the use of Ground Penetrating Radars (GPR) which also require compact antennas to operate at the same frequencies. And thus, we developed several antennas for such systems as well. Such antennas are very important since they are employed in many other systems as well such as: (1) See Through Wall Radars where the low frequency is required to penetrate lossy walls and the large bandwidth is required to achieve good spatial resolution [7], [20], (2) UWB communication systems where the large bandwidth is required to achieve very high data rate and the compact size is important to minimize the overall system size and weight [8] and (3) in UWB localization systems where the compact size is important to minimize the size of the localization tag and the bandwidth is required to achieve high localization accuracy [21], [22].

1.4 Thesis Framework

The different aspects of radar remote sensing in arid regions are summarized in Figure 1.7. The first three chapters will deal with the processing aspects of the problem. This includes the propagation and refraction effects through the top layer and the required. As will be shown in those chapters, some ground reference points are required at which the sand layer thickness has to be known. This requires the use of GPR at these points. These GPRs require antennas that operate at low frequencies to be able to penetrate through the sand layer. These antennas are also required to have very wide bandwidths to achieve good sand layer accuracy. The next two chapters (5 – 8) will deal with the design of compact ultra-wideband antennas for GPR and on-plane mounting

applications. These antennas are also very useful in other applications as mentioned in the previous sections such as see through wall radars and UWB communications applications. The chapters are organized as follows:

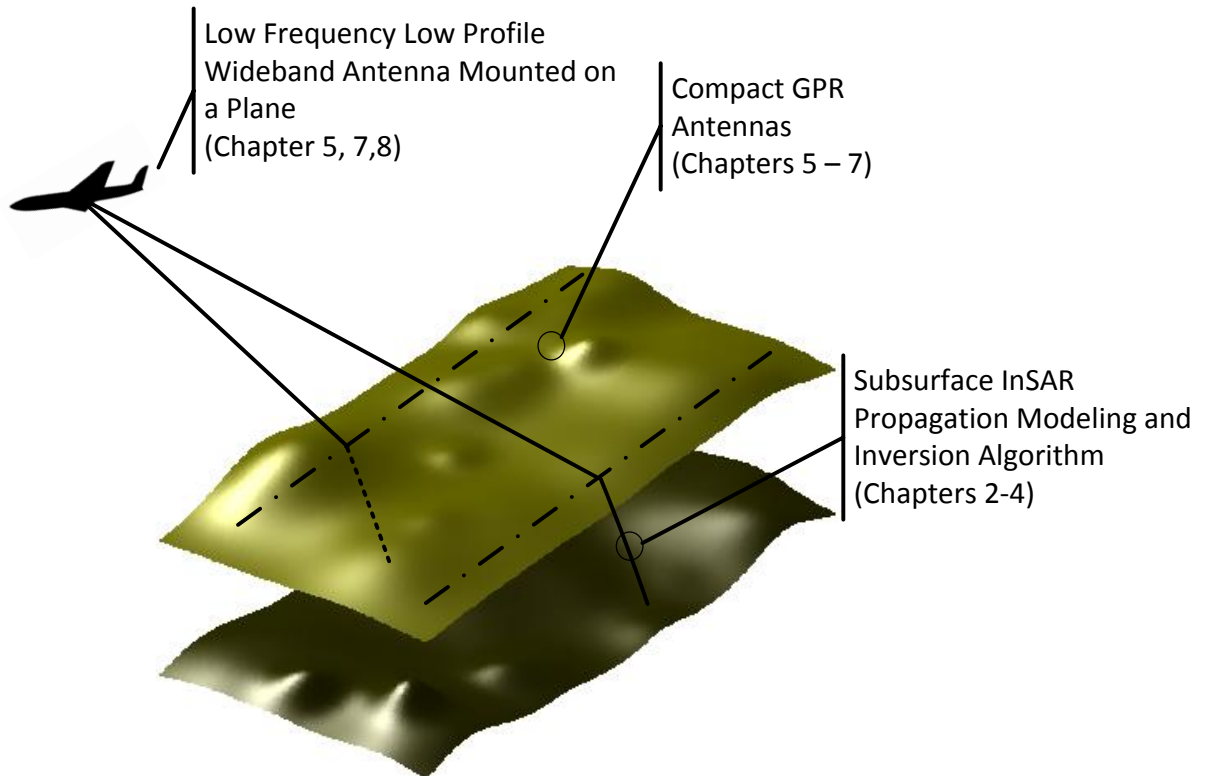


Figure 1.7: The Different Aspects of the Problem of Radar Remote Sensing of Arid Regions.

Chapter 2 introduces the design of the subsurface InSAR. First, relevant aspects of conventional SAR and InSAR processing are presented in more detail. Next, the scattering phenomena in arid regions are analyzed to estimate the appropriate operating frequencies. Finally, several radar design issues are discussed such as the SAR processing and left/right separation.

Chapter 3 presents the 2D implementation of the physics-based algorithm for subsurface mapping. A comprehensive sensitivity analysis is performed to determine the

effect of the different system, noise and environment uncertainties on the accuracy of the estimated height. The algorithm is then verified using scaled model measurements in the lab.

A fast 3D SAR simulator based on ray tracing is presented in **chapter 4**. Using the substantial speed advantage of this simulator, an efficient iterative algorithm for subsurface SAR focusing and image coregistration is developed. The algorithm is also verified using computer simulations and scaled model measurements in the lab.

Chapter 5 deals with the design of linearly polarized UWB antennas for radar applications. Three antennas based on the coupled sectorial loop antenna concept are presented. These antennas require the presence of a ground plane for operation which can be problematic in some radar design situations. To overcome these problems, waveguide based antennas are then developed.

Chapter 6 presents the design of UWB antennas for radar system level implementations. In such situations, the main limiting factor is the isolation between the transmitting and receiving antenna. This problem is discussed and the conventional techniques are presented. Then, an antenna design is presented which provides relatively high isolation with very small separation between the transmitting and receiving antennas.

For radar applications, dual polarized antennas are sometimes required for clutter reduction and/or target identification. Thus, in **chapter 7** three dual polarized compact UWB antennas based on the coupled sectorial loops antenna (CSLA) concept are introduced. The design and principle of operation of each antenna is presented. These

antennas are useful for radar and communication applications. The antennas' performance was again verified using laboratory measurements.

For on-plane mounting, two very low profile antennas are presented in **chapter 8**. Those antennas are designed to have a very low profile (5% and 6% of the maximum operating wavelength) to minimize the air drag when they are mounted on the plane fuselage.

The conclusion and some possible future work related to the subsurface inversion algorithm and wideband antenna design are presented in **chapter 9**.

Chapter 2

Subsurface InSAR Design

As described in the previous chapter, the optimum radar technology for mapping the subsurface topography is Interferometric Synthetic Aperture Radar (InSAR). In this chapter, a review on the operation of conventional InSAR systems is presented. It is shown that conventional InSAR does not provide enough information to estimate the subsurface topography. The required modifications of the InSAR for subsurface mapping are then presented together with its associated design issues such as subsurface focusing and left/right separation.

2.1 Conventional Interferometric SAR (InSAR)

The major steps for conventional InSAR processing are shown in Figure 2.1 [23]. First, two complex SAR images are generated for the same area using two slightly different flight paths. Those two images are then coregistered to account for the scene variations due to the different look angles. The cross-correlation of the two coregistered images is then generated. This is done by multiplying one of the images by the complex conjugate of the other image and then applying a moving average filter on the result. This results in a complex amplitude cross-correlation image. The phase of the cross-correlation image is referred to as the *phase interferogram* whereas the magnitude is referred to as the *coherence* image and it has values in the range 0-1. The regions in the interferogram image that have coherence values close to 1 have low phase noise whereas regions with low coherence values have high phase noise. Phase noise affect the accuracy

of the height estimation using InSAR and thus several techniques are used to improve the coherence such as interferogram filtering. The interferogram cannot be directly used to estimate the terrain height since it is wrapped between $-\pi$ and π (corresponding to the blue and the red colors in the phase interferogram plot in Figure 2.1, respectively). Thus, 2D phase unwrapping is applied on the interferogram to obtain the absolute phase [24]. This absolute phase is then used to estimate the terrain height by knowing the height of some reference points on the ground [25].

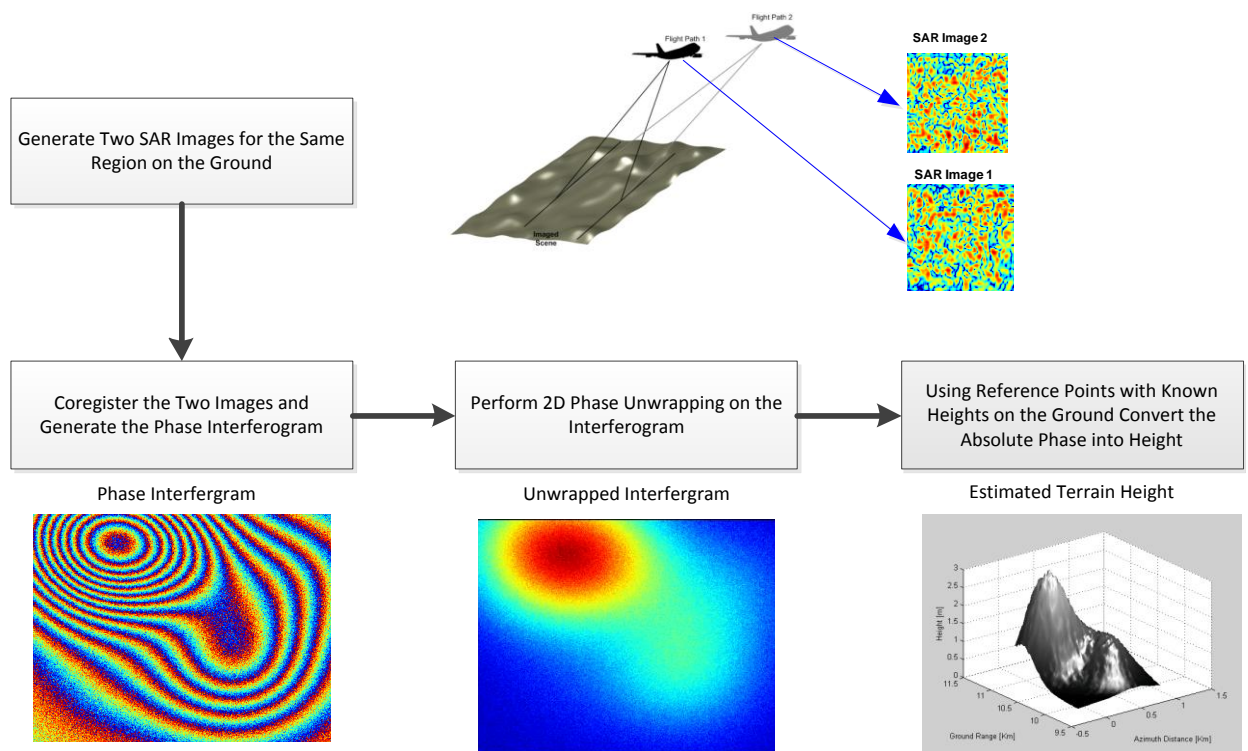


Figure 2.1: Steps for generating the terrain height using InSAR.

If the above technique could be extended to mapping the subsurface; very large regions can be mapped in a very fast and efficient way. A numerical example is shown in Table 1, where the times required for mapping an area of 100km x 10 km are shown.

From Table 1, we can see that InSAR processing is orders of magnitude faster than GPR. The main drawback is that InSAR processing is significantly more involved than GPR.

Table 2.1: Comparison of Times Required for Mapping an Area of 100 km x 10 km using the Different Techniques.

Technique	Time Required for Mapping an Area 100 km x 10 km
GPR (Ground Vehicle Mounted)	6 Days 23 Hours
GPR (Helicopter Mounted)	1 Day 22 Hours
InSAR	16 Minutes and 40 seconds (630x & 130x faster, respectively)

2.2 Extension of InSAR for Subsurface Mapping

2.2.1 Sample Scenario

As shown in

Table 2.1, using InSAR can provide huge speed advantage compared to GPRs for mapping large areas. However, conventional InSAR processing cannot be used to estimate the subsurface height. This is illustrated in Figure 2.2, where a conventional low frequency InSAR processing is used to estimate the bedrock height underneath an undulating sand layer. The low frequency is required for the electromagnetic signal to be able to penetrate the top sand layer and provide information about the bottom topography. However, as we can see from the figure, the information obtained also depends on the top layer topography which results in artificial undulations on the estimated bedrock height. Also, the propagation speed inside the sand layer is not the same as that in air which results in additional height error since conventional InSAR processing assumes

propagation in air. Thus, additional information about the top layer is required as well as modification in the InSAR processing in order to accurately estimate the subsurface topography.

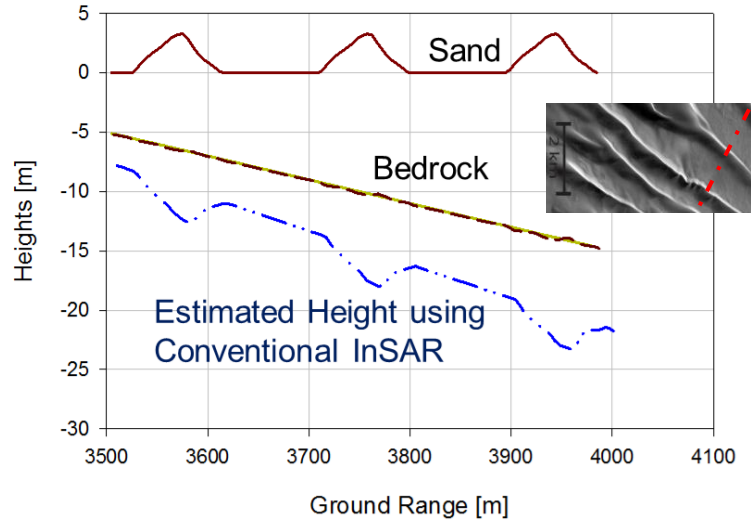


Figure 2.2: Using conventional InSAR phase-to-height equations results in severe errors in the estimated bedrock height.

2.2.2 Proposed System

The proposed system is shown in Figure 2.2 (a) and (b) [11]. A novel two frequency (Ka and VHF) airborne InSAR system is proposed. The Ka InSAR will be responsible for mapping the top interface topography since at such high frequencies, the propagation through the top layer is extremely lossy and most of the scattered waves are coming from the top surface. The VHF InSAR will be responsible for obtaining information about the subsurface since at these low frequencies, the waves can penetrate the top layer with minimal attenuation and scatter from the bottom interface giving information about its topography. The subsurface height is then obtained by correcting for the propagation effects through the sand layer using both the Ka and VHF InSARs data. The selection of the two frequencies is discussed in the following section.

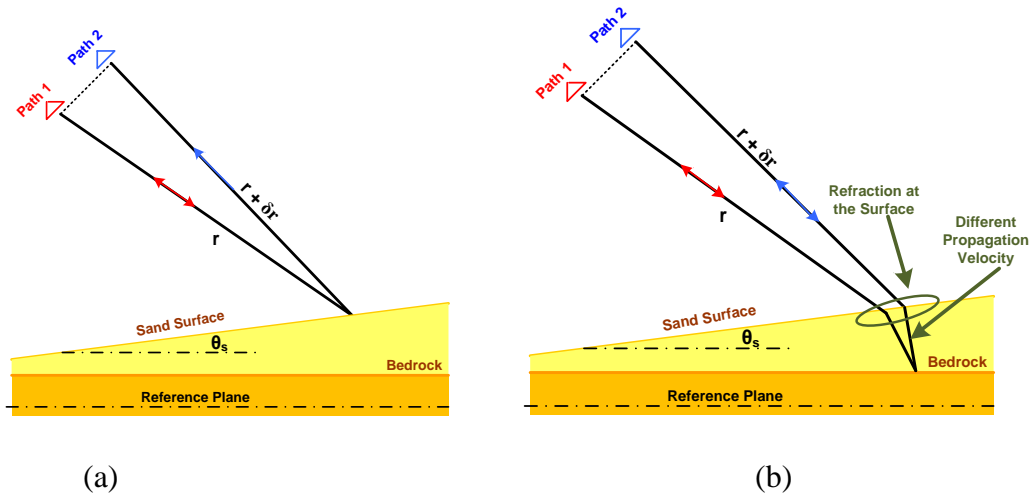


Figure 2.3: (a) Wave propagation path for the Ka-InSAR (high frequency) and (b) wave propagation path for VHF-InSAR (low frequency).

2.3 Scattering Phenomena

Some photos of the considered regions in Saudi Arabia are shown in Figure 2.4. To predict the dominant scattering phenomena that might exist in arid areas, some measurements and assumptions are made based on the field observations of the environment. The sand surface RMS roughness is measured to be on the order of few millimeters whereas its undulations (sand dunes) are on the order of tens of meters. The bedrock surface RMS roughness is estimated to be on the order of few centimeters.



Figure 2.4: Arid areas considered (in Saudi Arabia). The two figures on the left show the large scale undulations (with a person standing next to a sand dune in the leftmost photo for comparison) whereas the figure to the right shows the small scale undulations.

For such multilayered media with rough interfaces, several scattering mechanisms may exist and estimating the scattering coefficients can be very complex and time consuming [26]. However, for reliable and computationally efficient inversion, the operating frequencies have to be chosen to ensure simple scattering mechanisms are dominant for each frequency thus simplifying the processing. Considering the size and dielectric properties of sand particles as well as the order of its surface roughness, at very high frequencies the surface and volume scattering [27] from the sand and air-sand interface dominate the backscattering return as shown in solid arrow in Figure 2.5. On the other hand, at very low frequencies, where the wavelength is much larger than the RMS surface roughness of the air-sand interface but much smaller than the air-sand surface undulations, the electromagnetic waves can propagate through the sand and scatter back from the bedrock with small to moderate attenuation and negligible sand volume and surface scattering as shown in dash-dotted arrow in Figure 2.4. This penetration phenomenon was observed at L band (1.25 GHz) in several arid regions in northern Africa as shown in [28], [29], [30] and [31]. Radar was used to detect the presence of

subsurface features. Those two scattering mechanisms provide information about the sand surface height as well as the bedrock height (and equivalently the sand layer thickness). The multiple bounce component of the low frequency mechanism is neglected for the initial design, since for the proposed vertical polarization, the reflection coefficient is less than about -10 dB for the incidence angles of interest which is further reduced by attenuation due to the longer propagation distance through the sand for the multiple bounce components.

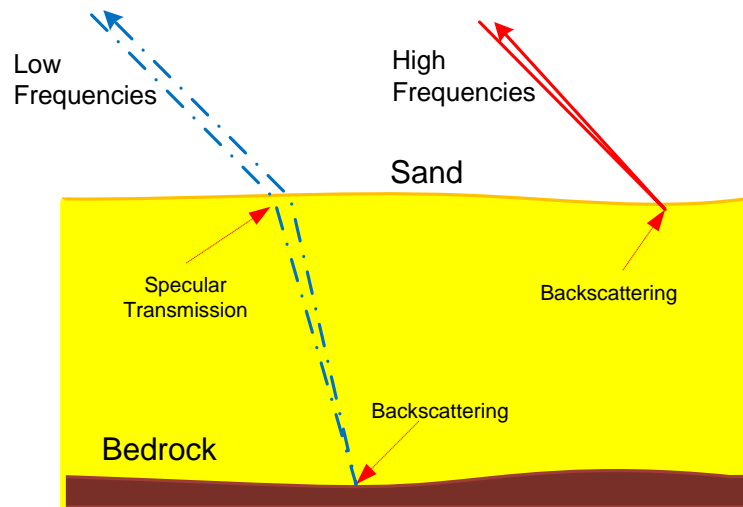


Figure 2.5: Promoted scattering mechanisms.

To determine the optimum operating frequencies, the scattering from the bedrock and the sand surface was calculated. To analyze the backscattering over a wide frequency band, the Integral Equation Method (IEM) was used [32]. For the sand surface scattering, the conventional IEM equations were applied. Whereas for the bedrock scattering, the backscattering calculated using the IEM was modified to include: (1) the change in the incidence angle due to the refraction through the sand surface, (2) the propagation constant used was that of the sand and (3) the two way transmission coefficient through the air-sand interface. The simulation results are shown in Figure 2.6. These simulations

do not include the volume scattering effects, which are relatively insignificant up to around 10GHz [27]. The parameters used in this simulation are shown in Table 2.2. The sand dielectric constant was measured at 150MHz and it was assumed constant with frequency (due to insufficient measurements) as a worst case scenario, since the sand losses increase with frequency which makes the sand backscattering even stronger at higher frequencies. For the VHF radar, it should be noted that, from a practical implementation point of view, the higher the operating frequency is the better the performance for several reasons, namely: (1) higher operating frequency simplifies the radar antenna and system design, (2) allows for higher bandwidth (and consequently higher resolution) for the same system complexity (same relative bandwidth) and (3) allows for using geometrical optics modeling for faster undulations in sand geometries (since the limitation of geometrical optics is that the radius of curvature of the sand undulations has to be much larger than the wavelength [33]). VHF SARs have been used in several applications such as target detection under foliage and terrain mapping [6], [34] and [35].

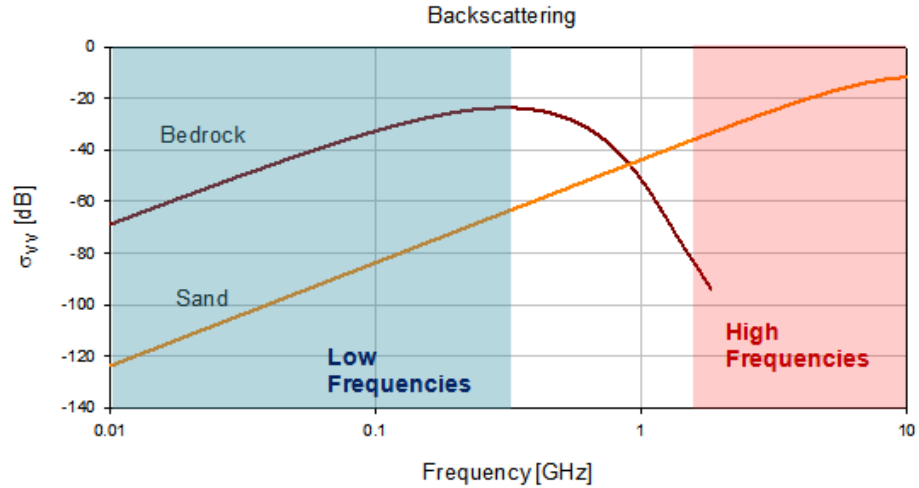


Figure 2.6: Simulated backscattering cross-section for the bedrock and sand surfaces using the parameters in Table 2.2. The decrease in the bedrock backscattering at higher frequencies is due to the attenuation through the sand.

Table 2.2: Backscattering Simulation Parameters

<i>Parameter</i>	<i>Value</i>
Incidence Angle	40°
Sand RMS Roughness	5 mm
Sand Correlation Length	5 mm
Bedrock RMS Roughness	5 cm
Bedrock Correlation Length	5 cm
Sand Dielectric Constant	2.9 - j0.02
Bedrock Dielectric Constant	5.8 - j0.04
Sand Layer Thickness	20 m
Sand Slope	0° (Horizontal sand surface)

From these simulation results, we can see that the bedrock backscattering is dominant (more than 40 dB above that of the sand) up to about 250 MHz for the given (worst case sand roughness) simulation parameters. For thinner sand layers, this frequency can be even higher. For the range of incidence angles and the sand layer

thicknesses considered, an operating frequency of about 150 MHz was chosen for the low frequency radar. On the other hand, for the high frequencies, since sand surface has very low RMS roughness in some areas, the volume scattering component must be considered as the dominant source of backscattering. Using random media theory, it was determined that to get sufficient volume backscattering from a smooth flat sand surface, the operating frequency has to be in Ka band (at about 35 GHz) as shown in Figure 2.7.

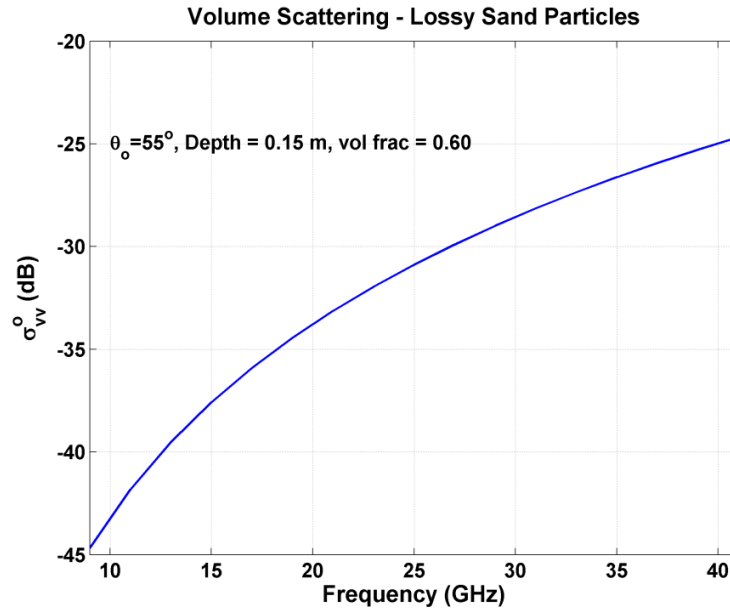


Figure 2.7: Numerically calculated backscattering coefficient of the c50-70 sand layer as a function of radar frequency. The sand layer was assumed 0.15 m thick, has 0.6 in volume fraction (from [36]).

2.4 Subsurface InSAR Processing

As shown in Figure 2.3, the conventional InSAR processing is adequate for Ka-band InSAR data. That is, two SAR images are generated from two slightly different flight passes (antennas 1 and 2). The two images are then co-registered and the phase interferogram and the coherence maps are generated. Finally, the phase interferogram is unwrapped and the terrain height is estimated using ground control points (GCP).

However, for VHF InSAR, several issues appear due to refraction and propagation of the signal in the sand layer. In this section, we will briefly highlight some of the processing issues and artifacts that appear due to these effects.

2.4.1 Subsurface Focusing

The first step in the InSAR processing is the generation of the SAR images. However, conventional SAR focusing does not correct for the refraction and propagation effects inside the sand as previously discussed. In order to quantify the resulting error when using conventional SAR processing for subsurface focusing, the scenario shown in Figure 2.8 was simulated, where an ideal point target was placed under flat horizontal sand at a depth of Z_t . The radar height and point target ground range are 5km and 2km respectively. The simulated center frequency is 150MHz and the bandwidth is 60MHz. The raw data was then generated using a subsurface SAR simulator that includes the frequency dependent attenuation and dispersion through the sand as well as the refraction and the different propagation velocity. The focusing was performed using the conventional back-projection technique [37] with a focusing plane at the sand surface using different integration angles. The integration angle is calculated as $(\theta_i + \theta_f) - 180^\circ$. The point target responses along the range and azimuth were normalized and displaced to a reference point to compare the image distortion.

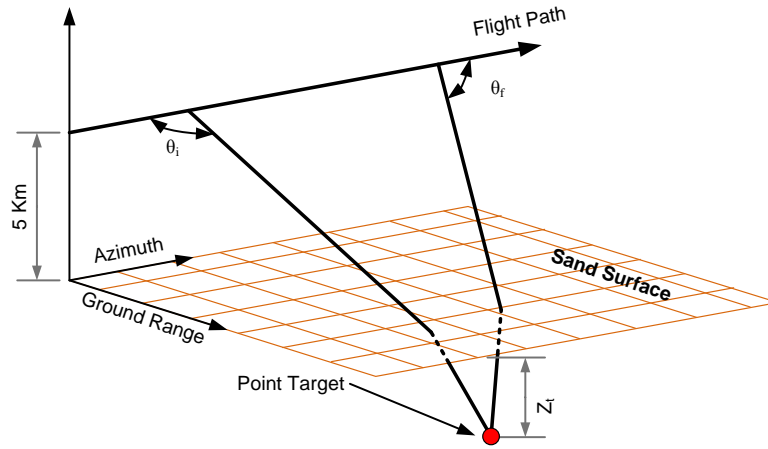


Figure 2.8: Simulation Scenario for VHF SAR focusing on a point target at depth Z_t below the sand surface.

The result is shown in Figure 2.9 (a)-(d). The range point spread function (PSF) section is almost independent on the integration angle and shows minimal distortion as expected due to the relatively low loss and dispersion of the sand at such low frequencies. However, there is significant distortion in the azimuth direction for large integration angles. This distortion is due to the fact that the standard focusing technique does not account for the sand propagation and refraction. However, as we can see from Figure 2.9 (b)-(d), by decreasing the integration angle, the SAR depth of focus is increased and thus a well-focused image can be obtained at the expense of reduced resolution. However, since the developed algorithm (Chapter 3) can estimate the target (bedrock) height, this information can be fed back into the SAR focusing and a higher resolution image can then be obtained through an iterative process. This will be shown in Chapter 4.

2.4.2 Image Coregistration

Due to the refraction through an undulating sand surface, the image will be distorted even if the bedrock is flat. An example is shown in Figure 2.10 where 56

uniformly distributed point targets are placed at a constant depth under an undulating sand surface. The raw SAR data was generated and focused using a conventional back projection processor with adjusted integration angle to achieve good focusing as discussed in the previous subsection. From Figure 2.10, we can see that the targets' image has been distorted due to the top surface topography. This could lead to significant coregistration error for relatively large baselines. For the baseline values considered in this thesis, the coregistration error was found to be relatively small when using conventional coregistration methods and the unequal ground range displacements are corrected through the proposed algorithm as will be shown in Chapter 3. However, for larger baselines (which might be required to achieve higher height accuracy), adaptive co-registration techniques have to be used.

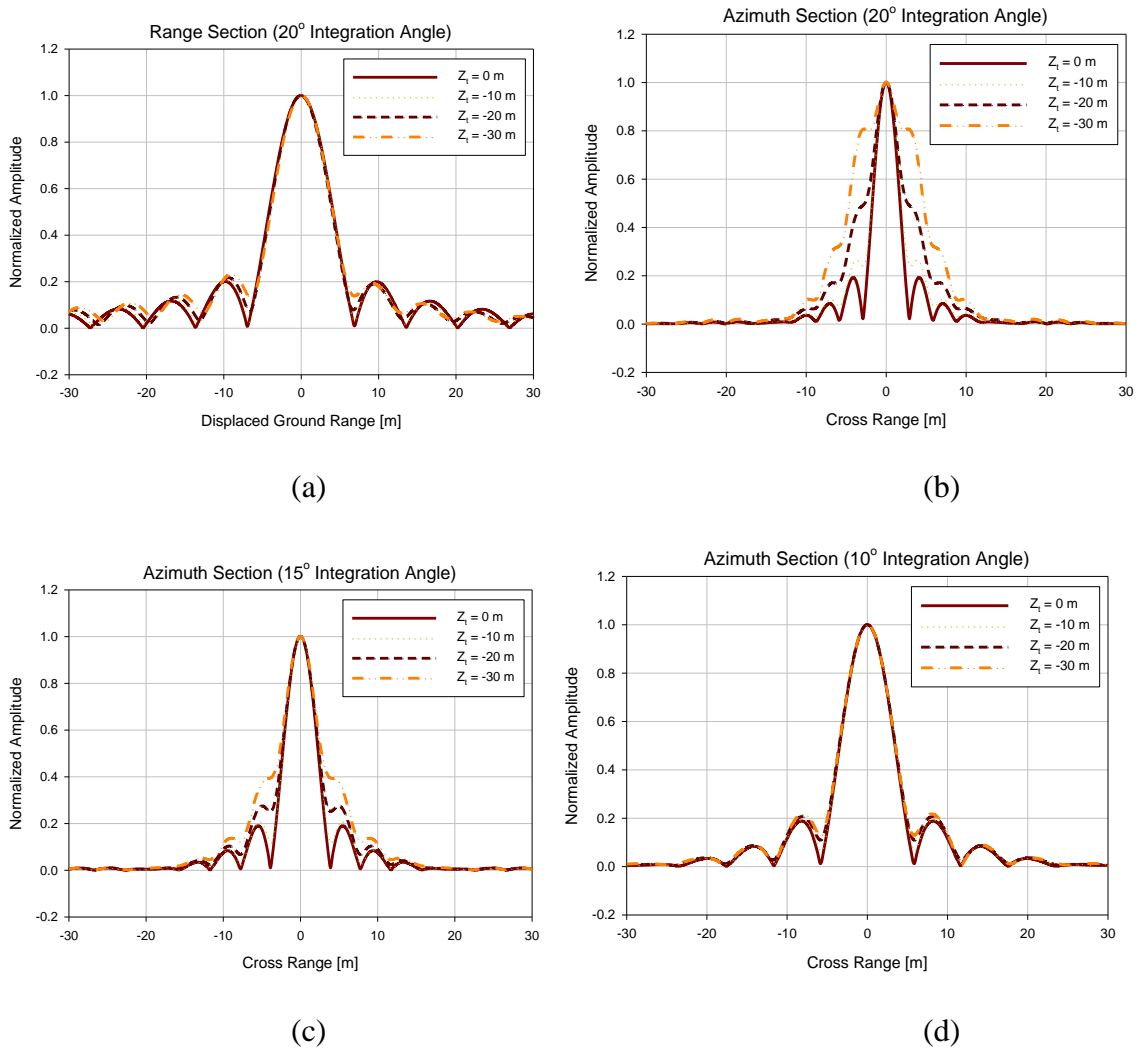


Figure 2.9: (a) PSF range section, (b) PSF azimuth section for 20o integration angle, (c) PSF azimuth section for 15o integration angle and (d) PSF azimuth section for 10o integration angle.

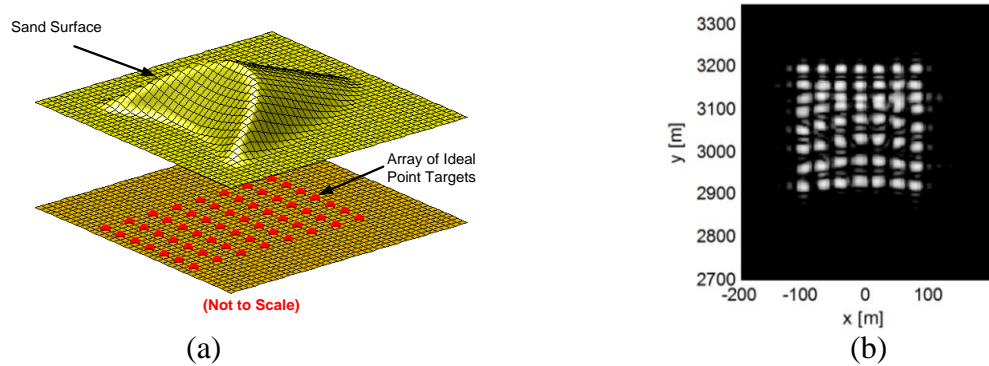


Figure 2.10: Image distortion due to top surface undulations (a) geometry and (b) focused SAR image.

2.5 Left/Right Separation

In conventional SAR operation, the antenna beam is in one direction as shown in Figure 2.11 (a). This can be easily achieved for high frequency operation, since the antenna size can be made several multiples of the operating wavelength. However, for low frequency operation, due to size limitations on the antenna for it to be mounted on an aircraft, the antenna pattern becomes much wider as shown in Figure 2.11 (b). This causes the backscattering signal at a certain range bin to come from two different sides of the airplane. SAR processing cannot be used to separate the two targets since they arrive at the same times.

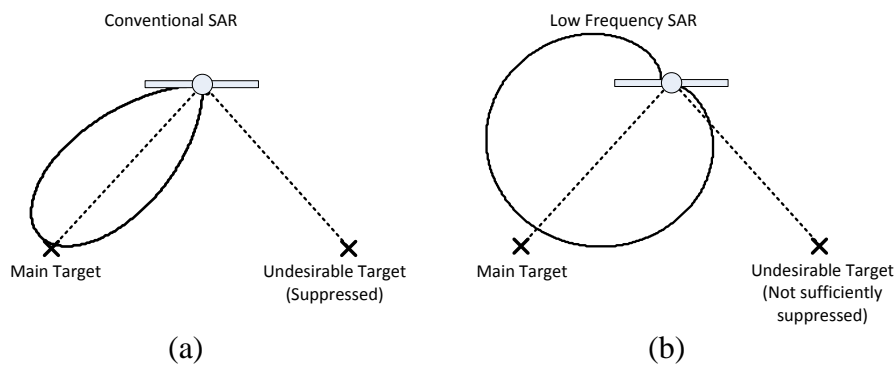


Figure 2.11: (a) The antenna pattern for conventional SAR operation and (b) for the VHF-SAR showing that the undesired targets on the other side of the plane are no longer suppressed by the antenna radiation pattern.

One way to significantly reduce or even remove this effect is by performing filtering on the InSAR interferogram. As shown in Figure 2.12, when two targets at the left and right of the airplane lie at the same range distance (R), they cannot be separated by range gating.

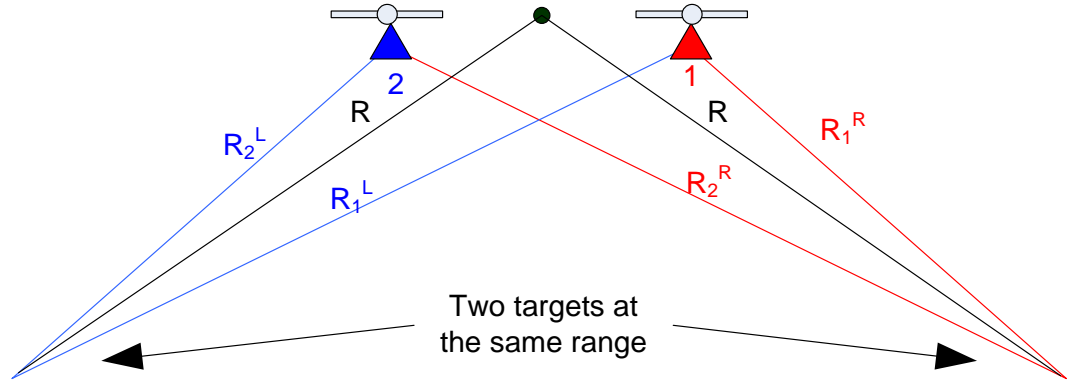


Figure 2.12: Left/right separation diagram.

However, after forming the interferogram, the resulting image would be:

$$\begin{aligned}
 F(R) = & \left\langle E_1^L(R) \cdot (E_2^L(R))^* \right\rangle \cdot e^{-ik(R_1^L - R_2^L)} \quad (\text{Left Component}) \\
 & + \left\langle E_1^R(R) \cdot (E_2^R(R))^* \right\rangle \cdot e^{-ik(R_1^R - R_2^R)} \quad (\text{Right Component}) \quad \boxed{2}
 \end{aligned} \tag{2.1}$$

Where $E_1^L(R)$ and $E_1^R(R)$ are the backscattered fields received at antenna 1 from the left and right sides of the plane respectively and similarly for $E_2^L(R)$ and $E_2^R(R)$. And the symbol $\langle \cdot \rangle$ is used to indicate averaging over a number of pixels.

From Figure 2.12, we can see that $R_1 - R_2$ is negative on the right side of the plane and positive on the left side. Thus, considering the above equation, it can be shown that the negative spatial frequencies in the interferogram correspond to the left component whereas the positive spatial frequencies correspond to the right component. This is provided that the averaged cross correlation of the fields is a smooth function of the range, R . A sample scenario with flat sand and bedrock, a 200m baseline distance and 10 MHz bandwidth is shown in **Error! Reference source not found.** where the single-sided partial-spectrum nature of each component is illustrated.

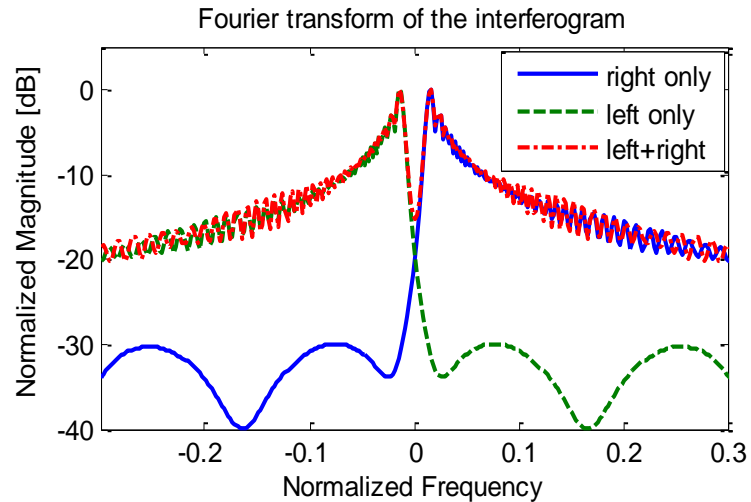


Figure 2.13: Fourier transform of the interferogram.

By filtering the interferogram, the left and right component can be separated. However, two parameters are very important in order to achieve accurate separation, namely the baseline distance and the operating bandwidth. An example for flat topography is shown in Figure 2.14 where a step filter was used to separate the left and right components. As shown in the figure, if the baseline distance is too small, the filtering process will not be very efficient since the two components will be very close to zero frequency and the resulting phase RMS error will be very high. On the other hand, if the baseline distance is too large, the spatial frequency is very high and thus frequency aliasing may occur due to the limited bandwidth (which corresponds to the spatial sampling distance). Thus careful selection of the baseline distance and the bandwidth has to be used.

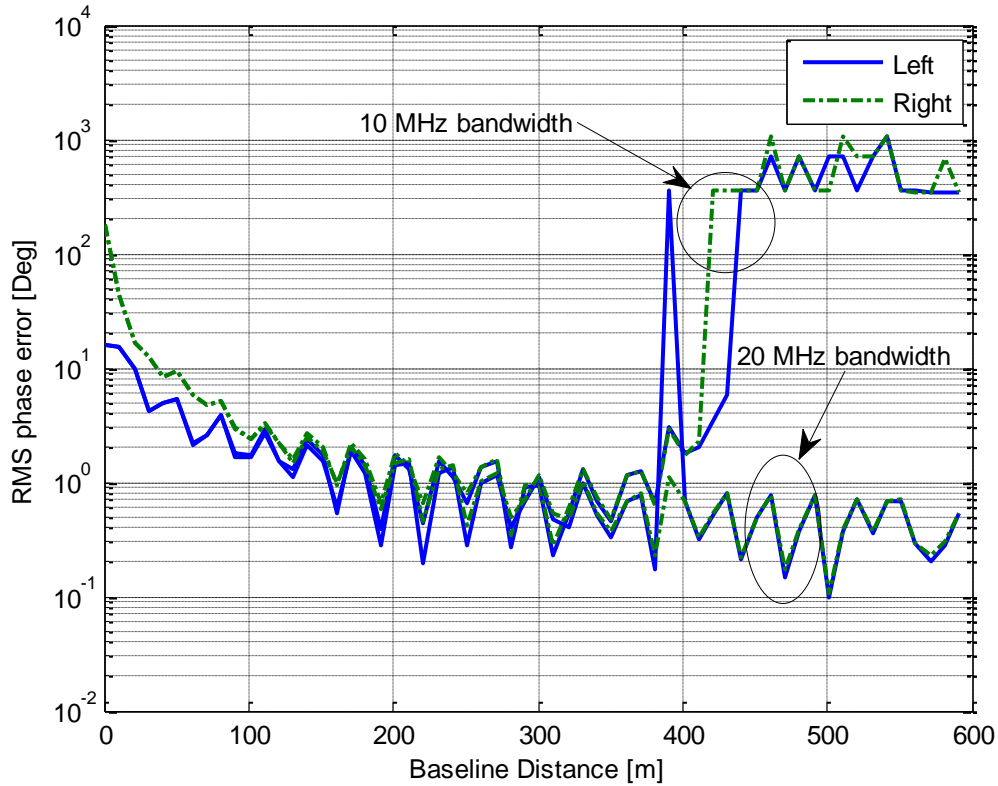


Figure 2.14: The RMS phase error after using two step filters to separate the left and right components for flat topography vs. the baseline for different operating bandwidths.

2.6 Conclusion

In this chapter, it is shown that conventional InSAR cannot be used to estimate the bedrock topography since it cannot account for the refraction and the different propagation velocity through the sand layer. Thus, we considered a two frequency InSAR system, the first one operating at the Ka-band where the scattering is dominated by the top sand surface thus this subsystem can provide the top layer topography. The second InSAR operates at the VHF frequency where it is shown that at this frequency the electromagnetic waves can propagate through the bottom layer and provide information about the bottom surface. We then discussed some of the SAR processing issues for the VHF InSAR such as SAR focusing and image distortion issues and the left/right

separation due to the low directivity of plane mounted antennas at VHF frequencies. In the following chapter, an inversion algorithm is presented that combines the data from the VHF and the Ka InSAR to correct for the refraction and the propagation through the top layer and provide an estimation of the bedrock height.

Chapter 3

Subsurface Topography Inversion Algorithm

The issues associated with the subsurface mapping InSAR design were addressed in the previous chapter. As was shown, conventional InSAR processing cannot be used to map the subsurface topography and modification in the processing has to be performed. In this chapter, the inversion technique that uses both the Ka- and VHF-InSAR data to obtain the subsurface height is discussed and its sensitivity to the different system and environment parameters is analyzed. The accuracy of the algorithm was verified using numerical simulations as well as scaled model measurements.

3.1 Subsurface Propagation Modeling

For the subsurface VHF InSAR processing, the conventional InSAR phase-to-height equations has to be modified to correct for the refraction and the different propagation speed inside the sand. For sand geometries with radii of curvature that are much larger than the wavelength (which is the aim of this paper), geometrical optics can be used to accurately relate the phase difference to the height. The geometry is shown in Figure 3.1 and the system of nonlinear equations relating the phase difference to the bedrock height and sand height and slope is summarized in Table 3.1. All the symbols refer to the VHF InSAR parameters except for $h_s(y)$ which refers to the sand height map obtained using the Ka-InSAR with conventional InSAR processing where h_s is the sand height and y is the ground range. All the dimensions and angles are in general dependent on the ground range (y) and/or radar azimuth position (x). In these equations, 2D sand

geometry is assumed (no variation with x). However, the extension for arbitrary 3D variations is straightforward by adjusting the azimuth position of the bedrock backscattering point according to the refraction through the sand surface.

Table 3.1: The system of nonlinear equations describing the phase difference between the two SAR images ($m=1,2$).

Description	Equation
Snell's Law	$\sin(\theta_{im}) = n_s \sin(\theta_{tm})$
Geometry	$\psi_m = \theta_{im} + \theta_{sm}$
Ground Range	$y_{sm} = y_m + (h_m - h_{sm}) \tan(\psi_m) + (h_b - h_{sm}) \tan(\theta_{tm} + \theta_{sm})$
Electrical Range	$R_{Em} = (h_m - h_{sm}) / \cos(\psi_m) + \text{Re}\{k_1\} / k_0 (h_b - h_{sm}) / \cos(\theta_{tm} + \theta_{sm})$
Phase Difference	$\delta\phi = 2(R_{E1} - R_{E2})$
Sand Map	$h_{sm} = h_s(y_{sm})$

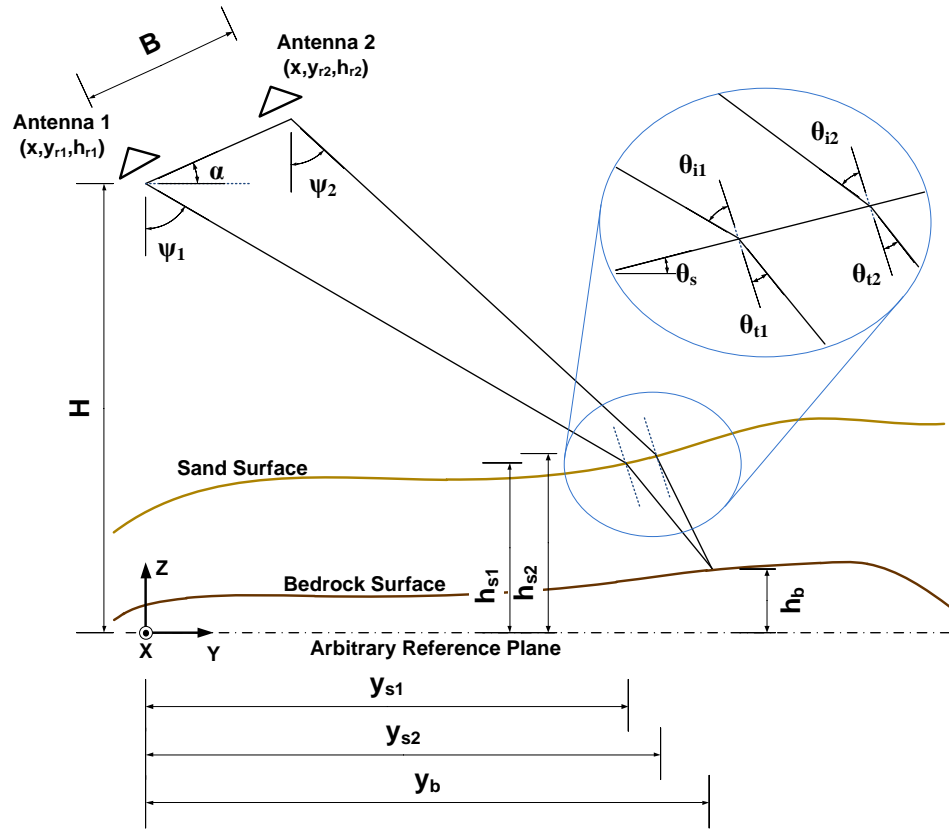


Figure 3.1: Geometrical optics modeling for subsurface imaging VHF InSAR (not to scale for clarity).

3.2 Inversion Algorithm

In the system of nonlinear equations in Table 3.1, the independent variables are chosen to be the look angle of antenna 1 (ψ_1) and the bedrock height (h_b). The VHF radar data provides $\delta\phi$, R_{E1} and R_{E2} . Several techniques are available to solve the above system of equations such as algebraic manipulation, least squares minimization and iterative techniques. However, since the sand map ($h_s(y_{sm})$) does not have a closed form for realistic sand surfaces, algebraic manipulation is not generally possible. Least squares minimization is very computationally intensive. Thus, we developed a physics-based iterative algorithm that can accurately and efficiently solve for the bedrock topography. The algorithm is summarized in the flowchart in Figure 3.2.

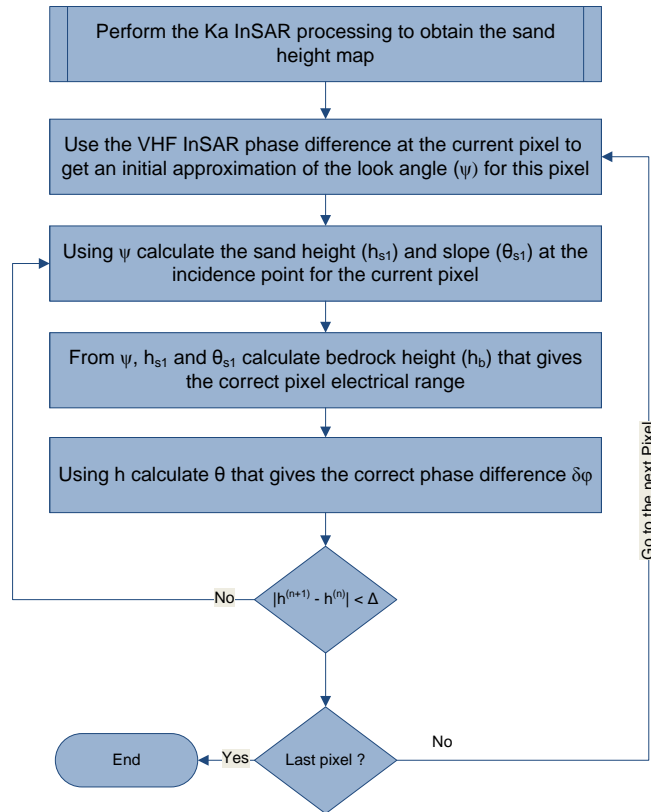


Figure 3.2: Flow chart of the proposed iterative algorithm for estimating the sand height above the underlying bedrock.

A walkthrough of the algorithm is shown in Figure 3.3 (a) - (c). After the sand surface height map ($h_s(y_{sm})$) is obtained from the Ka-InSAR, the algorithm proceeds as follows:

Figure 3.3 (a):

1. An initial estimation of the look angle ($\psi_1^{(0)}$) is calculated from the phase difference using the conventional InSAR equation:

$$\frac{\delta\phi}{2k_0} = B \sin(\alpha - \psi_1^{(0)})$$

This equation gives a reasonably close approximation since the sand layer thickness is typically much smaller than the radar height.

2. The look angle and the electrical range are then used to find an estimation of the ground range ($y_{s1}^{(0)}$) and height ($h_{s1}^{(0)}$) of the sand incidence point using:

$$y_{s1}^{(0)} = R_{E1} \cos(\psi_1^{(0)})$$

Figure 3.3 (b):

1. Knowing the sand slope and height, the ray from the first antenna can be propagated through the sand.
2. Estimate the bedrock height ($h_b^{(0)}$) that gives the correct electrical range to the first antenna (R_{E1}) using the equation in Table 3.1.

Figure 3.3 (c):

1. Knowing the bedrock height, find a new estimation of the look angle $\psi_1^{(1)}$ that gives the correct phase difference ($\delta\phi$).

2. Knowing the new look angle and the bedrock height, find a new estimation of the sand incidence point height and slope.

The process (b)-(c) is repeated until the magnitude of the change in the estimated bedrock height between two successive iterations $|h^{(n+1)} - h^{(n)}|$ is less than a prescribed error tolerance, Δh . Also, at this stage, the correct ground range of the scattering point (y_b) is already calculated.

The proposed algorithm was tested for several ideal and realistic sand surfaces and bedrock scenarios and was found to converge in less than 5 iterations in most cases. Some examples are shown in Figure 3.4 (a) and (b). The raw InSAR data for these examples were generated using geometrical optics modeling.

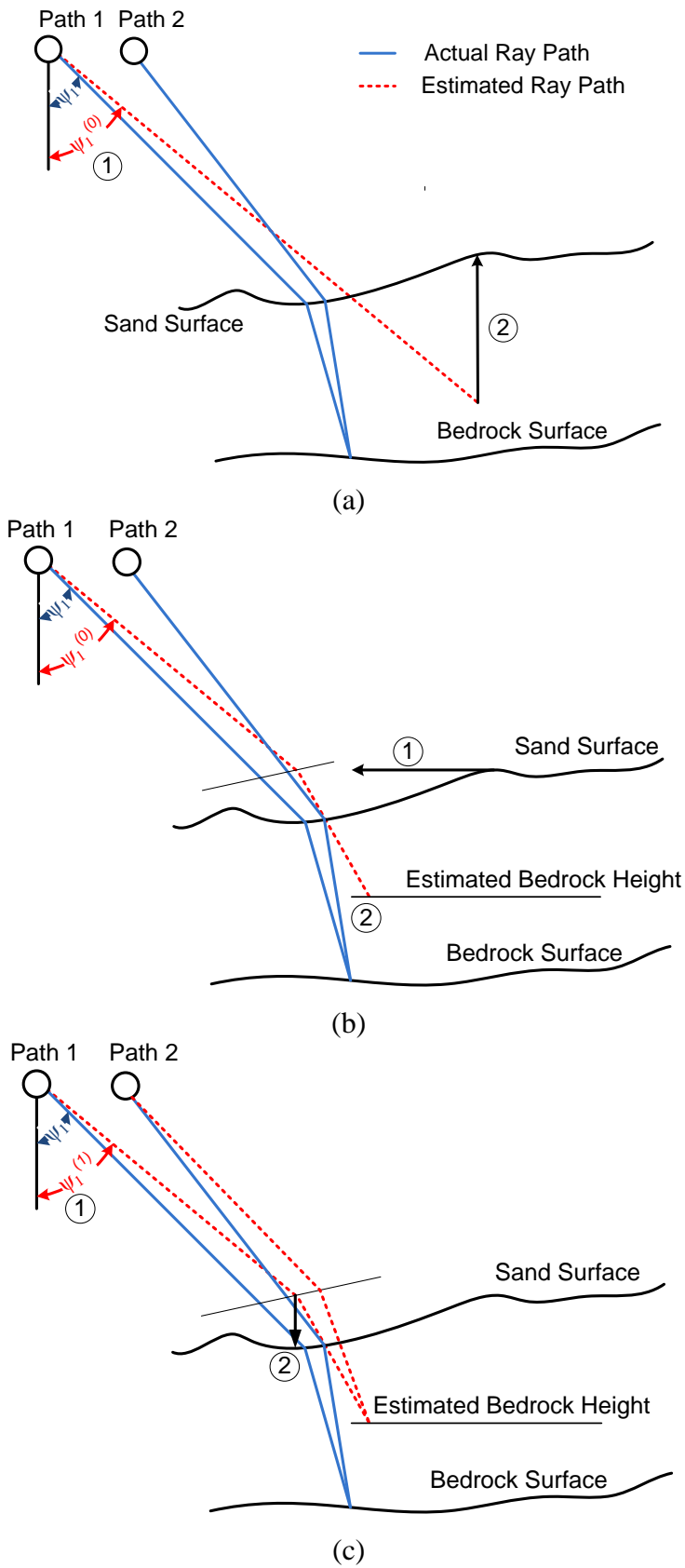
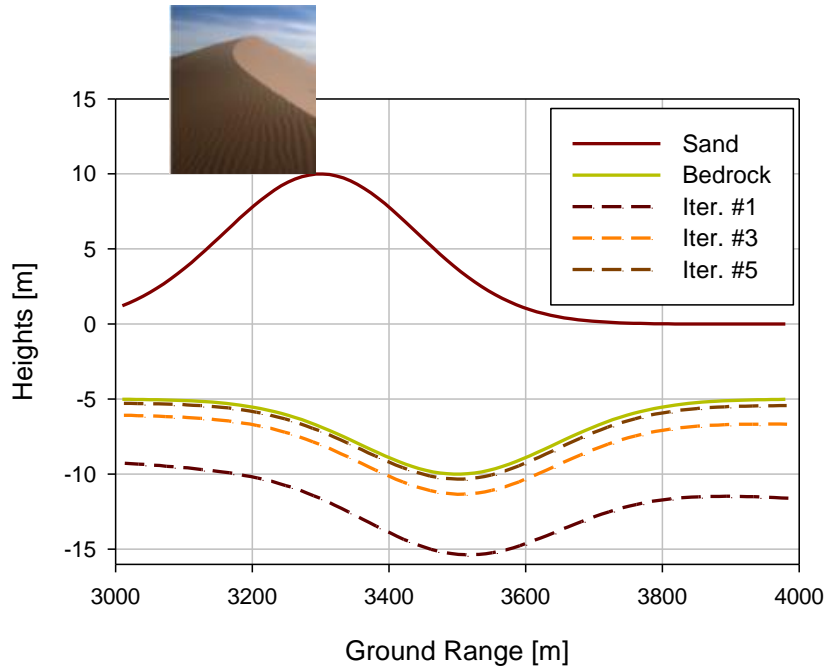
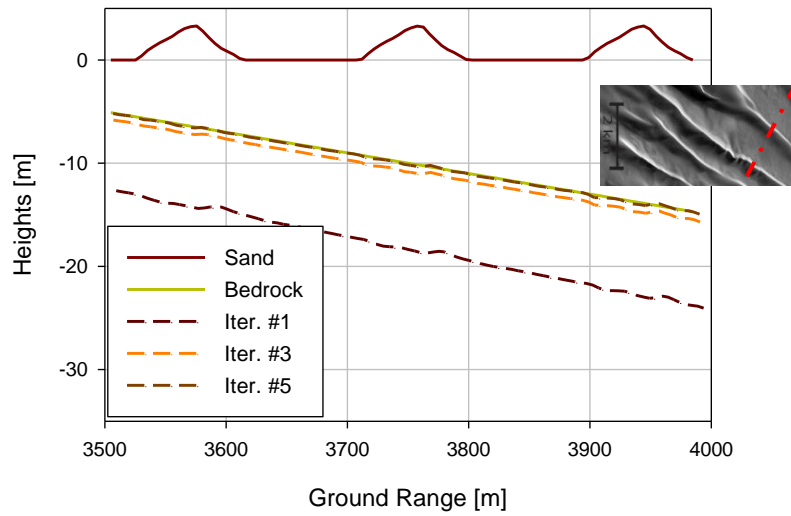


Figure 3.3: Illustration of the iterative algorithm.



(a)



(b)

Figure 3.4: Examples of the results of the iterative algorithm to some sand geometries, (a) Gaussian shaped dune on top of inverse Gaussian shaped bedrock and (b) linear sand dunes on top of flat sloped bedrock.

3.3 Sensitivity Analysis of the Height Estimation

Due to the unavoidable system errors and physical limitations, a sensitivity analysis has to be performed to characterize the height estimation accuracy in the presence of such errors. In this section, we summarize the limits of the height estimation accuracy due to errors in the sand dielectric constant as well as system limitations. The sand/bedrock scenario used in this section consists of flat horizontal bedrock underneath a flat sand with slope θ_s . In the following, unless otherwise stated, the dimensions are as summarized in Table 3.2 (the dimensions are defined in Figure 3.1).

Table 3.2: Sensitivity Analysis Scenario Parameters

<i>Parameter</i>	<i>Value</i>	<i>Parameter</i>	<i>Value</i>
α (Baseline Angle)	90°	y_b (Bedrock Ground Range)	3.5km
B (Baseline Distance)	100m	$h_b(y_b)$ (Bedrock Height)	0m
H (Platform Height)	5km	$h_s(y_b)$ (Sand Height)	10m
θ_s (Sand layer slope)	0°	Sand Layer Thickness ($h_s(y_b) - h_b(y_b)$)	10 m

Figure 3.5 shows the sensitivity of the inversion algorithm to errors in the sand dielectric constant. We can see that the percentage height error is relatively small for small variations in the sand dielectric constant for most realistic sand slopes. Similar results were obtained for different sand and bedrock scenarios. This allows the use of the proposed technique for different regions or slightly inhomogeneous sand layers with relatively small errors.

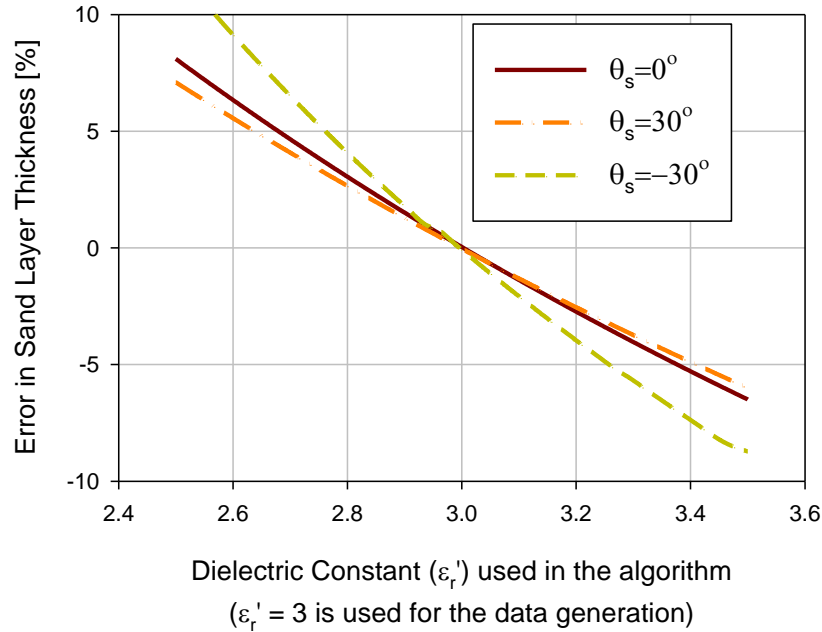


Figure 3.5: Sensitivity of height estimation to sand dielectric constant.

Another important system limitation is the phase accuracy of the generated interferogram. The phase accuracy is mainly limited by (1) the system thermal noise, (2) the decorrelation phase noise and (3) coregistration errors [23]. The plot in Figure 3.6 shows the height error due to phase difference errors which indicates that in order to obtain reasonable height accuracy baseline distance has to be maximized. However, increasing the baseline distance increases the decorrelation and consequently the phase noise. Thus, there is an optimum baseline distance at which maximum height accuracy is obtained. This optimum baseline distance depends on the subsurface statistics similar to conventional InSAR. Furthermore, the decorrelation noise can be significantly reduced at the expense of resolution by interferogram averaging [38]. For the baseline distances that are found from the simulation, single pass VHF interferometry cannot be performed

(maximum baseline distance is ~10m) and thus repeat pass interferometry is required [23].

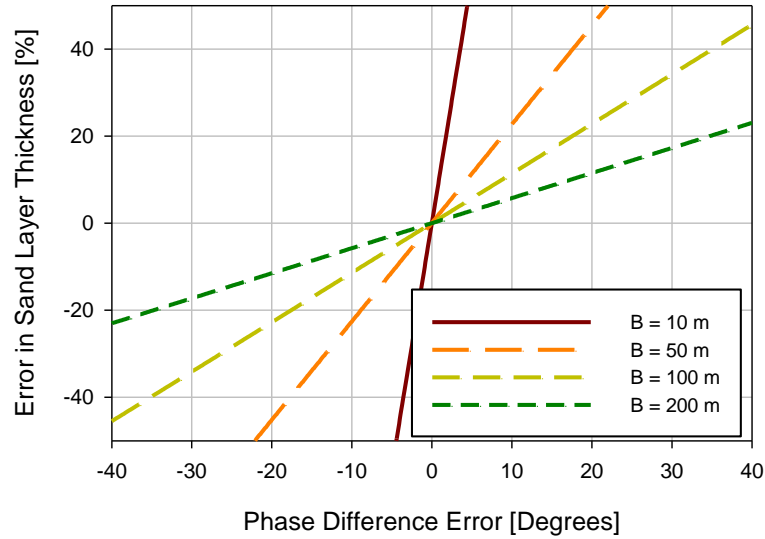


Figure 3.6: Sensitivity of height estimation to interferogram phase accuracy.

As discussed in the inversion algorithm, the absolute bedrock height estimation also depends on the accuracy of the range measurement (as is the case for the formal solution of the conventional InSAR processing). Since the range resolution is limited by the operating bandwidth, using larger bandwidth allows for better absolute height accuracy. The height error due to range measurement error is shown in Figure 3.7, where we can see that the absolute height error is very significant for small operating bandwidth. For example, 60MHz bandwidth yields range resolution of 2.5m which could result in bedrock height estimation errors as high as 10% depending on the sand slope. On the other hand, the simulations showed that the differential height error (the error in the bedrock height difference between two neighboring pixels) is very small (less than 1 meter for 1km pixel separation). This is again similar to the conventional InSAR case. To

obtain high accuracy in the absolute height measurements, an adequate number of Ground Control Points (GCPs) has to be used.

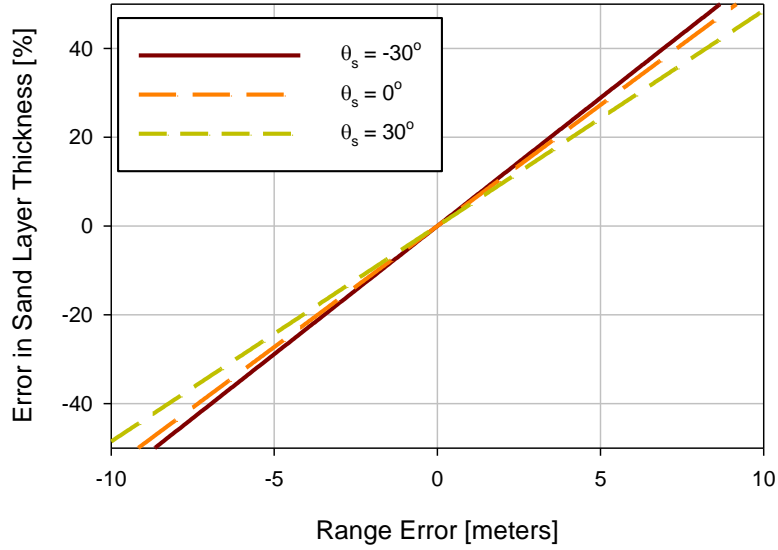
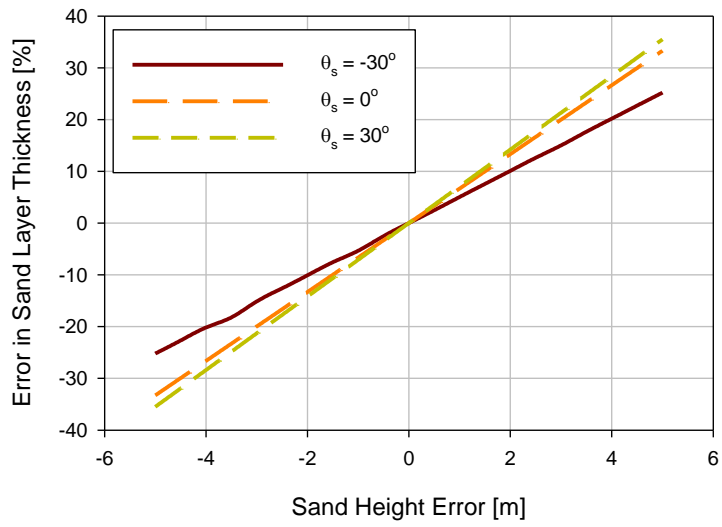
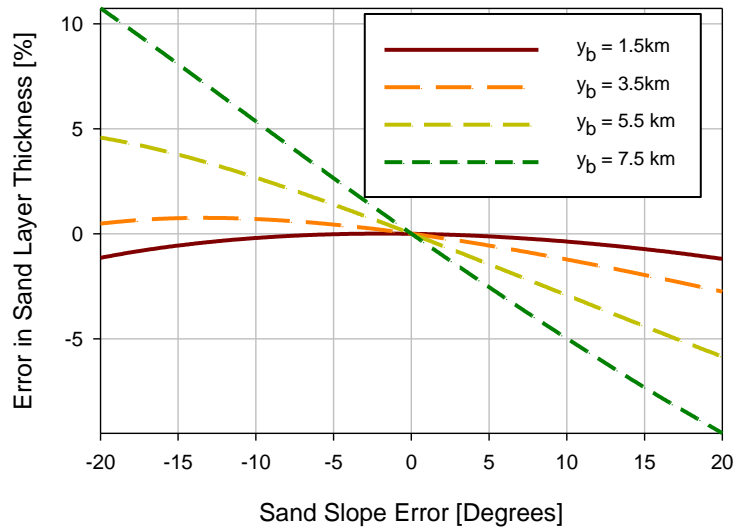


Figure 3.7: Relative sand thickness errors due to finite range accuracy.

Another source of errors is the accuracy of the Ka-InSAR sand height map. Figure 3.8 (a) and (b) show the effect of sand height and sand slope errors on the estimation of the bedrock height. As we can see from the figures, sand layer thickness estimation is moderately sensitive to sand height and slope errors. However, since a conventional InSAR system is used for sand height estimation, sand height accuracies less than 1m is easily achievable [14], [23]. For slope estimations, we found that higher order slope estimations yields reasonably good accuracy.



(a)



(b)

Figure 3.8: Bedrock height errors due to (a) errors in sand height estimation and (b) errors in sand slope estimation.

3.4 Experimental Results

In order to verify the simulation results, experimental measurements using a scaled model at 10 GHz in the laboratory was designed and implemented. The system is shown in Figure 3.9, where two antennas (Tx/Rx pair) were used together with a network analyzer to generate the SAR data. The two antennas are mounted on an XY table and are moved in two passes as shown in the figure to simulate two-pass interferometry.

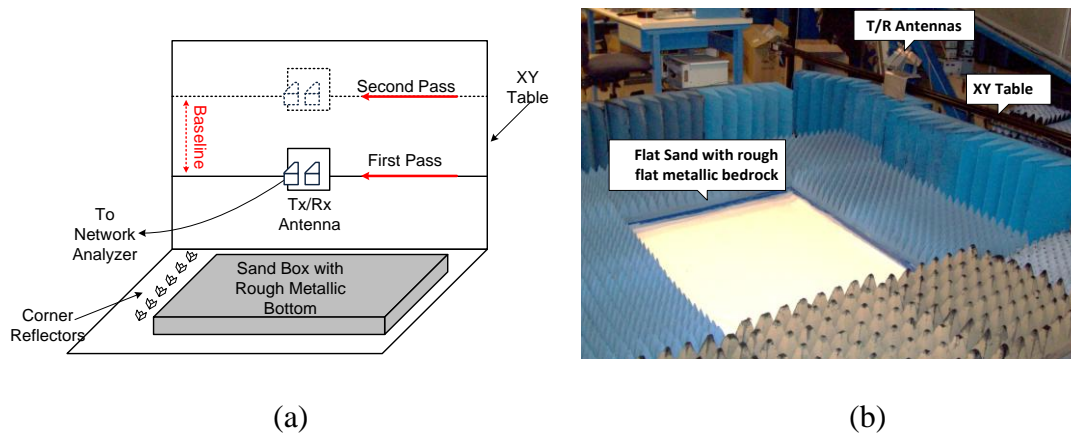


Figure 3.9: Scaled model for verification of the inversion algorithm, (a) schematic and (b) photo of the actual system.

Laboratory measurements have the advantage that they are in a controlled environment where all the dimensions and the component parameters are known. Table 3.3 shows the parameters of the implemented scaled model compared to the actual model and an ideal scaled model. Common sand is very lossy at 10 GHz. Thus, we used silica sand which, at 10GHz, has almost the same loss and dielectric constant of the common sand at 150MHz. Also, its particle size is much smaller than the wavelength at 10 GHz to avoid volume scattering. However, one limitation is the available space. As shown in Table 3.3, an ideal scaled model from 150MHz to 10GHz, needs the antennas to be 75m above the sand surface. Due to space limitations and the size of the XY table, the

maximum height of the antenna was reduced to 1.5m. Consequently, the sand thickness was reduced from the maximum value in the ideal scaled model and the integration angle was also reduced to avoid severe defocusing (since the antenna height is now comparable to the sand layer thickness and thus the doppler history will be significantly different unlike the actual InSAR where the doppler history does not change as much due to the relatively small sand layer thickness).

Table 3.3: Actual InSAR, Ideal Scaled Model and Implemented Scaled Model parameters.

	<i>Actual InSAR</i>	<i>Ideal Scaled Model</i>	<i>Implemented Scaled Model</i>
Operating Frequency	150 MHz	10 GHz	10 GHz
Operating Bandwidth	60 MHz	4 GHz	4 GHz
Fractional Bandwidth	40%	40%	40%
Sand Dielectric Constant	(common sand) $2.9 + i0.018$	$2.9 + i0.018$	(C50-70 Sand) $2.5 + i0.01$
Range Resolution	2.5 m	3.75 cm	3.75 cm
Antenna Height	5 km	$5 \times 0.15 / 10 = 75$ m	1.5 m (limited by the available space)
Incidence Angle Difference	$> \sim 1^\circ$	$> \sim 1^\circ$	$\sim 1^\circ - 2^\circ$
Sand Depth	$\sim 0 - 20$ m	0 – 30 cm	7.8 cm
HPBW _a (The antenna half power beamwidth in the azimuth direction)	180°	180°	$\sim 30^\circ$ (to have enough isolation as well as reduced clutter since the measurement is not done in the anechoic chamber)

The scenario consists of smooth flat horizontal sand on top of a rough metallic surface simulating the bedrock. The rms surface roughness of the bedrock is approximately 1.5mm (corresponding to normalized roughness of $k\sigma = 0.31$, where k is the free space propagation constant at the center frequency and σ is the rms roughness).

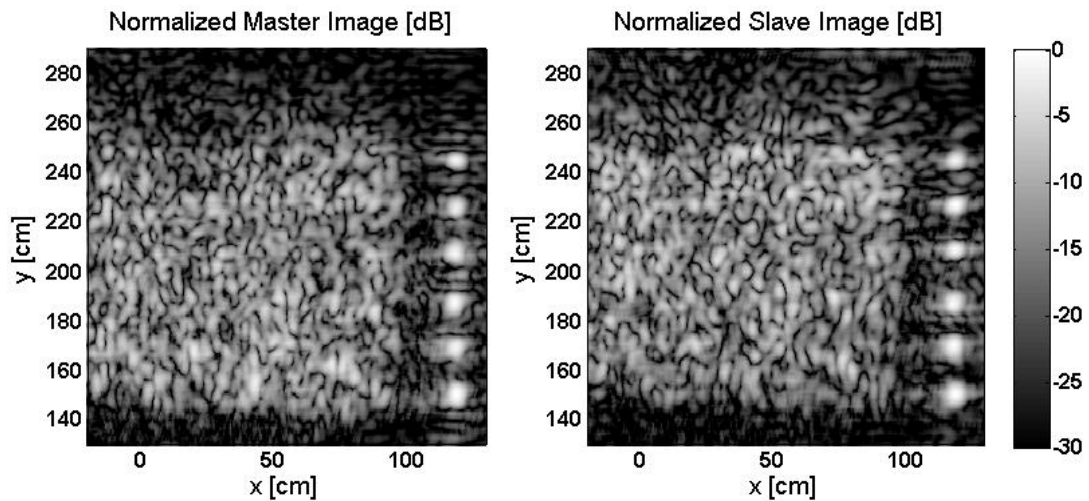
Six corner reflectors were placed at different range distances for image registration purposes, as shown in Figure 3.10 (a). Due to the relatively large operating relative bandwidth of the SAR, the data had to be calibrated to remove the frequency dependency of the cables and the antennas. The SAR data was calibrated using a 2" sphere. The optimum baseline for maximum height accuracy was experimentally found to be 25cm.

The two coregistered SAR images of the scene are shown in Figure 3.10 (b) for the two passes. Generating the phase difference between the two images (the phase interferogram) and using a 4x4 moving average, the phase interferogram is generated as shown in Figure 3.11 (a). The flat earth phase is then removed and 2D phase unwrapping is then applied to the interferogram to generate the unwrapped phase as shown in Figure 3.11 (b). The arbitrary constant in the phase interferogram is then determined knowing the height and the location of the corner reflectors. Conventional InSAR processing was then applied to the data. Then different constant azimuth sections in the generated 2D map were plotted in Figure 3.11 (c) for easy comparison. From the figure, we can see that conventional InSAR could accurately predict the height of the corner reflectors as expected, but it showed significant height error (up to 25%) and an artificial ramp in the bedrock height. This ramp is now noticeable because of the large change in the incidence angle across the map. The proposed algorithm was then applied to the data and the results are shown in Figure 3.11 (d). As we can see, both the corner reflectors and bedrock heights were accurately estimated with relatively small average error. The RMS error is 4mm. It is in part due to the defocusing through the sand layer, the coregistration errors and the geometrical decorrelation due to the baseline. The thermal noise

decorrelation was minimized by maximizing the transmitted power from the network analyzer and averaging the received signal at each position.

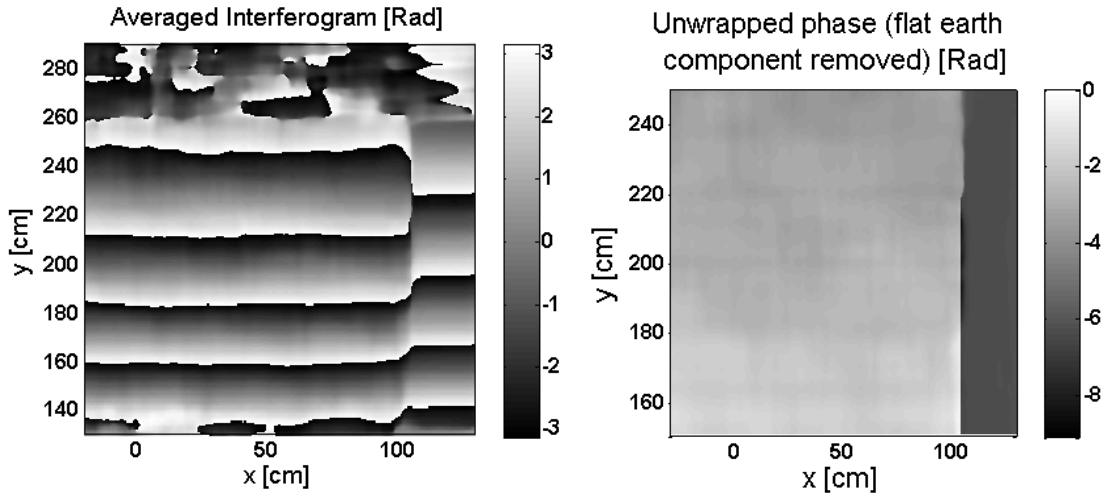


(a)



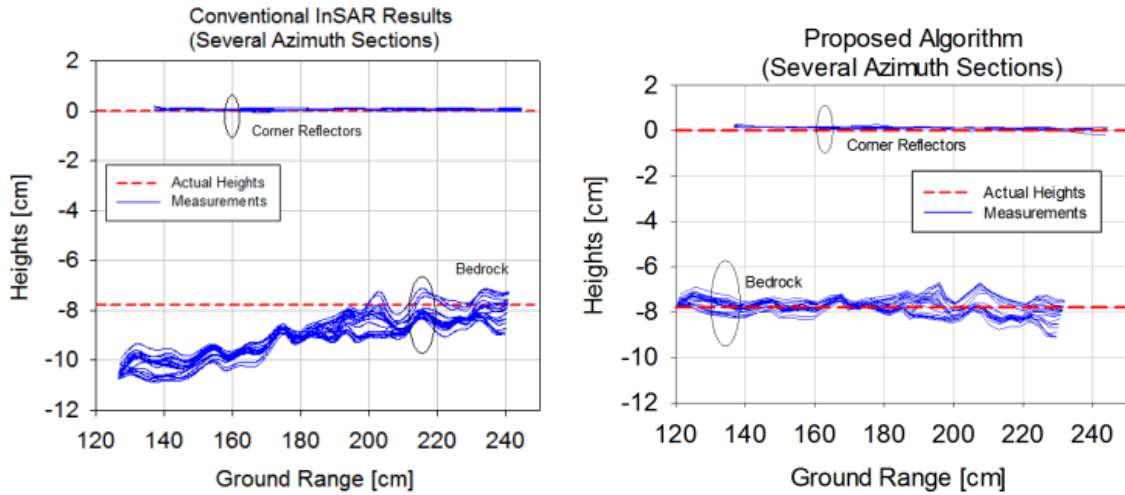
(b)

Figure 3.10: Experiment scenario, flat sand on top of horizontal bedrock. (a) A photo of the scene (the sand layer thickness is 7.8cm and the radar movement is along the horizontal direction), (b) the two SAR images for the two paths (x corresponds to the azimuth direction)



(a)

(b)



(c)

(d)

Figure 3.11: Scaled Model Results: (a) The averaged interferogram (4x4 boxcar averaging), (b) the unwrapped interferogram, (c) the estimated heights using the conventional InSAR and (d) the estimated heights using the proposed algorithm.

3.5 Conclusion

In this chapter, an inversion algorithm was presented that is able to use the sand map from the Ka-InSAR and the generated interferogram from the VHF-InSAR to estimate the bottom surface topography. The algorithm employs geometrical optics to model the propagation of the electromagnetic waves through the top surface. Some

scenarios for different top and bottom surfaces were simulated and it was shown that the proposed algorithm converges to the correct height within a few iterations. The effect of several the system and environment parameters on the height estimation accuracy was analyzed. It is shown that the baseline distance has to be at least a few tens of meters to achieve good height accuracy and thus single pass interferometry (two antennas mounted on the same plane) cannot be used. It is also shown that the height estimation is not very sensitive to the sand dielectric constant and thus slight sand inhomogeneities do not affect the bedrock height estimation. The algorithm was then verified using scaled model measurements in the lab.

Chapter 4

Image Distortion Effects in SAR Subsurface Imaging and a New Iterative Approach for Refocusing and Coregistration

In chapter 2, the effects of the defocusing and geometric aberrations in the subsurface SAR images were briefly discussed. Unfortunately, these aberrations cannot be corrected without the knowledge of the bottom surface topography which in turn is obtained from the subsurface SAR images using the algorithm described in chapter 3. Thus, in this chapter we propose an iterative approach where the SAR images are formed using conventional processing. Next, the subsurface inversion algorithm is used to obtain the subsurface height which is then used to refocus the images and remove the geometric aberration. The process is then repeated iteratively. We first present a fast subsurface SAR simulator that can generate the SAR data for arbitrary sand geometries. This simulator is then used to investigate the different image aberrations that result from the top surface topography including geometric and defocusing distortion. Next, the issue of subsurface caustics and their effect on the imaging is discussed. Then the iterative approach to estimate and correct for such aberrations is presented. It is shown using simulations and measurements that up to an order of magnitude improvement in the subsurface image resolution as well as significant improvement on subsurface interferogram coherence can be achieved. The approach is verified theoretically using 3D simulations and experimentally using scaled model measurements in the lab.

4.1 Fast Subsurface SAR Simulator & Subsurface Focusing Technique

The raw baseband range-compressed SAR image is a function of the radar position, x_j (slow time) and pulse time, t (fast time). For a number of discrete targets located at (x_i, y_i, z_i) , it can be expressed as [39]:

$$F(x_j, t) = C_1 \sum_{i=1}^N \frac{A_i(x_j) \text{sinc} \left(B \left(t - \frac{2R_i(x_j)}{c} \right) \right) \exp \left(-\frac{2i\omega_0 R_i(x_j)}{c} \right)}{R_i(x_j)^2} \quad (4.1)$$

where, C_1 is a constant that is dependent on the radar system parameters and the antenna gain, N is the number of scattering points in the scene, $A_i(x_j) = A(x_j, x_i, y_i, z_i)$ is an amplitude and phase factor that is dependent on the antenna radiation pattern and the transmission coefficient through the sand, B is the operating bandwidth, c is the speed of light in free space, ω_0 is the center angular frequency and $R_i(x_j) = R(x_j, x_i, y_i, z_i)$ is the effective range to each target defined as:

$$R_i(x_j) = |\bar{P}_{r,j} - \bar{P}_{inc i,j}| + \text{Re} \left\{ \frac{k_{sand}}{k_0} \right\} |\bar{P}_{inc i,j} - \bar{P}_i|, \quad (4.2)$$

where $\bar{P}_{r,j}$, $\bar{P}_{inc i,j}$, \bar{P}_i are the position vectors of the radar, the incidence point and the target, respectively as shown in Figure 4.1.

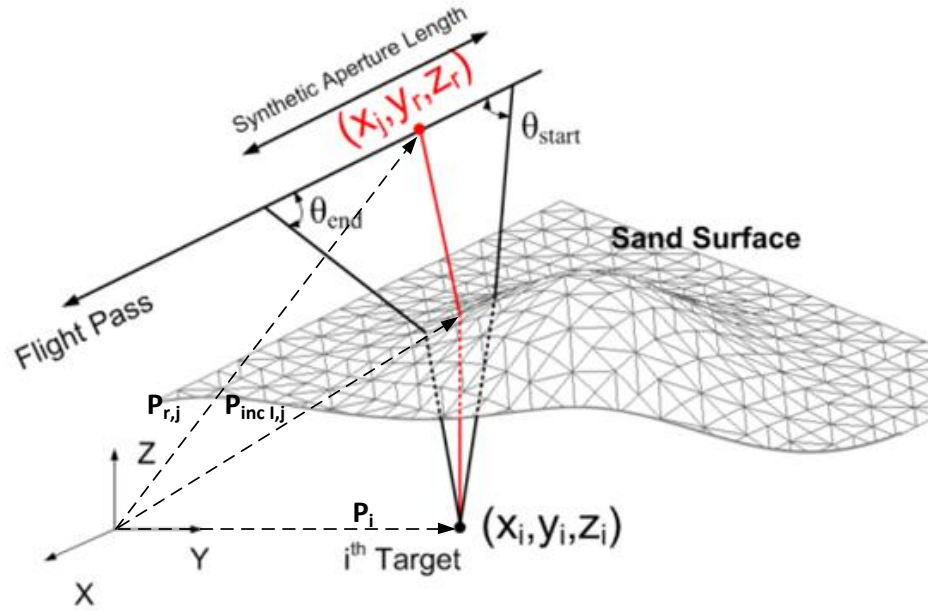


Figure 4.1: 3D SAR Geometry.

The above relations does not take into account the multiple reflections since for sand layers, the reflection coefficient for the vertical polarization is typically below 10dB as described in chapter 2. In addition, the sand propagation losses help in attenuating the multiple reflections further. The dispersion due to the propagation through the sand is not included either, since the sand dispersion is very small and can be neglected for sand layer thicknesses that are less than $\sim 50\text{m}$ for the bandwidth of interest as discussed in chapter 2. For distributed targets, the summation in (1) becomes a 2D integration, this is useful for including the speckle and the decorrelation effects, but it is not be considered in this work. The exponential term generates the phase history of each target (usually referred to as the Doppler history). Through this Doppler history, the image can be focused along the azimuth (or cross-range) direction through techniques such as back projection or omega-k algorithm by coherent summation at each pixel after correction for the phase history. The magnitude of the term A_i , performs a windowing effect on the

phase history and thus limits the resolution, whereas its phase variation causes distortion to the phase history and should be minimized through careful antenna and system design and/or calibration.

The ray path for a point target under an arbitrary sand geometry is shown in Figure 4.1. The direct method to form the raw SAR data (generate $R_i(x_j)$ and $A_i(x_j)$), is by solving the system of nonlinear equations describing the ray propagation through the sand surface for each target and each radar position. Here it is assumed that air-sand interface profile is known. It should be noted that in real practice the air-sand interface profile can be obtained directly using a high-frequency (Ka-band) InSAR. The direct method for generating raw SAR data for large number of targets is extremely time consuming. Thus, we developed a much faster and relatively accurate technique which can efficiently generate the raw SAR data for large number of targets without the computational cost of solving a large set of nonlinear equations. The approach can be summarized as follows (see Figure 4.2):

1. The sand surface is triangulated using a suitable resolution. Next, at each radar position, x_j , a number of rays are launched from the radar to the center of each sand surface facet.
2. Those rays are then refracted through the sand facets using geometrical optics and propagated through the sand in ΔR steps as shown in Figure 4.2. The electrical range to the radar, $R_n(x_j, x_n, y_n, z_n)$ and losses $A_n(x_j, x_n, y_n, z_n)$, are recorded at each ΔR step.
3. This results in the knowledge of the effective range and losses over the non-uniform grid (x_n, y_n, z_n) . Using interpolation over a non-uniform grid we can

obtain the electrical range and losses to each target (x_i, y_i, z_i) . We found that the required number of grid points (x_n, y_n, z_n) to achieve good range accuracy is relatively small since the range function is a relatively smooth function of the position for practical sand surfaces and radar heights as shown in the contour in Figure 4.2.

4. This process is then repeated at each radar position x_j to obtain the full phase history for each point in the scene. This technique is much faster since interpolation is a much less computationally intensive operation compared to the solution of nonlinear equations. However, interpolation can only be performed when there are no caustic conditions (ray intersection). For the considered sand layer depths and sand angle of repose (maximum slope), caustic conditions happen relatively rarely. In the regions where they occur, simple ray tracing cannot be used and a more rigorous approach has to be employed such as MLFMM or Physical Optics.

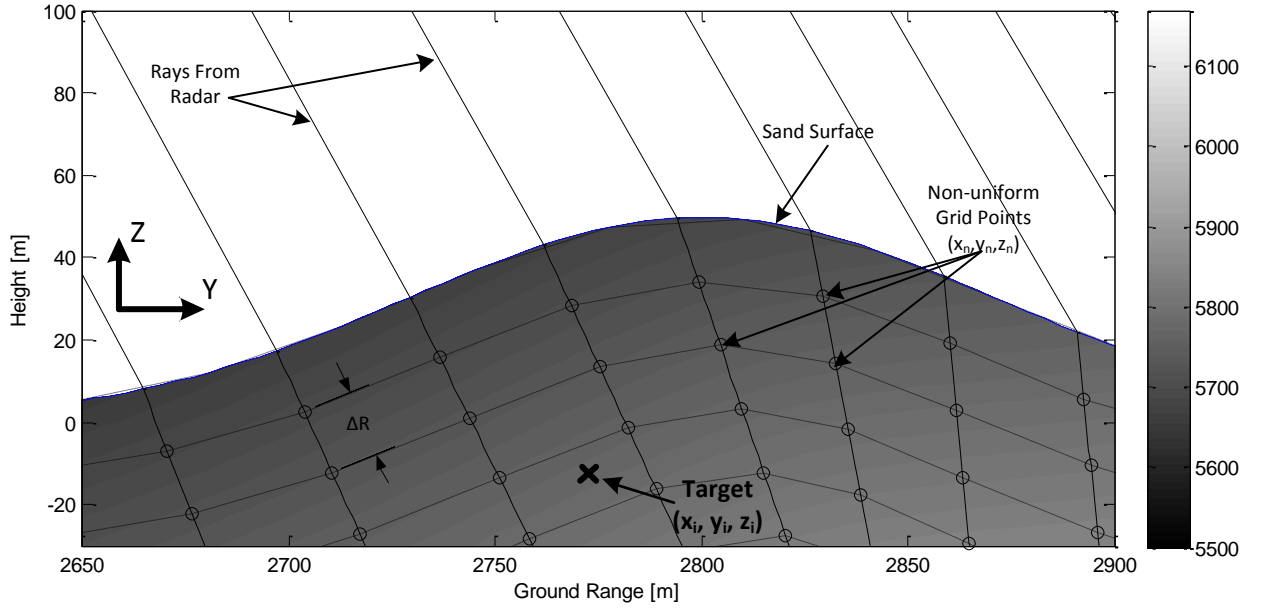


Figure 4.2: Interpolation over a non-uniform grid to obtain the target range history. The contour represents the electrical range to the radar position. The actual grid points and sand surface are 3D, but the 2D case is plotted for clarity.

The subsurface focusing is performed using a modified back-projection approach by coherently adding the raw SAR data $F(\cdot)$ knowing the phase history of each point on the focusing surface (the bedrock). This is done by performing the following summation at each focusing surface point (x_p, y_p, z_p) :

$$\begin{aligned}
 & I(x_p, y_p, z_p) \\
 &= \sum_j \frac{\exp\left(\frac{2i\omega_0 R(x_j, x_p, y_p, z_p)}{c}\right)}{A(x_j, x_p, y_p, z_p)} F\left(x_j, \frac{2R(x_j, x_p, y_p, z_p)}{c}\right) \quad (4.3)
 \end{aligned}$$

Here $I(x_p, y_p, z_p)$ is the pixel complex value at focusing surface (x_p, y_p, z_p) and $A(\cdot)$ and $R(\cdot)$ are obtained by 3D interpolation over the generated Doppler history $A_n(x_j)$ and $R_n(x_j)$ using the same technique as the SAR simulator. The summation is done over

the desired synthetic aperture length (or equivalently the integration angle, $\theta_{\text{end}} - \theta_{\text{start}}$) as shown in Figure 4.1. The amplitude term is omitted in the focusing since it tends to amplify the noise and it is very hard to accurately estimate the sand losses. Thus, the subsurface focused image can be formally written as:

$$\begin{aligned}
 & I(x_p, y_p, z_p) \\
 &= \sum_j \exp\left(\frac{2i\omega_0 R(x_j, x_p, y_p, z_p)}{c}\right) F\left(x_j, \frac{2R(x_j, x_p, y_p, z_p)}{c}\right) \quad (4.4)
 \end{aligned}$$

4.2 Defocusing and Distortion Effects in SAR Subsurface Imaging

Conventional SAR processing assumes that the ray path between the radar and the target is a straight line with a propagation constant equal to that of free space. For subsurface targets with top surface undulations, this results in two types of SAR image artifacts: 1) defocusing and 2) geometrical distortion. Furthermore, other geometric distortion effects common to conventional SAR, such as foreshortening and layover, also appear, but these become a function of the geometry of the top surface in addition to the bottom surface. In this section, we present these effects on some practical scenarios. The simulations in this section assumes a radar center frequency of 150 MHz, the bandwidth is 60MHz and the platform height is 5 Km.

4.2.1 Defocusing Effects

The first problem with subsurface SAR images are defocusing effects which can be separated into range defocusing and azimuth defocusing. Simulation results shows that range defocusing is much less significant than azimuth defocusing since dry sand dispersion is very small for the frequency range considered in this application as shown

in Chapter 2. However, azimuth defocusing is very significant and poses significant limitation on the achievable azimuth resolution. An example is shown in Figure 4.3 where a target was placed under a sand layer with flat interface at a ground range of 2km and a depth of Z_t that is varied from 0 - 40m. The target image was generated using conventional back-projection with focusing plane at the top surface. Figure 4.3 (a) shows that for small integration angle, the azimuth point spread function (APSF) of the target maintains its form up to a depth of approximately 20m (corresponding to long depth of focus) but has poor ground resolution. On the other hand, for larger integration angles (Figure 4.3 (b)), the APSF has much better ground resolution but keeps its form over much shorter distance of about 5m, beyond which the resolution degrades rapidly (short depth of focus). This is compared to the same target in air in Figure 4.3 (c) and (d), where we can see that the depth of focus is much larger and thus conventional SAR images does not require refocusing for small height perturbations unlike subsurface images. It should also be noted that for VHF SARs due to the low operating frequency and the limitations on the antenna sizes, larger integration angles are typically required to both achieve reasonable ground resolution as well as good SNR (e.g. 120° is used in [5]). Thus, accurate focusing is extremely important from both an image resolution and clutter reduction point of views.

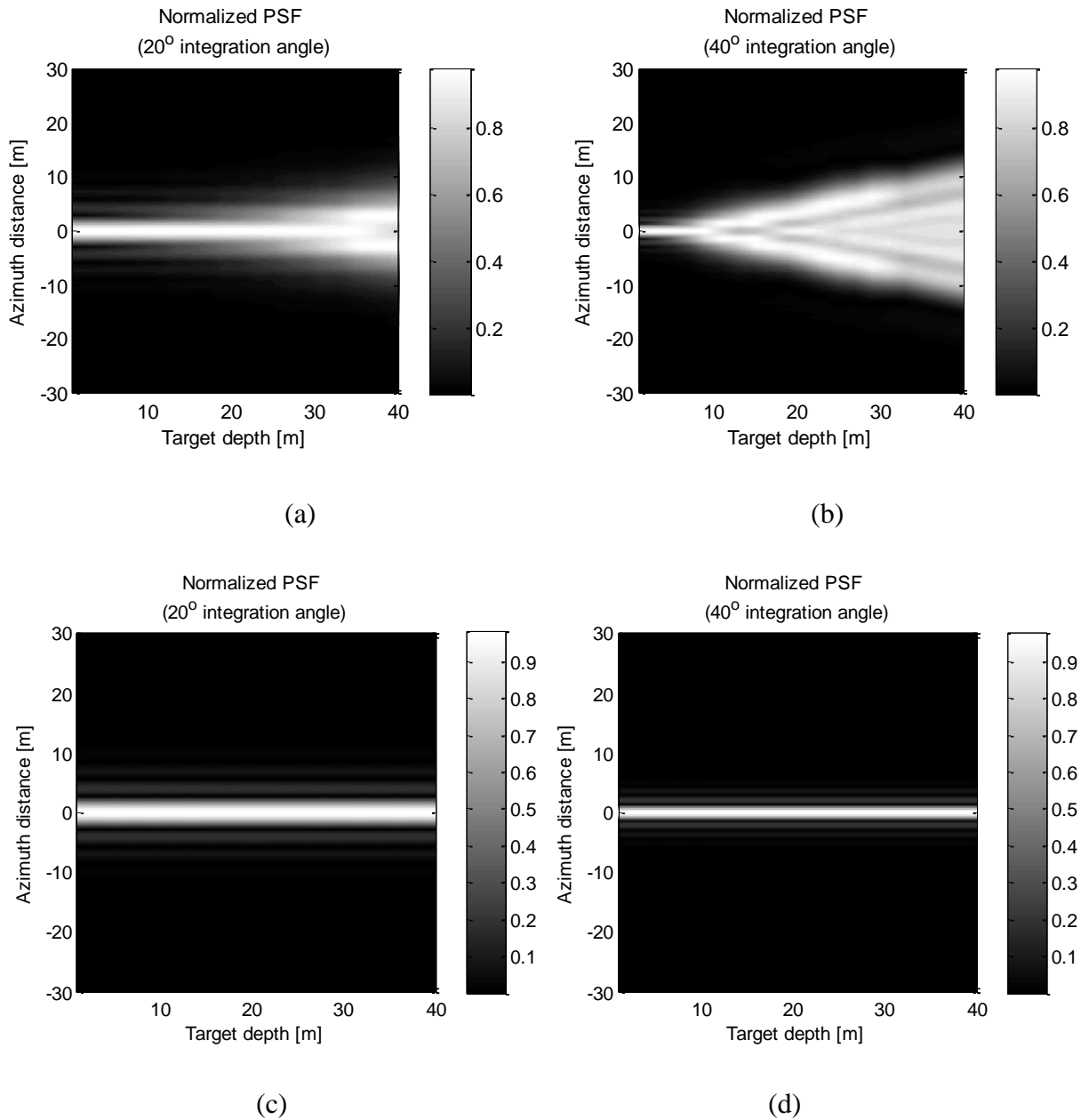
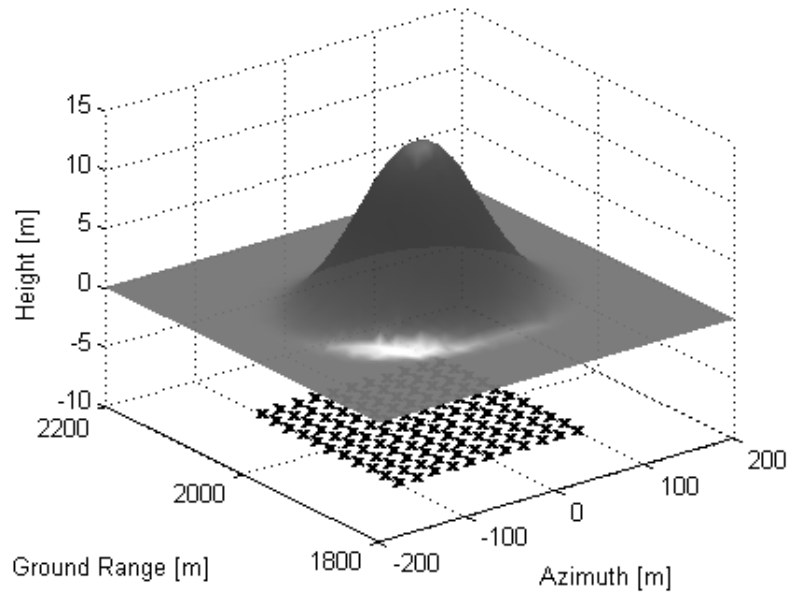


Figure 4.3: Azimuth Point Spread Function (APSF) of a point target vs. the target depth when using conventional focusing with focusing plane at the surface with (a) 20° integration angle and (b) 40° integration angle, (c) and (d) same scenarios as (a) and (b) but the target is assumed in air.

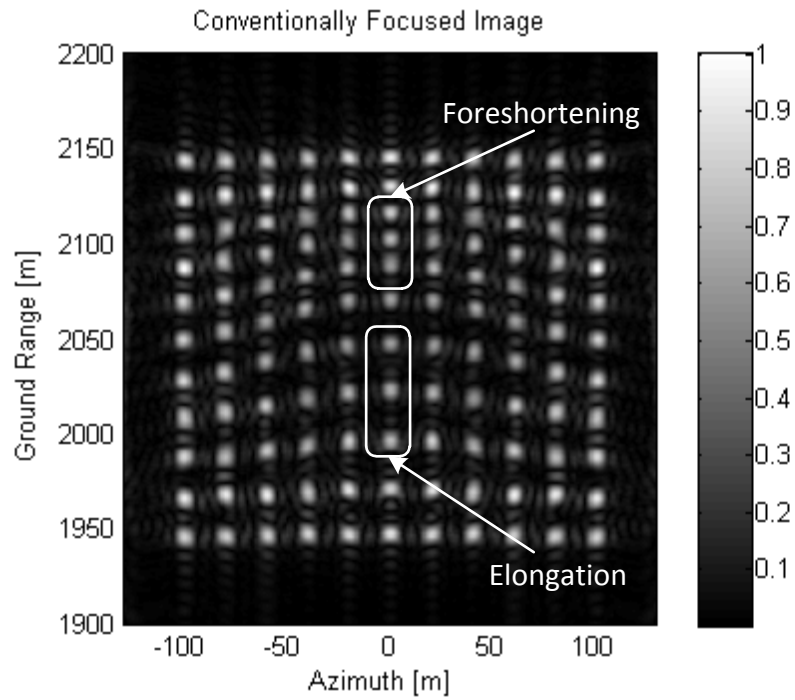
4.2.2 Geometric Distortion Effects

The second issue with conventional focusing is geometric distortion due to refraction effects through the top surface topography. A sample scenario is shown in

Figure 4.4 (a), where an array of 121 (11x11) point targets arranged uniformly over an azimuth range of 200m and ground range of 200m centered at (0, 2Km) is placed at a depth of 5 m under a Gaussian shaped sand dune with crest height of 15m and length of 100m. The integration angle was limited to 10° to avoid defocusing as discussed in the previous section. We can see that the point target locations are shifted due to the refraction through the top layer. The two shown effects in Figure 4.4 (b) correspond to foreshortening and elongation using conventional SAR processing. This limits the use of the subsurface InSAR in some applications such as mine detection. It also affects the image coregistration accuracy resulting in lower InSAR coherence since these distortion effects are strong function of the look angle. For larger slopes and/or deeper targets, foreshortening can become a special form of layover where caustic target location ambiguity can occur.



(a)



(b)

Figure 4.4: Sample scenario to illustrate geometric distortion in subsurface SAR images due to top layer propagation effects, (a) the simulation scenario and (b) the conventionally focused SAR image.

4.2.3 *Caustic Surfaces and their Effects*

Caustic (or focal) surfaces exist at ray intersections due to phase front aberrations at which the conventional geometrical optics solution is invalid and either extensions to physical optics (PO) or other numerical technique have to be used to estimate the fields at these locations. As mentioned before, the top air-sand interface curvature is large for most sand dune surfaces encountered. For these conditions, caustic surfaces generally exist at depths beyond the sand layer thickness above the bedrock. However, it is interesting to show how the caustic surfaces can be estimated and some of the geometric distortions that are introduced due caustics. It should be noted that the caustic surfaces change according to the source location (radar position) and thus have to be estimated at each position along the radar path.

4.2.3.1 *Estimation of caustic surfaces*

Estimation of caustic surfaces is a common problem in computer graphics [40], [41]. One common approach to characterize the caustic surface is the Jacobian method [40], [42]. This method is summarized as follows: the points along a ray emanating from the center of the surface triangular facet i downwards can be parameterized as:

$$\bar{p}_i(u) = \bar{C}_i + u \hat{k}_t = \langle x, y, z_s(x, y) \rangle + u \hat{k}_t \quad (4.5)$$

Here \bar{C}_i is the coordinate vector of the center of the triangular facet i , $z_s(x, y)$ is the sand surface height function and \hat{k}_t is the unit vector along the direction of propagation into the sand.

The refractive caustic surface (denoted as $\bar{\Gamma}$) is tangential to the refracted rays at one or more points, thus for the i^{th} ray, the caustic surface lies at certain u termed as u_c :

$$\begin{aligned}\bar{\Gamma}(x, y) &= \langle X_c(x, y), Y_c(x, y), Z_c(x, y) \rangle \\ &= \bar{C}_i(x, y) + u_c \hat{k}_t(x, y)\end{aligned}\tag{4.6}$$

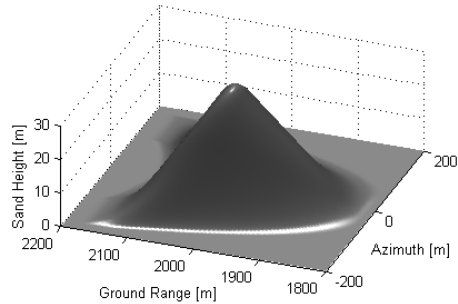
To find the value(s) of u_c at the tangent point, we use the fact that the rays bunch up close together at the caustic surface. Thus, in the limit, traversing infinitesimally along $\hat{k}_t(x, y)$ at the caustic is equivalent to traversing from one ray to the next. Therefore, at the caustic surface the determinant of the Jacobian $J(\bar{C}_i(x, y) + u_c \hat{k}_t(x, y))$ must vanish, i.e.:

$$\begin{vmatrix} 1 + u_c \frac{\partial k_t^X}{\partial x} & u_c \frac{\partial k_t^X}{\partial y} & k_t^X \\ u_c \frac{\partial k_t^Y}{\partial x} & 1 + u_c \frac{\partial k_t^Y}{\partial y} & k_t^Y \\ \frac{\partial z_s(x, y)}{\partial x} + u_c \frac{\partial k_t^Z}{\partial x} & \frac{\partial z_s(x, y)}{\partial y} + u_c \frac{\partial k_t^Z}{\partial y} & k_t^Z \end{vmatrix} = 0\tag{4.7}$$

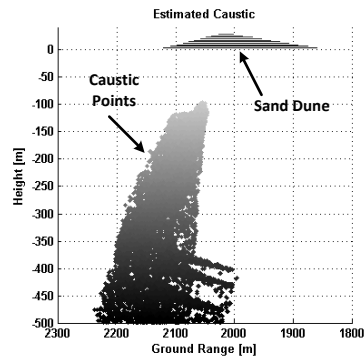
Where eqns. (4.6) was used and k_t^X, k_t^Y, k_t^Z are the x, y and z components, respectively, of the vector $\hat{k}_t(x, y)$.

Solution to (4.7) yields u_c and thus a number of points on the caustic surface equal to the number of top surface triangular facets. An example caustic surface for a barchan sand dune is shown in Figure 4.6 (a), (b) and (c) for one incidence angle and radar position. The slightly noisy nature of the generated estimation of the caustic surface at deeper locations is due to the low order estimation of the surface and surface normal partial derivatives used. The numerical noise can be reduced by increasing the order of the surface slope estimation technique. Due to the complex shape of the sand dune, the resulting caustic surface is relatively complex with several cusp curves (intersection between two caustic surfaces). It is interesting to note the different heights of the cusp curves corresponding to the different curvatures of the sand dune. The larger the radius of

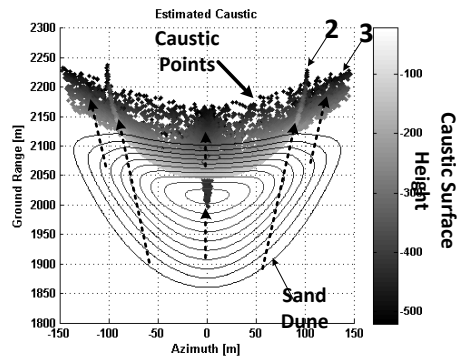
curvature, the larger is the depth of the cusp curves as shown by the dotted arrows in Figure 4.5 (c).



(a)



(b)



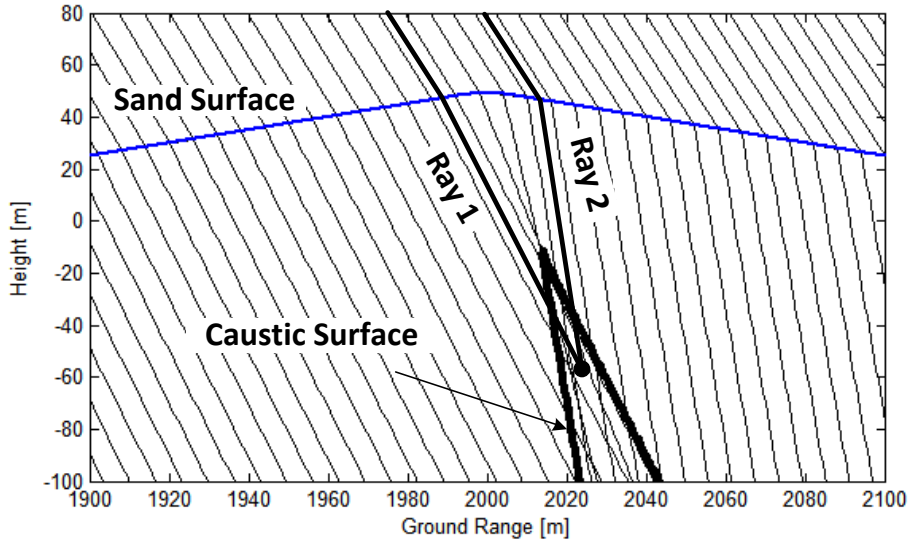
(c)

Figure 4.5: (a) The barchan sand dune, (b) side view and (c) top view of the estimated caustic surface with the sand dune. The dotted arrows in (c) show the caustic surfaces corresponding to each curved feature on the sand dune. The radar position is at (0, 0, 5 km).

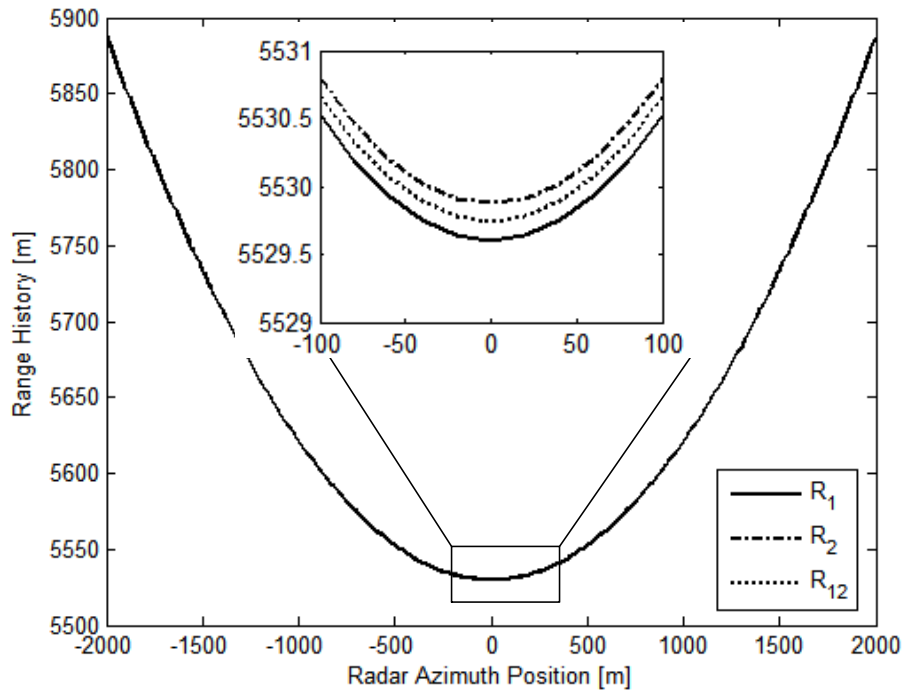
4.2.3.2 Image distortion due to caustic effects

As previously mentioned, the geometric optics solution is not valid at the caustic surface and within certain distance from it. However, it is known that the field reaches a maximum near the caustic surfaces. Below those surfaces, there are generally two or more rays that intersect and the geometrical optics can be used to estimate the incident fields at these locations. An example of a caustic surface under a 2D linear sand dune is shown in Figure 4.6 (a). We can see that for a scatterer below the caustic surface in this example it will appear at three ranges corresponding to the scatterer monostatic response along ray 1 and 2 and the scatterer bistatic response along the two rays. The interpolation technique can be extended to this case by separating the rays to two groups corresponding to negative and positive sand surface slopes. Then interpolation over each domain is performed as described in section II. For target locations inside the intersection between the two domains, three range values are generated corresponding to the three conditions. Those three ranges were calculated as a function of the radar position for the target shown Figure 4.6 (a) and are plotted in Figure 4.6 (b). Depending on the radar resolution and the target backscattering and bistatic response, the point target can appear as one, two or three point targets at each radar position which would correspond to a form of range distortion that is unique to submerged targets and not encountered for above surface targets. The interpolation technique can be further extended to other 2D and 3D surfaces. However, for relatively complex sand surfaces, the separation of the interpolation domains becomes nontrivial and direct ray calculation might be more computationally efficient for targets below the caustic surface. The electrical range difference between the two rays is very small even for such a deep target (about 100 m below the sand) and

is within the resolution of our proposed system thus the inversion algorithm would still obtain the correct height of the target.



(a)



(b)

Figure 4.6: (a) A target at (0, 2025, -60) enclosed within a simple caustic surface appearing at three different ranges and (b) the simulated range history of the target using the extended interpolation technique.

4.3 Iterative Approach

As discussed in the previous section, geometric and defocusing effects can be very noticeable and severely affect the quality and usability of the generated SAR image. It also affects the resolution and accuracy of the resulting InSAR subsurface topography map. To overcome these effects, subsurface focusing is required. However, as shown in (4.4), the correct subsurface height, z_p , is required. Since, the subsurface height can be obtained using the subsurface InSAR algorithm previously presented in chapter 3; we propose the use of an iterative approach as shown in Figure 4.7, where an initial focusing surface is used with small integration angle. This gives relatively deep depth of focus and thus minimizes the PSF distortion as shown in Figure 4.3. The InSAR interferogram is then formed and the subsurface height is estimated using the algorithm in chapter 3. Knowing the subsurface height, the image is then refocused using a larger integration angle giving a higher resolution interferogram and subsurface map. The iterative process is stopped when the difference in the obtained subsurface height between two successive iterations is less than a certain threshold or when the maximum integration angle is used.

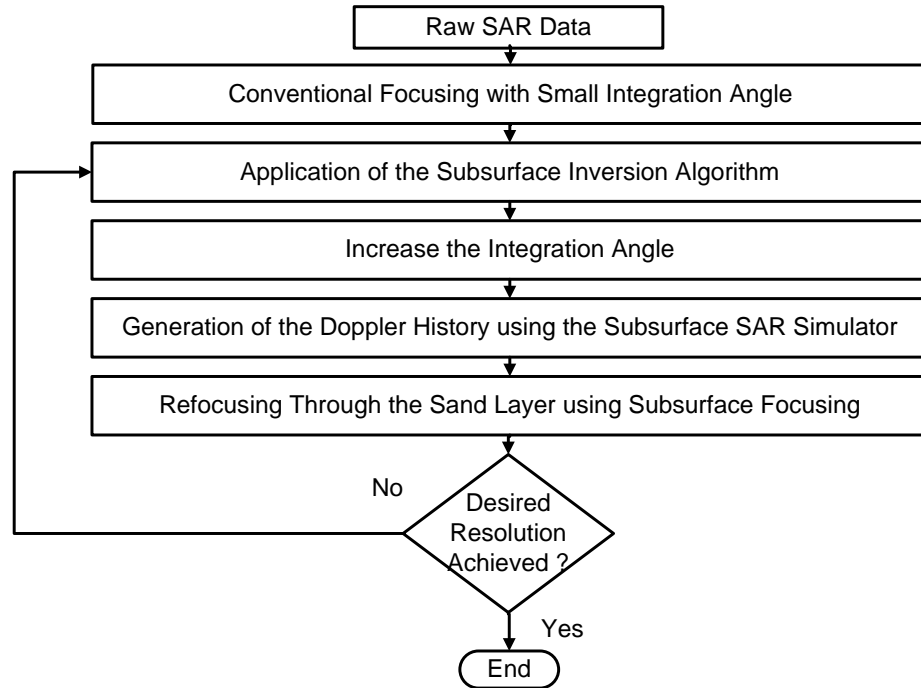


Figure 4.7: The proposed iterative scheme.

4.4 Simulation Results

The proposed iterative focusing approach was applied to two scenarios as shown in Figure 4.8 and Figure 4.9. In Figure 4.8 (a) a grid of ideal point targets spaced by 20 m along the azimuth and the ground range, placed on the surface of a cone is simulated under a linear sand dune. The results of applying conventional focusing with 10° and 40° on the sand surface are shown in Figure 4.8 (c) and (d). We can see that small integration angles yields relatively low resolution but the point targets responses do not show noticeable dispersion as indicated in Figure 4.3 whereas using large integration angles results in distorted response as expected. On the other hand, using the subsurface focusing technique, we started by an image very similar to that of conventional focusing. However, once the subsurface height is known and the focusing is performed at the correct point targets heights, the integration angle can be increased to 40° without any

noticeable distortion and the resulting resolution is very close to the ideal resolution. Furthermore, the geometric distortion is removed since the focusing is performed at the correct locations. It should be noted that since the resulting image is automatically geometrically projected to the grid, the geometric projection step in conventional InSAR is no longer needed. The coherence is also improved by more than 30% as shown in Figure 4.8 (b) as expected since the geometric and the defocusing decorrelation are removed. The coherence histogram is plotted for points on the image that are within 20dB from the maximum. A barchan sand dune is simulated as well and the results are shown in Figure 4.9, where we can also see the improvement in the coherence and the image resolution.

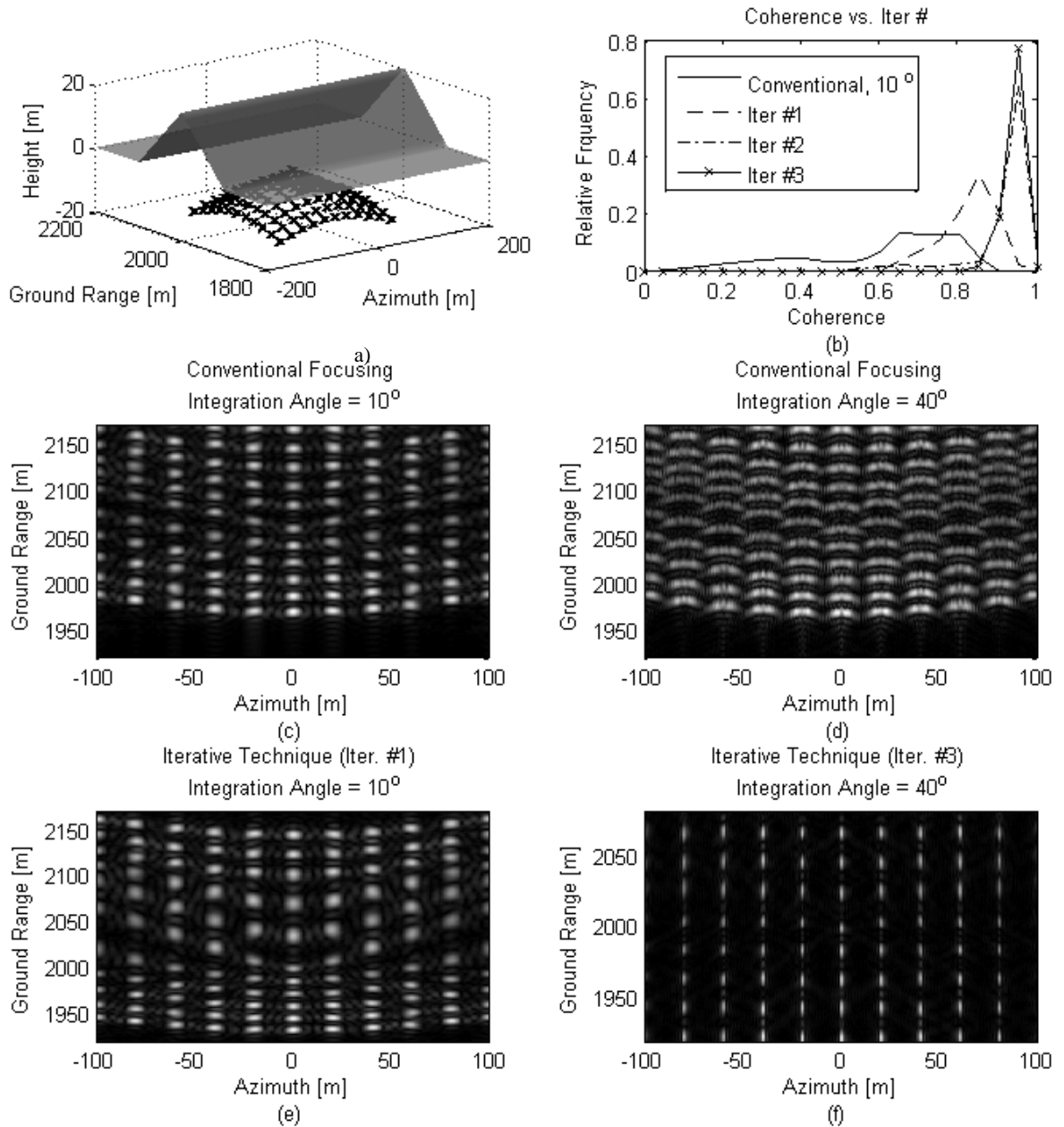


Figure 4.8: Results of applying the subsurface focusing algorithm: (a) scene consisting of a linear sand dune and a grid of point targets, (b) the improvement in coherence vs. different iterations, (c) normalized image from conventional focusing with 10° integration angle, (d) normalized image from conventional focusing with 40° integration angle, (e) first iteration of the subsurface focusing algorithm and (f) 3rd iteration with 40° integration angle.

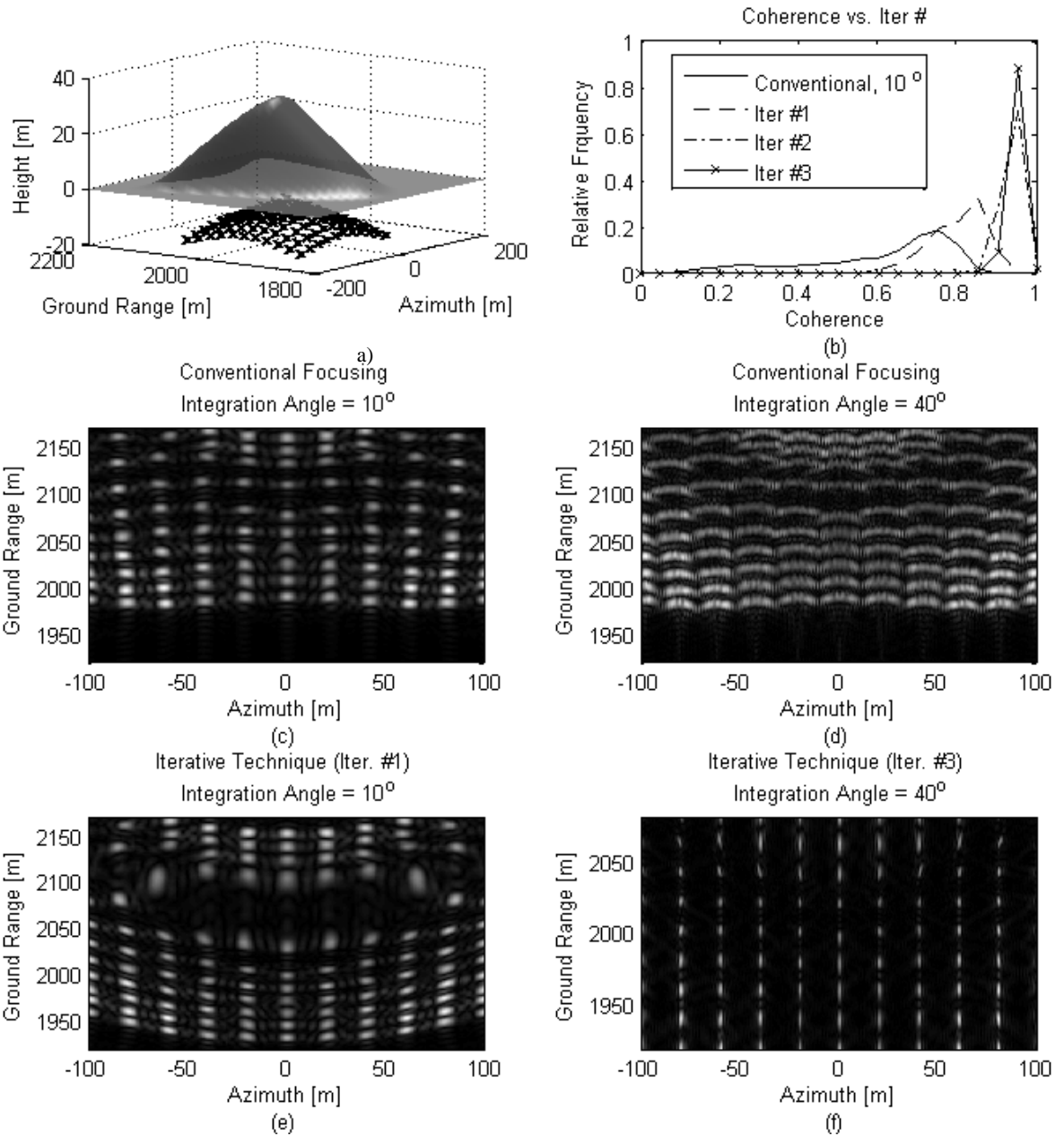
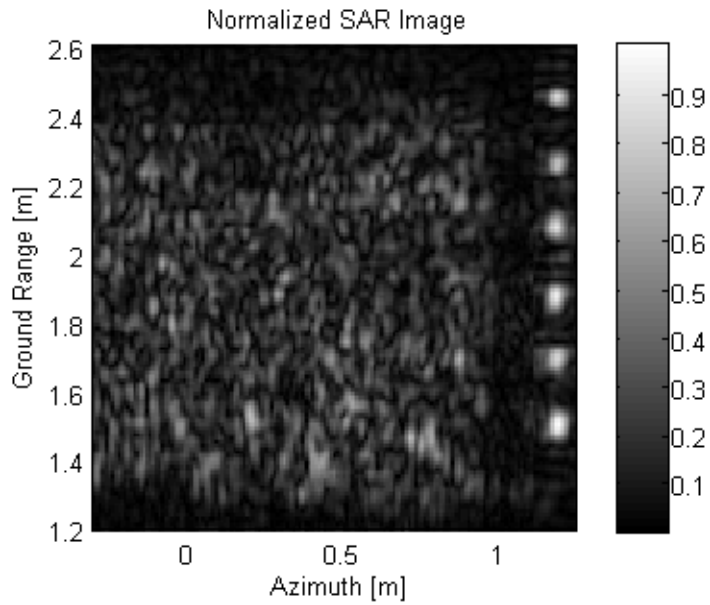


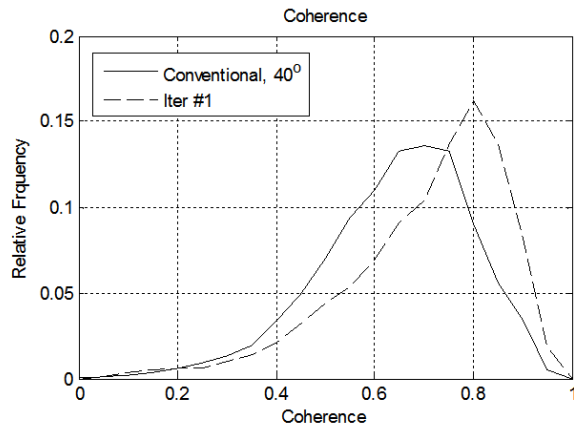
Figure 4.9: Results of applying the subsurface focusing algorithm: (a) scene consisting of a barchan sand dune and a grid of point targets, (b) the improvement in coherence vs. different iterations, (c) normalized image from conventional focusing with 10° integration angle, (d) normalized image from conventional focusing with 40° integration angle, (e) first iteration of the subsurface focusing algorithm and (f) 3rd iteration with 40° integration angle.

4.5 Scaled Model Measurement Results

To verify the performance of the proposed algorithm, we used a scaled model in the lab as described in Chapter 3. The resulting SAR image for one of the passes is shown in Figure 4.10 (a). The coherence results over the sand covered area using conventional focusing and using the proposed algorithm are shown in Figure 4.10 (b). The coherence was estimated using 4x4 resolution cells. The improvement in coherence is due to the correction for the geometric distortion and the improvement in the focusing which are not very severe in this scenario due to the flat surface and the relatively shallow sand layer. However, thicker sand layer or more complex top surface, the improvement in the coherence is expected to be even more pronounced.



(a)



(b)

Figure 4.10: (a) Conventionally focused SAR image of the scaled model and (b) comparison between the two coherence histograms obtained.

4.6 Conclusion

In this chapter, it was shown that the current conventional SAR focusing and InSAR coregistration techniques limit the resolution achievable by the subsurface mapping InSAR. To study these effects, we developed a 3D geometrical optics based

subsurface SAR simulator. Using the simulator, the two major types of artifacts are shown to be defocusing and geometric distortion. Defocusing severely limits the image resolution and geometric distortions limit its use in many applications. We then presented an iterative approach that combines the subsurface inversion algorithm and the 3D subsurface SAR simulator. The iterative approach is then applied to a simulated sample scene and was shown to remove all the geometric artifacts and to provide much higher resolution image. It was also experimentally verified using scaled model measurement. The main drawback of the proposed technique is the computational requirements of the subsurface SAR simulator and subsurface focusing. However, it can easily be parallelized to enhance the speed.

Chapter 5

Linearly Polarized Ultra-Wideband Antennas

The previous three chapters dealt with the propagation modeling and inversion parts of the subsurface topography estimation problem. The next three chapters deal with a very important system implementation problem which is the radar antennas for this system. The proposed subsurface topography estimation system requires an Ultra-Wideband (UWB) antenna to be mounted on the plane for the low frequency InSAR subsystem. The system also requires UWB antennas for the ground penetrating radars that are used to find the subsurface heights at the ground control points (GCPs). These antennas have to 1) operate at low frequencies (VHF) in order to penetrate through the sand layer, 2) operate over a very large relative bandwidth in order to provide good height resolution and 3) have compact size for mounting on the plane or on a vehicle. In this chapter, the design of a number of compact linearly polarized UWB antennas for these applications is presented. Incidentally, such antennas are also very useful in many other applications such as see through wall radars and communications applications. The antennas in the next chapters are scaled up in frequency so that they can be easily measured in laboratory environment. The chapter begins with the background information about UWB antennas and some of the standard designs then proceeds to the first set of the newly developed antennas.

5.1 Background

5.1.1 Definitions

There are two commonly used definitions for UWB Antennas (f_L is the minimum operating frequency of the antenna and f_H is the highest operating frequency) [43], [44]:

1. The Defense Advanced Research Projects Agency (DARPA) Definition:

$$\text{Fractional Bandwidth (FBW)} = 2 \frac{f_H - f_L}{f_H + f_L} > 0.25$$

2. The Federal Communications Commission (FCC) Definition:

$$\text{Fractional Bandwidth (FBW)} = 2 \frac{f_H - f_L}{f_H + f_L} > 0.2$$

Or

$$\text{Bandwidth (BW)} = f_H - f_L > 500 \text{ MHz}$$

In this thesis, most of the designed antennas have operating fractional bandwidths from 67% to more than 120% and bandwidths in excess of 1 GHz, and thus both definitions apply.

5.1.2 Design Issues

Unlike conventional narrowband antennas which operate over relatively narrow bandwidths with (mostly) one mode of operation and relatively constant radiation characteristics, UWB antennas operate over much wider bandwidths over which their radiation characteristics can change drastically. There are four major performance metrics for UWB antennas that are of interest for the applications considered in this thesis, namely: (1) overall efficiency, (2) radiation pattern, (3) time domain performance and (4) electrical size [45].

Overall efficiency is defined as the radiated power from the antenna divided by the incident power at its terminal. It is related to the antenna matching as well as the dielectric and metallic losses in the antenna. Some ultra-wideband antennas are miniaturized using lossy elements. However, this usually leads to degraded noise performance which limits their use in radars and high performance communication systems thus such antennas are not considered in this thesis.

The **radiation pattern** is very important in radar antenna designs. Radar antennas are designed such that they have low side lobes and large front-to-back ratios (ratio between the radiated power in the forward direction to that in the backward direction). This is because high side lobes cause the same target to be detected at different azimuth positions in a radar image which affect the quality of the image whereas low front-to-back ratio causes the operator and/or the mounting structure of the antenna to affect the generated image.

The **time domain performance** of the antenna is extremely important in radar and communication applications. This is because UWB radars and communication systems transmit and receive very narrow pulses in the time domain (and is thus very wide in the frequency domain). The antenna should not cause significant distortion to these pulses; otherwise the performance of the systems can degrade drastically. For example, if an antenna which has bad time domain performance is used in a radar system, a single target can appear as multiple targets at different ranges from the radar and mask weaker targets at other ranges. It can also cause significant bit errors in UWB communication systems.

The antenna electrical size is defined as the antenna physical size divided by the operating wavelength. For UWB antennas, due to the large bandwidth, the used wavelength is usually the wavelength at the minimum operating frequency or, equivalently, the maximum operating wavelength. The antenna size is required to be as small as possible for several reasons.

1. Many UWB radar systems such as GPRs and see-through wall radars operate at low frequencies in order to penetrate through moist soil and lossy walls. For these radars, antennas are the limitation on the overall system size. Thus, small antenna size is very important to reduce the overall system size and weight. This is also very important for plane mounted antennas for the InSAR system.
2. Some radars and communication systems use UWB arrays. From array theory, it can be shown that if the separation between the elements in an array is significantly larger than half the operating wavelength, grating lobes appear. Grating lobes are very large side lobes that can cause severe image artifacts in radars [45]. Grating lobes also greatly reduce the overall gain of the array which can cause significant noise issues in communication and radar systems. By reducing the antenna size, the spacing between the antenna elements can be maintained to be less than one half wavelengths over the operating bandwidth of the array.
3. Antenna size is also a limiting factor in many mobile communication systems. By reducing the antenna size, significantly smaller UWB mobile communication systems can be achieved.

5.1.3 Common Structures

Several UWB antennas were proposed in the literature such as UWB dipoles and monopoles [22], [46], Vivaldi antennas [47], dielectric rod antennas [48] and ridged horn antennas [49] as shown in Figure 5.1. UWB Monopoles, though they are compact in size, do not have a good front-to-back ratio. Log-Periodic antennas give severe signal distortion which complicates post processing [45]. Vivaldi and UWB dielectric rod antennas are of the traveling wave type and thus have to be few multiples of the operating wavelength to give sufficient gain and front-to-back ratio which makes them very large for low frequency operation. Ridged horns have very favorable radiation pattern and time domain characteristics but they are expensive to fabricate and still relatively bulky for operation at low frequencies.

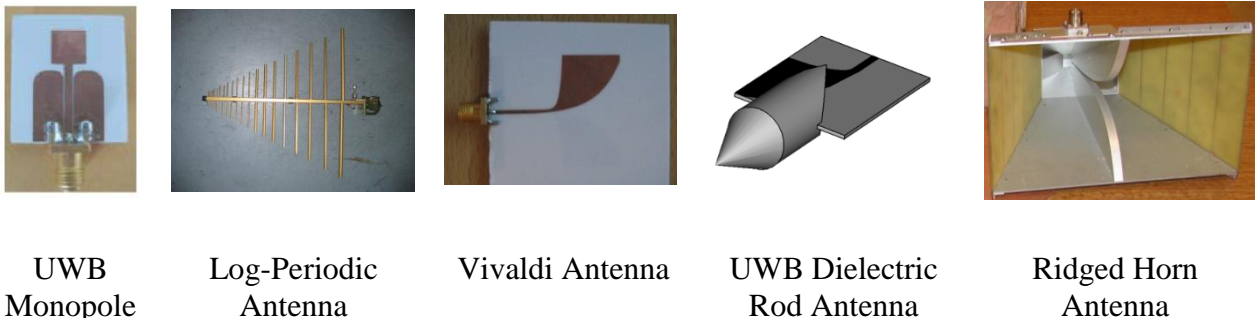


Figure 5.1: Some Conventional UWB Antennas

5.1.4 Omni-Directional Coupled Sectorial Loop Antenna (CSLA)

Due to the limitations of the previously discussed common structures, we considered a newly developed antenna at the university of Michigan; the Coupled Sectorial Loops Antenna (CSLA) [50]. Its structure is shown in Figure 5.2. It consists of two sectorial shaped loops (1 and 2) fed from the circle center using a coaxial cable. The

wideband nature of the CSLA is due to the strong frequency dependent magnetic coupling between the two loops which can be controlled by adjusting the angle α to obtain relatively constant input impedance with very small imaginary part. Since only a small portion of the field is in the substrate, the dependence of the antenna performance on the substrate material is small unless the substrate has a significantly high permittivity or large thickness (or equivalently large electrical thickness). However, a high permittivity substrate could have an impact on the input matching of the antenna and thus a thin low permittivity substrate is typically used.

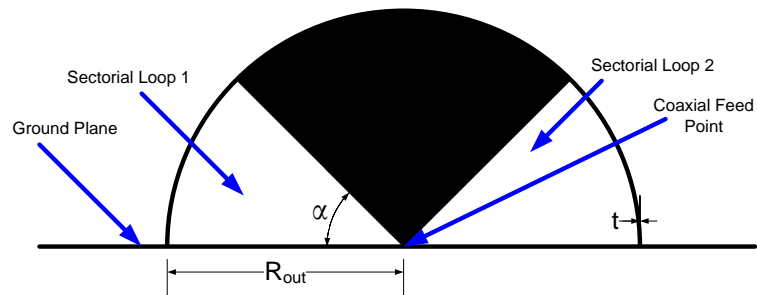


Figure 5.2: The CSLA Antenna Structure.

A sample CSLA antenna is designed and optimized using Ansoft HFSS. Then, the antenna is fabricated on a 30 mil Rogers 4003C substrate ($\epsilon_r = 3.38$) and measured. The dimensions of the fabricated antenna are $R = 150$ mm, $t = 1$ mm and $\alpha = 30^\circ$. The fabricated structure is shown in Figure 5.3 (a) and its measured and simulated VSWR are shown in Figure 5.3 (b). The measured and simulated results show very good agreement. It is observed that the antenna has a VSWR less than 2 over the frequency range 0.37 – 6 GHz (a 16:1 impedance bandwidth).

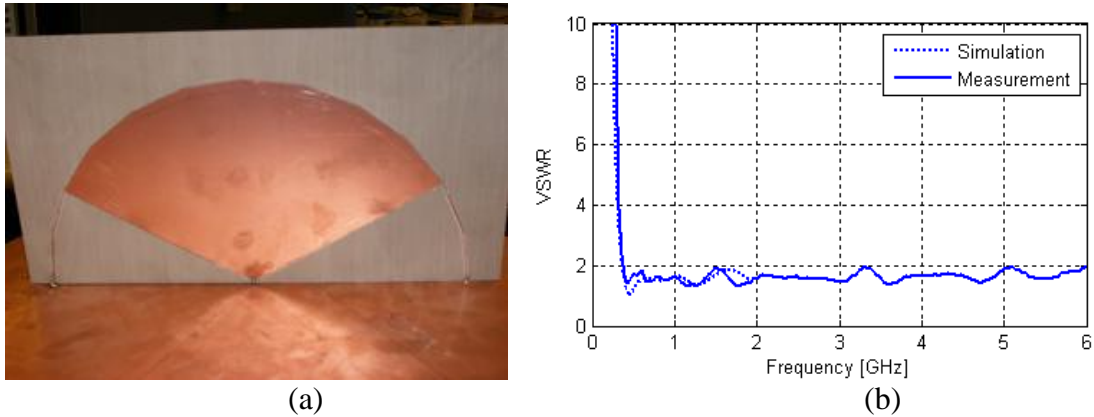


Figure 5.3: (a) the fabricated CSLA and (b) its simulated and measured VSWR.

The simulated radiation pattern at different frequencies is shown in Figure 5.4. The dominant polarization of the radiated field is vertical. From the radiation pattern plots, it can be seen that the CSLA has a very good cross polarization performance and a good omni-directional pattern over more than two octaves of bandwidth.

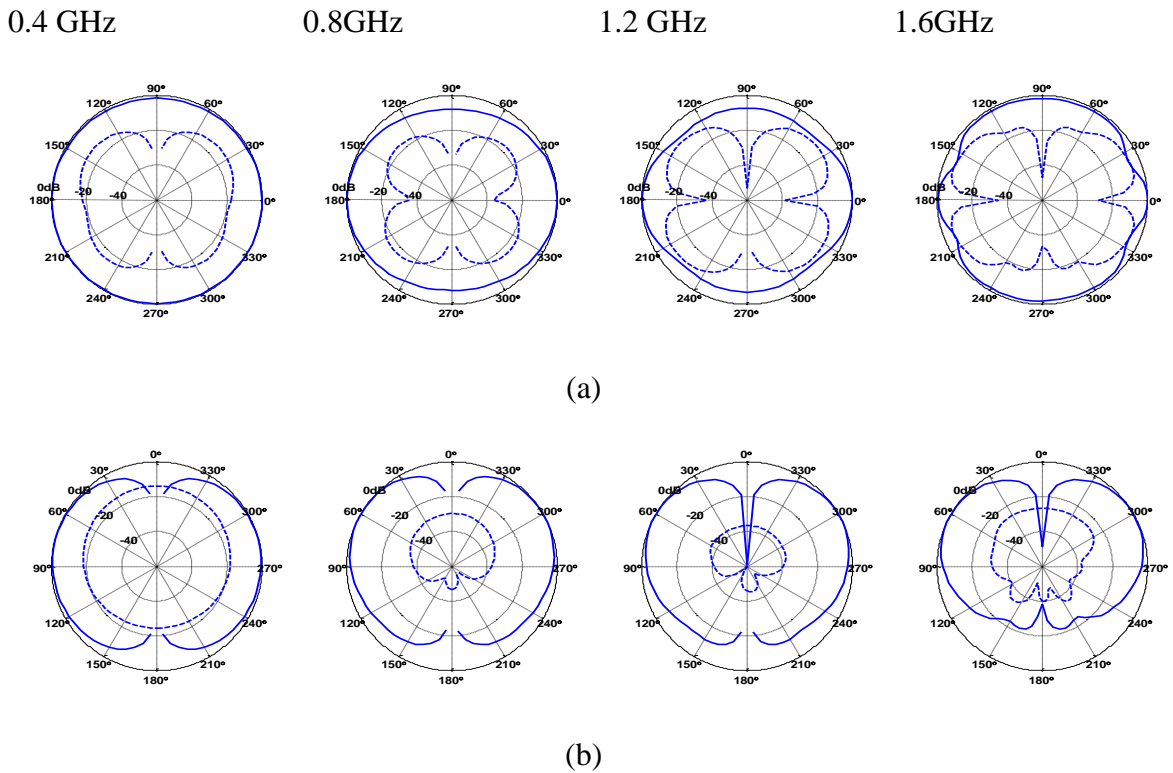


Figure 5.4: The normalized radiation pattern of the CSLA antenna in the (a) H-plane and (b) E-plane. (Solid line is the copolar component and the dashed line is the crosspolar component)

For some applications where planar structures are desired such as in small portable devices, the ground plane can be removed. A tapered microstrip line can be used to feed the antenna. This is because the antenna impedance in the monopole configuration (Figure 5.2) is 50 Ohms and thus for the dipole configuration it becomes 100 Ohms. The tapered microstrip line acts as an impedance transformer. The structure of this antenna is shown in Figure 5.5 (a). It employs the same UWB gap balun commonly used in UWB dipoles and monopoles. The loops are connected from the top layer to the bottom layer through vias as shown in the figure. Since the loops are no longer planar because of the vias, a slightly higher cross polar component is expected. This could be improved by using a thin substrate or using a coplanar waveguide or strip line feed instead of a Microstrip line. The simulated VSWR is shown in Figure 5.5 (b). The planar version has a good matching over almost the same band as the monopole version. This structure will be revisited in chapter 7 when considering the design of dual polarized antennas.

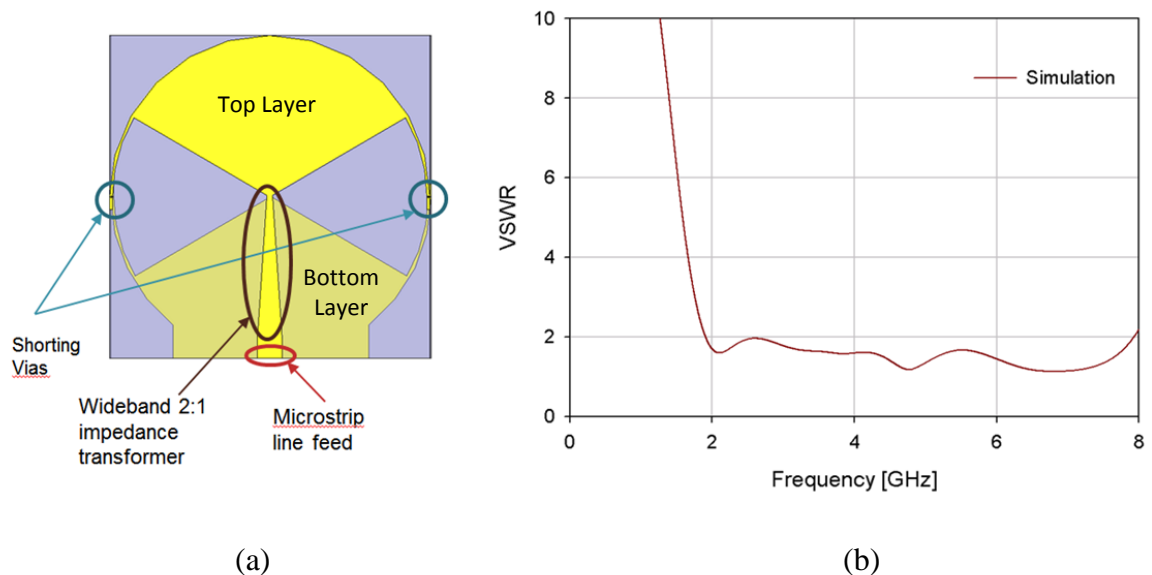


Figure 5.5: Fully planar CSLA: (a) Structure and (b) simulated VSWR.

5.2 Folded CSLA

The magnetic field distribution on the ground plane at the low frequency edge is shown in Figure 5.6 (a) and (b). Due to the circulating nature of the magnetic field, the antenna can be folded in order to further reduce its size as shown in Figure 5.7 (a). Folding the antenna allows for a much better space utilization and does not cause severe mismatch of the antenna even for small folding angles as shown in Figure 5.7 (b) because of the nature of the magnetic coupling between the two loops. However, it has an effect on the radiation pattern of the antenna causing it to be significantly more directional at higher frequencies. The H-plane (horizontal plane (XY)) radiation pattern of the CSLA is plotted at 4 frequencies 0.4, 0.8, 1.2 and 1.6 GHz for two folding angles; 45° and 135° as shown in Figure 5.8. From which it can be seen that over an octave of bandwidth, the radiation pattern remains omni-directional. However, at higher frequencies, the radiation patterns show an increase in the directivity especially for smaller folding angles.

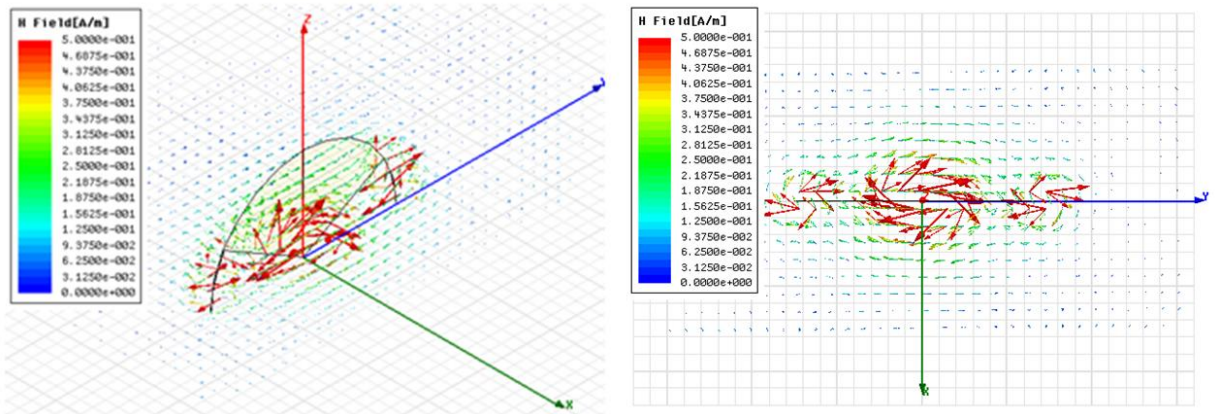


Figure 5.6: The magnetic field distribution of the CSLA on the ground plane at 0.5 GHz (a) isometric view and (b) top view.

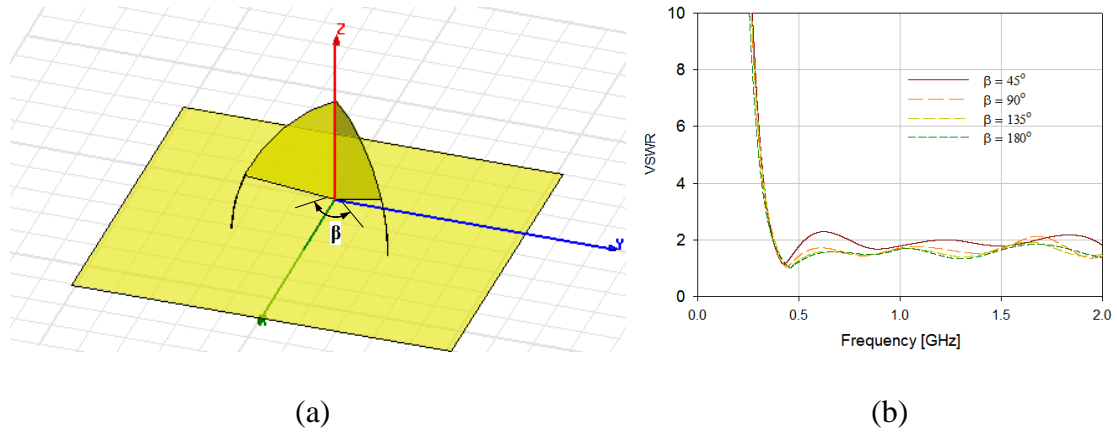


Figure 5.7: The structure of the folded CSLA and its simulated VSWR for different folding angles, β .

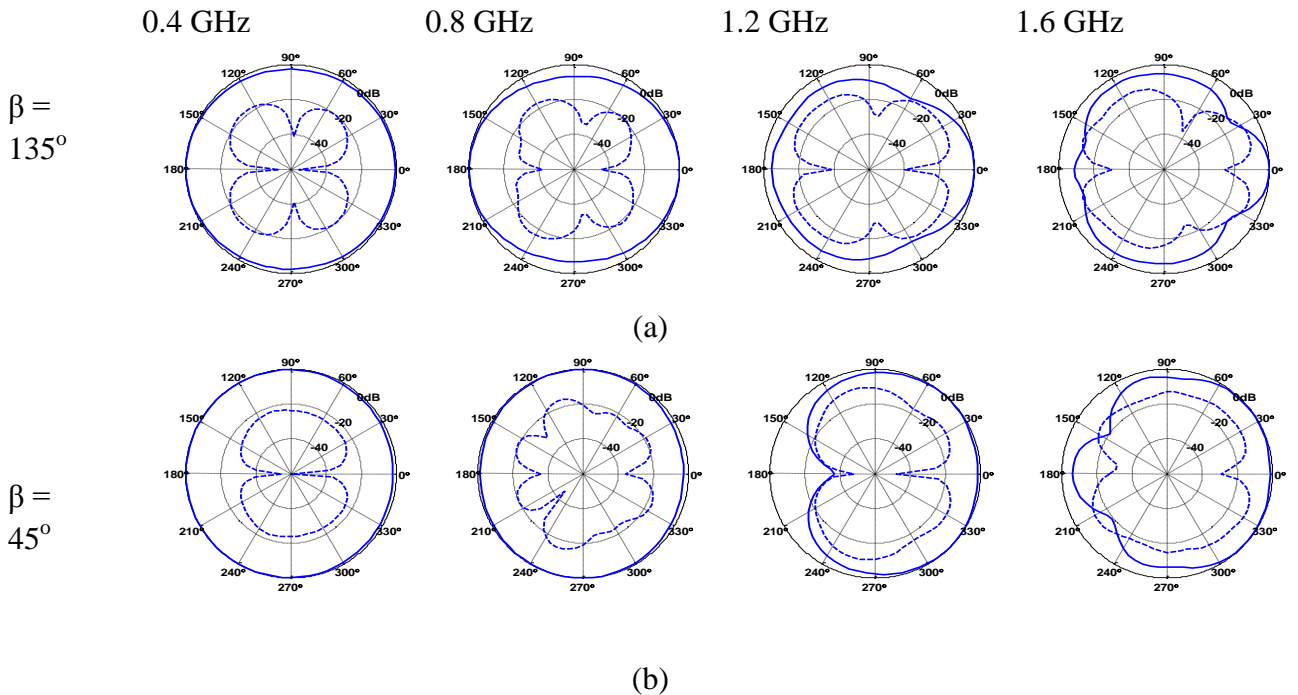


Figure 5.8: The normalized H-plane radiation pattern of the Folded CSLA antenna for a folding angle of (a) 135° and (b) 45° . (Solid line is the copolar component and the dashed line is the crosspolar component)

The antenna was fabricated by milling the two sectorial loops on Rogers' 4003C substrate. A copper sheet was soldered to the two parts to ensure electrical connection between the two metallic parts. The loops are then soldered to the coaxial connector at

the feeding end and to the ground at the other edge. A folded CSLA with a folding angle of 120° was fabricated and measured. The 120° was chosen because it is the maximum angle at which the VSWR remain below 2. The fabricated structure is shown in Figure 5.9 (a) and its measured and simulated VSWR are shown in Figure 5.9 (b).

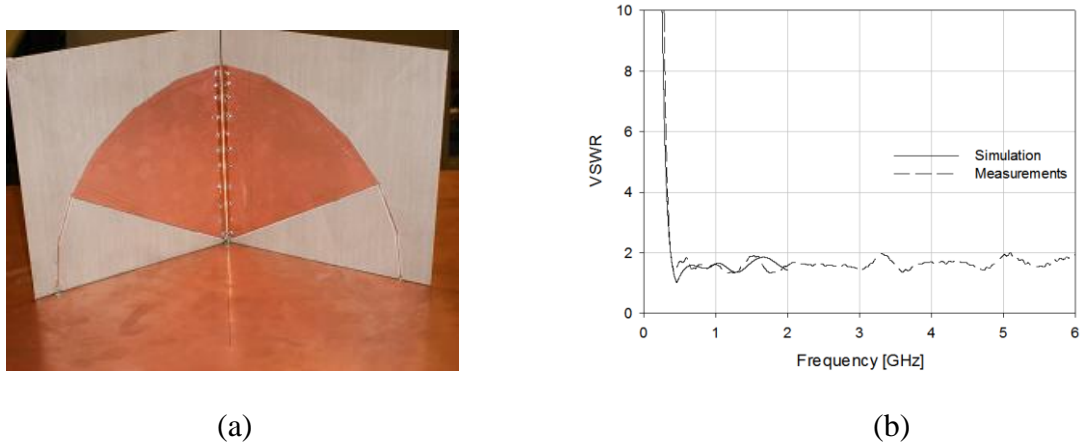


Figure 5.9: (a) The Folded CSLA antenna and (b) its simulation and measurement results.

The above structure is easily fabricated at low frequencies due to its relatively large physical size. However, for high frequency applications fully planar structures are preferred. For such applications, a relatively thick substrate can be used and the two sectorial loops can be fabricated on both sides and connected together using vias. An example is shown in Figure 5.10 (a) where the antenna was fabricated on a 125mil low permittivity substrate (Neltec NY9208 with $\epsilon_r = 2$). The simulation results are shown in Figure 5.10 (b) where we can see that the ultra-wideband performance is maintained with very good matching.

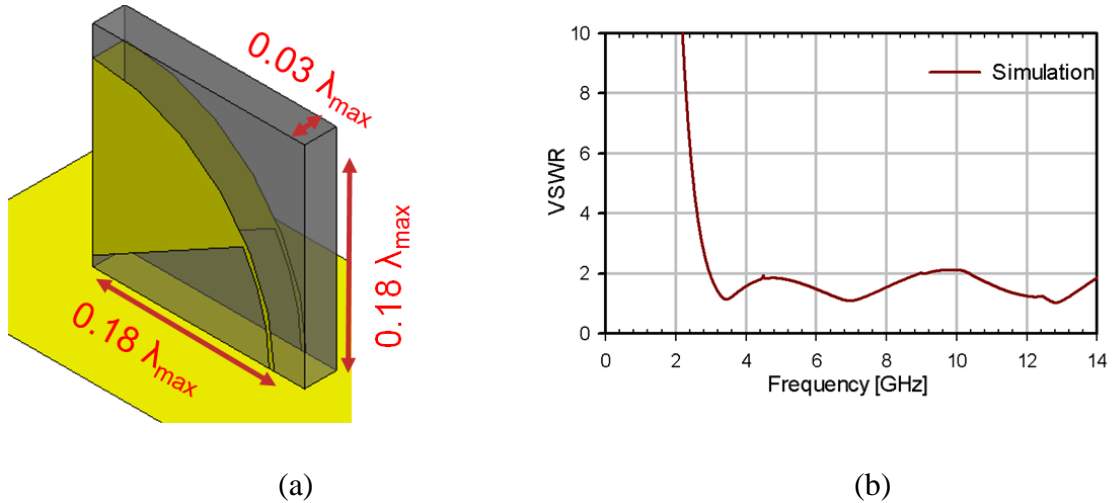


Figure 5.10: A fully planar folded CSLA (a) the structure and (b) the simulation results.

The increased directivity of the CSLA at high frequencies when it is folded, suggests that it can be used as a directional antenna if it is placed in front of a metallic reflector. However, because of the low front to back ratio even at higher frequencies, the direct and the reflected components of the waves will be comparable even at high frequencies. This leads to constructive interference at certain frequencies and destructive interference at other frequencies which can cause significant pulse dispersion. Thus, an additional modification is needed to be done on the folded CSLA is needed to favor the radiation in the forward direction and improve the front to back ratio before it can be used in conjunction with a reflector.

5.2.1 *Folded CSLA with Vivaldi Antenna*

One way of improving the front-to-back ratio at high frequencies of the folded CSLA is to combine it with a directional UWB antenna. A good candidate is the Vivaldi antenna [47], since it is a directional antenna, has a very wideband, its slotline feed is compatible with the grounded coaxial cable feed of the folded CSLA and it has the same

vertical polarization as the CSLA. Vivaldi antennas can have several taper shapes, such as exponential, elliptical or even circular. Exponential and elliptical tapers are usually preferred in most designs since they allow the antenna to be well matched to its feeding slot line. However, this is the case for a Vivaldi that is fed alone. When it is fed in parallel with a CSLA, we found that circular taper gives better overall radiation pattern performance and good matching performance since the taper shape affects the magnetic coupling between the loops of the CSLA and thus the input matching of the antenna. Based on that, a 120° folded CSLA combined with a Vivaldi with circular shaped inner and outer tapers was designed as shown in Figure 5.11 (a). The outer circular taper of the Vivaldi was found to improve the radiation pattern stability with frequency while not significantly affecting the matching. The combined structure has an improved matching compared to the folded CSLA at the low frequencies and its peak directivity is higher by about 3dB as shown in Figure 5.11 (b) and (c). The fabricated structure together with its measured and simulated VSWR are shown in Figure 5.12 (a) and (b) respectively.

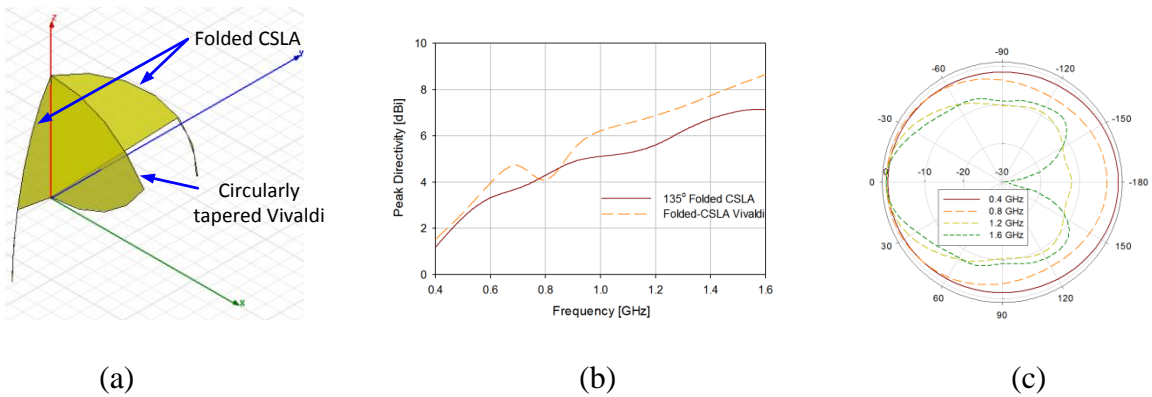
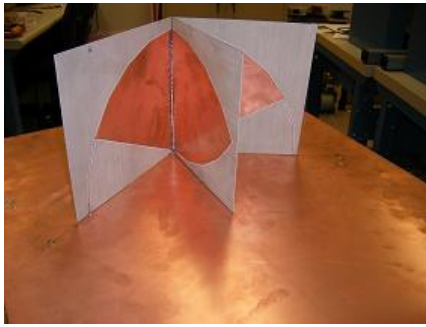
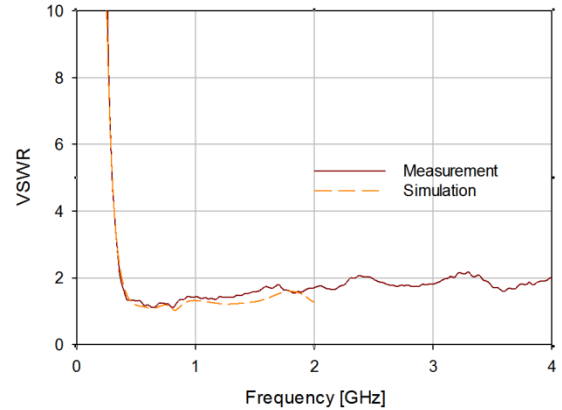


Figure 5.11: (a) The combined Folded CSLA and the Vivaldi Antenna, (b) comparison between the simulated directivity of the two antennas and (c) the H-plane radiation pattern of the combined antenna at different frequencies.



(a)



(b)

Figure 5.12: (a) The structure of the Vivaldi-CSLA antenna and (b) its simulated and measured VSWR.

From the simulated radiation patterns of the antenna shown in Figure 5.11 (d), it can be seen that the antenna has a more directive radiation at higher frequencies as compared to the folded CSLA. It also has a better front to back ratio, which means that a metallic reflector can now be used without causing severe variations in the gain at higher frequencies. Having a good gain at low frequencies is very important in many UWB radar applications; especially for through-wall imaging applications where most of the signal penetration occurs at the low frequency portion. The low directivity is a physical limit because of the small electrical dimensions of the CSLA. The reflector design for UWB operation is discussed briefly in the next section.

5.2.2 Reflector Design for UWB Operation

The use of flat or shaped reflectors for increasing the directivity of antennas is a very mature topic and several types of reflectors were presented in the literature such as the corner, parabolic and paraboloidal reflectors. Typically, reflectors are placed relatively far from the antenna in order not to severely affect its input impedance. For UWB radar applications, placing the reflector too far from the antenna can cause severe

pulse dispersion because the transmitted pulse will be composed of two components, the direct component from the antenna and the reflected component from the reflector. Also, this can cause significant variations of the radiation pattern as a function of frequency, since at some frequencies the two components will add up (constructive interference) leading to high gain along this direction, whereas at other frequencies they may cancel (destructive interference) leading to a null along the same direction. On the other hand, placing the reflector very near to the antenna can effectively short circuit the antenna and cause very inefficient radiation and severe input mismatch.

To obtain qualitative results about the radiation pattern performance of an antenna near a reflector, the structure shown in Figure 5.13 (a) is considered. It consists of a short dipole antenna backed with a flat metallic ground plane at a distance d . Using the image theory and the array factor of two elements that are 180° out of phase, the H-plane radiation pattern of the structure can be easily computed for different reflector spacing and the results are plotted in Figure 5.13 (b). From the figure, it can be seen that the resulting radiation pattern is acceptable up to a reflector spacing of about 0.3 wavelengths after which the main lobe starts to split and a null is formed in the boresight. Thus, for UWB operation, the reflector spacing can be up to 0.3λ at the maximum operating frequency while maintaining acceptable radiation pattern performance. For directional antennas, especially those whose directivity increases with frequency and have good front to back ratio such as the Vivaldi-CSLA, larger distances can be used which even helps increasing the gain at the low frequency end of the band while not affecting much the high frequency portion. Also, larger distances can significantly help in the input matching

at lower frequencies. The placement of a reflector in the back of the Vivaldi-CSLA is presented in the next section.

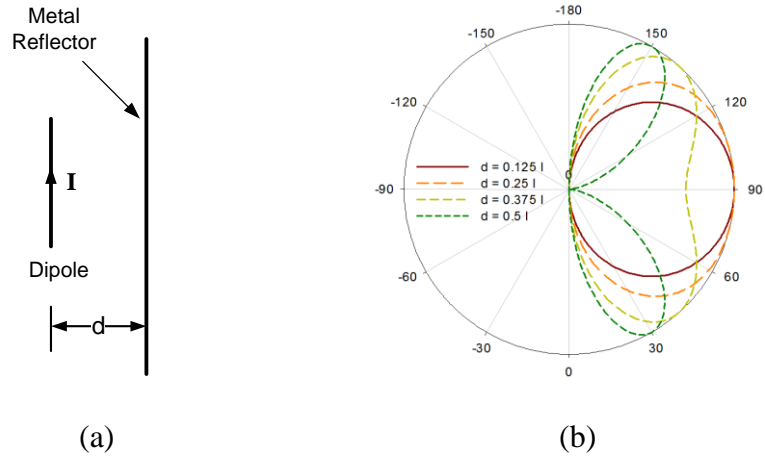


Figure 5.13: (a) A dipole parallel to a flat ground plane and (b) the resulting H-plane radiation pattern for different reflector spacings.

5.2.3 Vivaldi-CSLA Antenna with Reflector

5.2.3.1 Flat Reflector

Based on the analysis presented in the previous section, we investigated the placement of a reflector near the backside of the Vivaldi-CSLA as shown in Figure 5.14 (a). This is expected to significantly improve the directivity at low frequencies without adversely affecting the radiation pattern at higher frequencies since the antenna already has good directivity at high frequencies. It is also expected to further improve the front to back ratio over most of the band. However, placing a reflector very near to the coupled loops would severely impact the magnetic coupling between them and affect the low frequency end of operation. The simulation results of the peak directivity and the input VSWR are shown in Figure 5.14 (c) and (d) respectively. These figures show that the minimum operating frequency is strongly dependent on the placement of the reflector.

However, placing the reflector far from the antenna, impacts the directivity at higher frequencies.

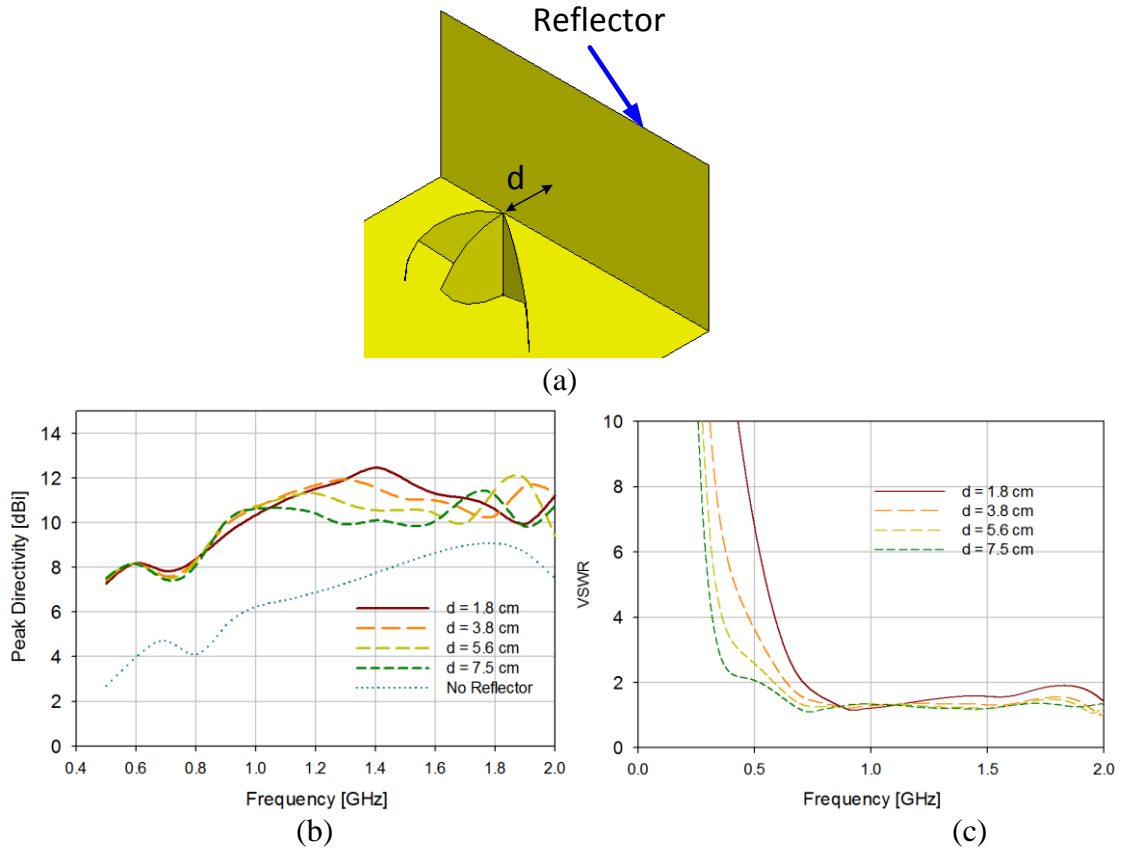


Figure 5.14: (a) The Vivaldi-CSLA placed in front of a flat reflector and the simulated (b) peak directivity of the Vivaldi-CSLA with a planar reflector and (c) the VSWR for different reflector spacing, d .

5.2.3.2 Corner Reflector

5.2.3.2.1 Structure

As seen from the directivity vs. frequency plots, placing a flat back reflector, significantly improves the low frequency directivity as expected (the directivity increased by about 4dB compared to the no-reflector case). However, it caused the radiation pattern and the directivity to have undesired fast variations at high frequencies. Thus, in order to further improve the antenna performance, a corner reflector is used instead of a simple

flat reflector. The final structure and its dimensions are shown in Figure 5.15 (a) – (c). The antenna dimensions are: $R_{out} = 150$ mm, $R_{in} = 149$ mm, $d = 80$ mm, $\alpha = 30^\circ$ and $\beta = 120^\circ$, unless otherwise stated. These dimensions are selected so that the antenna operates over the frequency band 0.5 – 2 GHz.

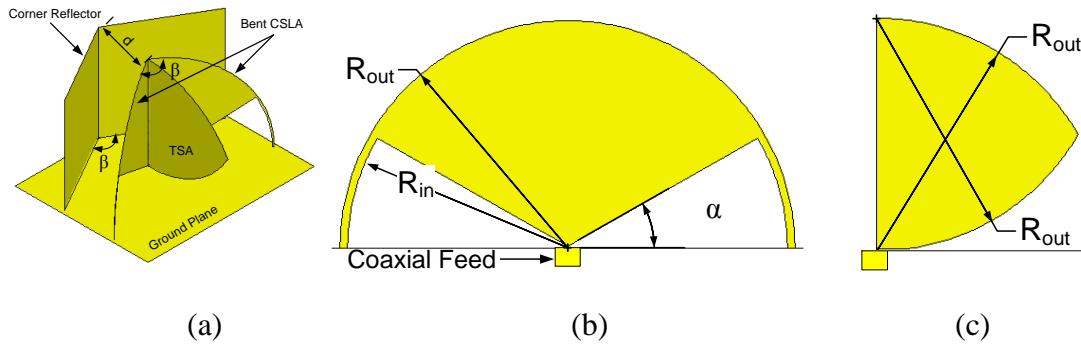


Figure 5.15: (a) The Vivaldi-CSLA with the corner reflector, (b) the dimensions of the CSLA part and (c) the dimensions of the Vivaldi part.

5.2.3.2.2 Parametric Study

The two most influential dimensions of the proposed antenna based on the previous discussions are the bending angle, β and the distance to the corner reflector, d . The bending (wedge) angle β was selected to be the same for the CSLA and the corner reflector as this was found to give optimum matching performance in a given size. Increasing the value of β improves the input impedance match as shown in Figure 5.16 (a). However, large values of β cause significant reduction in the gain at high frequencies as shown in Figure 5.16 (b) as well as undesired variations in the E-plane radiation peak direction. The optimum value of β is found to be 120° which gives good impedance matching, good gain over a wideband and smallest variations in the radiation peak direction.

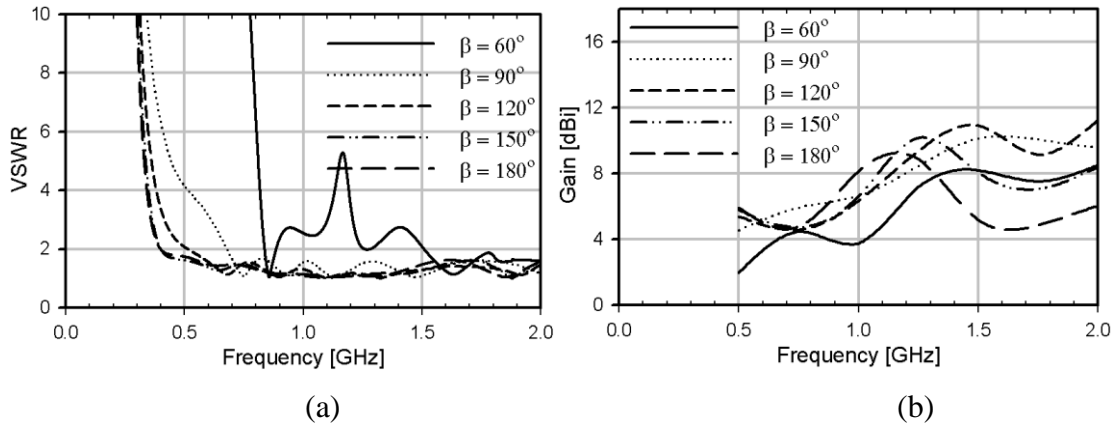


Figure 5.16: Simulated (a) VSWR and (b) antenna gain for different values of β .

The second parameter is the distance between the antenna and the corner reflector (d). As discussed in the previous section, the distance should be less than quarter a wavelength at the highest operating frequency. This corresponds to 3.75cm for an antenna operating over the band 0.5 - 2GHz. However, due to the fact that the antenna gain increases with frequency as previously discussed, d can be made significantly larger without affecting the high frequency gain performance. As shown in Figure 5.17 (a), increasing the distance between the antenna and the ground plane improves the matching as expected. However, Figure 5.17 (b) shows that larger values of d cause reduction of the gain at higher frequencies and undesirable variations in the radiation peak direction. The value of d was chosen to be 80mm to obtain good matching and maximizing the gain.

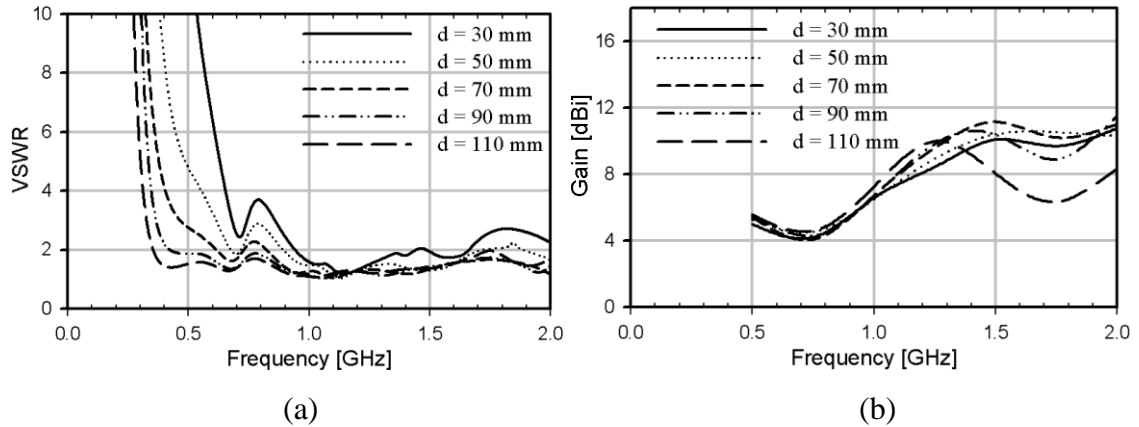


Figure 5.17: Simulated (a) VSWR and (b) gain for different values of d .

5.2.3.2.3 Measurement Results

The antenna was fabricated on a 60mil Rogers RO4003C substrate with a dielectric constant of 3.4. The measurement and simulation results of the input VSWR and the gain are shown in Figure 5.18 together with a photo of the fabricated antenna. The measured VSWR is better than 2 over the band 0.5 – 6 GHz (170% relative bandwidth). The measured gain is better than 5 dBi over the frequency band 0.5-2.25 GHz. And both the measured VSWR and gain show good agreement with the simulation results.

The measured H-plane and E-plane radiation patterns of the antenna are shown in Figure 5.19. The H-plane is defined to be in the direction of the radiation maximum at an angle 35° above the ground plane. From the measurement results it can be seen that the direction of the radiation peak is almost constant with frequency. This greatly simplifies the post processing required in radar applications. Also, the back radiation is minimized over most of the frequency band which helps in reducing the clutter.

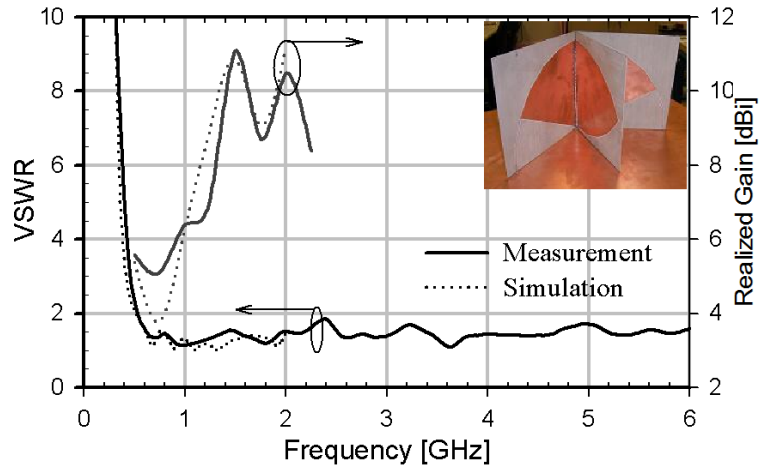


Figure 5.18: Measured and simulated input VSWR and gain of the directive CSLA.

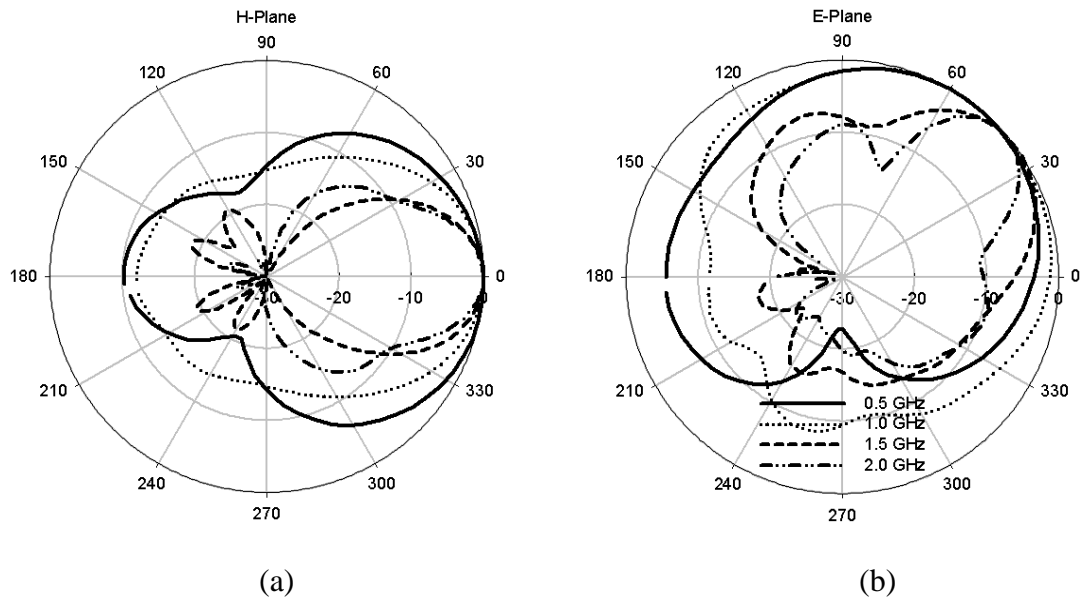


Figure 5.19. Measured radiation pattern over the operating frequency band: (a) H-plane and (b) E-plane.

Another important performance aspect of UWB antennas is their time domain radiation characteristics. To measure the antenna impulse response, a low dispersion omni-directional reference antenna was placed at the boresight of the directive CSLA. S_{21} was then measured using HP8720 network analyzer. The time domain response was then obtained through inverse Fourier transform after applying a Gaussian window to suppress the artificial time domain side lobes. The result is shown in Figure 5.20 where we can see

that there is slight pulse widening due to the time delay between the direct ray and reflected ray from the corner reflector. This corresponds to small loss in the range resolution for radar application. However the time domain side lobe levels are below 20dB and there is no apparent ringing in the time domain response. The measurements were not performed in the anechoic chamber and thus some multiple reflections due to nearby objects appear in the time domain as shown in the figure. The multiple reflection effects are reduced when using the directive CSLA compared to the reference antenna due to the more directive radiation pattern of the directive CSLA.

A size comparison between the proposed antenna and a standard ridged horn is shown in Figure 5.21. The proposed antenna size is almost one-eighth the size of the ridged horn while having comparable gain. The proposed antenna is also easily fabricated using PCB technology and does not require expensive high tolerance CNC machining and assembly that are required for the fabrication of ridged horn antennas. However, its operating bandwidth is only 4.5:1 compared to 18:1 of the ridged horn. But, for most radar applications, 4:1 bandwidth provides sufficient resolution with reasonable system and postprocessing complexity.

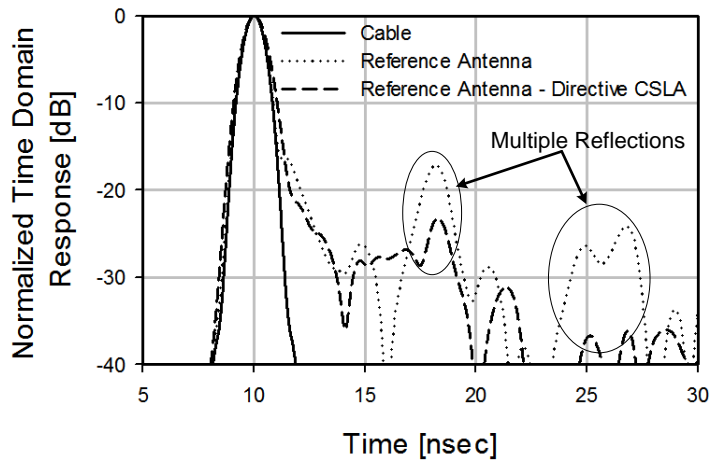


Figure 5.20: Time Domain Response.

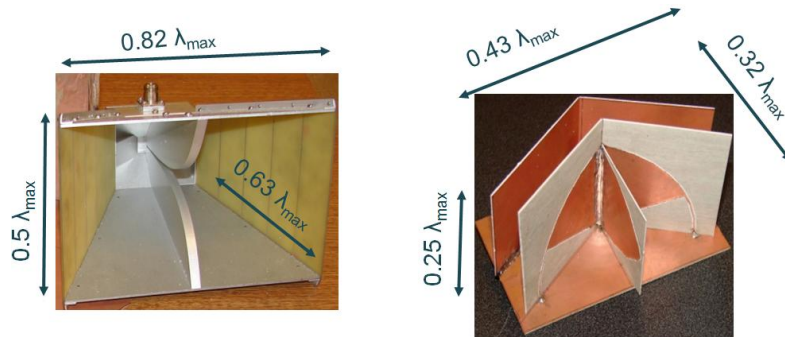


Figure 5.21: Comparison between the dimensions of a standard ridged horn and the dimensions of the proposed antenna. λ_{\max} is the wavelength at the minimum operating frequency.

5.3 Rectangular Waveguide UWB Antennas

5.3.1 Introduction

The CSLA based antennas that were presented in the previous section are useful in applications where the antenna is mounted on a ground plane (e.g. a vehicle or building). For other applications (e.g. in see through wall applications or airplane antennas), it is desired to have an antenna that does not require the presence of a ground plane. To address this problem, we developed a new compact lightweight UWB antenna

based on rectangular waveguides. The new antenna has comparable gain to ridged horns but is almost 1/8th of the size.

5.3.2 Antenna Structure and Operation

The proposed antenna is based on open ended rectangular waveguide antennas (OERWGA) [45]. OERWGA provide good radiation characteristics when TE_{10} mode is excited. Furthermore, because they have approximately the same effective aperture independent on the operating frequency (as long as only TE_{10} mode is excited) their gain increases with frequency which helps compensate for the higher free space propagation loss at higher frequencies in radar applications. Also, their beamwidth decreases at higher frequencies and this can be used to suppress their grating lobes when they are used in a UWB array or SAR.

However, conventional OERWGA are typically made long to ensure that the phase of the aperture electric field is approximately constant (the waveguide length is needed to suppress higher order modes) [51]. This puts a limit on the upper frequency which has to be chosen such that higher order modes are not excited since they severely affect the radiation pattern performance. Furthermore, typical OERWGA also have limited bandwidths due to the resonant feeds that are typically used. To overcome these limitations, we developed a new bowtie feed structure that can excite a TE_{10} -like aperture field for much shorter waveguide sections. It is a dipole structure, which helps further reduce the phase variation across the aperture compared to conventional monopole type feeds. It is also very wideband giving good impedance matching over about 1:4.5 bandwidth.

The proposed rectangular waveguide antenna (RWGA) is shown in Figure 5.22 (a) and (b). Its waveguide section length is only $0.18 \lambda_m$ and as will be shown later provides very good radiation pattern characteristics. The antenna dimensions are as follows: $W_{wg} = 15\text{cm}$, $W_1 = 9\text{cm}$, $W_s = 10.8\text{cm}$, $h_{wg} = 7.5\text{cm}$, $h_1 = 7.2\text{cm}$, $h_2 = 6.5\text{cm}$, $h_3 = 5\text{cm}$, $l_{wg} = 5\text{cm}$ and $l_{feed} = 2.5\text{cm}$.

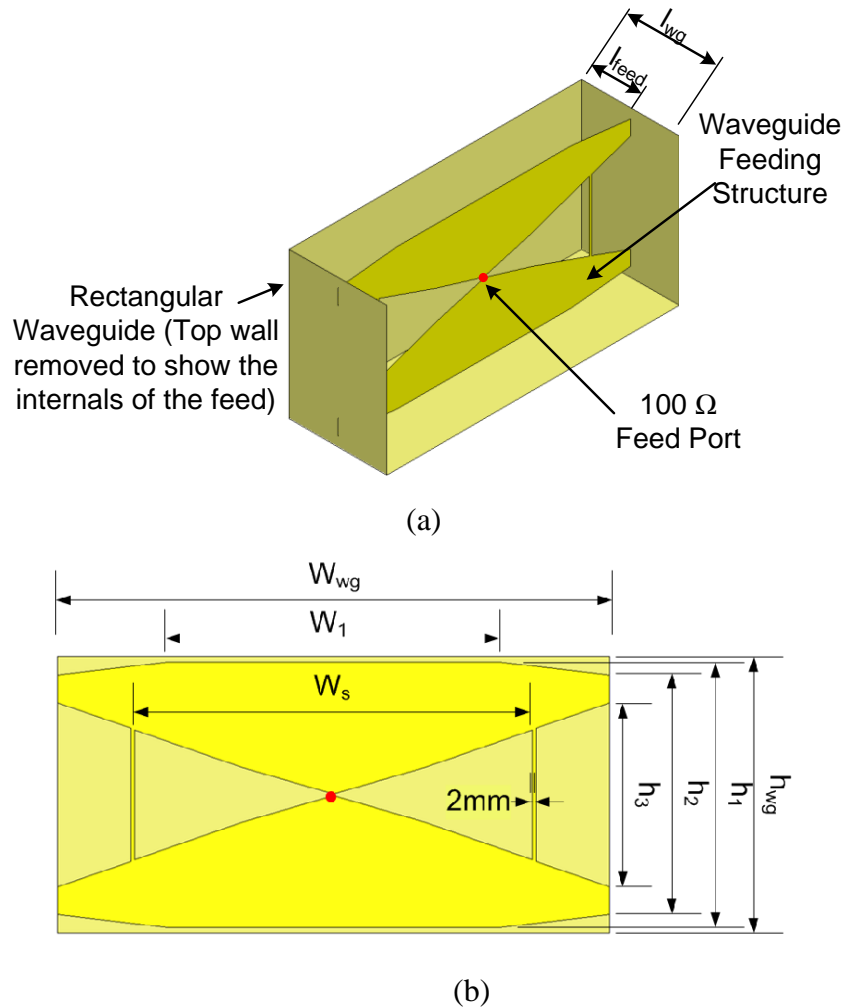


Figure 5.22: The proposed structure (a) isometric view and (b) front view.

To show the advantage of the proposed feed compared to the standard monopole feed, the field distribution at the waveguide aperture of the proposed feed and a probe fed waveguide section of the same length in Figure 5.23 (a) and (b) respectively. As Figure

5.23 (a) shows, the proposed feed generates a field distribution very similar to that of the TE_{10} excited aperture. On the other hand, as expected, the probe feed cannot establish the desired aperture field distribution for such a very short waveguide section as shown in Figure 5.23 (b). The resulting aperture field is considerably different than TE_{10} which results in lower aperture efficiency (approximately 20% lower than the proposed feed). Furthermore, due to the non-uniform and frequency dependent phase distribution at the aperture, the resulting radiation pattern is squinted and its direction of maximum radiation changes with frequency. This can affect the performance of radar systems and further complicates the post processing required to obtain high quality images.

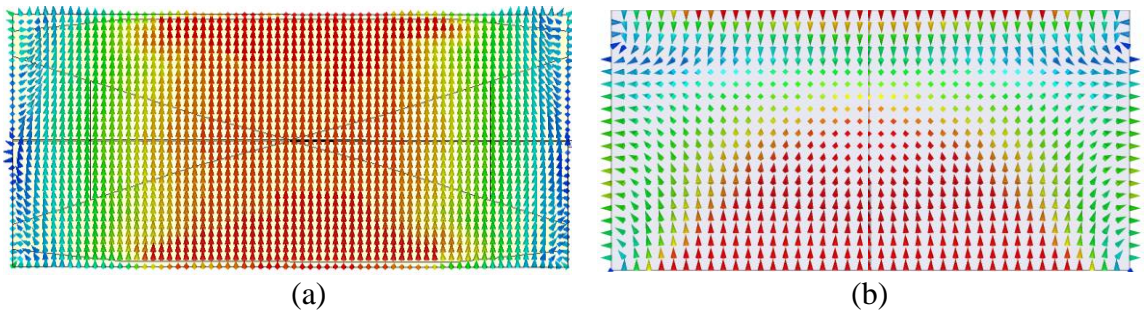


Figure 5.23: Field distribution at the waveguide aperture at 2.4 GHz using (a) the proposed feed and (b) probe feed (red: highest intensity, blue: zero intensity).

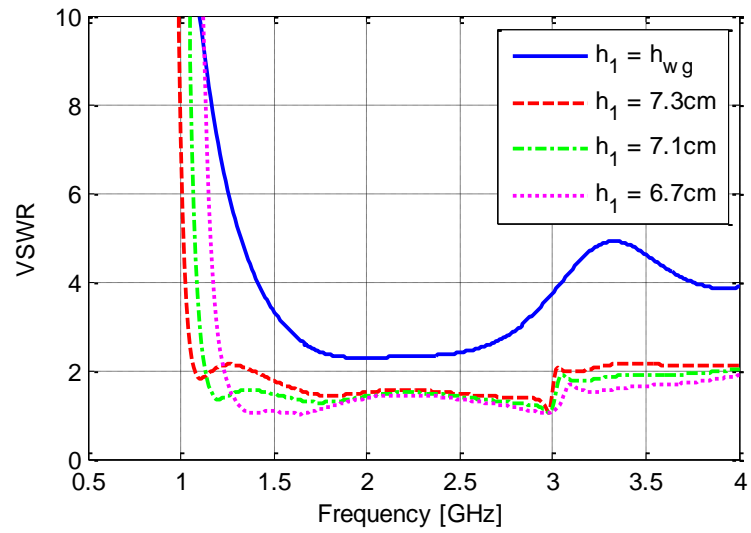
5.3.3 Design Process

The critical steps that lead to the optimized structure shown in Figure 5.22 are as follows: We started from a bowtie dipole as it provides wide impedance bandwidth compared to the conventional monopole/probe feeds. Also, a dipole is used instead of a monopole to avoid the squinted radiation patterns associated with monopoles. We then noticed that the bowtie provides optimum matching when its top and bottom corners are connected to the sidewalls of the waveguide while its wings are separated from the top and bottom walls of the waveguide. This top/bottom slots are required so that standing wave currents can be established on the bowtie wings. However, a drawback of these

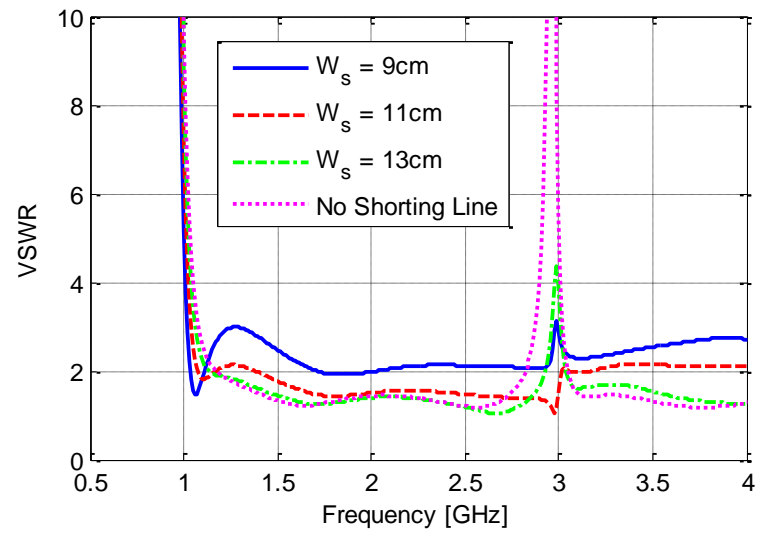
slots is that they create an unwanted resonance in the middle of the operating band. This resonance is related to the third resonance of these slots and it was suppressed using the shorting lines between the wings as shown in Figure 5.22 (b) thus reaching the final structure.

Two of the important tuning parameters of the antenna will be discussed. The first is h_1 which controls the capacitive coupling between the bowtie and the waveguide through the top/bottom slot widths. As shown in the simulation results in Figure 5.24 (a), reducing h_1 (increasing the slot width) helps in improving the matching but it also increases the minimum operating frequency which increases the antenna size for a given frequency band of operation and limits the resulting bandwidth. For optimum matching at smallest antenna size, h_1 was set to 7.2cm.

On the other hand, the top/bottom slots, even though they greatly help the matching, they also create a resonance in the band near their odd resonance at around 2.95 GHz as shown in Figure 5.25. To remove this resonance, we added a shorting line between the two wings as shown in Figure 5.22. By adjusting the separation W_s , we can adjust the two resonances to cancel each other as shown in Figure 5.24 (b).



(a)



(b)

Figure 5.24: Simulation results for (a) the effect of the top slot width h_1 and (b) the effect of the shorting line position on the antenna matching.

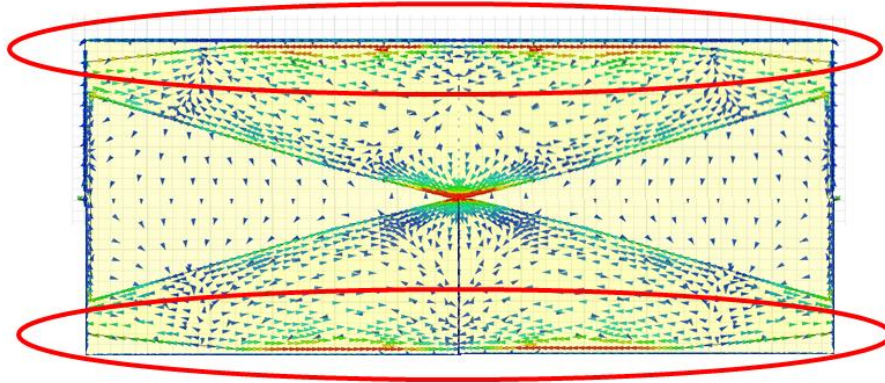


Figure 5.25: Current Distribution on the feeding structure at 2.95 GHz.

5.3.4 Feed design

The proposed rectangular waveguide exciter is a dipole-like structure which has the advantage of symmetric radiation pattern over the whole band but it requires a 100Ω balanced feed. In some systems, where push-pull type power amplifiers are used, the output of the amplifier is already balanced and can thus be connected directly to the antenna which eliminates the need for the output balun. However, in most situations the antennas are fed using coaxial cables and are typically required to have unbalanced 50Ω coaxial feed. This can be implemented using a 180° coupler and splitting the antenna in half at its electrical symmetry plane. However, this increases the cost, size and weight of the antenna. Also, low loss UWB 180° couplers are not available for all frequency bands. Thus, we designed an integrated planar 180° balun as shown in Figure 5.26, where the unbalanced 50Ω feeding microstrip line and its ground are gradually tapered to 100Ω balanced parallel strips line. This is very similar to the antipodal Vivaldi antennas feeding balun. Because this feed is very close to the antenna structure, we had an in-band resonance due to the coupling between the antenna and the feed line. However, by adjusting the feed distance d_{feed} , we could shift this resonance lower in frequency and out

of band. The loss of this feed was measured using a back-to-back junction and was found to be less than 0.5dB over 1-5GHz. The microstrip line is linearly tapered from $W_{ms_{start}}$ to $W_{ms_{end}}$. The ground was exponentially tapered from $W_{g_{start}}$ to $W_{ms_{end}}$ according to the equation:

$$W_g = A_1 e^{-r l} + A_2 \quad (5.1)$$

Where:

$$A_1 = \frac{e^{r l_{feed}} (-W_{ms_{end}} + W_{g_{start}})}{e^{r l_{feed}} - 1}, \quad (5.2)$$

$$A_2 = W_{ms_{end}} + \frac{W_{ms_{end}} - W_{g_{start}}}{e^{r l_{feed}} - 1},$$

and l is the distance from the coaxial feed position (varies from 0 to l_{feed}). The balun dimensions are given in Table 5.1.

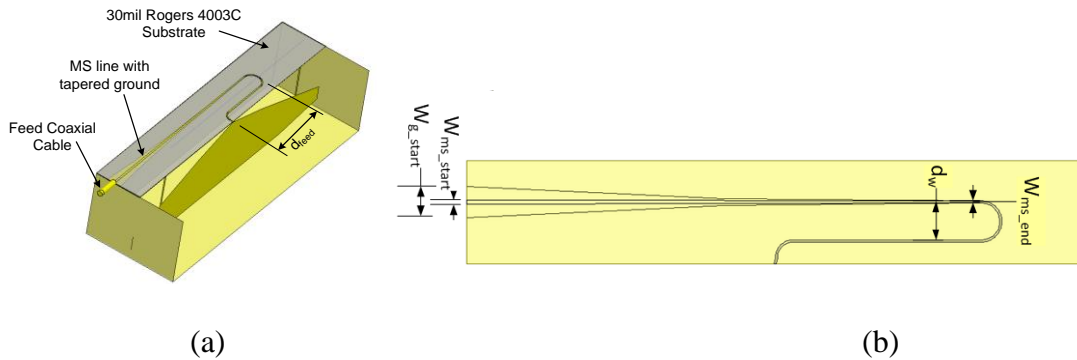


Figure 5.26: The used balun for feeding the bowtie fed RWGA: (a) A cross section of the RWGA at its electrical symmetry plane to show the feeding structure and (b) the balun dimensions.

Table 5.1: Integrated microstrip balun dimensions.

Parameter	l_{feed}	$W_{ms_{end}}$	$W_{ms_{start}}$	$W_{g_{start}}$	d_w	d_{feed}
Value	250 mm	1 mm	1.9 mm	15 mm	18 mm	109 mm

5.3.5 Measurement Results

The fabricated structure is shown in Figure 5.27 next to a ridged horn operating from the same minimum frequency (1 GHz). From the photo we can see the significant size advantage of the newly proposed antenna. The VSWR measurement results are shown in Figure 5.28 (a). The antenna has VSWR <2.5 over 1.08 - 4.9 GHz (1:4.5 impedance bandwidth) and the measured and simulated VSWR show very good agreement. The antenna gain was also measured and is plotted in Figure 5.28 (b) together with the gain of the ridged horn and the gain of an ideal TE_{10} aperture. The measured gain of the antenna varies from 4.5 – 12.5 dBi over the band. It is interesting to note that the proposed antenna has a gain within 2 dBi of the gain of the ridged horn while being less than $1/8^{\text{th}}$ of the size. This is expected since rectangular waveguide apertures have significantly better aperture efficiency compared to ridged waveguides.

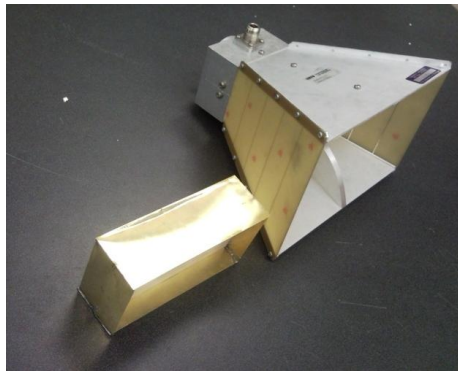


Figure 5.27: Photo of the proposed antenna next to a ridged horn antenna operating from the same minimum frequency.

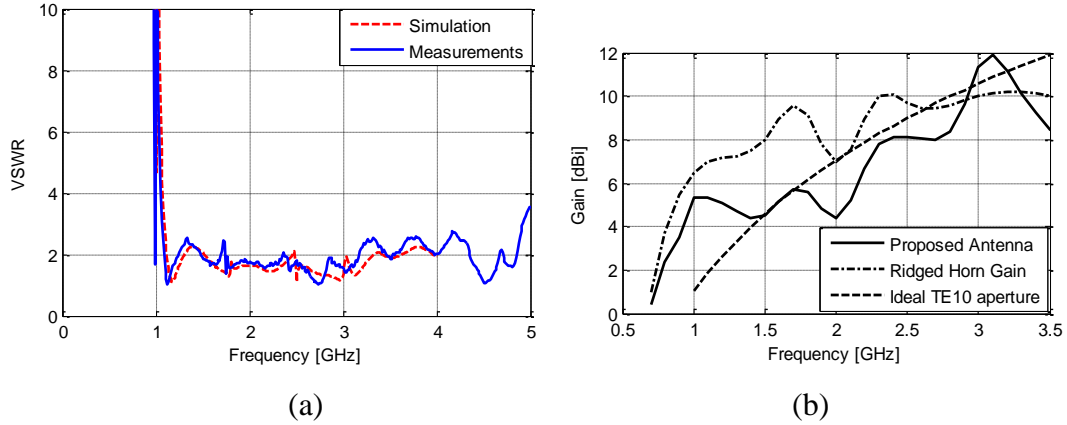


Figure 5.28: (a) The measured and simulated VSWR of the proposed antenna and (b) the measured and simulated gain compared to the gain of the ridged horn and that of an ideal TE_{10} aperture.

The radiation pattern of the antenna was measured in the anechoic chamber and the results are shown in Figure 5.29 (a) and (b) together with the simulation results. We can see excellent agreement between the simulation and measurement results. The radiation pattern had low side lobe levels up to about 3.5 GHz. These side lobes are mainly due to the larger phase variations across the aperture at higher frequencies.

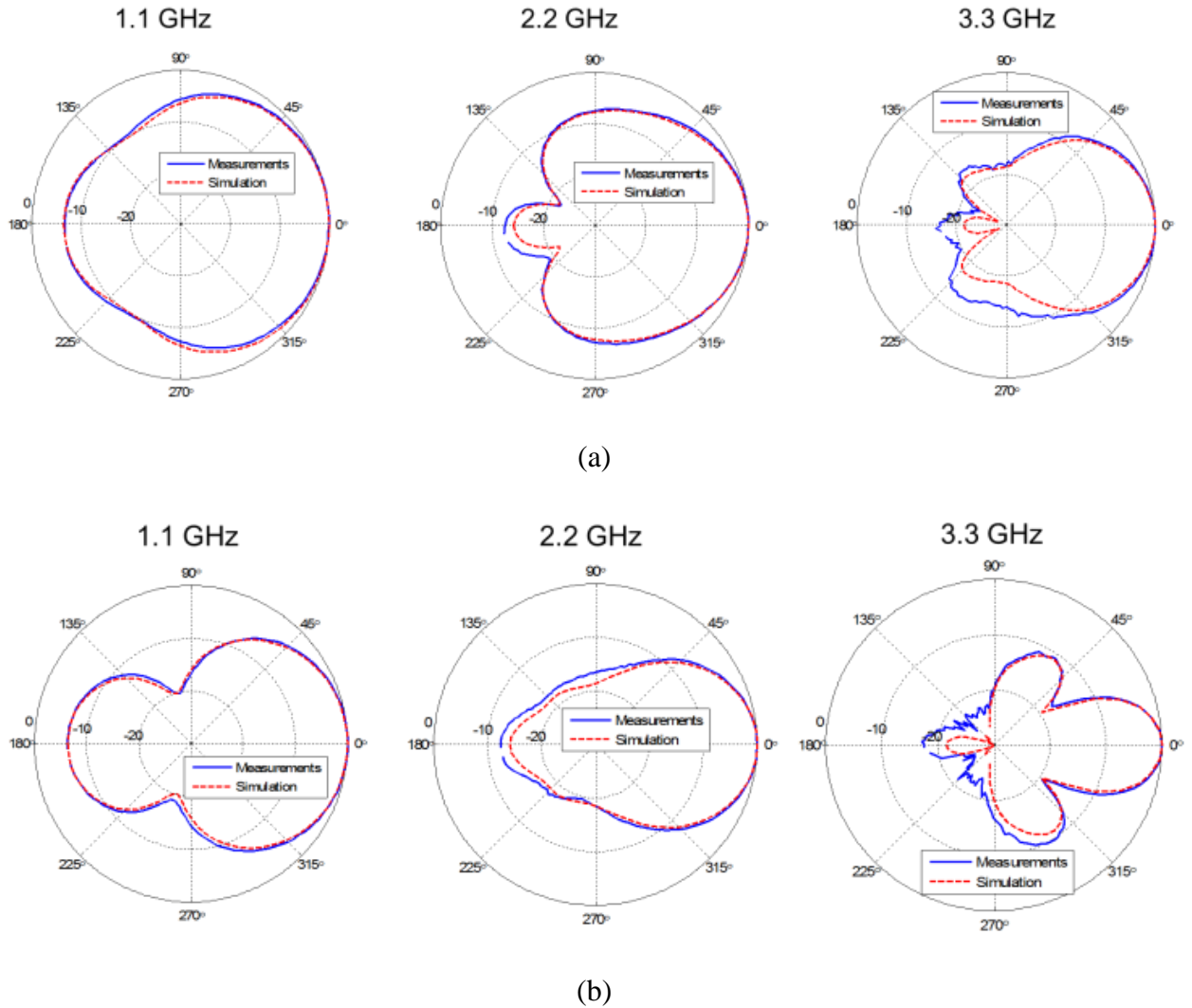


Figure 5.29: The measured and simulated radiation pattern of the antenna at different frequencies (a) E-Plane and (b) H-Plane.

As previously mentioned, the impulse response of the antenna is also very important as it can significantly reduce the required post processing time and allows the use of time domain hardware. The time domain response of the antenna was measured using an HP 8753D network analyzer by synthesizing a sinc pulse of bandwidth 1 - 4 GHz. The received pulses using two ridged horns and using a ridged horn and a RWGA are shown in Figure 5.30 compared to the normalized received pulse when connecting the cables directly (ideal case). The figure again shows that the proposed antenna has very

little dispersion and slightly lower gain than a ridged horn of 8 times its size (the peak pulse amplitude is lower by only 1.5dB).

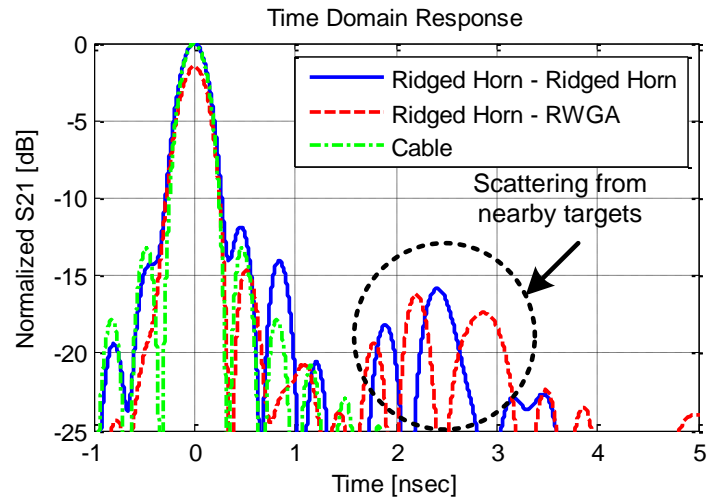


Figure 5.30: Time domain response measurements for the proposed antenna compared to ridged horn.

5.4 Conclusion

Due to the low frequency of operation of the proposed VHF InSAR system and GPRs and the required wide bandwidth of operation, conventional antenna designs are not suitable. To address this problem, we presented two wideband antennas with very compact dimensions. The first design is based on the coupled sectorial loop antenna and is a monopole type antenna that requires a ground plane and thus can be mounted on vehicle or plane external hull. The second design is based on utilizing a novel feed for rectangular waveguides. Both antennas were simulated and measured and good agreement between the simulations and the measurements was observed.

Chapter 6

High Isolation T/R UWB Antenna Pair

In airborne radars scenarios, there is a large time difference (compared to the transmitted pulse width) between the transmitted pulse and the backscattered signal from the target. This large time difference allows the use of time domain switching between the transmitter and receiver to separate the transmitted signal and the received signal. This prevents saturating the receiver due to the large magnitude difference between the transmitted and received signals. However, in GPR and other short distance radars, this time difference is not as large. In such case, the isolation between the transmitted and received signals is achieved by using two antennas and maximizing the isolation between them. In this chapter, we discuss the importance of this isolation in Radar and in communication systems. We then present typical examples of such antenna pairs. It is shown that these pairs have to be separated relatively far from each other to get better isolation. To address this problem, we present the development of a new cavity backed CSLA antenna pair that can provide good isolation in a relatively compact size.

6.1 Introduction and Motivation

Ultra-wideband antennas are considered critical components of ultra-wideband radar and communication systems that affect the performance and complexity of such systems. In radar applications, antennas are desired to have good front-to-back ratio, stable radiation characteristics, and be non-dispersive with well-defined and stable radiation phase center. Many radar systems that require high sensitivity use two separate

antennas for transmission and reception (T/R pair) instead of a single antenna and a circulator in order to avoid the strong reflections at the antenna input terminal as shown in Figure 6.1. Such strong reflections can saturate the receiver and negatively impact the minimum detectable signal for a given receiver dynamic range. This is especially true for UWB radars due to the fact that it is hard to obtain a reflection coefficient (S_{11}) that is significantly less than -10dB over the ultra-wide bandwidth of the antenna without using lossy elements. However, lossy elements will impact the radiation efficiency of the antenna. In addition, single antenna systems require ultra-wideband circulators which are not readily available for all operating bands. In high performance communication applications such as MIMO communications, multiple antennas are usually used. In these applications, it is desired to minimize the coupling between the two antennas in order to maximize the spectrum efficiency and thus maximize the data rate. The spectrum efficiency for an antenna pair is usually characterized by the envelope correlation coefficient, ρ_e , which is related to the antenna pair S-parameters as given by eqn. (6.1) [52]. This equation indicates that for a well-matched antenna pair with good isolation (S_{11} and S_{21} are small), the envelope correlation coefficient is minimal and thus the spectral efficiency is maximized.

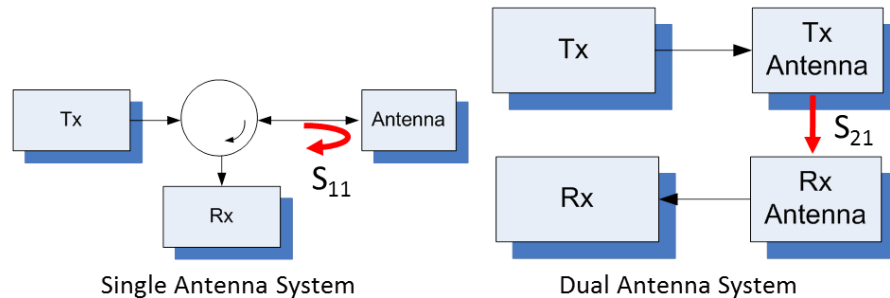


Figure 6.1: Single antenna and dual antenna radar systems.

$$\rho_e = \frac{|S_{11}^* S_{12} + S_{21}^* S_{22}|^2}{(1 - (|S_{11}|^2 + |S_{21}|^2))(1 - (|S_{22}|^2 + |S_{12}|^2))} \quad (6.1)$$

Single directional UWB antenna designs are presented in many publications and some of the designs were presented in the previous chapter. Some the standard techniques for increasing the isolation between two such antennas are shown in Figure 6.2 (a) – (c) and can be summarized as follows:

1. Increasing the physical separation between the two antennas. This is based on that the main coupling component is the near field coupling which decreases very rapidly with distance. This has the advantage that the isolation is high over a very wideband and further increases with the frequency. However, the overall system size increases. Also, larger separations violate the requirement that the two antennas should have very close phase centers so that the assumptions used in the single antenna system are still valid in the two antenna system (in order not to increase the complexity of the processing).
2. Adding lossy absorbing foam between the elements [53]. The main purpose of the absorbing foam is to absorb the coupled signal between the two antennas. This again results in good wide band isolation. However, this absorbing foam, since it is in the near field of the antenna, usually has the undesired characteristic of absorbing the transmitted signal from the antenna leading to significant decrease in the antenna radiation efficiency. As discussed in the previous chapter,

the antenna radiation efficiency is very important since it limits the overall radar noise performance.

3. Use of isolating elements between the two antennas [54], [55]. These elements resonate over a certain frequency band and generate an electromagnetic bandgap between the transmitting and receiving antennas. Using these structures, high isolation can be achieved between two electrically close antennas. However, due to the resonance nature of these structures, they are inherently narrowband and cannot be used in UWB radars such as the ones considered in this thesis.

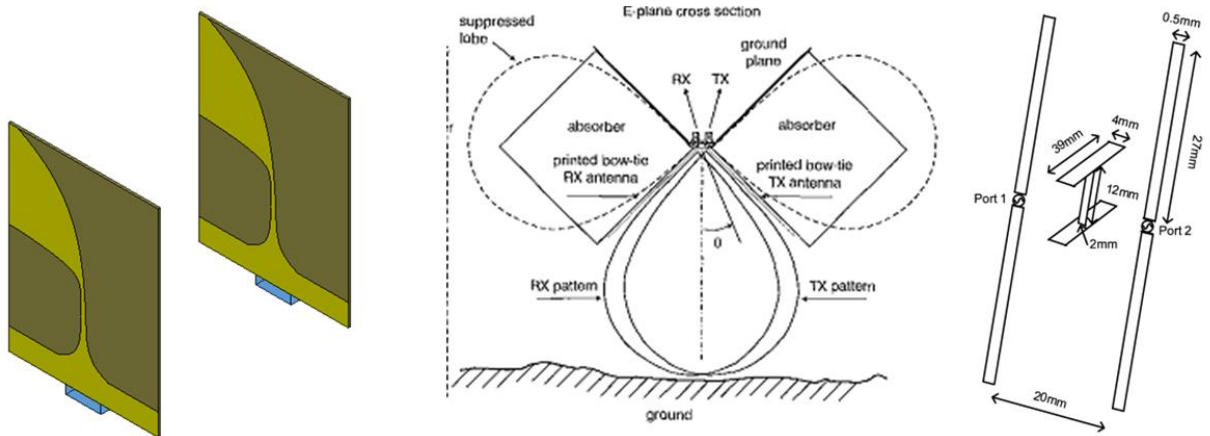


Figure 6.2: Standard methods for increasing the isolation between two antennas (a) increasing the physical separation, (b) use of lossy elements [53] and (c) use of isolating elements.

To address this problem, we present a T/R antenna pair for UWB applications that can achieve isolation better than 20dB over a very wide band in a relatively compact size and without the use of lossy elements. The proposed structure is backed by a cavity to make it unidirectional and easily mountable on metallic platforms. The structure also

allows placement of electronics directly behind the antenna which can further reduce the overall system size.

6.2 Antenna Structure and Operation

The proposed antenna structure is shown in Figure 6.3 (a) and (b). It consists of two coupled sectorial loops antennas (CSLA) separated by a ground plane and fed using a tapered microstrip line. The final antenna structure is achieved through the following steps:

- 1- We started with the original balanced CSLA placed in front of a cylindrical cavity. The cavity creates two significant problems for the antenna. The first problem is that the minimum operating frequency of the original CSLA is increased significantly due to the existence of the back metal plate. The second problem pertains to the generation of in-band cavity resonances which can severely limit the contiguous bandwidth of operation as shown in Figure 6.4 (b) and (c).
- 2- In order to retrieve the lost bandwidth (push the minimum operating frequency lower), we placed the two annular slots of width d_{slot} between the CSLA edge and the rim of the cavity as shown in Figure 6.5 (a) and (c).
- 3- In order to suppress the in-band resonances we placed wedge shaped metallic fins inside the cavity. The shape of this fin has to be optimized as a tradeoff between suppressing the internal cavity modes and the bandwidth. This is shown in Figure 6.5 (b) and (c).
- 4- Finally to convert the single antenna into a T/R pair we split the antenna at its electrical symmetry plane and used two individual unbalanced feeds instead of the original balanced feed. Each feed consists of a linearly tapered microstrip line

(from W_{ms_start} at the coax feed to W_{ms_end} at the antenna tip) on a 60mil RO 4003 substrate. The tapered feed helps further improve the matching of the antenna.

The antenna dimensions are summarized in Table 6.1. They are the nominal parameter values for the parametric study presented in the next section.

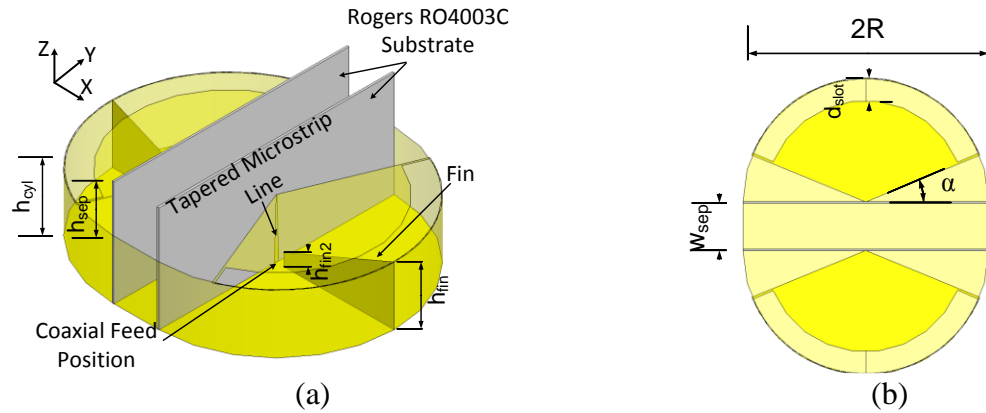


Figure 6.3: Proposed Antenna structure (a) isometric view and (b) top view.

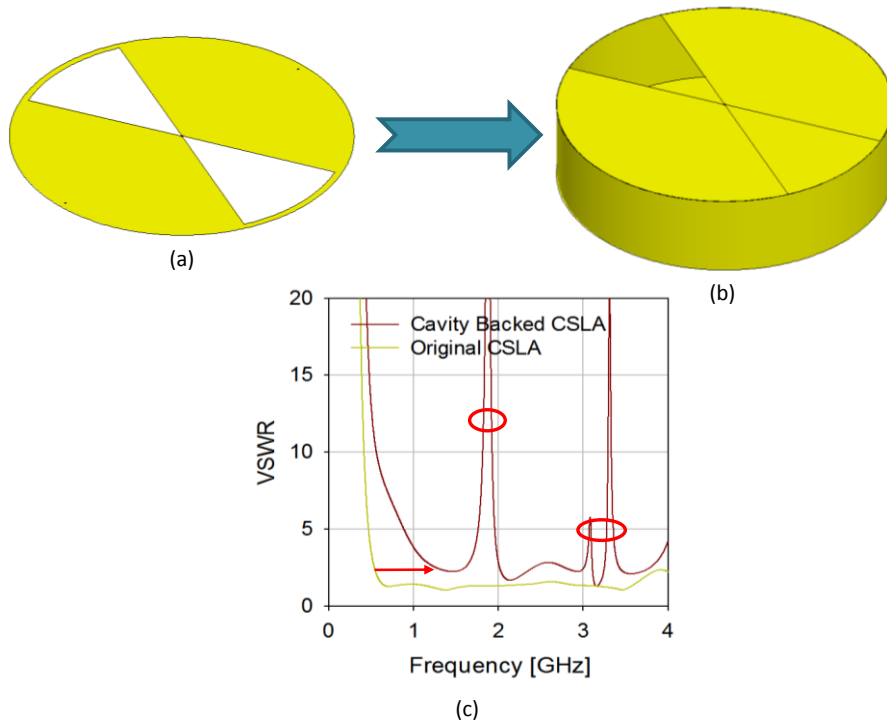


Figure 6.4: The first step for reaching the T/R pair (a) the original dipole version of the CSLA, (b) the cavity backed CSLA and (c) The VSWR of the two antennas showing significant increase in the minimum operating frequency and in-band resonances.

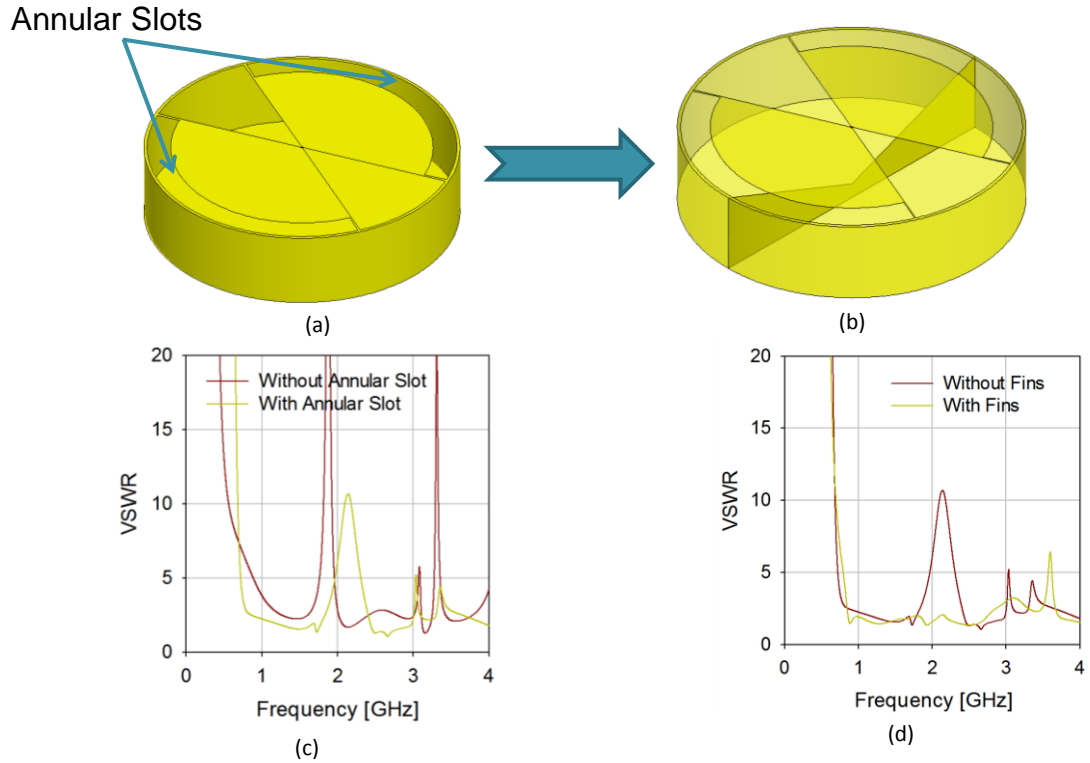


Figure 6.5: The second and third step for reaching the T/R pair (a) adding the annular slots to decrease the minimum operating frequency for the same antenna size, (b) adding the fins to remove the in-band resonances, (c) input matching before and after adding the annular slots and (d) input and output matching before and after adding the fins.

Table 6.1: Antenna Dimensions

R	α	d_{slot}	h_{cyl}	h_{fin2}
100 mm	22°	18 mm	50 mm	10 mm
h_{sep}	W_{sep}	W_{ms_start}	W_{ms_end}	h_{fin}
40 mm	40 mm	3.7 mm	0.7 mm	50 mm

6.3 Parametric Study

In this section a parametric study is presented to optimize the antenna performance in terms of impedance and radiation bandwidth as well as isolation. Even

though S_{21} can be used as a measure of the coupling between the two antennas, a more meaningful definition is the coupled power to one antenna relative to the transmitted power out of the other antenna. This will be referred to as “ I_{12} ” and it can be written in terms of the S-parameters for two identical antennas as:

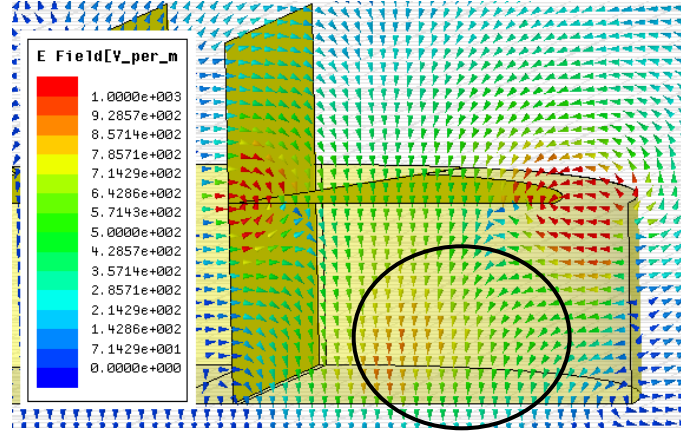
$$I_{12} = \frac{|S_{21}|^2}{1 - |S_{11}|^2} \quad (6.2)$$

Using I_{12} instead of S_{12} allows characterizing the isolation in a way that is independent on the input matching of the two antennas. In the simulation results that follow, the tapered microstrip line is removed and the antenna is fed using an ideal delta gap voltage feed at the sectorial loops tips to demonstrate the operation of the CSLA. The tapered microstrip line design will be presented later as a means to further increase the high frequency bandwidth.

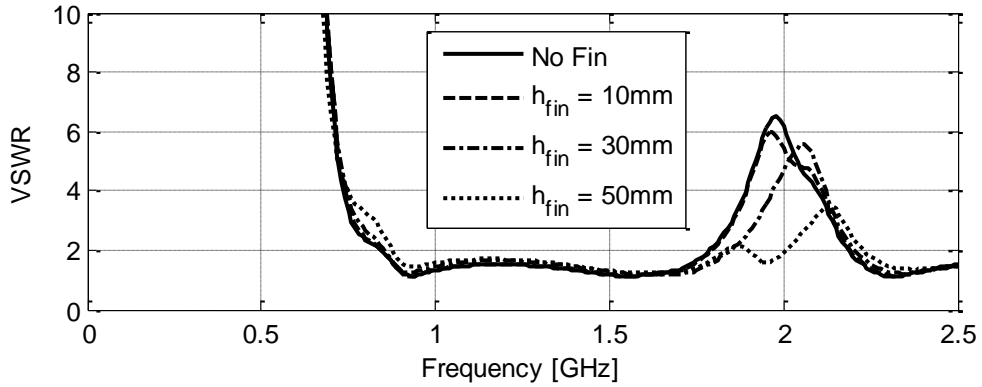
6.3.1 Cavity Fins

As mentioned before, due to the inherent very wide bandwidth of the original CSLA, many cavity modes can get excited. One strong cavity mode is observed at 2GHz. The electric field distribution was obtained using Ansoft HFSS when one of the antennas is excited and is shown in Figure 6.6 (a). The high electric field around the feed and the annular slot are expected and desired. However, the additional field peak (in the encircled region) corresponds to a cavity resonance which is the main reason for the poor impedance matching around 2 GHz as shown in the solid curve Figure 6.6 (b). In order to improve the matching, we placed trapezoidal metallic fins shown in Figure 6.3 (a). The tapered shape is chosen so that the circulating magnetic field between the two sectorial loops is not significantly affected and thus maintains the wideband operation of the

CSLA while suppressing the cavity resonance. The optimum fin height near the cavity edge is found to be equal to the cavity height, h_{cyl} , whereas near the center the optimum height is 10 mm.



(a)



(b)

Figure 6.6: (a) Electric field distribution inside the cavity at 2 GHz with the cavity resonance field component encircled and (b) the effect of the fin height near the cavity edge on the antenna input matching.

6.3.2 Sectorial Loop Angle

The CSLA sectorial loop angle, α , affects the coupling between the two half sectorial loops and thus affects the matching as shown in Figure 6.7 (a). The isolation between the two antennas also slightly increases as α increases as shown in Figure 6.7

(b). This is probably due to the movement of the radiation centers towards the annular slots and away from the center thus increasing the effective distance between the two antennas. To obtain the best matching over the widest bandwidth, we chose α equal to 22° .

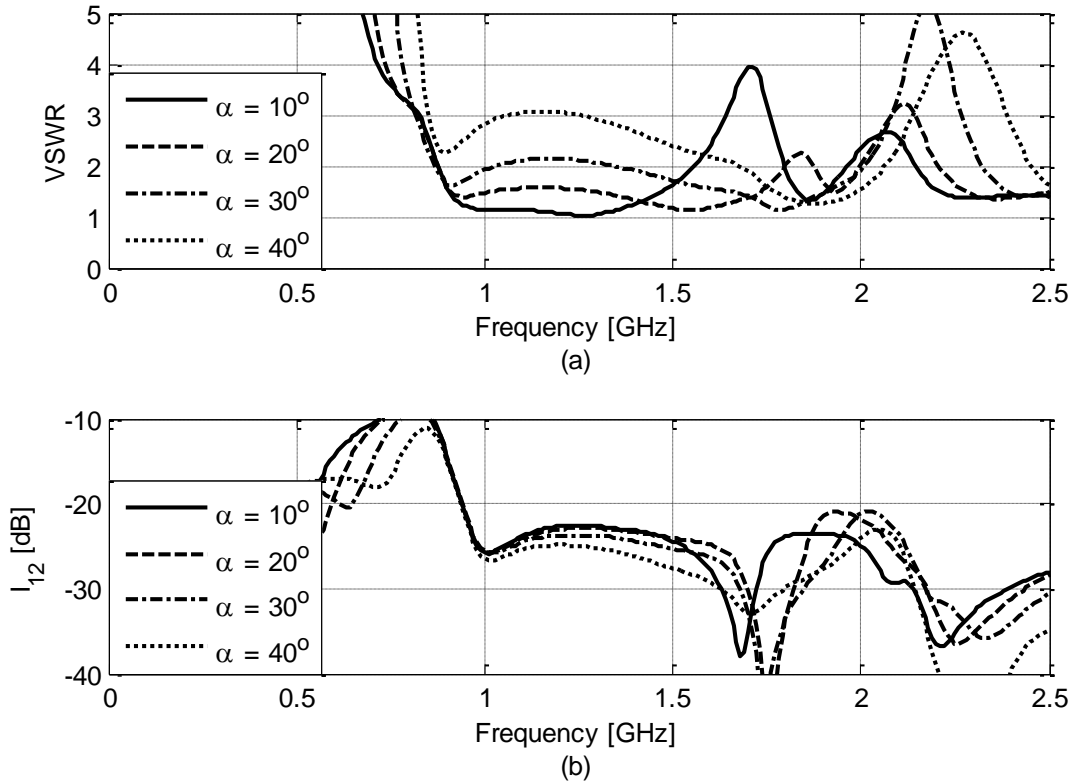


Figure 6.7: (a) The input matching and (b) isolation between the two antennas as a function of the sectorial loop angle, α .

6.3.3 The Cavity Height

The second parameter to consider is the cavity height, h_{cyl} . Its effect on the matching and isolation is shown in Figure 6.8 (a) and (b), respectively. Increasing the cavity height, h_{cyl} , improves the matching at lower frequencies since it reduces the effect of the bottom cavity wall on the coupling between the two antennas. However, deep cavities have more resonances within the frequency band of interest which limits the overall bandwidth of the antenna as shown in the figure. Also, increasing the cavity

height increases the overall antenna size by a factor that is significantly higher than the increase in the minimum frequency (e.g. going from $h_{cyl} = 50$ to 100mm increases the overall size by about 55% while decreasing the minimum operating frequency by only 25%). Furthermore, increasing the cavity height decreases the isolation between the two antennas. To obtain the optimum matching at small antenna size and maximum isolation we chose $h_{cyl} = 50\text{mm}$.

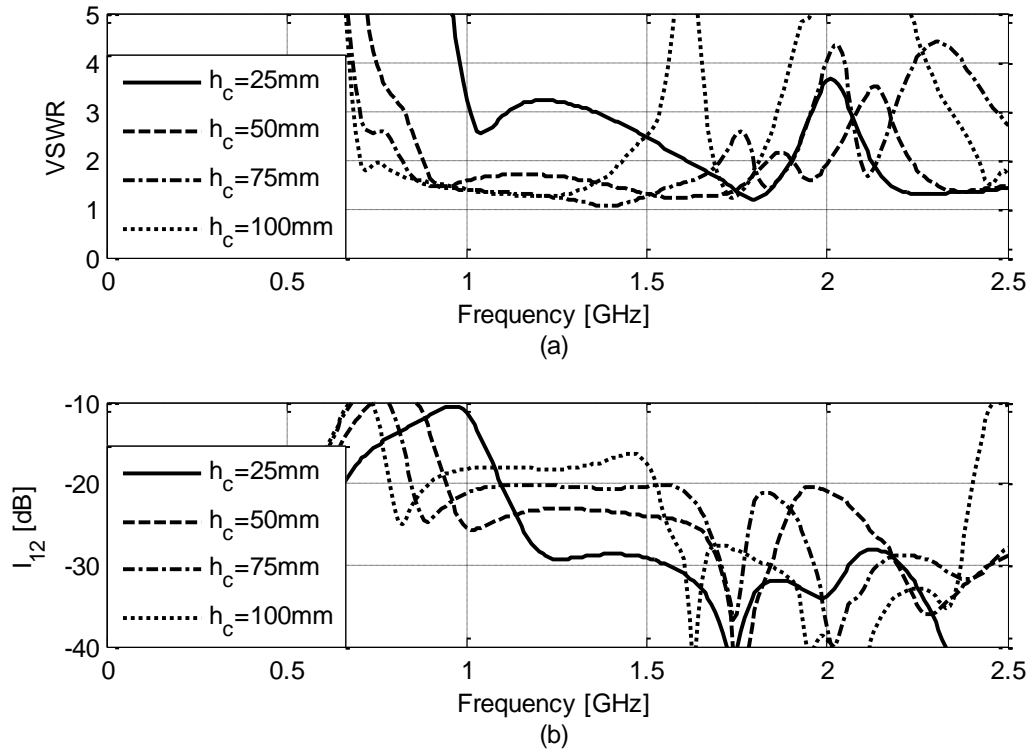


Figure 6.8: (a) The input matching and (b) isolation between the two antennas as a function of the cavity height, h_{cyl} .

6.3.4 Antenna Separation

The isolation between the two antennas can be controlled by adjusting the separation between the two antennas. The input impedance matching is relatively independent on the antenna separation whereas the isolation increases by about 1dB for

every 10mm increase in W_{sep} as shown in Figure 6.9 (a) and (b). For isolation better than 20 dB over the band, we used a separation of 40mm.

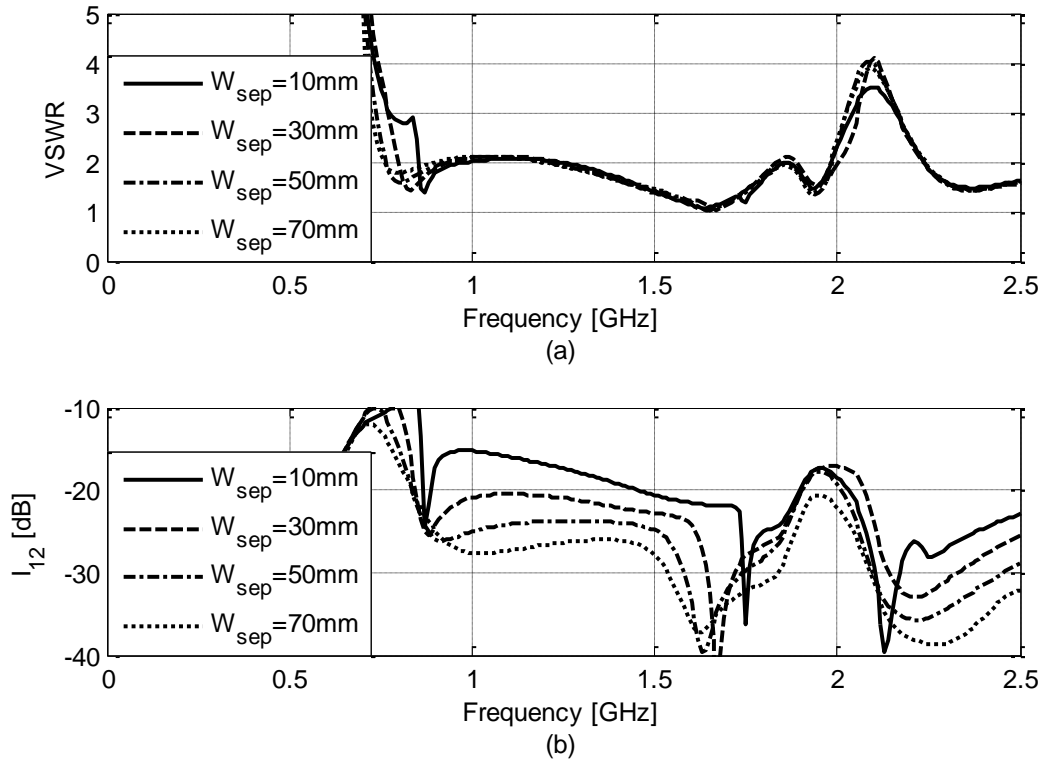


Figure 6.9: (a) The input matching and (b) isolation between the two antennas as a function of the antenna separation, W_{sep} .

6.3.5 Tapered Feed Line

Finally, in order to further increase the antenna bandwidth beyond 2GHz, we noticed that the input impedance at the sectorial loops terminals is close to 50Ω up to 2GHz then it increases to more than 100Ω beyond that. This affects the input matching above that frequency as shown in Figure 6.10 (a). To improve the matching, we used a linearly tapered microstrip line that has 50Ω characteristic impedance at the feed point and increases to about 110Ω at the CSLA feed point as shown in Figure 6.3 (a). Tapered line can act as wideband impedance transformers when the line length is larger than half the wavelength and thus can help improve the matching at higher frequencies without

severely affecting the matching at the lower frequencies. The design is shown in Figure 6.10 (b) where it can be seen that decreasing the taper width helps improve the matching beyond 2GHz. Choosing an end taper width, W_{end} , of 0.7mm gives good matching at both the high and low frequency portions of the band as shown in the figure.

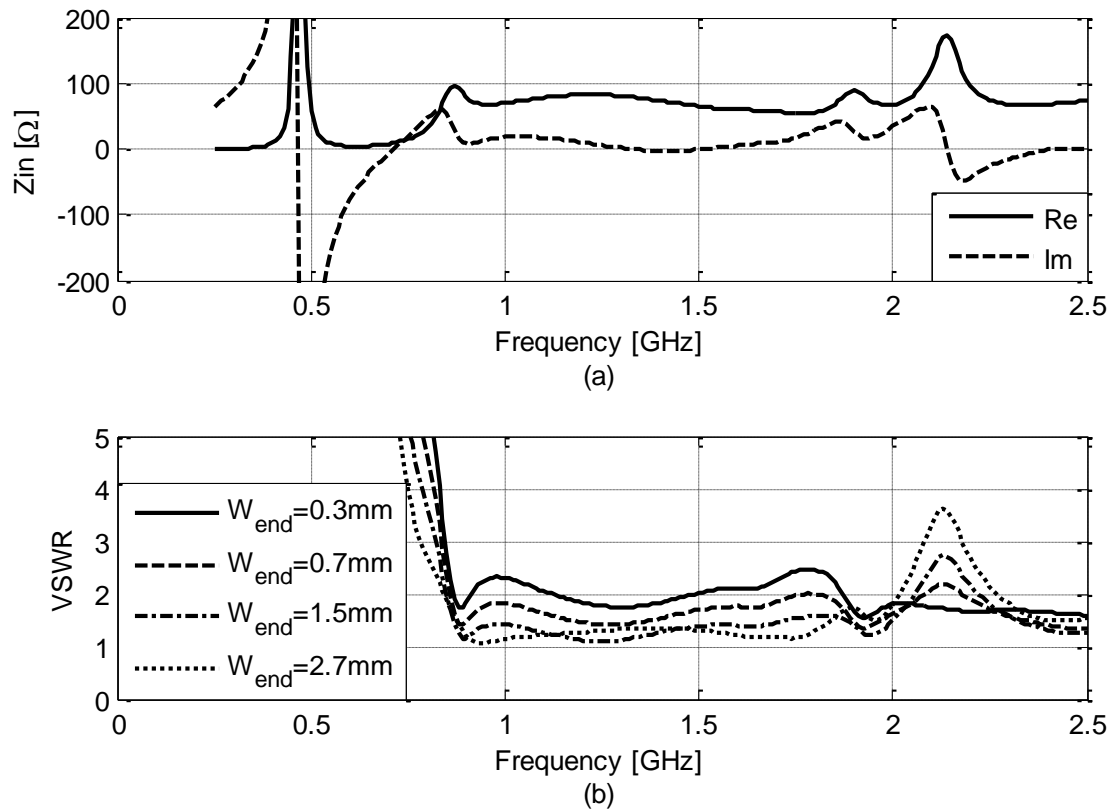


Figure 6.10: (a) The input impedance at one antenna port when the other port is matched and (b) the input VSWR as a function of the tapered microstrip line end width.

6.4 Measurement Results

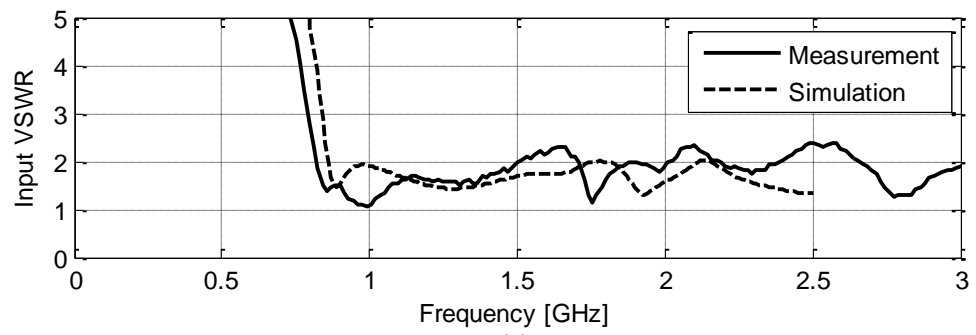
6.4.1 *Input Impedance and Pattern Measurements*

The fabricated antenna is shown in Figure 6.11 (a). The sectorial loops were fabricated on a 60 mil Rogers RO4003 substrate while the cavity was made using copper sheets. The measured and simulated VSWR and isolation of the antenna pair show good agreement and are plotted in Figure 6.11 (b) and (c) respectively. The small discrepancies are probably due to fabrication tolerances. The measured VSWR and isolation were less than 2.4 and -20 dB respectively over 0.9-3 GHz (impedance relative bandwidth of 3.3:1).

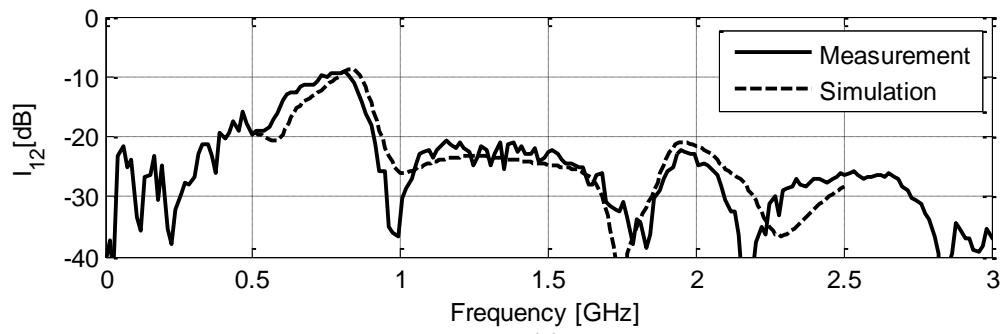
The pattern is squinted from the boresight direction in the E-plane due to the finite length of the ground plane in front of each antenna and the asymmetric structure. The squint angle becomes comparable to the antenna beamwidth at high frequencies which limits the usable bandwidth of the antenna for radar applications to about 1 GHz. However, this does not pose a limitation for communication and radiation diversity applications. The measured and simulated radiation patterns of the antenna pair in the E-plane (YZ) and H-plane (XZ) at 1.5 GHz when one of the antennas is excited are shown in Figure 6.12 (a) and (b).



(a)



(b)



(c)

Figure 6.11: (a) The fabricated antenna pair and the measured and simulated (b) input VSWR and (c) isolation.

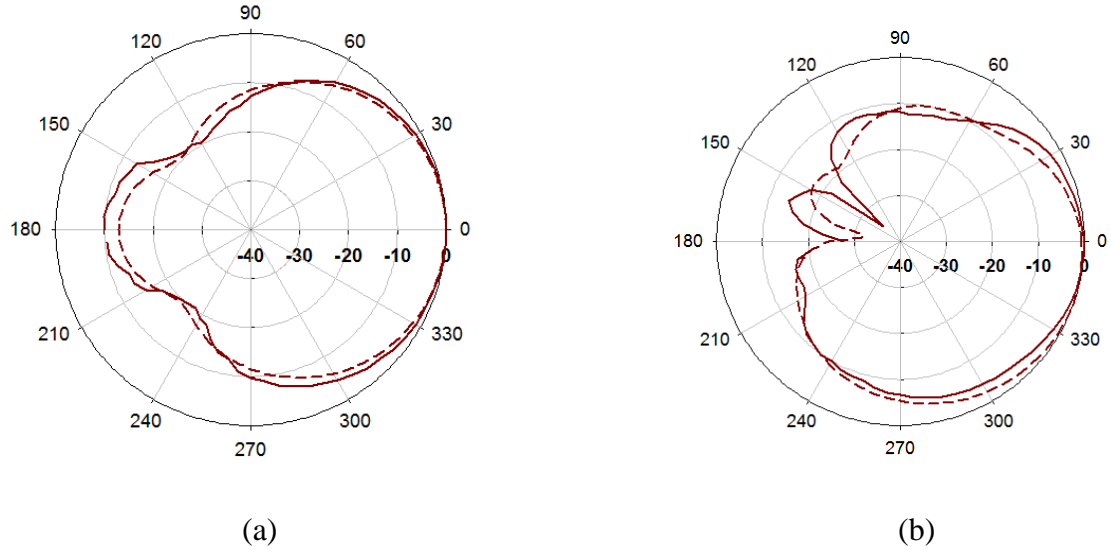


Figure 6.12: Measured (solid line) and simulated (dashed line) single element radiation patterns at the center frequency (1.5 GHz) in the (a) H-plane and (b) E-plane.

The antenna dispersion is a very important parameter in UWB applications. A non-dispersive antenna with stable radiation phase center can be analyzed by examining its time domain transmission response between two identical elements or through reflection measurement of the antenna in front of a large ground plane (mirror). The time domain transmission response presented here was obtained using the mirror approach. Basically the antenna pair was placed in front of a large ground plane and a 1.3 GHz pulse (corresponding to 0.9- 2.2GHz) was synthesized using an HP 8720D network analyzer. The response (S_{11}) for the single antenna excitation and for the transmit/receive antenna pair (S_{21}) for radar applications are measured. The results are shown in Figure 6.13 (a) and (b). The first peak in the two figures is the reflection at the antenna terminal and the coupling between the two antennas, respectively. The second pulse is the reflected signal from the ground plane. We can see that in both cases the received pulse is well defined with little dispersion (as show in the enlarged view in Figure 6.13 (c)) and

no ringing in the time domain. The figures also illustrate the importance of using two high isolation transmit receive antenna pair in order to maximize the sensitivity of the radar system.

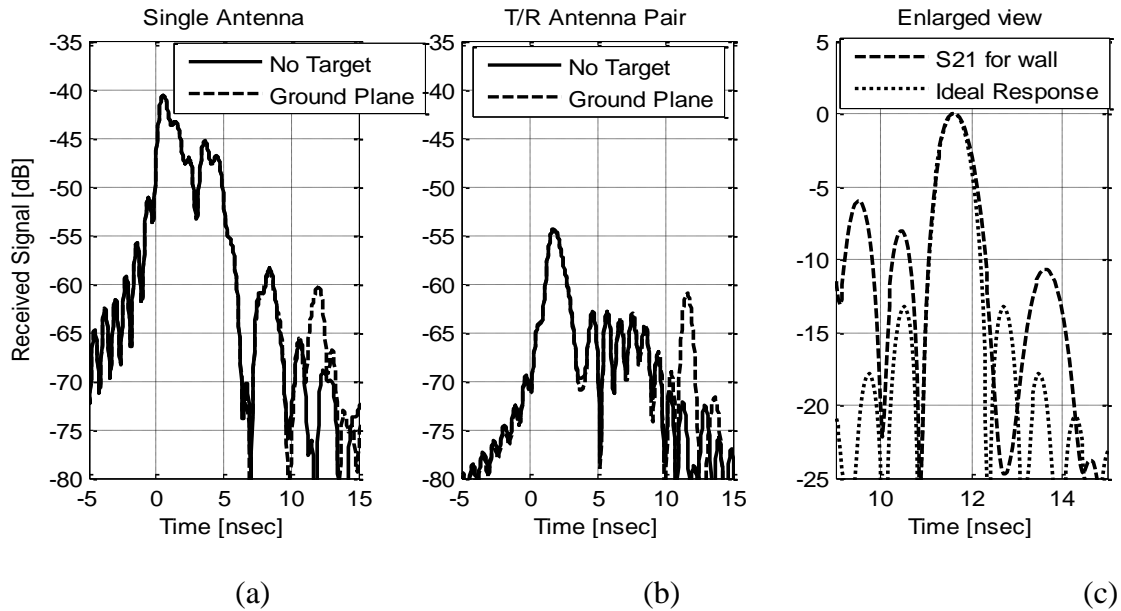


Figure 6.13: Time domain responses for (a) single antenna, (b) transmit receive antenna pair and (c) enlarged view of the S21 response overlaid over the ideal sinc pulse.

6.5 Comparison to other structures

The proposed antenna pair was compared to a ridged horn antenna pair and a pair of the directional CSLAs presented in the previous chapter as shown in Figure 6.14 (a) – (d). To achieve high isolation between two directional CSLAs, the structure shown in Figure 6.14 (d) had to be used where a metallic plate and a foam absorber had to be inserted between the two antennas to obtain high isolation. From

Table 6.2, we can see that the proposed antenna is less than $1/4^{\text{th}}$ the size of the ridged horn pair while having comparable isolation. It is also less than half the height of the ridged horn pair. From the table we can also see that the new antenna pair is comparable in size to the directional CSLA pair. However, the absorbing foam in the later pair causes significant reduction in the radiation efficiency. Also, the new antenna pair is much more robust and easier to fabricate than the CSLA pair.

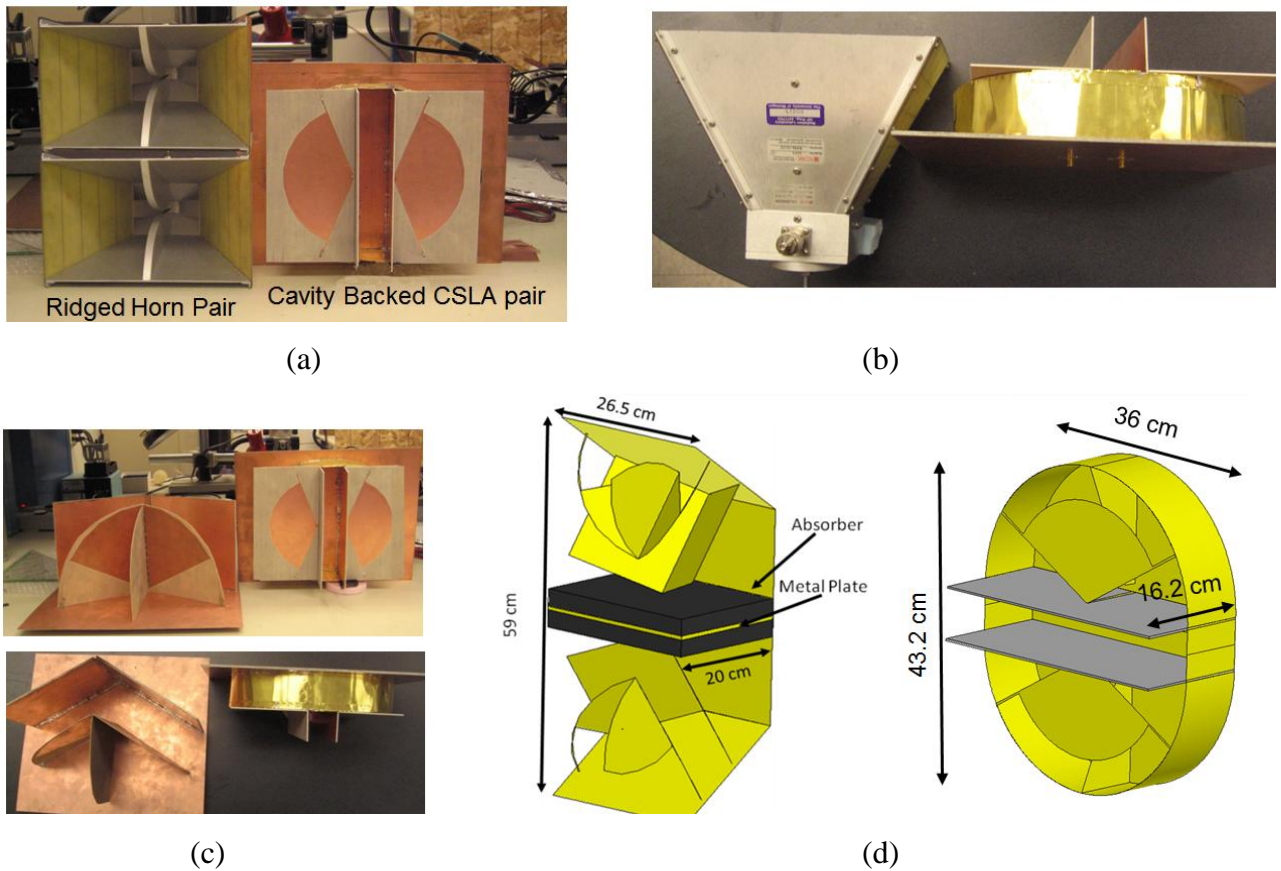


Figure 6.14: Size comparison between the proposed antenna pair and ridged horn antenna pair ((a) and (b)) and a directive folded CSLA pair ((c) and (d)).

Table 6.2: Comparison between the different antenna pairs.

	<i>Ridged Horn Pair</i>	<i>CSLA Pair</i>	<i>Proposed Antenna</i>
Antenna Dimensions	$1\lambda \times 0.82\lambda \times 0.63\lambda$	$0.98\lambda \times 0.44\lambda \times 0.33\lambda$	$0.72\lambda \times 0.6\lambda \times 0.27\lambda$
Minimum Isolation	22 dB	26 dB	21 dB
Size	$0.52 \lambda^3$	$0.14 \lambda^3$	$0.12 \lambda^3$
Directivity	8-10 dBi	5 - 8 dBi	5 - 8 dBi

6.6 Conclusion

High isolation transmit receive antenna pairs are very useful in communication and radar applications. However, high isolation is typically achieved either by using absorbing foam between the antenna elements which reduces the radiation efficiency or by increasing the elements spacing which increases the overall size and weight of the system. To address this problem, we presented a high isolation T/R antenna pair based on the coupled sectorial loops antenna concept. The design issues associated with the matching and isolation were discussed. The antenna was fabricated and measured. The measurement results agreed well with the simulation results. The antenna pair showed high isolation and good matching over a relative bandwidth of 3.3:1 as well as very good time domain characteristics. These characteristics show that proposed antenna pair is very suitable for use in UWB radar as well as communications diversity applications.

Chapter 7

Dual Polarized UWB Antennas

The previously discussed antennas are all linearly polarized. However, in some radar applications, dual polarized antennas are used. The extra polarization information can provide extra information about the target which helps in target recognition. This information can also help in reducing the clutter at the receiver. The two polarizations can be obtained using two orthogonal antennas, one for each polarization, such as the ones previously described in the previous two chapters. However, this again results in an increase in the system size. Also, the two antennas are in the near field of each other which can affect their input matching, radiation pattern and polarization purity. Thus, it is preferable to directly design antennas for dual polarization operation. In this chapter, we will present three antenna designs. Two of them are directive for radar applications and one is omni-directional for diversity communications applications.

7.1 Dual Polarized Directional Cavity Backed CSLA

7.1.1 Antenna Structure

The proposed cavity-backed CSLA antenna structure is shown in Figure 7.1 (a) and (b). The single polarization element is an asymmetrical CSLA with two sectorial loops as shown in Figure 7.1. For the single element the two loops couple through the generated circulating magnetic field which results in good impedance matching over a wide band. The back metallic plane and the cavity wall ensure directional radiation.

However appropriate spacing between the feed and the back plate and other structures, such as tapered fin, in the cavity are needed to avoid field cancelation at the antenna boresight. As will be shown, the coupling between the two loops can be controlled through the loop angle α and the cavity fin angle that is determined by W and h_{c1} to achieve ultra wideband operation. The electric field polarization is parallel to the loops plane in the boresight direction. Dual polarization operation can be achieved by placing two such CSLAs (designated by v and h) perpendicular to each other as shown in Figure 7.1 (a). The electric field from the “v” CSLA is perpendicular to the “h” CSLA and thus the coupling is ideally zero between the two elements. However, in practice, isolation levels of 20-30 dB can be expected depending on fabrication tolerances and feed coupling. The feed for both polarizations is at a common point between the two loops as shown in Figure 7.1 (a). Each antenna requires a 200Ω balanced feed. For low frequencies, transformer baluns can be used. For high frequencies, integrated microstrip baluns can be used as will be shown for the radiation diversity antenna design in the following section. For example, a feed similar to the one presented in [56] can be used. The antenna dimensions for the simulations that follow are summarized in Table 1.

Table 7.1: Directional Antenna Dimensions.

<i>Dimension</i>	W	R	A
<i>Value</i>	50mm	150mm	20°
<i>Dimension</i>	h_c	h_{c1}	t
<i>Value</i>	60mm	50mm	2mm

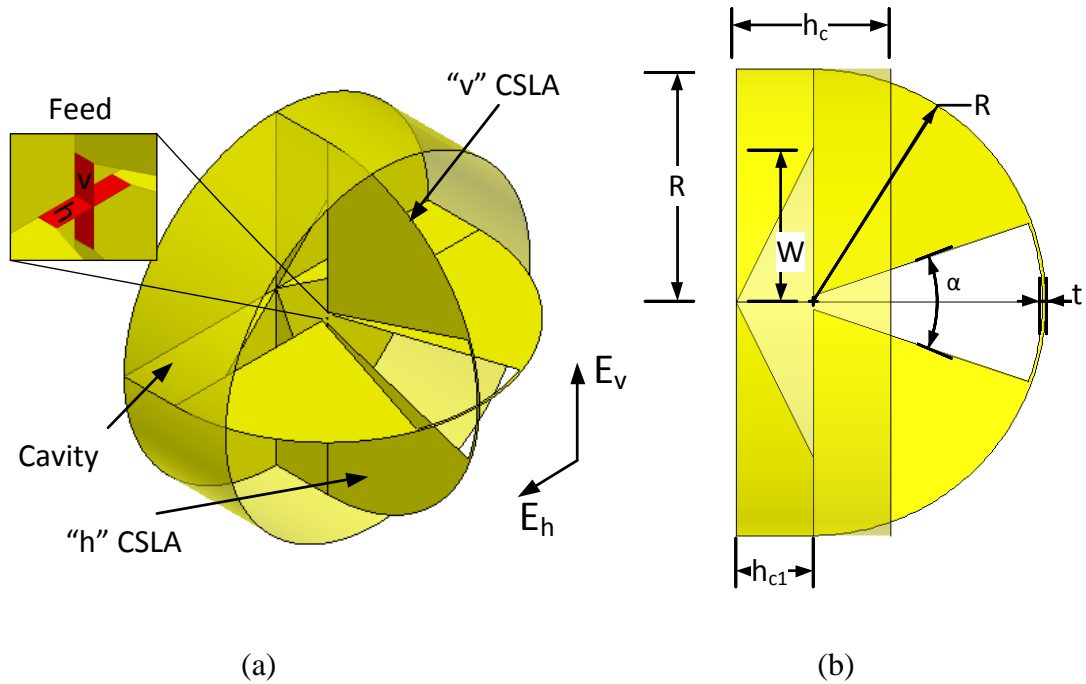


Figure 7.1: (a) Dual-polarized cavity-backed CSLA structure (cavity walls transparent for clarity) and (b) side view along one of the polarization planes. (The antenna is not drawn with the correct dimensions to clarify some of the dimensions.)

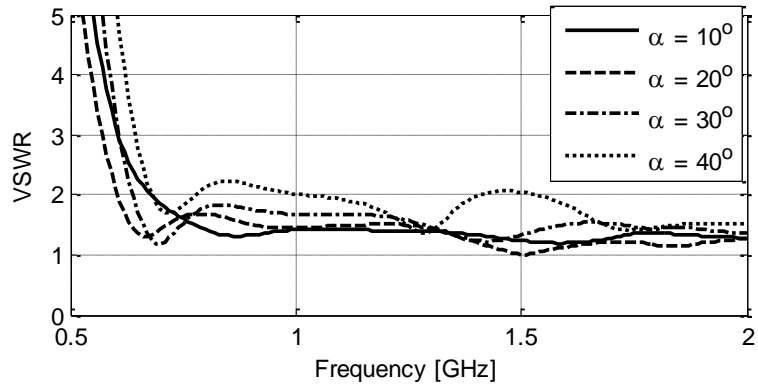
7.1.2 Parametric Study

The sectorial loop angle, α , affects the matching as shown in Figure 7.2 (a) since it controls the coupling between the two loops. It has a small effect on the directivity as shown in Figure 7.2 (b). We chose $\alpha = 20^\circ$ since it gives good impedance matching over the desired band and has the lowest minimum operating frequency thus resulting in the smallest antenna size.

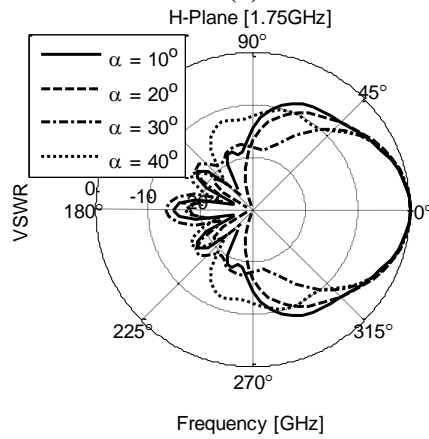
Increasing the back loop height, h_{c1} , improves the impedance matching as shown in Figure 7.3 (a) since it reduces the impact of the metallic plane on the magnetic coupling between the two loops. However, large values results in cavity resonances in the band (e.g. at $h_{c1} = 11\text{cm}$). Furthermore, larger cavity heights result in lower directivity at higher frequencies as shown in Figure 7.3 (b). This is due to the destructive interference

between the direct ray from the loop and the reflected ray from the metallic plate at the back of the cavity. To achieve good matching while maintaining wide gain bandwidth, we chose $h_{cl} = 50$ mm.

A unique feature in this antenna is that its directivity can be easily controlled by adjusting the cavity sidewall height h_c , increasing h_c reduces the beamwidth and thus increases the directivity since it decreases the radiation along angles away from the boresight as shown in Figure 7.4 (a). However, since increasing h_c reduces the radiation in other directions and affects the coupling between the two loops, it increases the minimum operating frequency of the antenna as shown in Figure 7.4 (b). This is expected due to the fundamental relation between the antenna gain and its size which predicts higher gain for antennas with larger electrical dimensions.

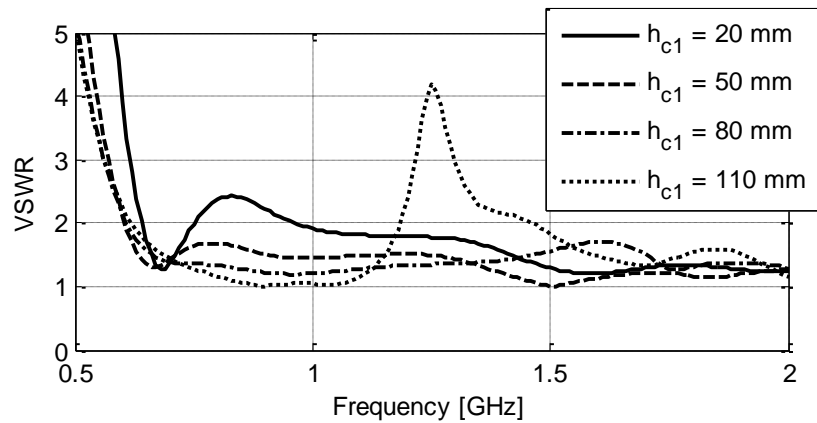


(a)

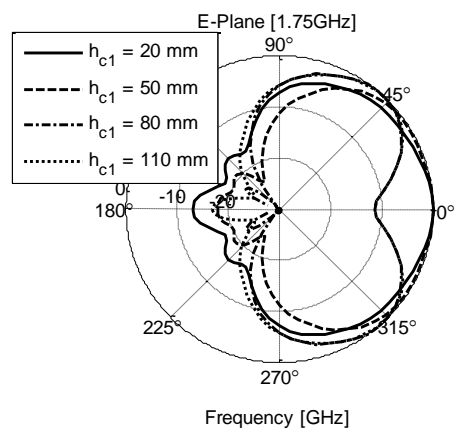


(b)

Figure 7.2: Effect of the sectorial loop angle, α , on (a) the input matching and (b) the H-plane radiation pattern at 1.75 GHz.

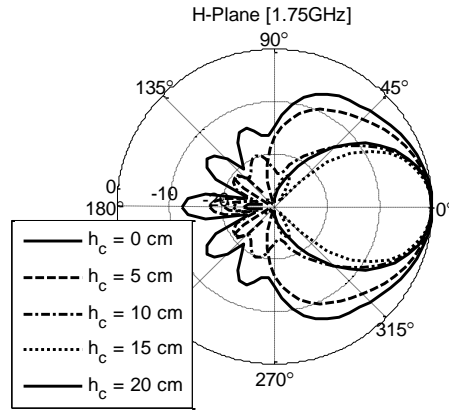


(a)

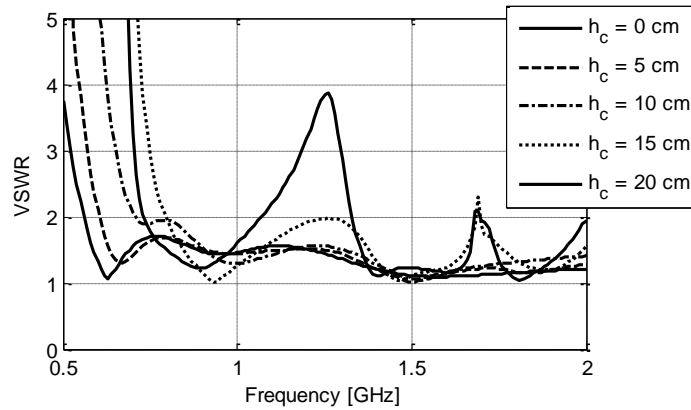


(b)

Figure 7.3: Effect of the cavity height, h_{c1} , on the antenna (a) input matching and (b) E-plane radiation pattern at 1.7 GHz.



(a)



(b)

Figure 7.4: Effect of the cavity sidewall heights on (a) the H-plane radiation pattern at 1.75 GHz and (b) the input matching.

7.2 Diversity Omni-Directional CSLA

7.2.1 Antenna Structure

Many communications applications require a unidirectional antenna with polarization and/or pattern diversity. This is helpful in conventional mobile communication systems where the direction and polarization of the incoming signal are unknown and good reception quality is required independent of antenna location or orientation. It is also used in the relatively recent Multiple Input Multiple Output

(MIMO) communication systems where pattern and polarization diversity are very important to achieve the maximum possible effective channel capacity and consequently the highest data rate. The CSLA can be adapted to polarization and pattern diversity using two techniques as shown in Figure 7.5 (a) and (b). The first option shown in Figure 7.5 (a) uses the same principle as the directional CSLA presented in the previous section, where the “v” CSLA is placed at the electrical symmetry plane of the “h” CSLA thus ensuring zero coupling without any adverse effect on the operation of either elements. The advantage is that the antenna design is exactly the same as the original CSLA and provides extremely wide bandwidth. However the resulting structure is non-planar which is less desirable for many applications. Thus, we chose to use the other design shown in Figure 7.5 (b). It is a fully planar design which makes it much easier to fabricate using standard printed circuit technology. The antenna has two design parameters, the sectorial loops angle, α , and the arm width, t , while the antenna radius is used to define the minimum operating frequency. The feed consists of two overlapping balanced 120Ω ports. The practical implementation of this idealized feed will be presented in Section IV.

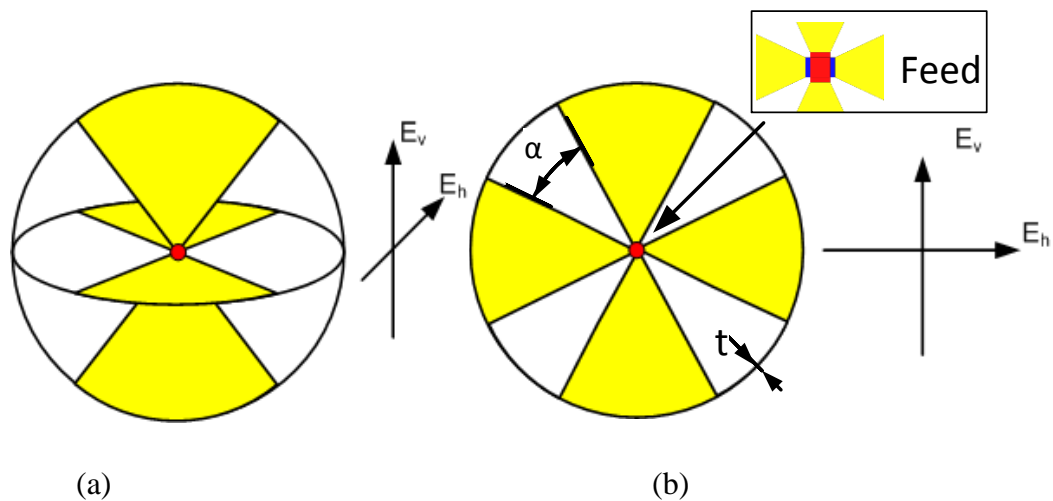


Figure 7.5: Diversity CSLA (a) 3D structure and (b) planar structure.

The current distribution on the CSLA at 0.5 GHz for the horizontal polarization feeding case is shown in Figure 7.6 (a) and (b) where we can see that the current is circulating around the “v” port resulting in no net current flowing into it and thus very high isolation between the V and H polarization. This is expected since for balanced feed, each port is at the virtual ground of the other port. It is also interesting to note the direction of the current which shows two dual-sectorial-loops that are coupled together. Those two dual-loops are common between the two feeding modes but the configuration changes as shown in Figure 7.7 (a) and (b). This reuse of the loops is the reason that the antenna dimensions are comparable to the original CSLA. The antenna could be matched to 120Ω by controlling the sectorial loops angle as shown in Figure 7.8.

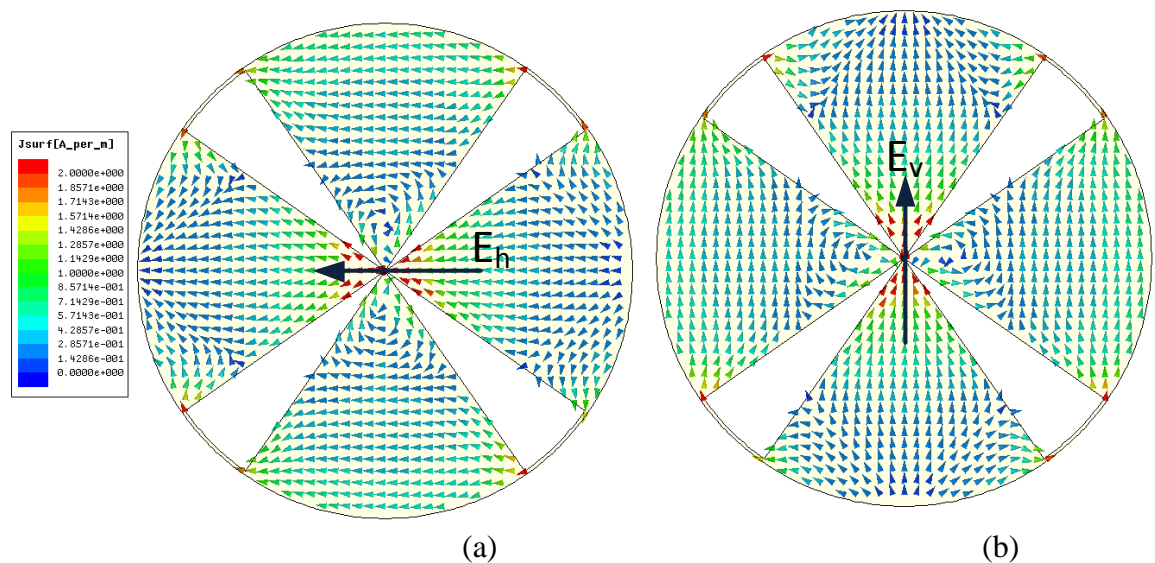


Figure 7.6: Current distribution on the antenna for the two polarizations: (a) horizontal and (b) vertical.

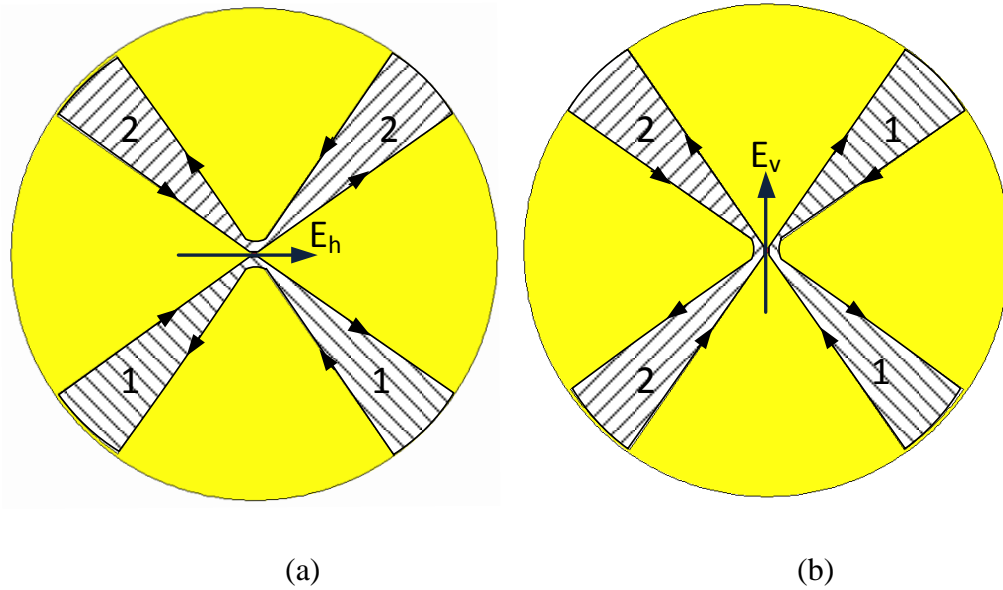


Figure 7.7: Illustration of the reuse of the same V shaped loops for the two polarizations: (a) horizontal and (b) vertical.

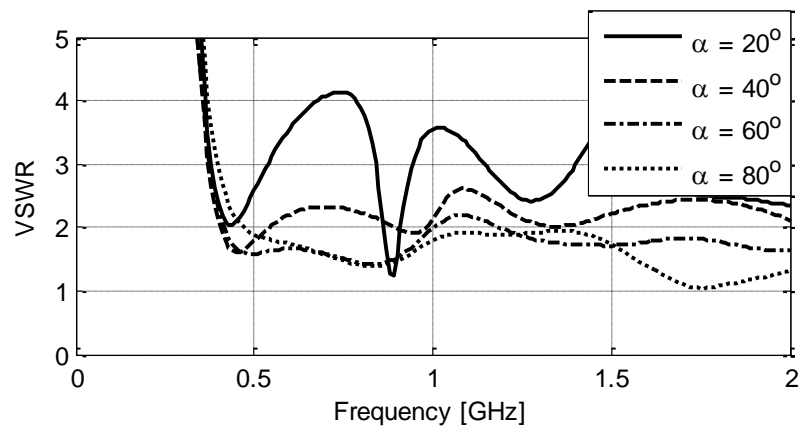


Figure 7.8: Effect of the sectorial loop angle on the matching.

7.2.2 Measurement Results

The diversity antenna was fabricated on a 60mil RO4003 substrate. The structure with the integrated feed balun is illustrated in Figure 7.9 (a) and (b). It is fed using a linearly tapered microstrip line balun. The ground of the microstrip line is the metallic sector. Two metallic sectors are fabricated on each side of the substrate. The measured input VSWR for one of the arms is shown in Figure 7.10 where we can see good

agreement between the simulation and measurements. The antenna had an input VSWR less than 2.5 over 0.48-2.4 GHz. The measured isolation between the two ports is measured to be better than 25 dB as shown in Figure 7.10. The E- & H- plane radiation patterns were also measured and are shown in Figure 7.11 together with the simulation results and they both show very good agreement and a good omni-directional pattern over more than one octave.

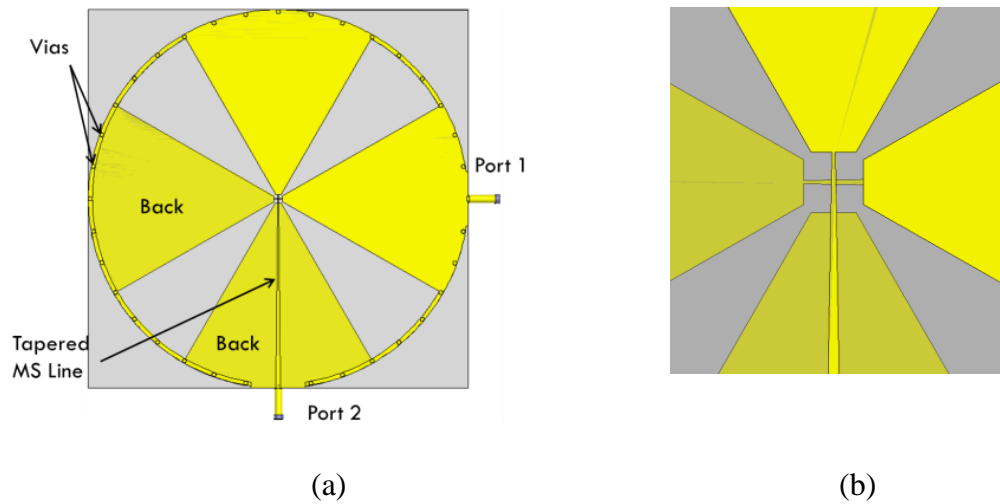


Figure 7.9: (a) Structure of the fabricated diversity antenna and (b) enlarged view of the feed region (darker yellow traces are on the bottom layer).

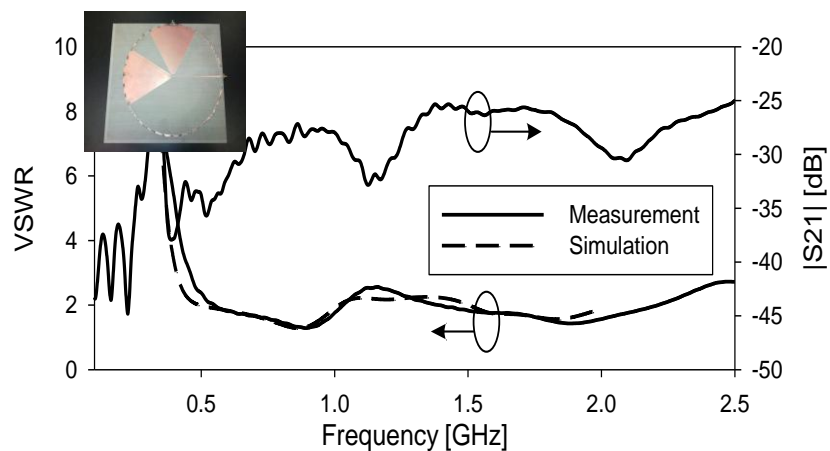


Figure 7.10: Input VSWR and isolation of the antenna.

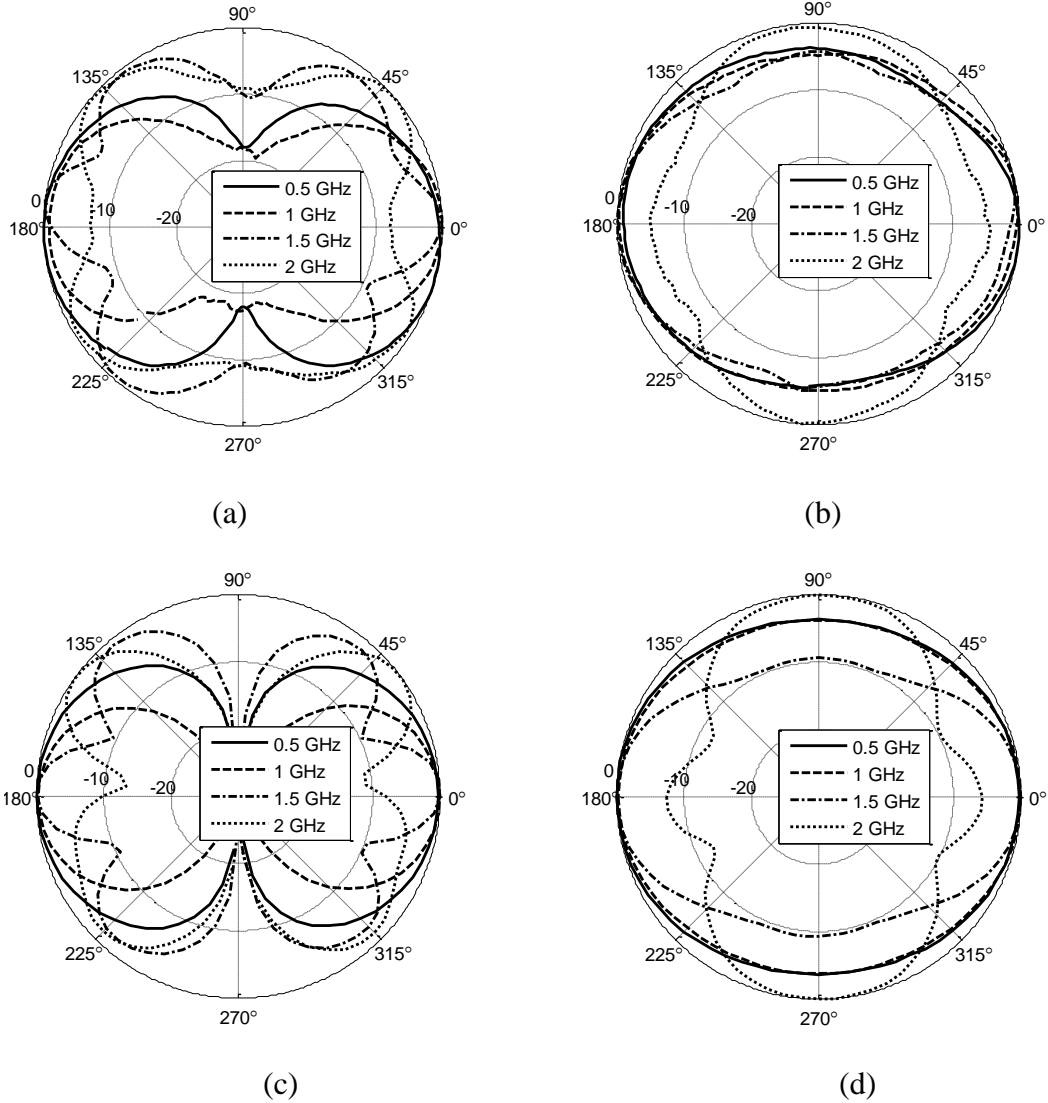


Figure 7.11: Measured (a) E-plane and (b) H-plane patterns and simulated (c) E-plane and (d) H-plane patterns.

7.3 Directional Cavity Backed Dual-Polarized CSLA

7.3.1 Antenna Structure and Principle of Operation

The directive antenna presented in section 7.1 is relatively hard to fabricate since it requires two crossed substrates and jump over wires for the feeding. Thus, we considered using the omni-directional antenna presented in the previous section inside a cavity with square cross section. The proposed antenna structure is shown in Figure 7.12

(a) and (b). It consists of a dual polarized exciting element backed by a rectangular cavity with square cross-section. The polarizing element consists of two orthogonal identical bowtie dipoles shorted together using square ring. To illustrate the operation of the antenna in this section, the excitation is modeled using two ideal voltage gap sources as shown in Figure 7.12 (b). The antenna dimensions are (unless otherwise stated): $h_c = 60\text{mm}$, $W_c = 160\text{mm}$, $\alpha = 29^\circ$ and $t = 1\text{mm}$. The cavity width, W_c was chosen to be 160mm so that the cutoff frequency of the two degenerate fundamental modes of the square waveguide (TE_{10} and TE_{01}) is 0.95 GHz. This allows for a minimum frequency of operation of the antenna near the desired 1 GHz.

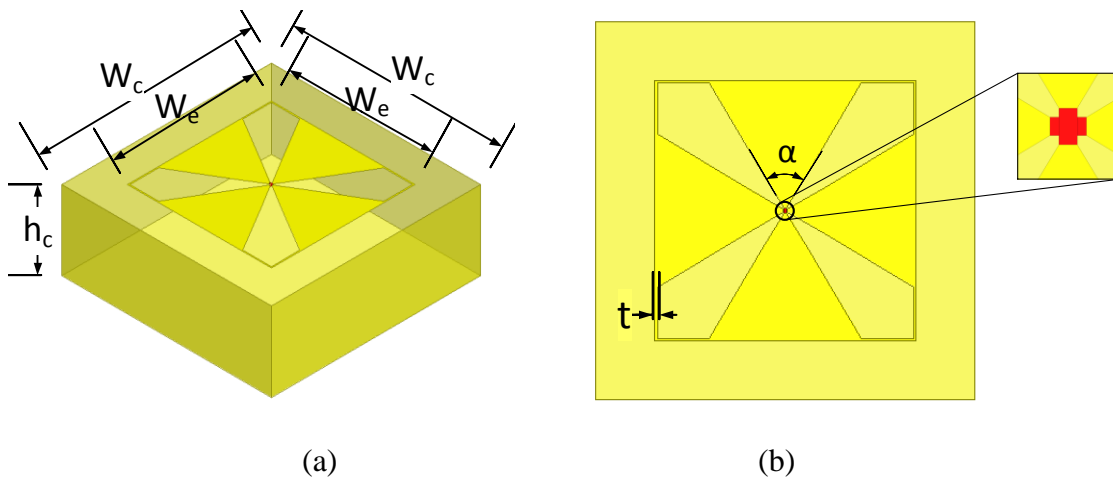


Figure 7.12: Antenna structure (a) isometric view and (b) top view showing the ideal feeding structure.

The current distribution on the exciting element is shown in Figure 7.13 (a)-(d) for both vertical and horizontal excitations, together with the electric field distribution inside the cavity (midway between the exciting element and the back metallic plane) at 1.5 GHz. From the current distribution on Figure 7.13 (a), we can see that all the vertical currents are in the same direction thus enhancing the vertical polarization radiation whereas all the horizontal currents are opposite to each other thus cancelling the

horizontal radiation along the principal planes. The opposite is true for the horizontal excitation as shown in Figure 7.13 (c). Also, the excited field distribution inside the cavity is very close to the TE_{10} mode for the vertical excitation (Figure 7.13 (b)) and the TE_{01} mode for the horizontal excitation (Figure 7.13 (d)). However, at higher frequencies (above 1.9 GHz) other waveguide modes get excited which affects the performance of the antenna and limits its bandwidth to about one octave. It is also interesting to note the geometric orthogonality between the two modes which ensures high isolation between the two ports. This is very important in most dual polarized applications.

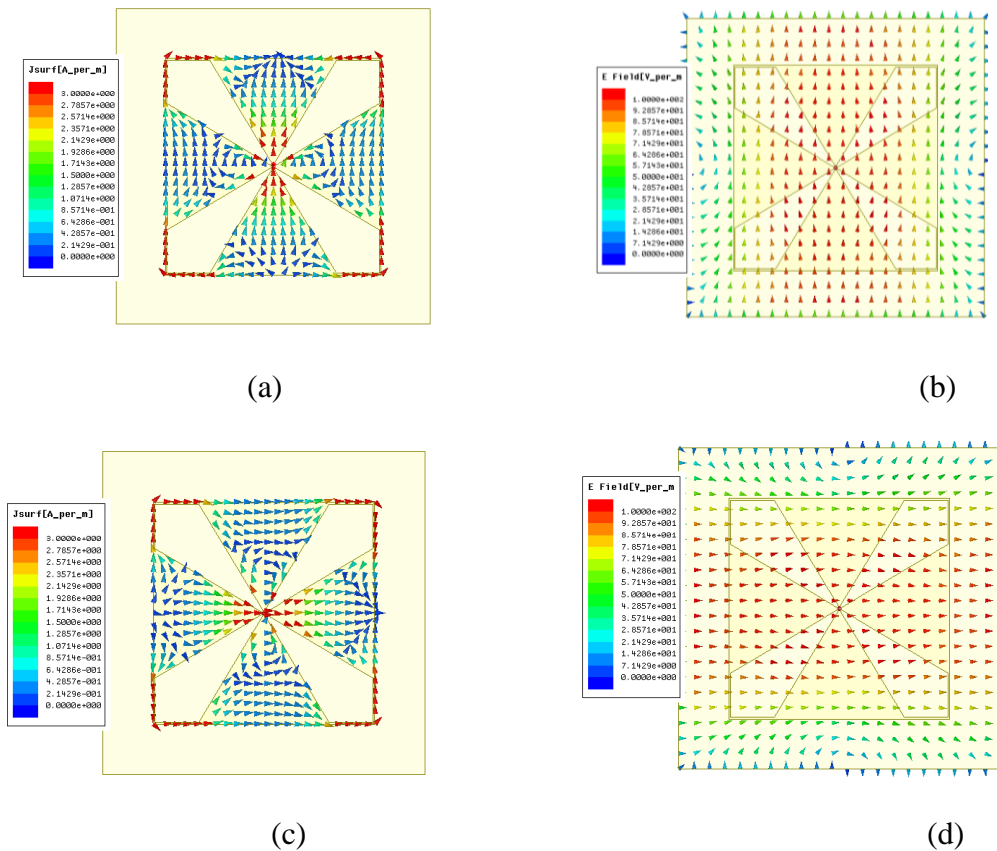


Figure 7.13: (a) and (c) the current distribution on the exciting element and (c), (d) the electric field distribution inside the cavity at 1.5 GHz for both the vertical and horizontal excitation modes.

7.3.2 Parametric Study

As will be shown in the next section, the input impedance of the antenna will be matched using a multi-section microstrip line. To study the effect of the different parameters on the antenna in a manner that is independent on the characteristic impedance of the feed line, the characteristic impedance used to calculate the input reflection coefficient was optimized for each individual case to minimize the average VSWR within the band 0.95-1.9 GHz (the TE_{10} & TE_{01} operating band). This characteristic impedance is the value that should be used in the impedance matching network design and is written in parenthesis in the legend of each figure in this section. The VSWR in this case will be referred to as the minimum achievable VSWR, MA-VSWR.

The first parameter to consider is the cavity height, h_c . The effect of the cavity height on the minimum achievable VSWR is shown in Figure 7.14 (a). For very short cavities (e.g. 20mm), the back metallic plane is very close to the radiating element effectively shorting it at lower frequencies which makes matching the antenna over a wideband very difficult as shown in the figure. On the other hand, very long cavities (e.g. 80 & 100 mm), makes the ground plane half wavelength away at the higher frequencies thus again shorting the feed element at this frequency and resulting in relatively narrower band in addition to larger size. Furthermore, for deep cavities the direct ray from the radiating element and the one reflected from the metallic plane destructively interfere with each other resulting in significantly decreased directivity at higher frequencies as shown in Figure 7.14 (b) and (c). From the figures, we can see that a cavity height of about 60 mm

(about 0.2 wavelengths at the minimum frequency) provides the widest operating bandwidth as well as good radiation pattern over the band.

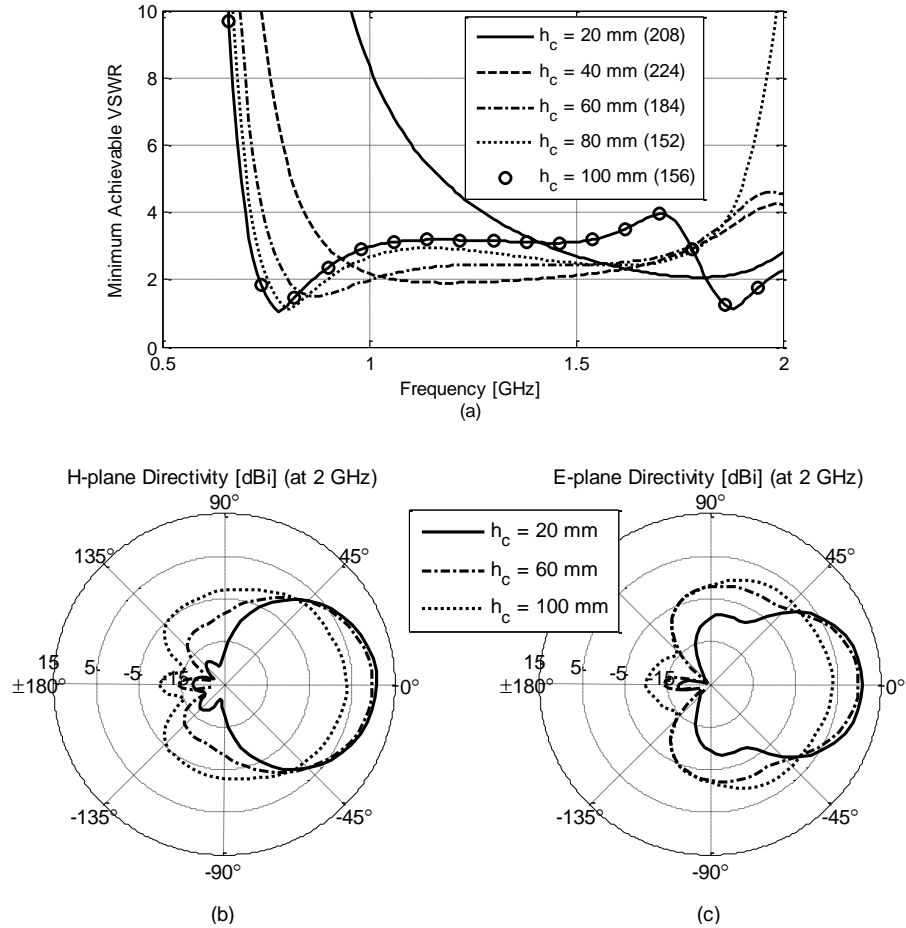


Figure 7.14: The dependence of (a) the MA-VSWR, (b) E-plane and (c) H-plane directivity at 2 GHz on the cavity height, h_c .

The second parameter to consider is the bowtie angle, α . It controls the coupling between the 4 rhombic shaped slots and controls their width at the same time. From Figure 7.15 (a), we can see that it has a small effect on the maximum achievable bandwidth for relatively small angles up to 30° . For large bowtie angles (e.g. 40°), the slots become very narrow resulting in very small bandwidth (or equivalently much higher MA-VSWR). Another interesting phenomenon is the effect of the bowtie angle on the

required feed line characteristic impedance for optimum matching. Increasing the bowtie angle (decreasing the slot angles) results in a reduction of the input impedance at the antenna terminals. This can be explained by noting that the feed port impedance can be viewed as the parallel combination of the two perpendicular bowtie shaped tapered slot lines terminated with inductive trace. When a standing wave is excited on these lines, it excites the TE_{10} and TE_{01} modes in the cavity which are then radiated. Increasing the slots' angles corresponds to narrowing the slot line thus reducing its characteristic impedance and reducing the input impedance at the antenna ports. Depending on the chosen feeding structure, the appropriate bowtie angle can be selected.

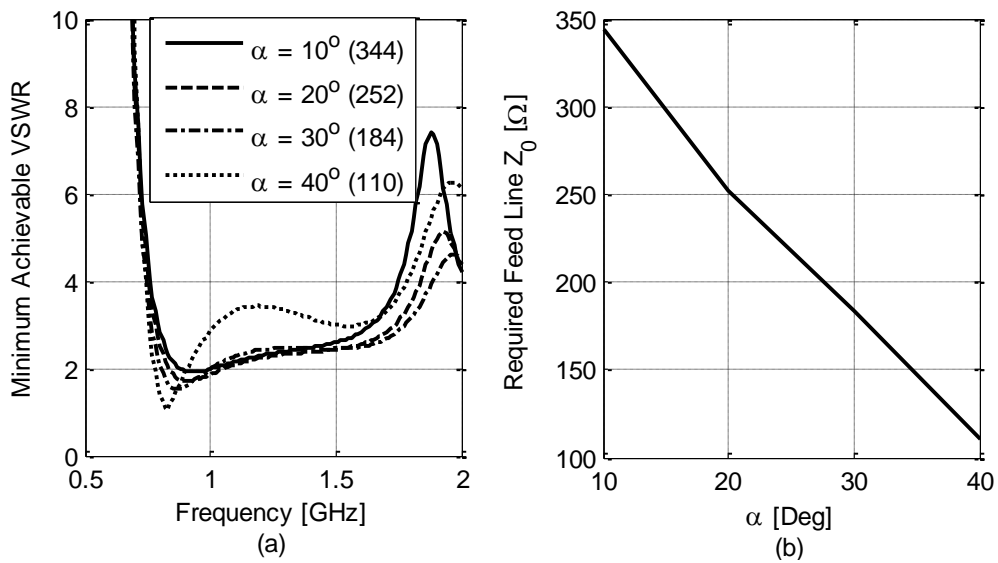


Figure 7.15: Effect of the bowtie angle on the (a) MA-VSWR and (b) the required characteristic impedance of the feed line for optimum VSWR.

The final parameter considered in this study is the feeding element width, W_e . The effect of W_e on the MA-VSWR is shown in Figure 7.16 (a). Increasing W_e reduces the intrinsic resonance of the exciting element allowing it to operate at lower frequencies as shown in Figure 7.16 (a). However, since the cavity does not support frequencies

significantly lower than its fundamental modes cut-off frequencies, the optimum achievable matching is negatively affected (e.g. at $W_e = 140$ mm). On the other hand, small elements have relatively high intrinsic resonance which increases the lowest operating frequency and thus increases the overall size of the antenna (e.g. $W_e = 60$ mm). The optimum width would make the intrinsic reactive field components of the exciting element cancel that of the cavity. From the figure, we can see that this value exists close to $W_e = 110$ mm which gives the widest good matching bandwidth. The exciting element size also affects the radiation pattern as shown in Figure 7.16 (b) and (c). Small elements result in lower directivity whereas large elements produce side lobes since they excite higher order waveguide modes at higher frequencies. Again, the optimum directivity is obtained at W_e close to 110mm.

7.3.3 Actual Feeding Structure

Due to the dual polarization nature of the antenna, feeding structures that exploits the symmetry planes such as the one described in chapter 6 cannot be used. One option is to use discrete balun transformers and feed the antenna from the center. In this case, the feed design is relatively straight forward and the analysis in the previous section directly applies. This is allowable for low frequency applications such as ground penetrating radars since balun transformers have relatively low loss in this band.

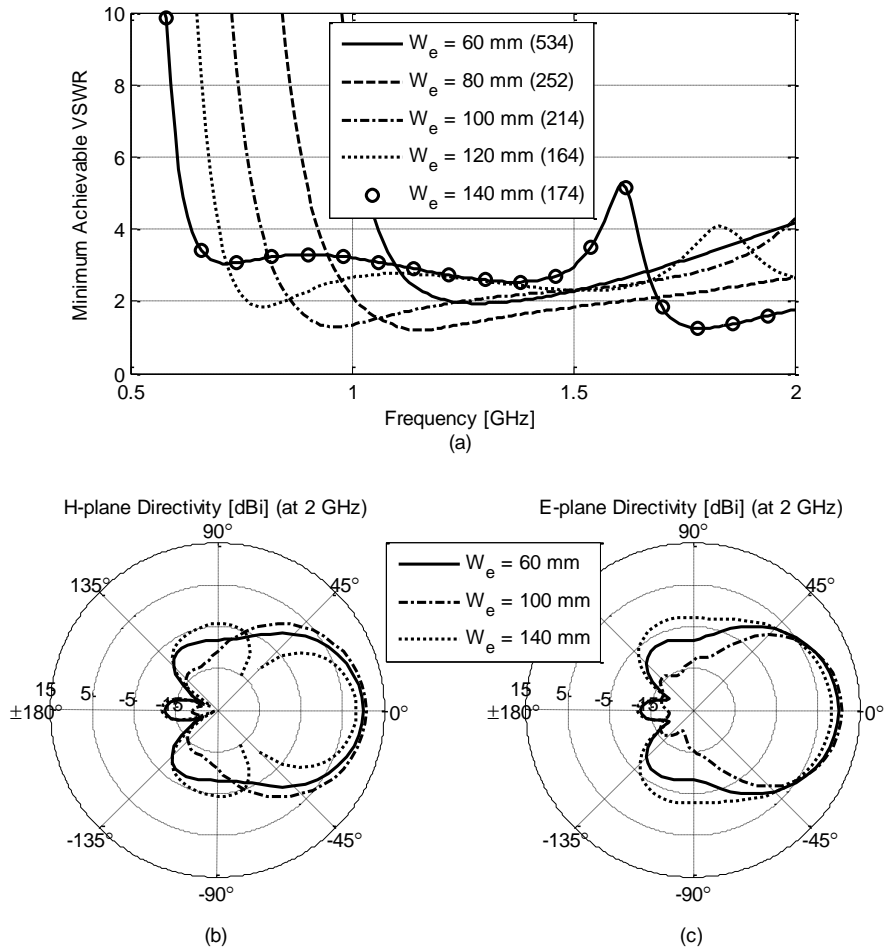


Figure 7.16: The effect of the feed element width on (a) the MA-VSWR and (b) the E-plane and (c) H-plane radiation patterns.

However, in other applications, transmission line baluns are preferable either due to the unavailability of low loss discrete balun transformers in the desired operating band or to minimize the fabrication and assembly costs. For these applications, we present a distributed balun in this section. We used semi-rigid coaxial cables and a multi-section microstrip line feed as shown in Figure 7.17 (a) and (b). For each polarization, one of the bowtie triangles acts as the microstrip line ground whereas the other triangle is connected to the microstrip line end as shown in Figure 7.17 (b). This is helped by the fact that the triangles sides near the cavity wall have small current density which allows their use as

baluns to suppress the undesired unbalanced currents on the outer shield of the coaxial cable as described in [rahmatt samii AP magazine paper on UWB baluns]. Two vias are used to connect the two halves of the ring together across the substrate. The multi-section microstrip line is used to match the relatively high antenna impedance at the input terminals (about 200 Ohms). The tapered microstrip line ground together with the back cavity act as a balun to suppress the unbalanced currents on the outer shield of the coaxial cable. The exciting element size had to be modified to accommodate the different feeding technique, so its width, W_c , was reduced to 90mm. The substrate used is a 60mil RO4003C and the microstrip section dimensions are: $L_1 = 21\text{mm}$, $W_1 = 2\text{mm}$ and $W_2 = 0.5\text{ mm}$. Due to the relatively short MS line section allowed when using this feeding technique, the minimum frequency shifted from around 0.85 GHz to 1 GHz. The current distribution on the antenna terminals for the horizontal polarization is shown in Figure 7.18 (a). We can see that the current distribution is very similar to that of the ideal case. The electric field inside the cavity is also plotted in Figure 7.18 (b), where we can see that it is slightly affected by the presence of the two coaxial cables but the general distribution remains the same. This is due to the fact that the two cables are perpendicular to the direction of the electric field. However, since the structure is no longer fully symmetric, the isolation between the two polarizations will decrease as will be shown in the following section.

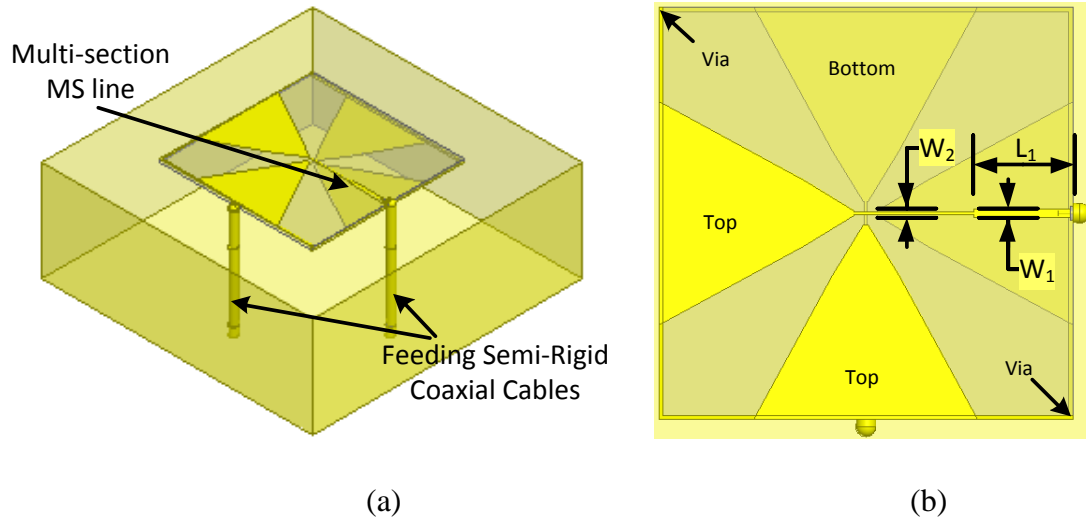


Figure 7.17: The actual feeding structure using multi-section microstrip line, (a) isometric view and (b) top view of the exciting element.

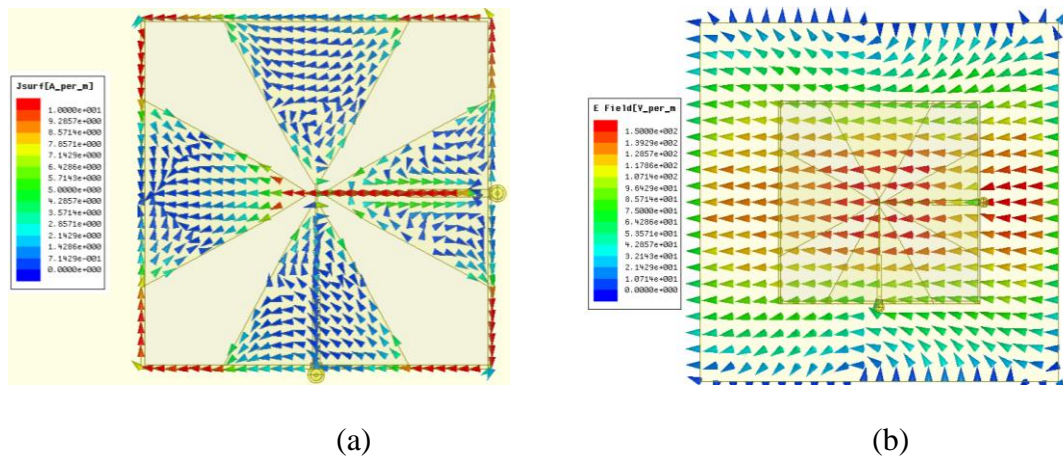


Figure 7.18: (a) The current distribution on the exciting element and (b) the electric field distribution inside the cavity at 1.5GHz when using the MS line feed.

To verify the correct operation of the feed, the radiation pattern of the antenna was simulated and the results are shown in Figure 7.19 (a) and (b) in the E- and H-planes for the vertical polarization. We can see that the pattern is symmetric in the H-plane (perpendicular to the feed line) since the antenna structure is symmetric around that plane. However, in the E-plane, the pattern is slightly squinted by about 4 degrees. This is in part due to the asymmetric cavity structure in this plane (due to the presence of the

coaxial cable on one side but not the other) and in part due to the non-perfect operation of the microstrip balun. However, the squint is small compared to the half power beamwidth and is acceptable in many applications.

7.3.4 Measurement Results

The antenna was fabricated on RO4003 substrate and fed using semi-rigid coaxial cables. The fabricated structure is shown in the inset in Figure 7.20 (a). The input VSWR and isolation were measured and the results are shown in Figure 7.20 (a) and (b). The input VSWR shows reasonable agreement with the simulation results and is below 2.5 over 1-1.95 GHz. Also, the isolation is better than 28 dB over the same band. The discrepancy between the simulation and measurements result is probably due to the fabrication tolerances and the simplifications used to model the coaxial cable to MS line transition.

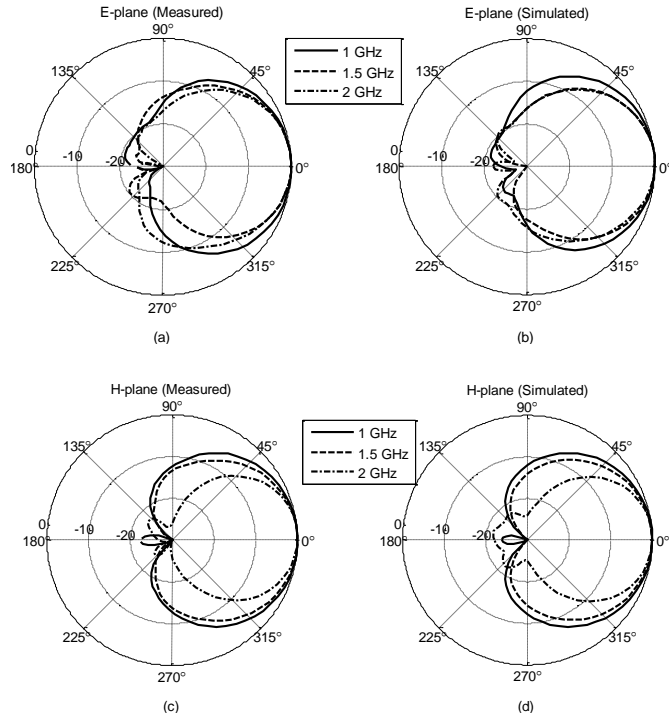


Figure 7.19: Measured and simulated radiation patterns in the (a), (b) E-plane and (c), (d) H-plane of the antenna.

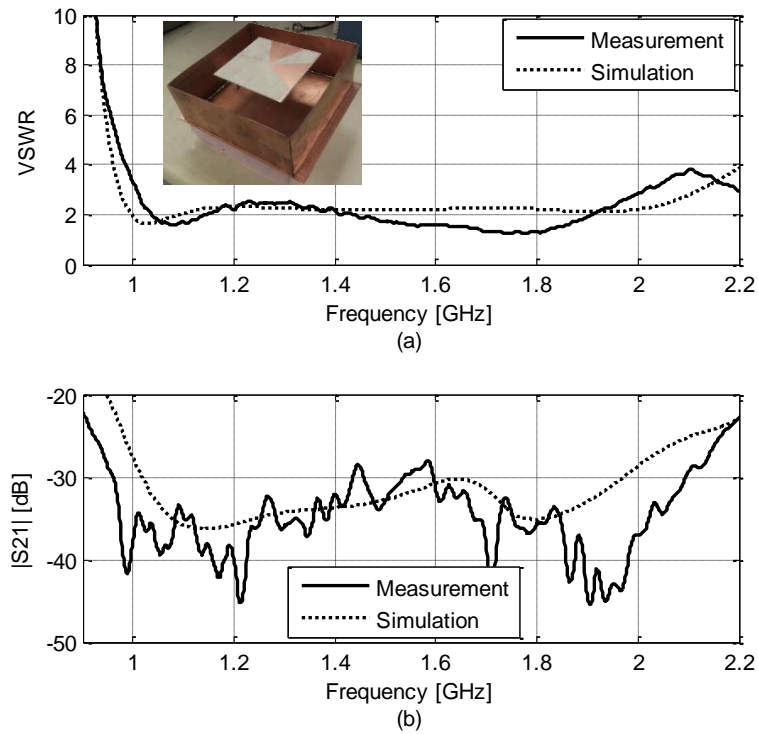


Figure 7.20: (a) Measured and simulated VSWR and (b) measured and simulated S_{21} .

7.4 Conclusion

Three dual polarized antennas, based on the coupled sectorial loops antenna principle, were presented. The first is a directional antenna for radar and communications applications which utilizes asymmetrical loops and cavity backing to provide directional radiation. It is shown that ultra wideband operation can be achieved and that the antenna gain can be controlled by varying the cavity wall height. The second antenna is a diversity antenna for communications application. It provides polarization and pattern diversity. The design is fully planar and relatively compact. For this reason, it was converted into a directional design by placing it inside a cavity with square cross-section. Two of the proposed antennas were fabricated and measured and good agreement between the simulation and measurements was observed.

Chapter 8

Very Low Profile UWB Antennas

The antennas presented in the previous chapters are relatively compact and can be used for the GPR portion of the system. Depending on the aircraft used and the operating frequency used, some of the previously presented antennas cannot be used for on-plane mounting. This is because some of those antennas are relatively high profile which results in significantly increased air drag if those antennas are mounted on the aircraft fuselage. For this reason, we considered other antenna designs that (1) can be mounted on a ground plane (an approximation of the plane fuselage), (2) have very low profile to reduce the air drag and (3) have very wide bandwidth. In this chapter, we present two designs. One of them is based on top loaded monopole antennas and the other design is based on a hybrid TEM Horn – wide current loop. Both designs have very low profile (5.3% and 6.3% of the minimum operating wavelength respectively) as well as very wide bandwidth (more than one octave).

8.1 Very Low Profile UWB Monopole

8.1.1 Introduction

In certain low frequency applications, such as our VHF UWB InSAR system, it is required to have a very low profile antenna operating at VHF frequencies that can be mounted on a plane. In such situations, the antenna height from the plane fuselage has to be as small as possible in order to minimize the air drag. This is also required in some

low frequency UWB military communication applications where it is again desired to have low profile antenna to reduce the overall communication system size and weight.

Several UWB monopole structures have been proposed in the literature, such as [57], [50]. They are planar structures and relatively easy to fabricate. However, their height above the ground plane is relatively high (about $0.18\lambda_0$). Other antennas include the monopole versions of biconical antennas such as [45] but they are still relatively high profile and are even more difficult to fabricate. To reduce their size, it was found that adding inductive shorting pins between the top and bottom creates a parallel resonance at the low frequency end thus lowering the minimum operating frequency of the antenna and consequently reduces the antenna size [5]. However, the structure presented in [58] is not easy to fabricate, relatively heavy for low frequency implementations and its size is still large ($\sim 0.17 \lambda_0$ for the dipole version) which is 38% higher profile than the design presented in this paper.

Other monopole structures have also been presented in the literature such as [59]. These also suffer from relatively high profile (25% higher profile than our design), heavy weight and require special fabrication for body of revolution structure which increases their fabrication cost and required tolerances.

To address these issues we developed a new structure based on the shorted biconical antenna. However, the new structure is fabricated using PCB technology which allows us to have much better control on the feeding structure dimensions and allows for much more precise tuning which allowed us to achieve a significantly smaller height of $0.053 \lambda_0$ compared to the previously mentioned structures. It is also relatively easy and low cost to fabricate. In the following section, we will present the steps we used to reach

the final structure and the principle of operation. Next, we will present a parametric study to show the effect of different antenna dimensions on its performance. Finally, we will present the measurement results and the conclusion.

8.1.2 Antenna Structure and Operation

To design a low profile UWB antenna, we started with the top loaded monopole antenna shown in Figure 8.1 (a). This structure is similar to a short monopolar biconical antenna. However, this form is chosen over the conventional solid or wire biconical since it can be easily fabricated using standard PCB technology and fabrication with good repeatability can be achieved. Also it is very lightweight which is very important for the low frequency applications considered where the antenna size is physically large. However, as shown in Figure 8.2 (a) and (b), due to the very short height of this antenna, the reactive component is very high at low frequencies and thus the antenna has to be relatively tall to have good matching.

One technique to lower the minimum operating frequency is to use inductive shorting pins to the ground which adds a low frequency resonance that nicely merges with the high frequency biconical mode of the antenna as shown in Figure 8.2. Those pins can be integrated into the fabricated feed PCBs as traces with controllable width as shown in Figure 8.1 (b). As will be shown in the next section, the inductance of these inductive traces control the first resonant frequency and can be easily controlled for optimum low frequency matching.

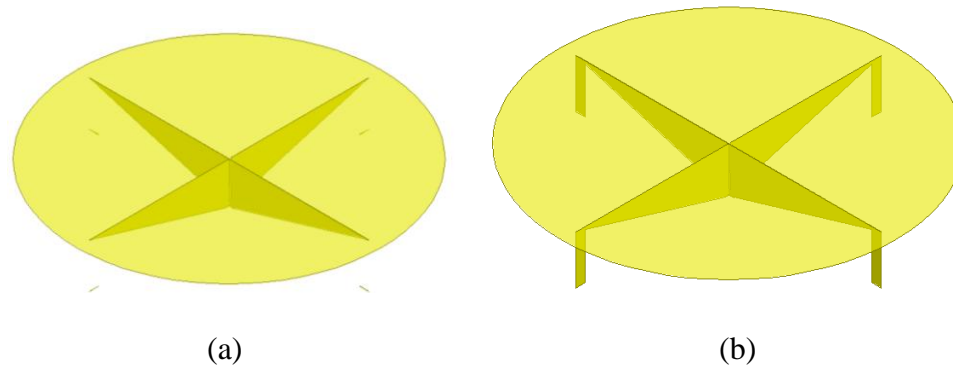


Figure 8.1: (a) Initial PCB compatible monopole and (b) the monopole with the inductive pins. The top circular plate is semi-transparent to show the feed structure. The two antennas are simulated on an infinite ground plane and fed using an SMA coaxial cable at the apex.

The structure can be made even smaller and have better matching by adding a series coupling capacitive slot as shown in Figure 8.3 (a) and (b). This capacitance provides additional tuning parameter to control the input impedance which helps to further reduce the minimum operating frequency and improve the high frequency matching performance.

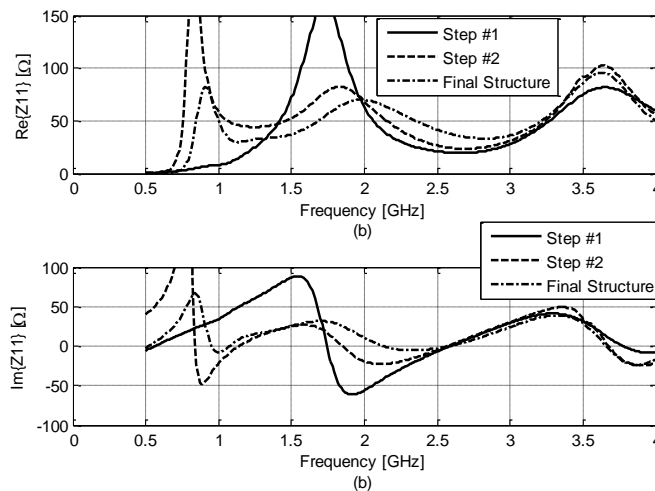


Figure 8.2: The (a) real and (b) imaginary parts of the input impedance of the different structures.

The antenna structure and dimensions are shown in Figure 8.3 (a) and (b). The antenna dimensions are summarized in Table 8.1. The antenna consists of a top circular plate with

an annular slot. The plate is connected to 4 feeding/shorting arms printed on two crossed substrates. The shorting pins are responsible for the low frequency operation of the antenna whereas the annular slot as well as the slots in the feeding arms help in controlling the input impedance to match it to the feed.

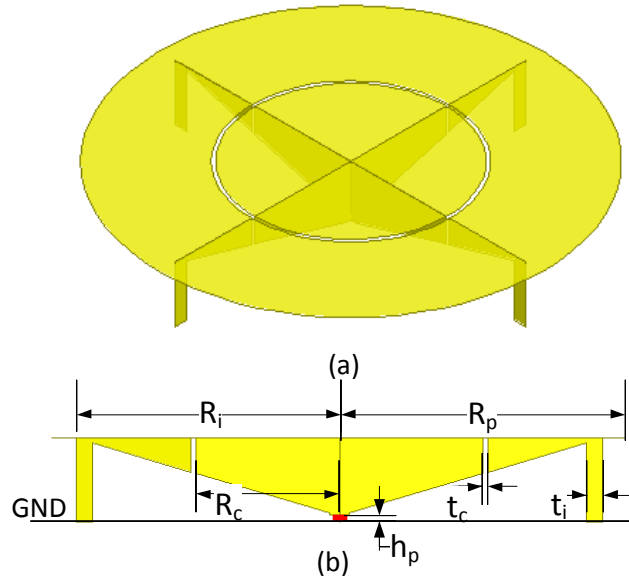


Figure 8.3: Antenna Structure (a) Isometric view and (b) side view with dimensions (the substrate is not shown for clarity).

Table 8.1: Nominal Antenna Dimensions.

R_p	R_i	R_c	
60 mm	55 mm	30 mm	
t_c	t_i	h_p	h
1 mm	3.5 mm	1.5 mm	17.5 mm

The current distribution on one of the antenna fins at different frequencies is shown in Figure 8.4. This figure indicates that at low frequencies, the electric current density is very strong on the inductive traces. This is expected since the low frequency operation of the antenna is attributed to them. As the frequency increases, the currents on these traces become relatively small indicating that they no longer contribute much to the radiation. In

fact, at higher frequencies, the radiation is mainly due to the 4 tapered slot lines near the feed. This is because at high frequencies, the end slot width becomes comparable to the wavelength and each slot line acts as a tapered slot antenna [60].

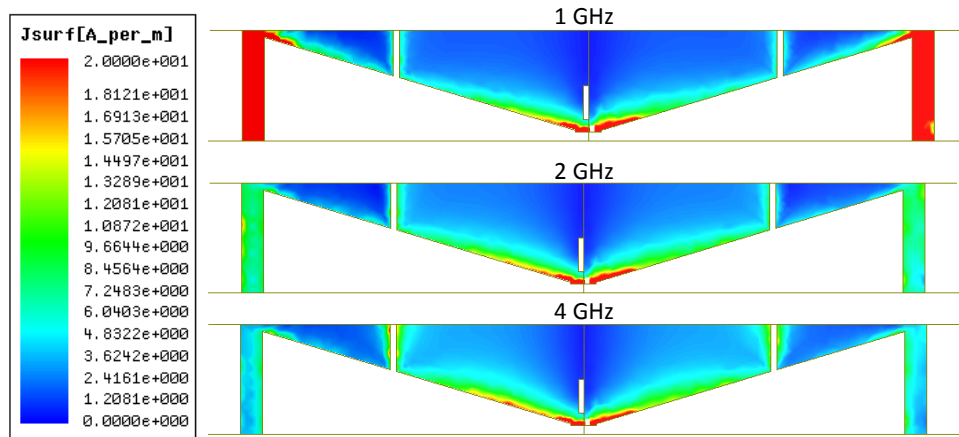


Figure 8.4: Current distribution on the antenna feed at different frequencies.

8.1.3 Parametric Study

The first parameter to consider is the width of the shorting pins, t_i . The width of the shorting pins controls their inductance and thus affects the resonance frequency of the first mode. Increasing the width results in lower inductance and thus increases the frequency of the first resonance as shown in Figure 8.5 (a) and (b). It is also interesting to note the case without the inductive pins, where the antenna starts to operate at almost twice the minimum operating frequency of the inductively loaded monopole. In this case, the monopole height is approximately $0.11\lambda_0$ which is half the height of a biconical antenna. The resemblance in the input impedance at high frequencies shows that the antenna starts to operate as a short biconical antenna after ~ 2 GHz.

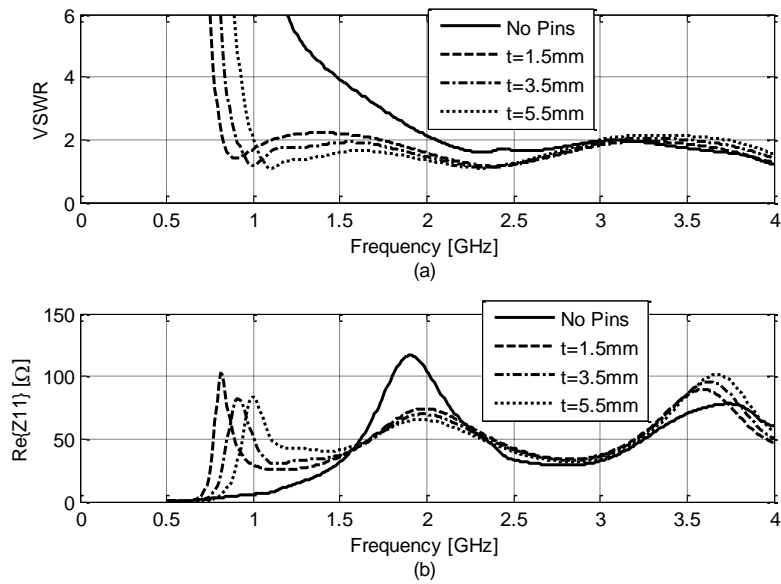


Figure 8.5: The effect of the inductive pins width on the (a) input VSWR and (b) the real part of the input impedance.

The second parameter is the antenna height, h shown in Figure 8.6 (a) and (b). As expected, increasing the antenna height increases the real part of the input impedance at low frequencies since increasing the length of inductive pins enhances the radiation from them. It also decreases the minimum resonance frequency since increasing the length of the inductive traces increases their inductance thus decreasing the first resonant frequency. The high frequency matching is improves as well since increasing h increases the size of the radiating aperture of the 4 tapered slot antennas.

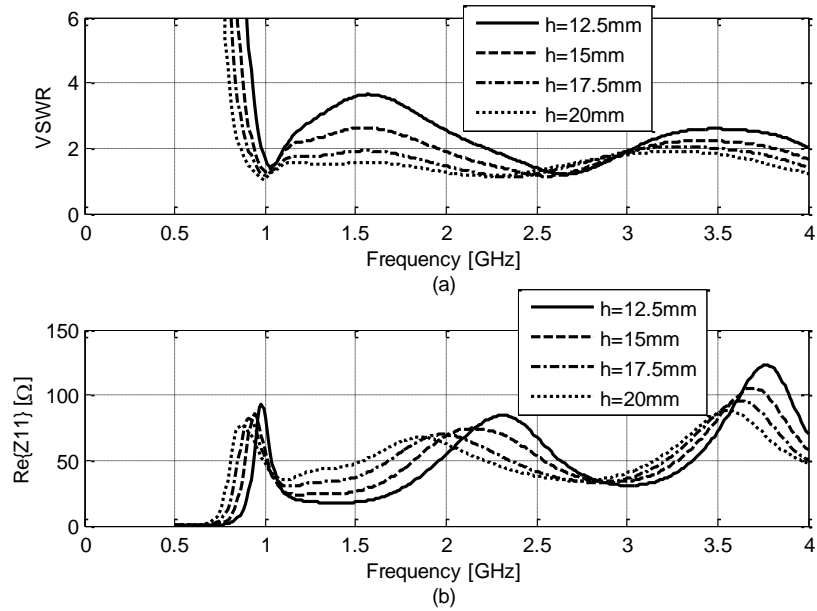


Figure 8.6: The effect of the monopole height on the (a) input VSWR and (b) the real part of the input impedance.

The third parameter that significantly affects the antenna input matching is the feed apex height above the ground plane, h_p . It controls the capacitance near the feed location and also controls the characteristic impedance of the 4 slot lines connected to the feed. Its effect on the input VSWR and input impedance is shown in Figure 8.7 (a) - (c). Decreasing h_p increases the capacitance near the feed point resulting in less inductive input impedance at low frequencies as shown in Figure 8.7 (c) which results in better matching at lower frequencies. However, higher parallel capacitance near the feed point results in lower input impedance at higher frequencies which results in worse matching. Furthermore, very small feed apex height makes the fabrication relatively difficult since the soldering will be too close to the feeding connector. As a trade-off, we used a feed point height of 1.5 mm which still gives good matching and makes the antenna relatively easy to fabricate.

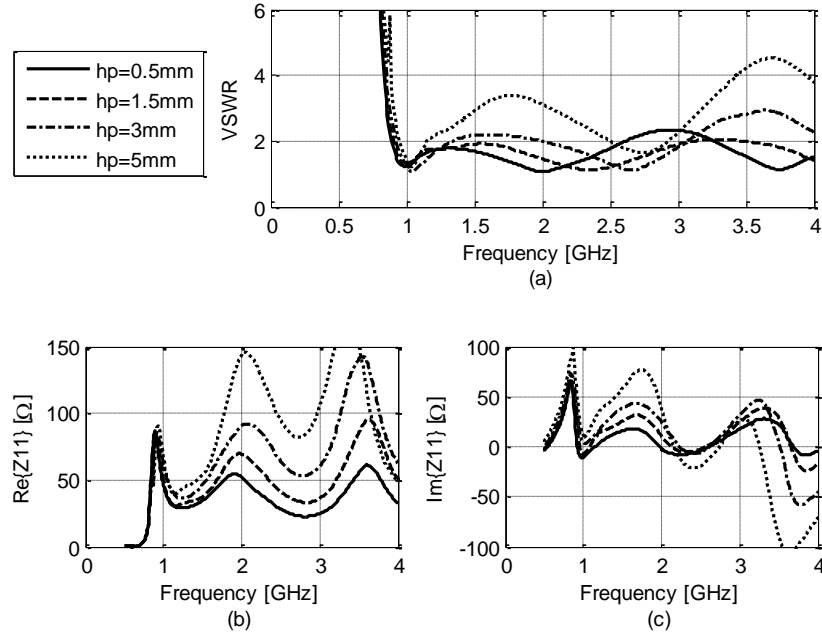


Figure 8.7: Effect of the feed apex height on (a) the input VSWR and (b) the real and (c) the imaginary parts of the input impedance.

Another very important parameter for monopole antennas in general is the dependence of their input impedance on the ground plane size, l_g . The proposed antenna is fabricated on a 30 cm x 30 cm square metallic plate. However, as shown in Figure 8.8, the input impedance is not significantly affected by the ground plane size even for relatively small ground plane size. However, the low frequency pattern is affected by the ground plane size as expected. This is shown in Figure 8.9 (a) where for relatively small ground plane size, the antenna pattern becomes relatively close to a dipole pattern. However, for ground plane sizes larger than 30 cm, the patterns become relatively independent of the ground plane size. At higher frequencies, the ground plane size does not significantly affect the pattern as shown in Figure 8.9 (b).

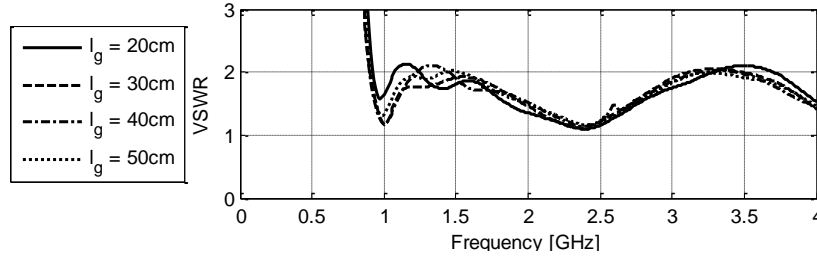


Figure 8.8: Effect of the ground plane size, l_g , on the input matching.

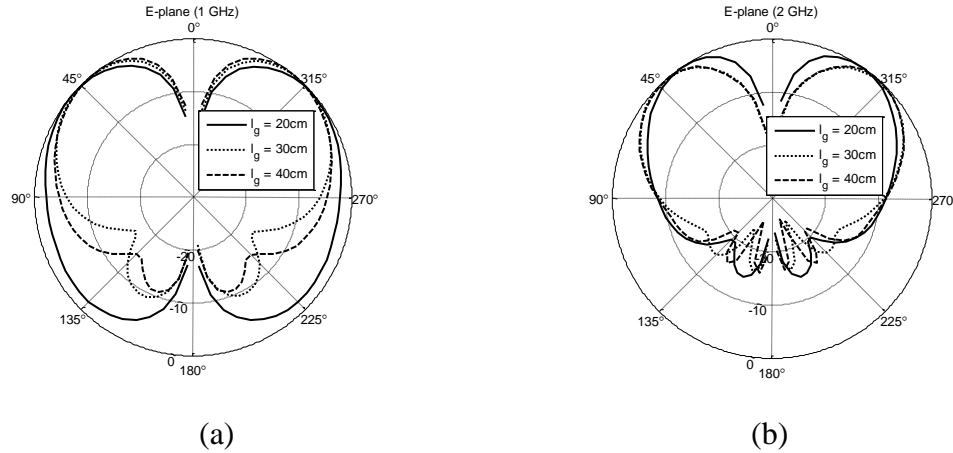
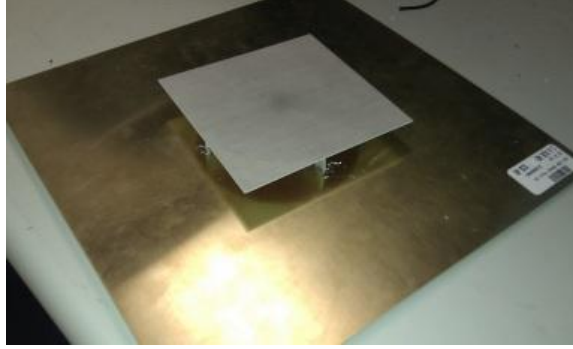


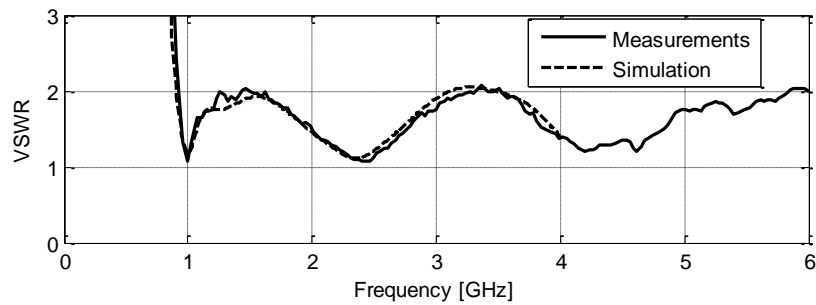
Figure 8.9: Effect of the ground plane size on the E-plane pattern at (a) 1 GHz and (b) 2 GHz.

8.1.4 Measurements Results

The antenna was fabricated on a 30 mil Rogers RO4003 substrate and fed using a standard SMA coaxial cable. The fabricated antenna is shown in Figure 8.10 (a). It was measured using an HP 8753D network analyzer and the simulated and measured VSWR are shown in Figure 8.10 (b) where we can see very good agreement between the simulation and measurements. The antenna has an input VSWR < 2 over the band 0.9 – 6 GHz corresponding to 148% relative bandwidth.



(a)



(b)

Figure 8.10: (a) The fabricated antenna and (b) the measured and simulated input VSWR.

The pattern of the antenna was also measured. The measured E- and H-plane patterns are shown in Figure 8.11 (a) and (b) and compared to the simulations in Figure 8.11 (c) and (d). Again we can see that the measurements and the simulation show very good agreement. The figures also show that the H-plane pattern has relatively small variations up to about 4 GHz. The depth of the E-plane nulls in the measurements is not as deep as the simulation due to our measurement system dynamic range.

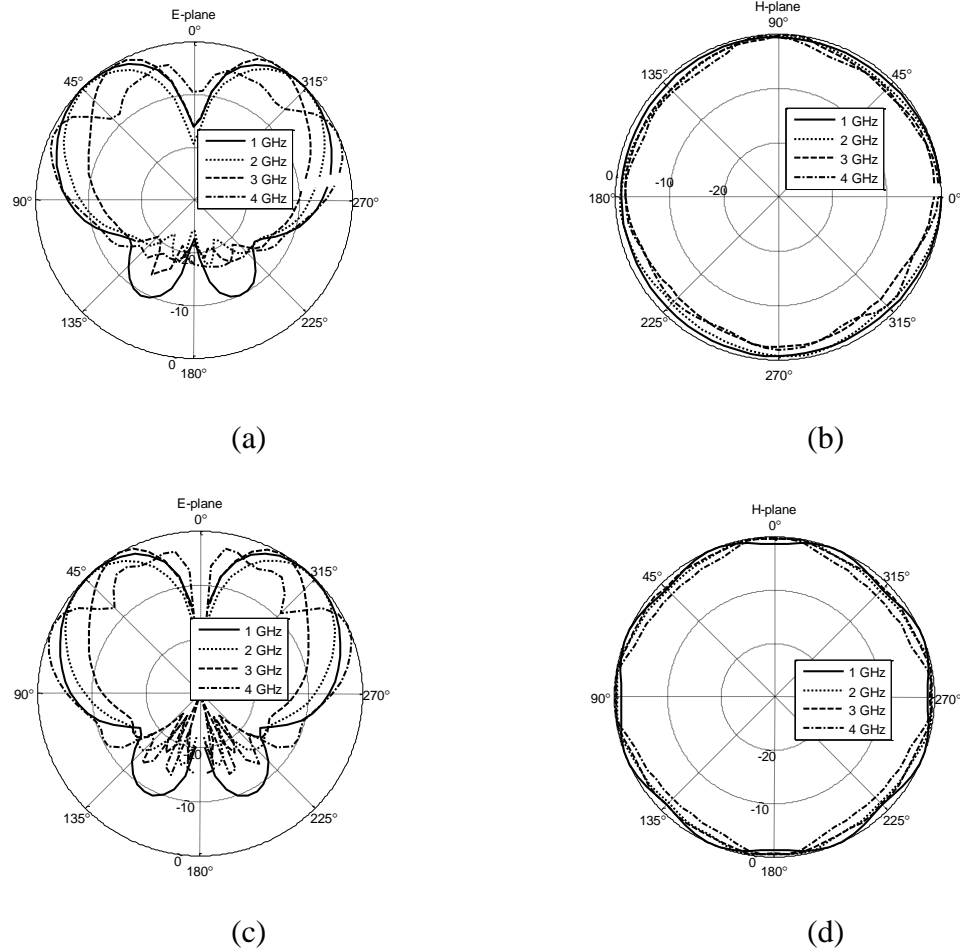


Figure 8.11: Measured (a) E-plane and (b) H-plane and simulated (c) E-plane and (H-plane).

8.2 Very Low Profile Directive Antenna

Low profile monopoles such as the one presented in the previous section are not sufficiently directive which can be an important factor in the radar designs with constrained power budget. Wideband variants of patch antennas are directive and have relatively low profile but their bandwidths are still limited for many of such radars. To address this problem, we developed a new very low profile antenna with a footprint parallel to the plane fuselage of $w \times h = 0.06\lambda_0 \times 0.15 \lambda_0$. The antenna is still directive due to its relatively long length, l , of $0.5\lambda_0$ with directivity above 6dB over the

bandwidth. It has good matching and directive pattern over about an octave of bandwidth. The antenna is also relatively easy to fabricate and its dimensions can be tweaked to achieve the desired directivity. In this section, we first present the antenna structure and theory of operation, followed by a parametric study to show the effect of the different parameters on the antenna performance. Then, the measurement results are presented.

8.2.1 Antenna Structure and Operation

Conventional UWB antennas mounted on a ground plane with direction of maximum radiation normal to the ground plane typically have high profile. They can be generally categorized into two categories: (1) a dipole in front of a ground plane and (2) a traveling wave antenna (e.g. horn antenna). Placing a dipole in front of a ground plane results in directional radiation if it is placed less than a quarter wavelength from the ground plane [61]. However, a dipole cannot be placed too close to the ground plane; otherwise wideband antenna matching becomes very difficult. This results in a relatively high profile designs. On the other hand, traveling wave antennas have to be a significant fraction (and even multiples) of the minimum operating wavelength which also results in high profile design.

For these reasons, we decided to select a different approach to achieve very low profile directive radiation. We chose a very low height half TEM horn as shown in Figure 8.12 (a). This antenna is oriented such that its traveling wave direction is parallel to the ground plane which would result in direction of maximum radiation along the ground plane for conventional TEM horns. However, since the aperture height of this antenna is very small in the E-plane (YZ plane), its pattern is very wide in the E-plane as shown in Figure 8.12 (b) and is relatively narrow in the other plane orthogonal to the ground plane

(XZ plane) since the antenna aperture is relatively long in this direction as shown in Figure 8.12 (b). These types of patterns are actually desirable in airborne SAR applications since it suppresses the Doppler ambiguities and allows wide swath coverage. However, in spite of its desirable radiation characteristics, the antenna suffers from resonant input impedance that makes matching it difficult over a wideband as shown in Figure 8.12 (c).

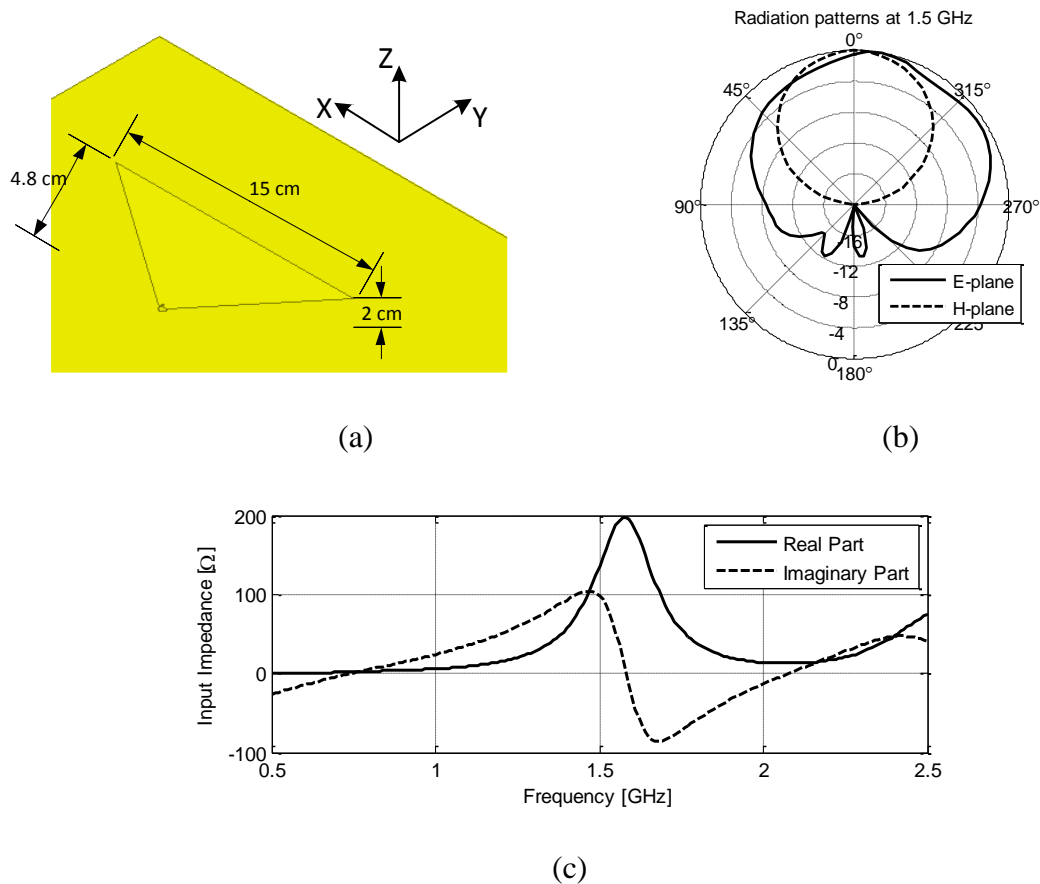


Figure 8.12: (a) Short TEM horn dimensions, (b) its radiation patterns in the E- and H- planes and (c) its input impedance.

To improve the input impedance matching, we used an inductive shorting trace as shown in Figure 8.13 (a). This trace creates a resonance at lower frequencies that can be shifted by controlling the inductance using the trace width, W_s , as shown in Figure 8.13

(c) and (d), where increasing W_s decreases the inductance and thus shifts the lower resonance frequency higher. By bringing the two resonances closer, good matching can be achieved as shown in the figure. The improved radiation is because the inductive trace acts as a loop and contributes to the total radiation from the antenna. We found that good matching is achieved when the width of the shorting trace is equal to that of the TEM horn. Increasing the trace width also reduces the pattern side lobes as shown in Figure 8.13 (b).

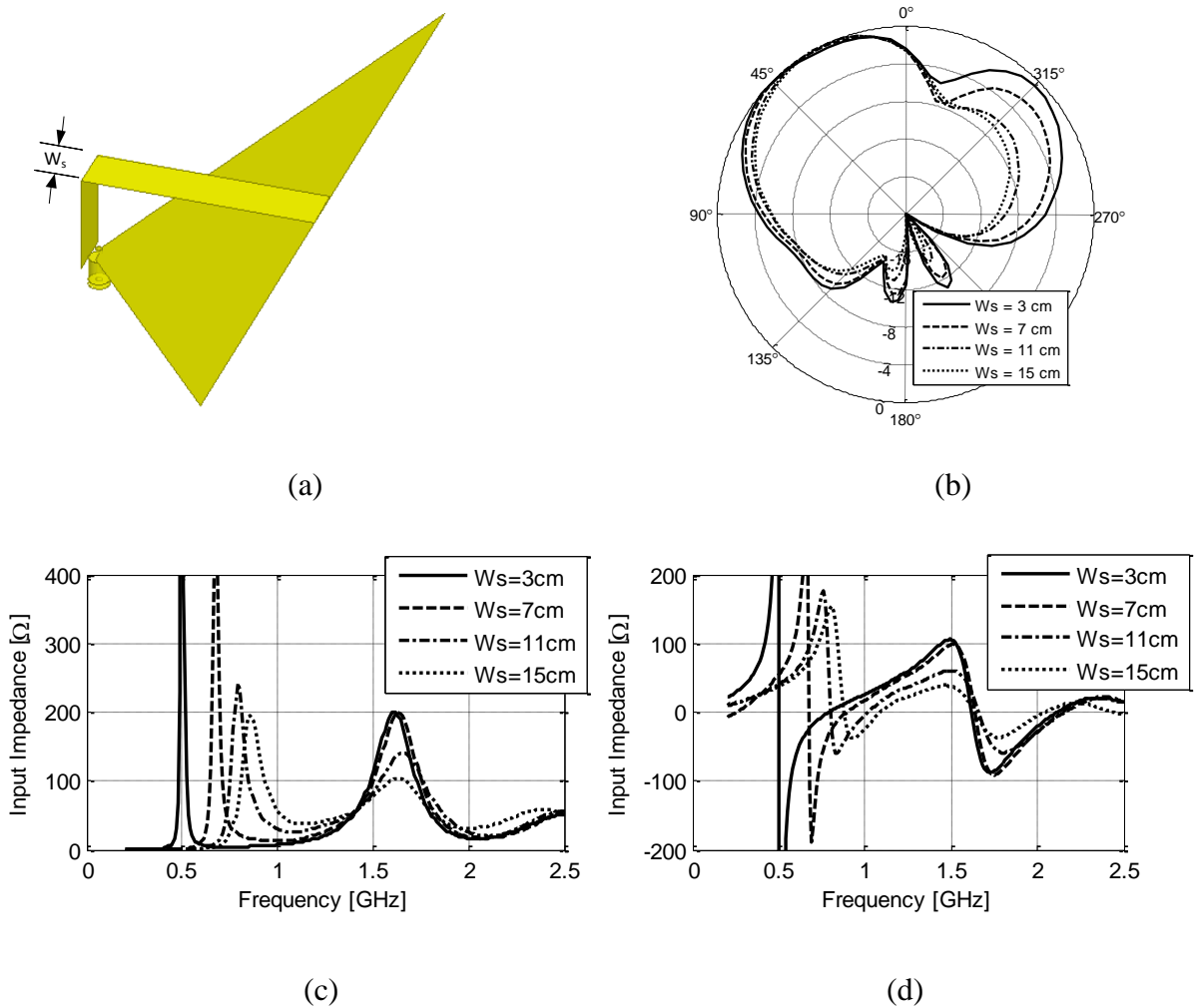


Figure 8.13: (a) Shorted TEM horn structure, (b) effect of the shorting trace width on the E-plane radiation pattern and on the (c) real and (d) imaginary parts of the input impedance.

The final antenna structure and dimensions are shown in Figure 8.14 (a) and (b). It consists of a TEM horn antenna combined with a sheet metallic loop fed from the same point at the TEM horn apex. To simplify fabrication, and verify the antenna operation, the antenna was designed to operate from 1 GHz. However, the antenna can be directly scaled to operate at any other frequency. The antenna dimensions are shown in Table 8.2 and the antenna was placed on a 30cm x 30cm metallic ground plane.

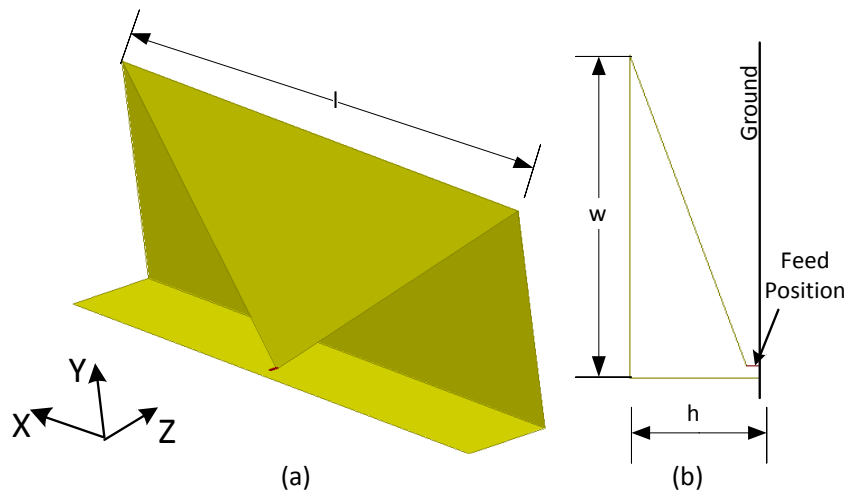


Figure 8.14: Antenna structure and dimensions (a) isometric view (ground not shown for clarity) and (b) side view.

Table 8.2: Nominal Antenna Dimensions.

W	l	h
4.7 cm	15 cm	2 cm

8.2.2 Parametric Study

The first parameter to consider is the antenna length, l . As shown in Figure 8.15 (a), it does not significantly affect the matching, unless the length is very small. It is also

interesting to see that it does not affect the antenna's first resonance frequency as shown in Figure 8.15 (a). This is because the first resonance frequency is due to the overall loop length which is independent on the antenna width. On the other hand, increasing l , results in higher directivity as shown in Figure 8.15 (b) since it decreases the antenna beamwidth in the H-plane. However, increasing W also results in larger phase variations across the aperture at high frequencies. This results in beam splitting at higher frequencies resulting in reduced directivity. To maximize the usable bandwidth, we chose 15 cm as the antenna width which gives directivity better than 6 dB over slightly less than one octave as well as good matching.

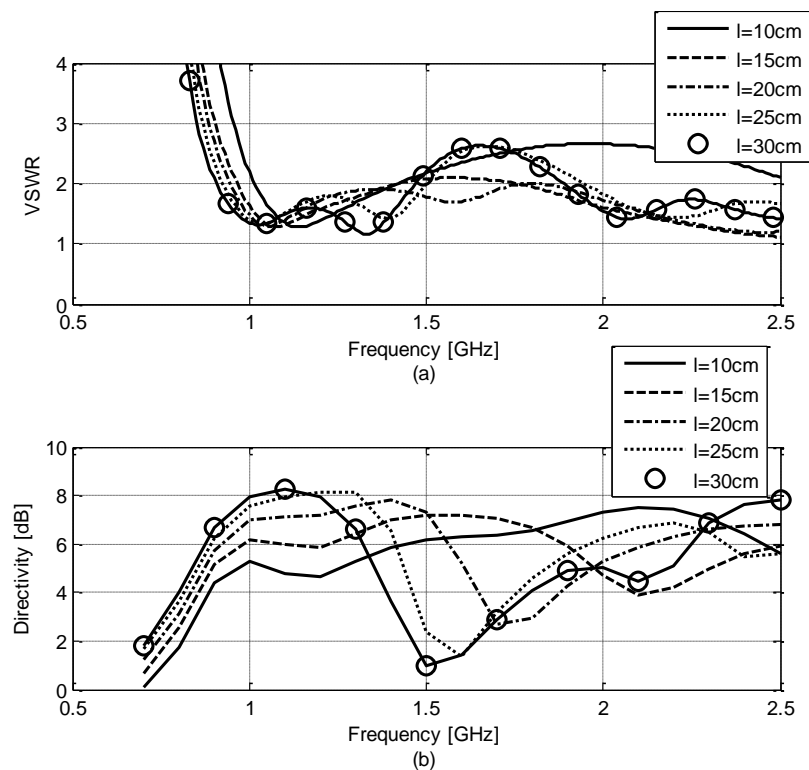


Figure 8.15: The effect of the antenna length, l , on the (a) input VSWR and (b) the boresight directivity.

The second parameter is the antenna width, W . It mainly affects the low frequency matching of the antenna as shown in Figure 8.16 (a). This is because it affects the

inductance of the loop by increasing its length and thus lowers the minimum resonance frequency of the antenna. It has a relatively negligible effect on the antenna pattern and directivity as shown in Figure 8.16 (b) since the values of W considered for our applications are relatively small compared to the operating wavelength (as required by its design constraints).

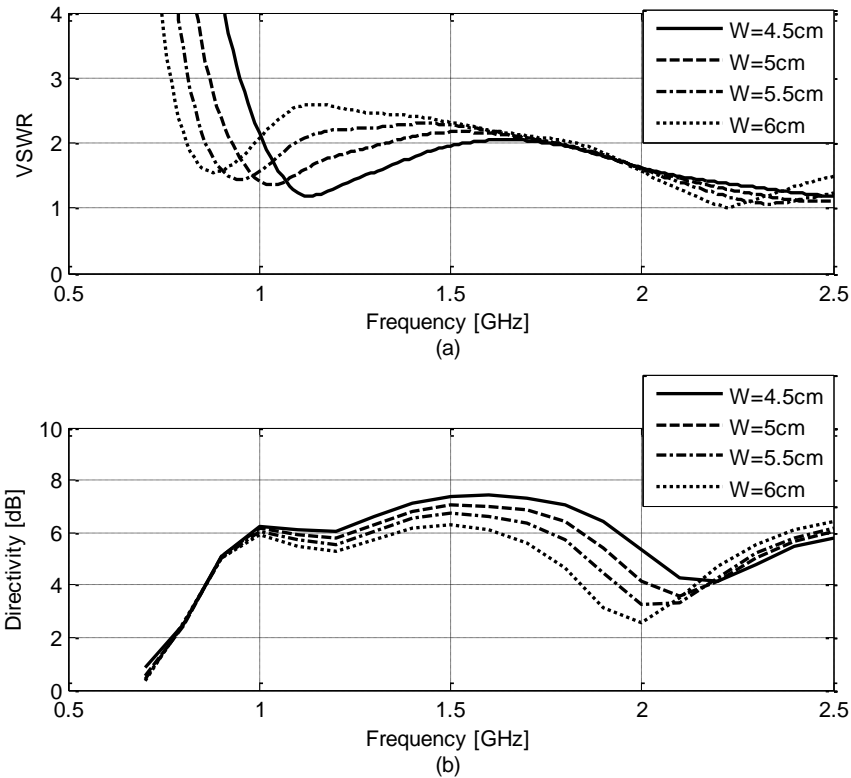


Figure 8.16: Effect of the antenna length on (a) the input VSWR and (b) the real and (c) the imaginary component of the input impedance.

The final antenna parameter is the antenna height, h . Very short antenna heights results in almost total current cancellation of the currents on the Horn antenna and thus the antenna essentially acts as a loop antenna with several resonances and anti-resonances as shown in Figure 8.17 (a) for very small h . As h increases, the antenna operates in its

desired mode of a combined TEM horn and a loop antenna. h does not significantly affect the boresight directivity except at very high frequencies as shown in Figure 8.17 (b).

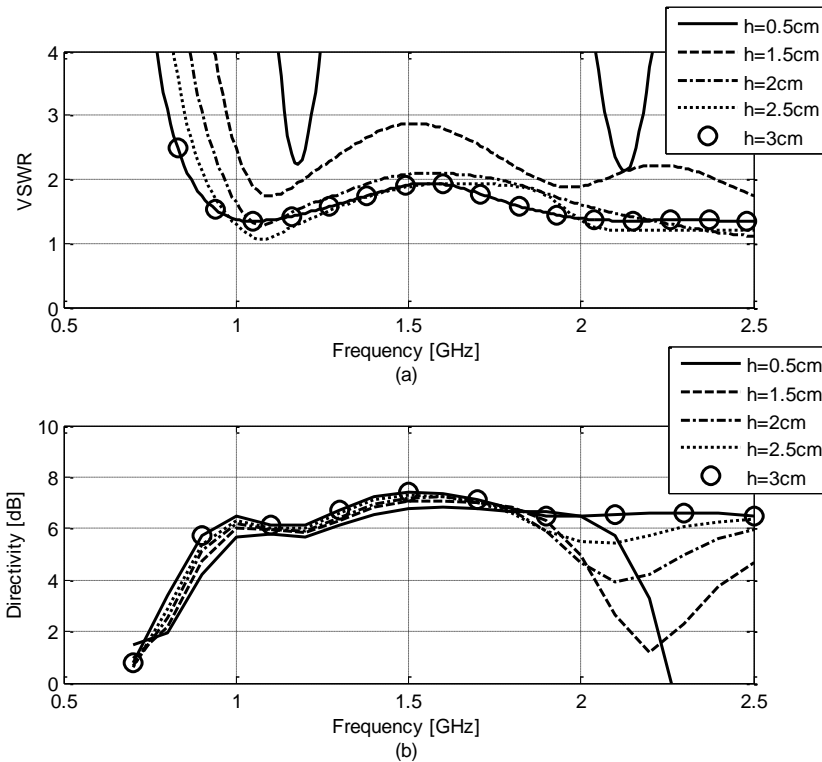
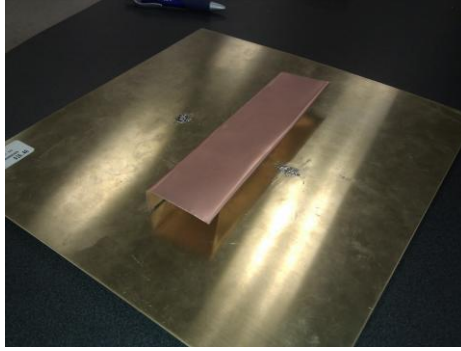


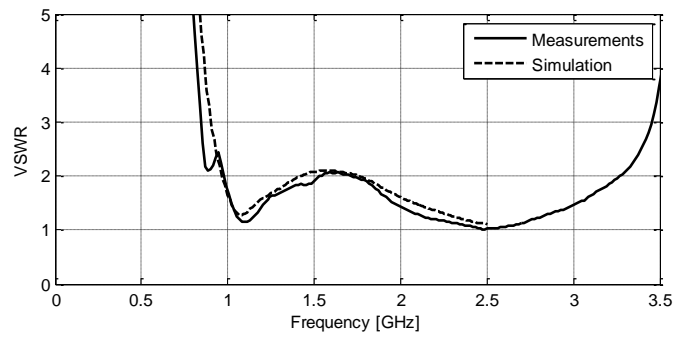
Figure 8.17: Effect of the antenna height on the antenna's (a) input VSWR and (b) real and (c) imaginary components of the input impedance.

8.2.3 Measurement Results

The antenna was fabricated on a 10mil Rogers RO4003C substrate and placed on a 30cm x 30cm metallic ground plane as shown in Figure 8.18 (a). The antenna input impedance was measured and the results are shown in Figure 8.18 (b) where we can see very good agreement between the measurements and the simulation.



(a)



(b)

Figure 8.18: (a) A photo of the fabricated antenna and (b) the measured and the simulated input VSWR.

The antenna co-pol pattern was also measured in the E- and H-planes as shown in Figure 8.19 (a)-(d). From the two figures, we can see very good agreement between the simulated and measured patterns.

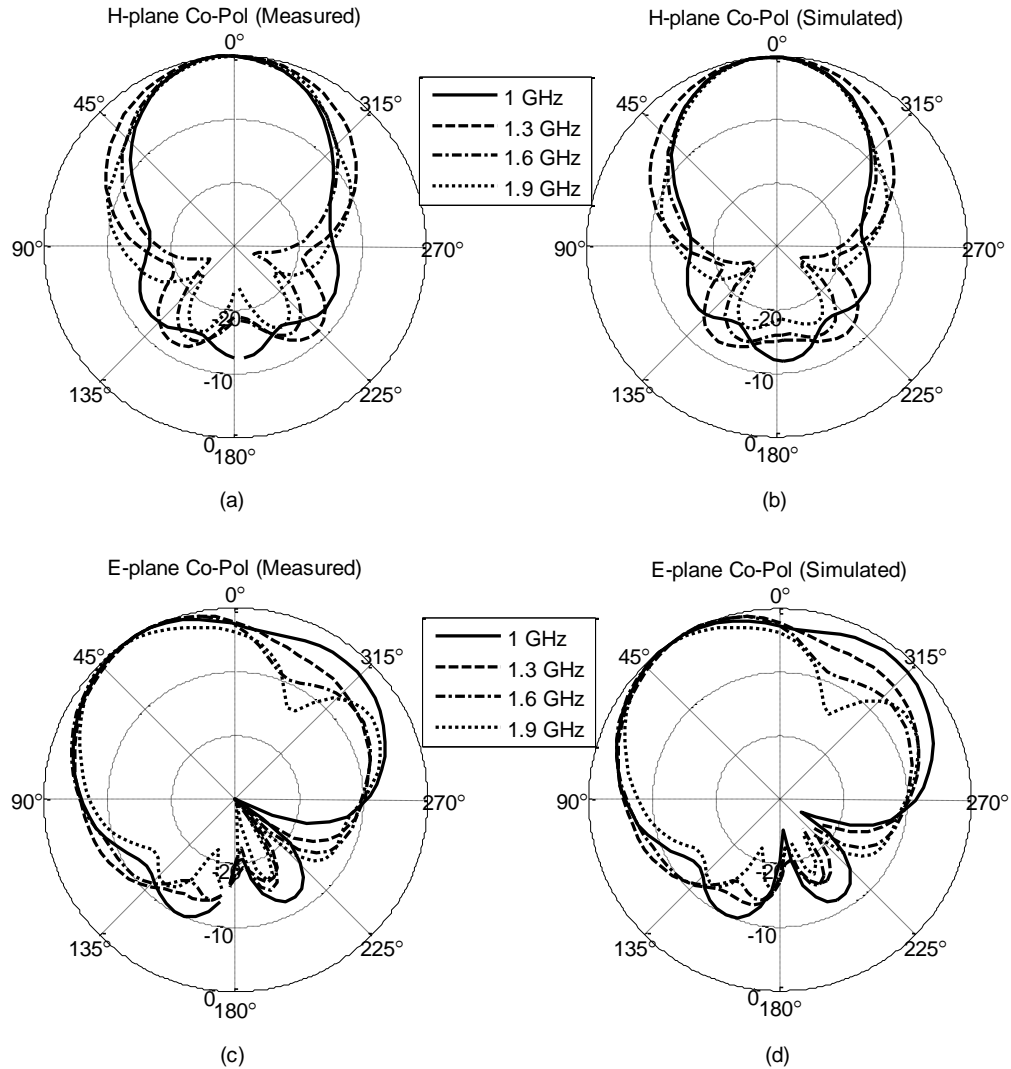


Figure 8.19: (a) Measured and (b) simulated H-plane Co-Pol radiation patterns, (c) measured and (d) simulated E-plane Co-Pol radiation patterns at different frequencies, (e) measured and (f) simulated H-plane Cross-Pol Patterns (normalized to the peak of the co-pol component).

8.2.4 Improving the Cross-Pol Components

As shown in the previous section, the proposed antenna is very compact and has good impedance matching. However, it suffers from relatively high cross-pol component in the H-plane at high frequencies (above around 1.5 GHz). This can be explained by plotting the current distribution on the antenna as shown in Figure 8.20. From the figure, we can see that in the E-plane, the current distribution is symmetric thus the cross-pol

components cancel out in this plane. However, at any point in the H-plane away from the boresight, the cross-pol components do not cancel out due to the path difference between the two currents at the antenna edges. This is usually not a problem for conventional TEM horns since the taper angle is much smaller (l/W is small) and thus the currents are very close to each other resulting in relatively small cross-pol. However, for the proposed design, this ratio is relatively large and thus the cross-pol component is relatively large and increases very rapidly as the observation point moves away from the boresight in the H-plane. There are two solutions to this problem in situations where the cross-pol component has to be small over a very wide bandwidth.

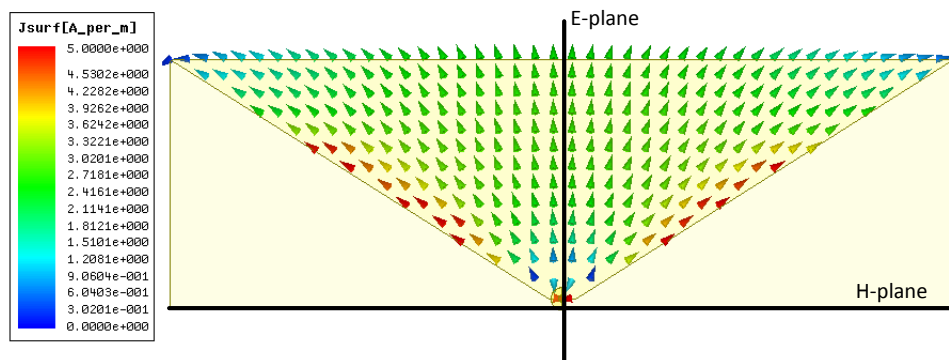


Figure 8.20: Current distribution on the TEM horn portion of the antenna at 2 GHz.

One modification to improve the cross-pol performance of the antenna is shown in Figure 8.21 (a), where two identical antennas are placed back-to-back and fed out of phase. In this case, the pattern has a peak in a direction normal to the ground plane and the cross-pol is nullified in the two principal planes. Also, in this case, since the vertical shorting strip is at the virtual ground, it can be removed thus simplifying the antenna fabrication. Another option is to use the antenna to feed a wide narrow TE aperture as shown in Figure 8.21 (b). The TE aperture suppresses the cross-pol radiation since it is in

deep cutoff for the cross-pol component (very narrow in the cross-pol direction) thus acting as a filter for the cross-pol radiation. The TE aperture has to be made wider than the original TEM aperture so that it is reasonably far from cutoff for the co-pol electric field.

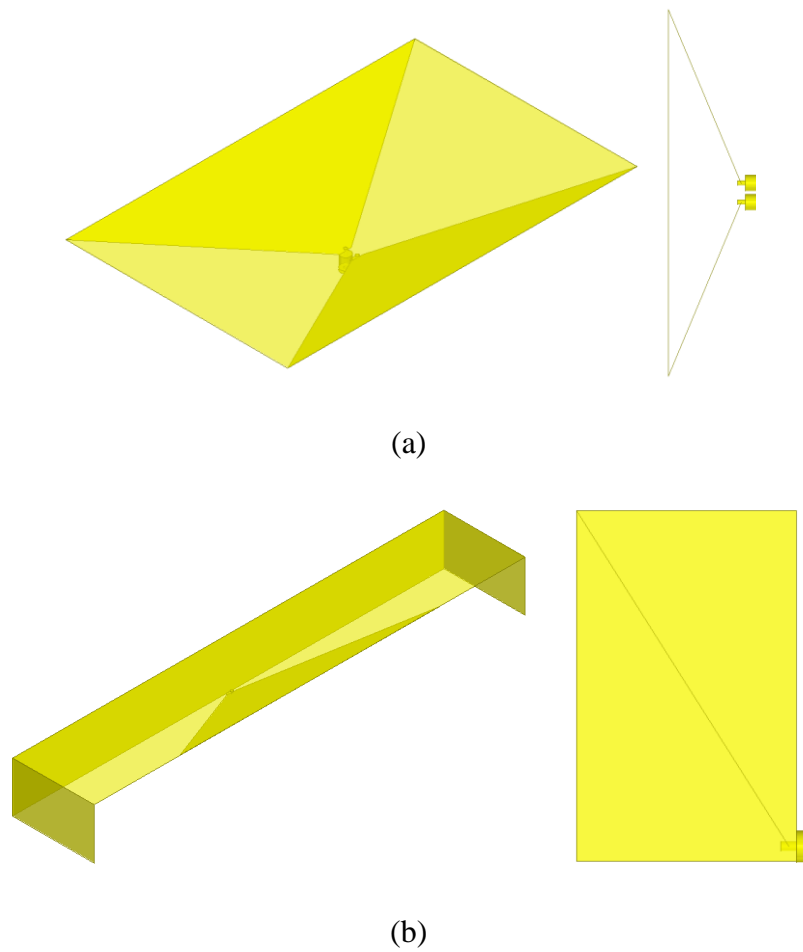


Figure 8.21: Variations on the proposed antenna to improve the H-plane cross-pol performance, (a) back to back and (b) TE aperture.

8.3 Conclusion

In this chapter, we presented two ultra-low profile UWB antennas. The first design is a very low profile UWB monopole antenna. The antenna size is $0.05\lambda_0 \times 0.36\lambda_0 \times 0.36\lambda_0$. The antenna is relatively easy to fabricate using two crossed substrates and a

top substrate. The effects of the different antenna dimensions on the performance are investigated. Of particular importance in monopole designs is the effect of the ground plane. It was found that for this design, the ground plane does not have significant effect on the input impedance matching and mainly affects the radiation patterns at lower frequencies. A prototype antenna was fabricated and measured. The measured results agree very well with the simulations where it is shown that the antenna operates over 0.9-6 GHz with $VSWR < 2$. Also, as well as an omnidirectional pattern over more than two octaves is observed. This antenna can be very useful in many low frequency radars and military communications applications.

The monopole antenna presented have low profile and is relatively compact. However, when placed on a plane fuselage for SAR ground imaging applications, approximately half of the radiated power is wasted away towards the atmosphere which can be a problem in some SAR applications that have constrained power budget. To address this problem, we presented a directive design based on shorted short TEM horn. The proposed antenna height is $0.063\lambda_0$ and has good matching and radiation characteristics over more than an octave. It is based on the principle of an inductively shorted TEM horn. However, unlike the standard TEM horn structures, the proposed structure is designed to enhance the radiation in a direction perpendicular to the TEM horn axis. This limits the maximum pattern bandwidth to about one octave but allows the antenna height along the direction of maximum radiation to be very small. The antenna was fabricated and measured. The measured results agreed well with the simulation results and both showed that the antenna can operate over 1 – 2 GHz with good radiation and matching performance within the fabrication tolerances. The antenna had relatively

high cross-pol component above around 1.5 GHz, and two design modifications were proposed to address this problem.

Chapter 9

Conclusion and Future Work

9.1 Conclusions

In this thesis, we considered the problem of subsurface remote sensing in deserts and arid regions. This problem has several aspects; it requires the study of the surface, subsurface and volumetric scattering phenomena. The use of low frequency to allow penetration through the top layer resulted in some additional system complexity due to antenna size and the required wide relative bandwidth to achieve good spatial resolution.

9.1.1 Scattering Phenomena

The problem of subsurface scattering from arbitrarily two layers rough surfaces is very complex and is still undergoing active research. This makes the inverse problem of estimating the height of each layer using radar data significantly more complex. To overcome this issue, we chose to use the two frequency extremes. At low frequencies (VHF), the scattering from the top surface (sand surface) is negligible since the surface undulations are much smaller than the wavelength at these frequencies. At high frequencies (Ka), the surface and volumetric scattering from the top layer is dominant and due to the high attenuation, the scattering from the bottom surface is negligible. This lead to the simplified scattering model used for the forward and the inverse problem.

9.1.2 Subsurface Processing

For the Ka InSAR, the processing is relatively straightforward. However, for the VHF InSAR, it was shown that conventional processing cannot be directly used due to the refraction and propagation through the top layer. This lead to two main problems: image distortion and inaccurate subsurface height estimation. Image distortion consisted of SAR image azimuth defocusing as well as geometric distortion due to the top surface undulations. It was also shown that range defocusing is relatively negligible due to the relatively low loss of the sand at VHF frequencies.

9.1.3 Inversion Algorithm

If the top surface height is known, the subsurface height can be uniquely identified using the VHF InSAR data. Thus we developed a new inversion algorithm that utilizes the top surface topography map obtained from the Ka InSAR and the VHF InSAR data to obtain the subsurface height. The inversion algorithm is physics based and iteratively solves the nonlinear equations describing the propagation through the top layer. It was shown to work in several top and bottom layer scenarios. The sensitivity of the algorithm to systematic, measurement and environmental errors were also analyzed. Of which, it is worth noting that the height error due to small variations in the sand dielectric constant is relatively small which means that the algorithm can still provide good results for slightly inhomogeneous layers. The algorithm was verified using 2D and 3D simulations as well as scaled model measurements in the lab.

9.1.4 Image Correction Algorithm

Several image distortion effects were observed in the obtained subsurface InSAR images. As mentioned, they include SAR image defocusing as well as geometric distortion. In order to correct for these effects, both the top surface topography *and* the bottom surface topography have to be known. We noticed that the SAR image does not suffer significant defocusing when the integration angle is small (low resolution) and the defocusing gets progressively more pronounced as the integration angle increases (higher resolution). Thus, we considered an iterative approach, initially focusing using small integration angle thus producing two accurate albeit low resolution SAR images. The two images are then used to obtain the subsurface height using the developed inversion algorithm. The two raw images are then refocused on the correct subsurface height. The process is repeated until the largest integration angle is used. The refocusing process can be extremely time consuming due to the large number of nonlinear equations required to describe the propagation through the top layer. Thus, we developed a fast subsurface SAR simulator and processor based on 3D interpolation. Other issues such as the estimation of the caustic surfaces and their effect on the image were also discussed. The algorithm was verified using 3D simulations of realistic sand dunes and using scaled model measurements in the lab.

9.1.5 Compact UWB Antennas

One of the major practical issues that appeared during the subsurface InSAR development is the design of compact wideband antennas for both the VHF InSAR and for the ground penetrating radar used to obtain the ground control points required for the phase unwrapping. Due to the low operating frequency and consequently the large

operating wavelength, the antenna size becomes relatively large which causes practical limitations for plane mounting as well as in GPR vehicle mounting. This is a very common in many other applications as well such as see through wall radars where the operating frequency has to be low to allow penetration through lossy concrete walls. It also exists in many UWB and MIMO communication applications where compact antennas are also desired. For these reasons, we chose to address this problem in detail and developed a number of UWB antennas for InSAR and GPR applications. The developed antennas can also be used in the mentioned see through wall radar and communication applications.

9.1.6 Linearly Polarized UWB Antennas

We developed a number of linearly polarized antennas based on the coupled sectorial loops antenna (CSLA) principle. First, we showed that using the fact that the magnetic field is circulating around the antenna; we could reduce the antenna maximum dimension by 50%. Next, we noticed that the antenna pattern became directional at higher frequencies especially when combining the CSLA with a tapered slot antenna. Using this frequency dependent directivity, we combined the CSLA with a corner reflector. The resulting antenna showed very good matching and radiation pattern over a bandwidth of more than two octaves as well as very good time domain characteristics. Compared to a ridged horn antenna, the new structure provides comparable gain while being almost 1/8th the size.

The previous design requires the presence of a ground plane which makes it unsuitable in some radar and communication applications. Thus, we developed another directive UWB antenna based on open ended rectangular waveguide antennas

(OERWGA). Conventional OERWGAs are narrow band due to the resonant feeds typically used. They are also typically long and bulky since the waveguide length is required to suppress the higher order modes excited by the feed. To overcome these limitations, we used a bowtie feed which can excite an aperture field distribution very similar to that of the fundamental mode of the rectangular waveguide using very short waveguide section and over an ultrawide band. The antenna had good matching and radiation pattern over a relative bandwidth of 3.3:1 as well as good time domain characteristics. It had 1.5dB less gain than a ridged horn antenna while being less than $1/8^{\text{th}}$ the size and $1/4^{\text{th}}$ the height.

9.1.7 High Isolation Antenna Pair

In some applications such as GPR, see through wall radar as well as MIMO communications, two or more antennas are used. In these situations, it is desired to have the two antennas electrically close to reduce the overall system size and weight. However, placing two antennas very close to each other results in strong mutual coupling between them. This causes increased quantization noise in radar applications. Also, in communication applications, this coupling increases the correlation between the received signals at the two antennas which reduces the effective number of channels (and consequently the maximum data throughput). To address this problem, we developed a transmit/receive antenna pair with directive pattern and isolation better than 20 dB over an octave of bandwidth. The high isolation is due to the use of an isolating structure consisting of a parallel plate waveguide and a rectangular waveguide.

9.1.8 Dual Polarized Antennas

In some radar applications, additional polarization provides extra information that can be used in target recognition and/or clutter reduction. In communication applications, it can increase the channel capacity and/or improve the received signal to noise ratio due to polarization diversity. Thus, we developed a number of dual polarized antennas based on the coupled sectorial loops. Two designs are directional for radar and communication applications. An additional dual polarized diversity antenna was designed for communications applications.

9.1.9 Very Low-Profile Antennas

For airborne applications, the antenna's profile from the plane fuselage becomes an important issue. In some applications, the antenna can be flushed into the plane fuselage and in such situations some of the presented antennas can be used. However, in other applications, the antenna has to be mounted on the plane fuselage and the profile of the antenna is desired to be as low as possible. For these situations, we developed two very low profile antennas, one of them is based on the inductively loaded biconical antenna. This antenna is omni-directional and has a very low profile of 0.053 of the minimum operating wavelength. However, about half of the power is wasted into the atmosphere when it is side mounted on an airplane which can be important in some power budget limited SAR designs. The other low profile antenna is directive and thus does not suffer this problem. It has slightly higher profile at 0.064 of the minimum operating frequency and a narrow beam in the H-plane which allows relatively wide swath coverage with reduced Doppler ambiguities. The original antenna has relatively

high cross-pol at higher frequencies and thus two different variations on the original design are presented to address this issue.

9.2 Future Work

9.2.1 Scattering from Targets under a Rough Surface

In this thesis, the main goal was the estimation of the topography of relatively deep bedrock (tens of meters). In some applications, such as mine detection, it is desired to detect relatively shallow targets with higher ground resolution. In such situations, the frequency used will be higher (UHF range) to allow for wider bandwidth and thus higher resolution. In such situations, the surface roughness might become significant and the interaction between the subsurface targets and the top interface becomes important. The InSAR correction algorithm can also be used to accurately register the correct location of these targets.

9.2.2 Scattering from Large Dunes

In the analysis performed in this thesis, the scattering from the top surface is neglected. This is true for most parts of the map except for the dune peak curves where the surface slope changes relatively fast. The method suggested in this thesis is to detect these parts of the map using the Ka-InSAR map and remove it from the VHF-InSAR map. However, depending on the peak direction and the radar incidence angle, the actual scattering from it might not be very strong. Using high frequency techniques with the top surface map, the locations of the high scattering points can be estimated much more accurately and maybe even subtracted from the radar signal.

9.2.3 Scattering and Propagation in Dense Random Media

The current theories for wave propagation in random media are based on either the wave approach which is very computationally intensive and requires certain approximations to make it computationally feasible. Some of these approximations are not valid for dense random media such as sand. The other approach is based on radiative transfer theory, which is much less computationally intensive. However, it requires the knowledge of the phase and extinction matrices for the medium which are not straightforward to obtain. This problem can be approached using a hybrid numerical and radiative transfer model where a packing algorithm can be used to calculate the pair distribution function and a numerical technique is used to compute the effective permittivity of the dense medium using Monte-Carlo simulations as well as phase and extinction matrices which are then employed in the radiative transfer formulation. Also, the interaction between volume and surface scattering for natural surfaces should be analyzed.

Bibliography

- [1] Denham, L.R., "Seismic interpretation," Proceedings of the IEEE , vol.72, no.10, pp. 1255- 1265, Oct. 1984.
- [2] C. S Bristow, S. D Bailey and N Lancaster, "The sedimentary structure of linear sand dunes", Nature, pp. 56-59, July 2000.
- [3] A. P. Annan, "GPR—History, trends, and future developments," Subsurface Sens. Technol. Appl., vol. 3, no. 4, pp. 253–270, Oct. 2002.
- [4] D. L. Moffatt and R. J. Puskar, "A subsurface electromagnetic pulse radar," Geophysics, vol. 41, pp. 506-518, June 1976.
- [5] H. Brunzell, "Detection of shallowly buried objects using impulse radar," IEEE Trans. Geosci. Remote Sensing, vol. 37, pp. 875–886, May 1999.
- [6] H. Hellsten, L. M. H. Ulander, A. Gustavsson and B. Larsson, "Development of VHF CARABAS II SAR," in Proc. Radar Sensor Technology, SPIE vol. 2747, Orlando, FL, April 8-9, 1996, pp. 48-60.
- [7] Dehmollaian, M.; Sarabandi, K.; , "Refocusing Through Building Walls Using Synthetic Aperture Radar," Geoscience and Remote Sensing, IEEE Transactions on , vol.46, no.6, pp.1589-1599, June 2008.
- [8] M. Ghavami, LB Michael, and R. Kohno.
- [9] http://en.wikipedia.org/wiki/Ground-penetrating_radar.
- [10] Elsherbini, A.; Sarabandi, K.; , "Topography of sand covered bedrock using two-frequency airborne interferometric SAR measurements," Geoscience and Remote Sensing Symposium,2009 IEEE International, IGARSS 2009 , vol.2, no., pp.II-250-II-253, 12-17 July 20.
- [11] Elsherbini, A.; Sarabandi, K.; , "Mapping of Sand Layer Thickness in Deserts Using SAR Interferometry," Geoscience and Remote Sensing, IEEE Transactions on , vol.48, no.9, pp.3550-3559, Sept. 2010.
- [12] http://www.msss.com/mars_images/moc/8_10_99_releases/moc2_170/.
- [13] http://science.nasa.gov/headlines/y2002/06dec_dunes.htm.
- [14] Richards, M.A.; , "A Beginner's Guide to Interferometric SAR Concepts and Signal Processing [AESS Tutorial IV]," Aerospace and Electronic Systems Magazine, IEEE , vol.22, no.9, pp.5-29, Sept. 2007.
- [15] C. Prati and F. Rocca, "Limits to the resolution of elevation maps from stereo SAR images," Int. J. Remote Sensing 11, 2215-2235 (1990).
- [16] Chevrel, M, Curtis, M and Weill, G "The SPOT satellite remote sensing mission" Photogrammetric Eng. Remote Sensing Vol. 47, No 8 (1981) pp 1163-1171.
- [17] Flood, M., 2001, Laser altimetry: from science to commercial LIDAR mapping.

- Photogrammetric Engineering & Remote Sensing, 67(11), 1209-1217.
- [18] Chu, L. J.; , "Physical Limitations of Omni-Directional Antennas," Journal of Applied Physics , vol.19, no.12, pp.1163-1175, Dec 1948.
- [19] Geyi, W.; , "Physical limitations of antenna," Antennas and Propagation, IEEE Transactions on , vol.51, no.8, pp. 2116- 2123, Aug. 2003.
- [20] Dehmollaian, M.; Sarabandi, K.; , "Analytical, numerical, and experimental methods for through-the-wall radar imaging," Acoustics, Speech and Signal Processing, 2008. ICASSP 2008. IEEE International Conference on , vol., no., pp.5181-5184, March 31 2008-A.
- [21] Mahfouz, M.R.; Cemin Zhang; Merkl, B.C.; Kuhn, M.J.; Fathy, A.E.; , "Investigation of High-Accuracy Indoor 3-D Positioning Using UWB Technology," Microwave Theory and Techniques, IEEE Transactions on , vol.56, no.6, pp.1316-1330, June 2008.
- [22] Elsherbini, A.; Cemin Zhang; Fathy, A.E.; Mahfouz, M.; , "Notch bandwidth and filter order trade-offs in band-notched monopole antennas for UWB applications," Antennas and Propagation Society International Symposium, 2008. AP-S 2008. IEEE , vol., no., pp.
- [23] Rosen, P.A.; Hensley, S.; Joughin, I.R.; Li, F.K.; Madsen, S.N.; Rodriguez, E.; Goldstein, R.M.; , "Synthetic aperture radar interferometry," Proceedings of the IEEE , vol.88, no.3, pp.333-382, Mar 2000.
- [24] DC Ghiglia and MD Pritt Two-Dimensional Phase Unwrapping: Theory, Algorithms and Software, Wiley, Chichester, New York (1998).
- [25] Zebker, H. A., R. M. Goldstein (1986), Topographic mapping from interferometric synthetic aperture radar observations, J. Geophys. Res., 91, 4993-4999.
- [26] A. Tabatabaenejad and M. Moghaddam, "Bistatic scattering from three-dimensional layered rough surfaces", Geoscience and Remote Sensing, IEEE Transactions on , vol.44, no.8, pp.2102-2114, Aug. 2006.
- [27] A. Nashashibi and K. Sarabandi, "Volume scattering from a layer of sand at Ka-Band: Measurements and simulations," Antennas and Propagation Society International Symposium, 2009. APSURSI '09. IEEE, pp.1-4, 1-5 June 2009.
- [28] P. Paillou, S. Lopez, Y. Lasne, A. Rosenqvist and T. Farr, "Mapping subsurface geology in Arid Africa using L-band SAR," Geoscience and Remote Sensing Symposium, 2007. IGARSS 2007. IEEE International , pp.2685-2688, 23-28 July 2007.
- [29] J. F. McCauley, G. G. Schaber, C. S. Breed, M. J. Grolier, C. V. Haynes, B. Issawi, C. Elachi and R. Blom., "Subsurface valleys and geoarchaeology of the eastern Sahara revealed by Shuttle Radar," Science, vol. 218, pp. 1004-1020, 1982.
- [30] Ph. Paillou, A. Rosenqvist and T. Farr, "A JERS-1 radar mosaic for subsurface geology mapping in East Sahara," Proc. IGARSS'03, Toulouse, France, July 2003.
- [31] K. K. Williams, R. Greeley, "Radar attenuation by sand: laboratory measurements of radar transmission," Geoscience and Remote Sensing, IEEE Transactions on , vol.39, no.11, pp.2521-2526, Nov 2001.
- [32] A. K. Fung, Z. Li and K. S. Chen, "Backscattering from a randomly rough dielectric

- surface”, IEEE Transactions on Geoscience and Remote Sensing, vol.30, no.2, pp.356-369, Mar 1992.
- [33] P. Beckman and A. Spizzichino, “The scattering of electromagnetic waves from rough surfaces”, Oxford: Pergamon, 1963.
- [34] L.M.H. Ulander et al, “Development of the ultra-wideband LORA SAR operating in the VHF/UHF-band,” in Proc. IGARSS’03, Toulouse, France, July 21-25, 2003, pp. 4268-4270.
- [35] M.E. Davis, “Technical challenges in ultra-wideband radar development for target detection and terrain mapping,” in Proc. 1999 IEEE Radar Conference, Waltham, MA, April 20-22, 1999, pp. 1-6.
- [36] K. Sarabandi (PI), "Topography of Sand Covered Bedrock Using a Two-Frequency Interferometric SAR Measurements", Technical Report, University of Michigan.
- [37] L. M. Ulander, H. Hellsten and G. Stenstrom, “Synthetic-aperture radar processing using fast factorized back-projection”, IEEE Transactions on Aerospace and Electronic Systems, vol.39, no.3, pp. 760-776, July 2003.
- [38] Jong-Sen Lee, K. W. Hoppel, S. A. Mango and A. R. Miller, “Intensity and phase statistics of multilook polarimetric and interferometric SAR imagery”, IEEE Transactions on Geoscience and Remote Sensing, vol.32, no.5, pp.1017-1028, Sep 1994.
- [39] G. FRANCESCHETTI AND R. LANARI, Synthetic Aperture Radar Processing, CRC Press, New York, 1999.
- [40] Xuan Yu, Feng Li, Jingyi Yu. Image-space Caustics and Curvatures. In Proceedings of 15th Pacific Conference on Computer Graphics and Applications, pp. 181-188, 2007.
- [41] M. A. Shah, J. Konttinen, and S. Pattanaik. Caustics mapping: An image-space technique for real-time caustics. IEEE Transactions on Visualization and Computer Graphics, 13(2):272–280, 2007.
- [42] A.J. Rosakis and A.T. Zehnder, On the method of caustics: an exact analysis based on geometrical optics, Journal of Elasticity 4 (1985), pp. 347–367..
- [43] M. Di Benedetto, T. Kaiser, D. Porcino, A. Molisch, and I. Opperman, UWB Communication Systems A Comprehensive Overview. Hindawi Publishing, May, 2006.
- [44] H. Schantz, The art and science of ultrawideband antennas, Artech House, Boston, 2005.
- [45] C. A. Balanis, Antenna Theory, 2nd Ed., John Wiley & Sons, Inc., New York, 1982, pp. 214-217.
- [46] Xue Ni Low; Zhi Ning Chen; See, T.S.P.; , "A UWB Dipole Antenna With Enhanced Impedance and Gain Performance," Antennas and Propagation, IEEE Transactions on , vol.57, no.10, pp.2959-2966, Oct. 2009.
- [47] E. Gazit, “Improved design of the Vivaldi antenna,” Proc.
- [48] Adel Elsherbini et al., "UWB antipodal vivaldi antennas with protruded dielectric rods for higher gain, symmetric patterns and minimal phase center variations," 2007 IEEE Antennas and Propagation International Symposium, pp. 1973-1976, June 2007.

- [49] Bruns, C.; Leuchtman, P.; Vahldieck, R., "Analysis and Simulation of a 1-18-GHz broadband double-ridged horn antenna," *Electromagnetic Compatibility, IEEE Transactions on* , vol.45, no.1, pp. 55-60, Feb 2003.
- [50] Behdad, N.; Sarabandi, K.; , "A compact antenna for ultrawide-band applications," *Antennas and Propagation, IEEE Transactions on* , vol.53, no.7, pp. 2185- 2192, July 2005.
- [51] R. E. Collin, *Field Theory of Guided Waves*, 2nd ed. IEEE, New York, 1991.
- [52] Blanch, S.; Romeu, J.; Corbella, I.; , "Exact representation of antenna system diversity performance from input parameter description," *Electronics Letters* , vol.39, no.9, pp. 705- 707, 1 May 2003.
- [53] Eide, E.S., "Ultra-wideband transmit/receive antenna pair for ground penetrating radar," *Microwaves, Antennas and Propagation, IEE Proceedings -* , vol.147, no.3, pp.231-235, Jun 2000.
- [54] Mak, A.C.K.; Rowell, C.R.; Murch, R.D., "Isolation Enhancement Between Two Closely Packed Antennas," *Antennas and Propagation, IEEE Transactions on* , vol.56, no.11, pp.3411-3419, Nov. 2008.
- [55] Young Jun Song; Sarabandi, K.; , "Suppression of the mutual coupling between two adjacent miniaturized antennas utilizing printed resonant circuits," *Antennas and Propagation Society International Symposium, 2009. APSURSI '09. IEEE* , vol., no., pp.1-4, 1-.
- [56] Adamiuk, G.; Beer, S.; Wiesbeck, W.; Zwick, T., "Dual-Orthogonal Polarized Antenna for UWB-IR Technology," *Antennas and Wireless Propagation Letters, IEEE*, vol. 8, pp. 981-984, 2009.
- [57] Jianxin Liang; Chiau, C.C.; Xiaodong Chen; Parini, C.G., "Study of a printed circular disc monopole antenna for UWB systems," *Antennas and Propagation, IEEE Transactions on* , vol.53, no.11, pp. 3500- 3504, Nov. 2005.
- [58] Amert, A.K.; Whites, K.W., "Miniaturization of the Biconical Antenna for Ultrawideband Applications," *Antennas and Propagation, IEEE Transactions on* , vol.57, no.12, pp.3728-3735, Dec. 2009.
- [59] Nakano, H.; Morishita, K.; Yamauchi, J.; , "Extremely Wide-band, Low-profile BOR-SPR Antenna," *Antenna Technology: Small Antennas and Novel Metamaterials, 2008. iWAT 2008. International Workshop on* , vol., no., pp.20-23, 4-6 March 2008.
- [60] Schaubert, D.; Kollberg, E.; Korzeniowski, T.; Thungren, T.; Johansson, J.; Yngvesson, K., "Endfire tapered slot antennas on dielectric substrates," *Antennas and Propagation, IEEE Transactions on* , vol.33, no.12, pp. 1392- 1400, Dec 1985.
- [61] Elsherbini, A.; Sarabandi, K.; , "Directive Coupled Sectorial Loops Antenna for Ultrawideband Applications," *Antennas and Wireless Propagation Letters, IEEE* , vol.8, no., pp.576-579, 2009.